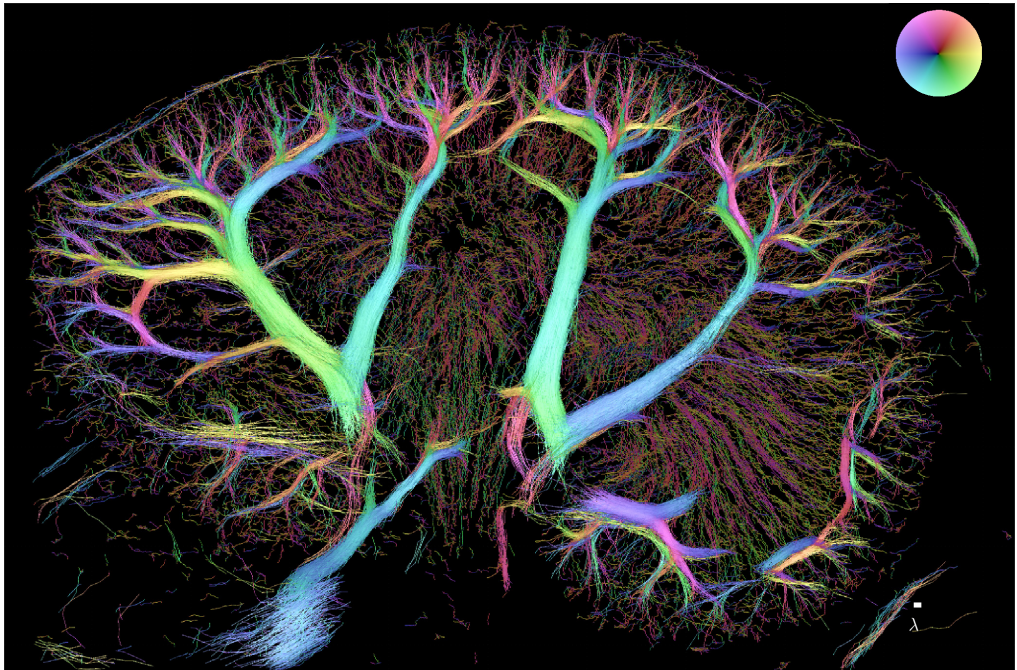


Ph.D. Thesis



Super-resolution ultrasound imaging

Author: Iman Taghavi

Supervised by: Prof. Jørgen Arendt Jensen, Ph.D., Dr. Techn.

Co-supervised by: Assoc. Prof. Matthias Bo Stuart, Ph.D.

Technical University of Denmark, Kgs. Lyngby, Denmark, 2022

Cover image: Super-resolution ultrasound image of a rat kidney. Illustrating the capability of ultrasound imaging systems in visualization of deep vessel structure down to micrometer scale and with sub-wavelength resolution.

Center for Fast Ultrasound imaging (CFU)

DTU Health Tech

Department of Health Technology

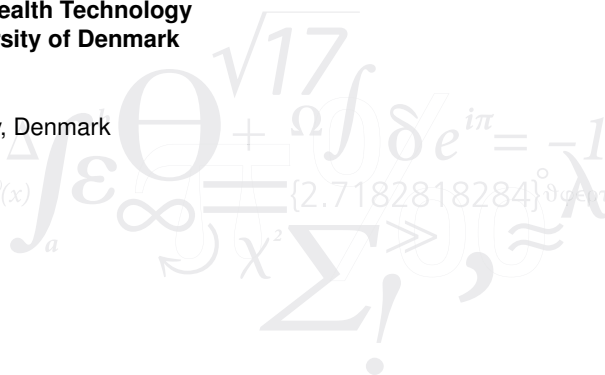
Technical University of Denmark

Ørsteds Plads

Building 349

2800 Kgs. Lyngby, Denmark

$$f(x+\Delta x) = \sum_{i=0}^{\infty} \frac{(\Delta x)^i}{i!} f^{(i)}(x)$$



{2.7182818284} διαφέρουσα ποσότητα

Preface

This Ph.D. thesis has been submitted to the Department of Health Technology at Technical University of Denmark (DTU) in partial fulfillment of the requirements for acquiring the Ph.D. degree. The research providing the foundation for this thesis has been conducted for three years, from March 1st, 2019 to February 28th, 2022, at the Center for Fast Ultrasound Imaging (CFU), Department of Health Technology. The project has been supervised by Prof. Jørgen Arendt Jensen, Ph.D., Dr. Techn., and co-supervised by Assoc. Prof. Matthias Bo Stuart, Ph.D.

Iman Taghavi
Kgs. Lyngby, Denmark
February 2022

Contents

Preface	iii
Summary	vii
Resumé	ix
Acknowledgments	xi
List of Figures	xiii
List of Tables	xix
Abbreviations	xxi
1 Introduction	1
1.1 Background	1
1.2 Purpose and Motivation	4
1.3 Scientific Contributions	4
1.3.1 Journal papers	4
1.3.2 Publications not included in the thesis	6
1.3.3 List of Presentations	7
1.4 Outline of Thesis	7
2 Simulations and measurements	9
2.1 Simulations	9
2.2 Data acquisition	12
2.3 Phantom measurement	14
2.4 Animal experiments	18
3 Super-resolution Imaging	21
3.1 Detection	21
3.1.1 Optimized threshold	23

3.1.2	Simulation results	25
3.2	Motion Correction	26
3.2.1	Method	26
3.2.2	Evaluation	28
3.2.3	Results	28
3.2.4	Discussion	36
3.3	Tracking	40
3.3.1	Tracking algorithms	40
3.3.2	Evaluation	45
3.3.3	Simulation results	45
3.3.4	Measurement results	49
3.3.5	In vivo results	50
3.3.6	Forward-backward tracker	56
3.3.7	Discussion	57
4	Blood Vessel Segmentation	63
4.1	Method	63
4.1.1	Vessel Classification	63
4.1.2	Vessel Segmentation	65
4.1.3	Characterization	67
4.2	Results	69
4.3	Discussion	78
5	Conclusion	81
	Bibliography	83
	References from Chapter 1	83
	References from Chapter 2	87
	References from Chapter 3	88
	References from Chapter 4	90
	References from Chapter 5	91
	Appendices	93
	Paper 1: In vivo Motion Correction in Super Resolution Imaging of Rat Kidneys	93
	Paper 2: Super-resolution imaging with ultrasound for visualization of the renal microvasculature in rats before and after renal ischemia: A pilot study	107
	Paper 3: Evaluation of 2D super-resolution ultrasound imaging of the rat renal vasculature using <i>ex vivo</i> micro-computed tomography	123
	Paper 4: Ultrasound Super-Resolution Imaging with a Hierarchical Kalman Tracker	137

Paper 5: Blood Vessel Segmentation in Super-Resolution Ultrasound Imaging of Healthy Rat Kidneys	157
Paper 6: Super-resolution ultrasound imaging can quantify alterations in intrarenal microbubble velocities in rats	169
Paper 7: Super-Resolution Ultrasound Imaging of Rat Kidneys before and after Ischemia-Reperfusion	185
Paper 8: Tracking Performance in Ultrasound Super-Resolution Imaging	191
Paper 9: Super-resolution Ultrasound Imaging of the Renal Microvasculature in Rats with Metabolic syndrome	197
Paper 10: Automatic Classification of Arterial and Venous Flow in Super-resolution Ultrasound Images of Rat Kidneys	203
Paper 11: Microbubble tracking with a forward-backward strategy	207
Patent: Ultrasound Super-resolution Imaging	215

Summary

Super-resolution ultrasound imaging (SRI) can achieve a resolution beyond the spatial resolution imposed by the conventional diffraction-limited imaging systems. SRI combines many image and signal processing methods to detect and track contrast agents, i.e., microbubbles (MBs), down to the very smallest vessels. The technique can resolve tiny vessels that are impossible to image with conventional ultrasound imaging. Therefore, SRI has a big potential in medical imaging with clinical applications in diagnosing and monitoring vascular diseases, cancer, and diabetes. However, various trade-offs make SRI challenging in many scenarios. Spatial vs. temporal resolution, acquisition time vs. MB concentration, MB concentration vs. localization precision, and tissue motion vs. image resolution are only some of the known trade-offs. This Ph.D. project aimed to develop an improved processing pipeline that can cope with tissue motion and MB tracking in a complex vascular tree such as the rodent renal vasculature.

All the data for the projects were acquired with a commercial BK5000 scanner with a frame rate of 50 Hz and a linear array probe or their equivalent simulation models. An SRI processing pipeline, adapted to the BK5000 scanner, was outlined prior to this Ph.D. project, and my work involved making the pipeline more robust.

The first improvement was attained by adding a motion correction algorithm to the SRI processing pipeline. The timing between the CEUS and B-mode images was used to bind motion field and MB positions together, providing motion-corrected MB positions. The in-plane motion was estimated with a mean precision below $10\ \mu\text{m}$ in the rat kidneys, resulting in an enhancement in the resolution from $90\ \mu\text{m}$ before the motion correction to $55\ \mu\text{m}$ after the motion correction.

Next, the SR images were improved by employing more advanced tracking methods. It was shown that the tracking performance can be improved by using Kalman and hierarchical Kalman trackers. This part of the project has been continued by upgrading the Kalman-based trackers with a forward-backward approach.

Lastly, the quantification of SR images was investigated. A primary classification and segmentation method showed the possibilities for quantifying the morphology and dynamics of the attained SR images of the rat renal vasculature. The statistically significantly different features between vein and artery tracks in the SR images were investigated to explore possibilities for automated image segmentation, and the challenging problems with quantifying the track-based vascular structures and dynamics were discussed.

Resumé

Med super-resolution ultrasound imaging (SRI) kan man opnå en billedopløsning, som er ud over den, de konventionelle diffraktionsbegrænsede ultralydssystemer kan opnå. SRI kombinerer mange billed- og signalbehandlingsmetoder til at detektere og spore mikrobobler (MB, ultralydskontrast) på deres vej ud i de allermindste kar. Teknikken har et stort potentiale inden for medicinsk billeddannelse til diagnosticering og behandlingsmonitorering af vaskulære sygdomme, cancer og diabetes. Forskellige elementer i SRI-billeddannelsen gør teknikken udfordrende at anvende i mange situationer. Rumlig opløsning vs. tidsmæssig opløsning, scanningstid vs. MB-koncentration, MB-koncentration vs. lokaliseringspræcision og vævsbevægelse vs. billedopløsning er blot nogle af de forhold, man skal afveje, når man skal scanne og processere super-resolution (SR)-billederne.

Dette ph.d.-projekt havde til formål at udvikle en forbedret processeringspipeline, der kunne korrigere vævsbevægelser og forbedre sporingen af MB'er i et komplekst vaskulært netværk med udgangspunkt i rottenyrers kar. Data blev indsamlet med en kommerciel BK5000-scanner med en billedhastighed på 50 Hz og en lineær transducer, eller tilsvarende simuleringer til in silico forsøg. En SR-processeringspipeline, tilpasset BK-5000 scanneren, blev skitseret forud for dette Ph.D. projekt, og mit primære arbejde lå i at gøre pipelinen mere robust.

Den første forbedring af pipelinen blev opnået ved at udvikle en algoritme til korrektion af vævsbevægelser. Tingen mellem de kontrastforstærkede billeder af MB'erne og B-mode billederne blev brugt til at koble bevægelsesfeltet og MB'ernes positioner sammen, hvilket gav bevægelseskorrigerede MB-positioner. Når vi scannede rottenyrerne blev bevægelsen i billedplanet estimeret med en gennemsnitlig præcision under $10 \mu\text{m}$, hvilket resulterede i en forbedring af opløsningen fra $90 \mu\text{m}$ før bevægelseskorrekturen til $55 \mu\text{m}$ efter bevægelseskorrekturen.

Dernæst blev SR-billederne forbedret ved at anvende mere avancerede sporingsmetoder. Arbejdet viste, at sporingen af MB'er kan forbedres ved at bruge Kalman og hierarkiske Kalman-trackere. Sidenhen er denne del af projektet blevet videreført ved at opgradere de Kalman-baserede trackere med en fremad-bagud tracking-teknik.

Slutteligt blev kvantificering af SR-billederne undersøgt. En klassifikations- og segmenteringsmetode blev brugt til at vise mulighederne for at kvantificere henholdsvis morfologiske og dynamiske dele af rottenyrekarrene. Statistisk signifikante forskelle

på forskellige karakteristika mellem vene- og arterie-tracks blev undersøgt i forhold til automatisk adskillelse af arterier og vener, og de mange udfordrende problemer i forhold til kvantificering af kar baseret på MB-tracks blev diskuteret.

Acknowledgments

I would like to express my gratitude to my supervisors Prof. Jørgen Arendt Jensen and Assoc. Prof. Matthias Bo Stuart for being patient and supporting me during my Ph.D. study over the past three years. I could have completed my Ph.D. study successfully with your supervision and intellectual insight. I thank the collaborators: Prof. Michael Bachmann Nielsen, Asst. Prof. Charlotte Mehlin Sørensen, and Sofie Bech Andersen from the University of Copenhagen and Copenhagen University Hospital (Rigshospitalet). It was a great pleasure for me to experience and learn new perspectives to my work and broaden my knowledge. I would like to thank my colleagues at the center for fast ultrasound, Technical University of Denmark. Professionally and personally, I enjoyed working with you. Mikkel for his knowledge in ultrasound, detailed explanations, and helping me being familiar with the Danish culture, Sofie for medical knowledge and support with English writing skills, Jihwan and Lasse for help with running jobs on the cluster, Isabella and Sigrid for the positive talks during our coffee breaks. Finally, I thank my family and friends for the love and support you gave me on this journey.

List of Figures

2.1	The geometry of the <i>in silico</i> rat kidney phantom. The red structures have upwards flow and the blue downwards to emulate the arterial and venous flow. <i>Copyright ©2021, IEEE</i>	10
2.2	An example of low, medium, and high density scenarios. The ground truth microbubble (MB) positions in a random frame were convolved with a Gaussian point spread function for better visualization.	12
2.3	The scanner and transducer, used for <i>in vivo</i> and <i>in vitro</i> measurements	13
2.4	BK5000 combined imaging scheme. A contrast sequence is 3×91 emissions followed by a B-mode sequence with 91 emissions. As each image line in the contrast and B-mode images refers to the same lateral position, there is a unique delay between the time of formation of each line in the contrast images to the corresponding line of the B-mode image varying from $f_r/4$ to $3f_r/4$. <i>Copyright ©2021, IEEE</i>	14
2.5	A snapshot of streaming the B-mode and contrast enhanced ultrasound (CEUS) data from BK5000 scanner. The bottom image shows B-mode image of a rat kidney, and the top image shows the CEUS image of that kidney at the same time with some bright MBs.	15
2.6	Experimental setup for phantom measurement	16
2.7	(a) Design of channels in the phantom (b) The 3D printed hydro-gel phantom with micrometer size channels during the perfusion testing.	17
2.8	Schematic of the measurement setup and important parameters.	17
2.9	Data acquisition setup (Credit: Created with BioRender.com)	19
2.10	A simplified drawing of the rat's renal vasculature (coronal view).	20
3.1	Super-resolution processing pipeline	22
3.2	Optimal thresholding based on generalized contrast-to-noise ratio (gCNR). $p_{SN}(x)$ and $p_N(x)$ are the probability distribution of pixel values inside and outside region of interest (ROI)s. P_{fa} is probability of false alarm and P_{miss} is the probability of miss-detection.	23

3.3	(a) Contrast image decomposed to (b) ROIs and (c) background. Notice the low dynamic range and discrete values of contrast image.	24
3.4	Thresholding in theory and practice	25
3.5	Interpolated motion field for a single frame. The arrows indicate direction and magnitude of the motion for a specific time frame. <i>Copyright ©2021, IEEE</i>	26
3.6	The red rectangle in the B-mode image indicates the local region used to estimate the dynamics of the motion.	29
3.7	The estimated motion from the B-mode image in the lateral (bottom) and axial (top) directions, where the blue curve is the estimated motion and the red is the ground truth. <i>Copyright ©2021, IEEE</i>	30
3.8	Position of a non-flowing scatterer after motion compensation. The blue cross indicates the position in the reference frame and the red trajectory indicate its corrected positions in the subsequent frames. <i>Copyright ©2021, IEEE</i>	30
3.9	Motion in the lateral (bottom) and axial (top) directions during the entire experiment. <i>Copyright ©2021, IEEE</i>	31
3.10	Spectral decomposition of the motion signal in the lateral (bottom) and axial directions. <i>Copyright ©2021, IEEE</i>	32
3.11	Three components of the motion estimates in the lateral (bottom) and axial (top) directions. <i>Copyright ©2021, IEEE</i>	33
3.12	Mean and standard deviation (SD) of aligned responses for the heart beating (left) and breathing (right) motion in the lateral (bottom) and axial (top) directions. <i>Copyright ©2021, IEEE</i>	34
3.13	Precision of motion estimates for all rat experiments in the lateral (bottom) and axial (top) directions. <i>Copyright ©2021, IEEE</i>	35
3.14	Intensity and velocity maps of a rat kidney (a) without motion correction, (b) with local motion correction, and (c) with motion field correction. Four profile markers on the intensity and velocity maps were selected exactly at the same place, in which the polynomial fitted profiles to the pixel values of the maps were obtained. <i>Copyright ©2021, IEEE</i>	37
3.15	(a)-(c): Fourier ring correlation (FRC) curves and bit-based information threshold for super-resolution (SR) images. (d): Box plots of FRC metric with one-bit threshold for 3 scenarios for 10 experiments. <i>Copyright ©2021, IEEE</i>	38
3.16	Kalman parameters coarse tuning. (a) shows the full view and the red rectangles are the zoomed regions shown in (b). The <i>in vivo</i> data were processed using the Kalman filter with various parameters σ_ϵ and σ_ν	42
3.17	Hierarchical Kalman tracker flowchart	43

- 3.18 (a) The ground truth tracks marked by several green cross-sections over which the velocity and intensity profiles were calculated. SR images attained by (b) nearest-neighbor, (c) Kalman, and (d) hierarchical Kalman trackers in a scenario with an uncertainty of $\lambda/5$ and medium MB density. 46
- 3.19 Intensity profiles for large (right) and small (left) vessels in a scenario with localization uncertainty of $\lambda/5$ and medium MB density. Each intensity profile is normalized to the value of the intensity at the center of the vessel. 47
- 3.20 (a) Mean and (b) instantaneous velocity profiles for large (right) and small (left) vessels. The ground truth (GT) is the blue parabolic profile. The shaded region indicates the standard deviation. 48
- 3.21 Instantaneous velocity profiles of small vessel with different peak velocities for a scenario with localization uncertainty of $\lambda/5$ and medium MB density. 50
- 3.22 The structure of the tubes inside the phantom is shown in (a) by accumulated CEUS images (left) and SR intensity map (right). The zoomed on the fourth pair of tubes with (b) NN, (c) K, and HK (d) trackers. The flow direction is encoded by colors corresponding to the color wheel (*e.g.*, a vessel with flow from left to the right is shown in yellow). 51
- 3.23 The reconstructed tracks at different levels using the proposed hierarchical Kalman (HK) tracker. The Images show a coronal view of the first kidney in a velocity map. The maximum velocities are corresponded to the maximum velocity range at each level of HK tracker, *i.e.* 3, 6, 9, 12, and 15 mm/s. Small arteries with faster flows are indicated by arrows. 52
- 3.24 Intensity maps of the renal vessels, constructed by (a) NN (b) K and (c) HK trackers. The dynamic range in all images is 60 dB. 53
- 3.25 Velocity maps of the renal vessels, constructed by (a) NN (b) K and (c) HK trackers. The flow direction is encoded by colors corresponding to the color wheel (*e.g.*, a vessel with flow from left to the right is shown in yellow). The velocity magnitude from 0 to 15 mm/s are also encoded by color brightness. 54
- 3.26 Zoomed-in cortical (top) and medullary (bottom) regions of velocity maps, constructed by (a) NN (b) K, and (c) HK trackers. The red markers shows the vessels selected for diameter estimation and the red dashed regions shows the area for calculation of velocity distribution. 55
- 3.27 Distribution of velocity in the (a) cortical and (b) medullary regions. 55

3.28 Comparison of 3-lvl (left), 5-lvl (middle), and 15-lvl (right) HK trackers. The entire kidney is shown in (a) including red rectangles which are zoomed in (b).	56
3.29 Block diagram for tracking MBs in a forward-backward manner	57
3.30 Relative bias (RB) and relative standard deviation (RSD) of velocity profiles of small (top) and large (bottom) tubes. The velocity is estimated using the nearest-neighbor (NN), Kalman (K), and hierarchical Kalman (HK) trackers with forward (F) and forward-backward (FB) configurations. Dashed lines shows the mean profile and shaded area is the standard deviation around the mean value.	58
3.31 Super-resolved velocity map of the cortical region of a rat kidney with a hierarchical Kalman tracking in (a) forward and (c) forward-backward manner. The scale bar in the bottom right is a wavelength. Three regions of (a) and (c), marked by rectangles, are zoomed in (b) and (d).	59
4.1 Super-resolution ultrasound image processing scheme	64
4.2 Zoom in regions of a velocity map demonstrating unclassified vessels. For example, a red color can represent a vein in a region and at the same time an artery in another region.	65
4.3 Manual labeling of different regions (dashed lines) and arterial flow direction in each region (arrows) based on the anatomical information.	66
4.4 Preprocessing steps for track isolation. (a) shows three examples of classified tracks in the outer medulla (left), cortex (middle), and larger vessels (right) with red regions, zoomed in (b). (c): Gaussian filtering. (d): adaptive thresholding.	67
4.5 Steps from isolated tracks to extraction of centerlines in the isolated area. Red dots in the graph show pendant vertices, and green circles are vertices with higher degrees.	68
4.6 Examples of different morphological quantification metrics. Dashed lines are estimated centerlines. (a) diameter and length, (b) tortuosity: ratio of length over distance, (c) Track density: measuring track density in overlapped patches, and (d) Intersegment distance: average distance of a centerline to its adjacent centerlines.	70
4.7 Classified tracks into groups of arteries and veins. (a) classified arteries (b) classified veins, and (c) combination of arteries and veins after classification. Comparing (c) with (a) and (b), the dashed oval region shows a noticeable sparser arteries compared with veins in the cortex, and the dashed rectangles show two example of the region with many arteries behind the veins.	72

4.8	Automatic segmentation of examples in Figure 4.4 (left: outer medulla, middle: cortex, right: larger vessels). Red dashed lines are the estimated centerlines, and yellow dashed lines are estimated vessel walls.	73
4.9	Velocity distribution in different regions of the kidney	73
4.10	CDF plots of velocity estimates in the arteries (red) and veins (blue) in various regions for 10 rat kidneys. Solid line is the mean CDF plot and the shadow area is the standard deviation of the CDFs for 10 rats. Peak velocity is marked by \times	74
4.11	Distribution of estimated diameters in the outer medulla	74
4.12	Segment lengths distribution in the IM and OM regions.	75
4.13	Distribution of tortuosity in the outer medulla	76
4.14	Track density distribution in different regions of the kidney	76
4.15	The moving average blood velocity in the DVR (red) and AVR (blue) of the outer medulla in 10 healthy kidneys. The moving average window size is 1 minute. In all the cases, a lower velocity in the AVR was observed.	77
4.16	SR images of the classified vessels on the other 9 kidneys. Arterioles are shown in red and venules in blue. The kidney for rat 5 is shown in Fig 4.7.	78

List of Tables

2.1	Parameters used in the <i>in silico</i> rat kidney phantom, <i>Copyright ©2021, IEEE</i>	11
2.2	Parameters used in the <i>in silico</i> X-phantom	11
3.1	Overall precision of motion estimates for all rat experiments. All values in μm . <i>Copyright ©2021, IEEE</i>	34
3.2	Observations regarding large and small values of σ_ν and σ_ϵ	44
3.3	Definition of profile-based metrics.	46
3.4	Assignment-based ranking for Nearest-Neighbor (NN), Kalman (K), and Hierarchical Kalman (HK) trackers using 100 independent simulations for each scenario. The tracker with the best metric for various uncertainty ($\lambda/20 \sim \lambda/2$) and MB density (low, medium, high) scenarios is included in the Table. In scenarios where the best tracker was not significantly superior, the other trackers with relative metric difference less than 2% are included as well.	47
3.5	Profile-based metrics for a medium density scenario with localization uncertainty of $\lambda/5$	49
3.6	Statistics of the instantaneous velocity profiles for a medium density scenario with localization uncertainty of $\lambda/5$	49
3.7	Diameters of the four marked vessels in Figure 3.26.	56
4.1	Median and inter-quartile range of estimated features for the classified arteries/DVR bundles (red) and veins/AVR bundles (blue) in three regions. The 95% confidence interval and p -value for each metric are reported. The gray highlighted metrics were considered statistically significant by the Wilcoxon signed-rank test ($p \leq 0.006$).	71

Abbreviations

AVR	Ascending vasa recta
BPM	Beats per minutes
CEUS	Contrast enhanced ultrasound
CNR	Contrast-to-noise ratio
CO	Cortex
CT	Computed tomography
DVR	Descending vasa recta
FN	False negative
FP	False positive
FRC	Fourier ring correlation
FWHM	Full width at half maximum
gCNR	Generalized contrast-to-noise ratio
HK tracker	hierarchical Kalman tracker
IM	Inner medulla
IQR	Interquartile range
JSC	Jaccard similarity coefficient

K tracker	Kalman tracker
MAP	Mean arterial pressure
MB	Microbubble
MI	Mechanical index
NN	Nearest neighbour
OM	Outer medulla
PDF	Probability density function
PEGDA	Polyethylene glycol diacrylate
RB	Relative bias
RF	Radio-frequency
RMSE	Root mean square error
ROI	Region of interest
RSD	Relative standard deviation
SD	Standard deviation
SNR	Signal-to-noise ratio
SR	Super-resolution
SRI	Super-resolution imaging
SRUS	Super-resolution ultrasound
SVD	Singular Value Decomposition
TP	True positive
ULM	Ultrasound localization microscopy

1.1 Background

The spatial resolution of imaging systems has conventionally been limited by diffraction, meaning that it has not been possible to resolve two structures located spatially closer than half of a wavelength. Many efforts have been made to acquire images with high resolution, literally named super-resolution imaging. A direct approach to increase the resolution is using higher frequency (Lockwood et al. 1996); however, this is limited by both hardware and attenuation of high frequencies in the tissue. Since the spatial resolution close to the probe is proportional to the distance with respect to the object rather than the wavelength, near-field imaging can be employed for super-resolution imaging in the shallow depths (Fink and Tanter 2010; Shekhawat and Dravid 2005).

In this study, the terms ultrasound super-resolution imaging (SRI), ultrasound localization microscopy (ULM), or super-resolution ultrasound (SRUS) refer to ultrasound imaging techniques that can achieve a sub-wavelength resolution (λ/n with $n > 2$) in the deep tissue. These techniques were primarily inspired by the breakthrough invention in optical microscopy (Barnett and Ziskin 2007; Hess, Girirajan, and Mason 2006; Rust, Bates, and Zhuang 2006), which led to the 2014 Chemistry Nobel Prize to Eric Betzig, Stefan Hell, and William Moerner. Their techniques were based on fast cameras and switchable fluorescence sources, of which only a selective subset of sources was activated in each image to avoid the diffraction limit of the close sources. The accumulation of a stack of these images, each with a different subset of spatially separated sources, allowed the creation of a final image with a resolution beyond the diffraction limit, although each frame were diffraction-limited.

This idea was brought to ultrasound imaging in 2010 (Couture, Tanter, and Fink 2010) and the first *in vitro* SRI was acquired in 2011 (Couture, Besson, et al. 2011), showing the ability of the SRI technique to visualize a single micro-channel containing microbubble (MB)s. The first *in vivo* SRI was introduced at the same time (Siepmann et al. 2011), where a diluted infusion of contrast agents was used to provide isolated MBs in the diffraction-limited frames. An *in vitro* investigation of resolving two spatially close channels confirmed that SRI could resolve vessels with a distance less than half of a wavelength (Viessmann et al. 2013). Since then, the field has been progressed rapidly and comprehensive reviews of the field can be found in (Couture, Hingot, et al. 2018) and (Christensen-Jeffries, Couture, et al. 2020).

The challenges in making and using an super-resolution (SR) image can be divided

into five categories: 1) detection of individual MBs, 2) tissue motion correction, 3) MB tracking, 4) interpretation of the data, and 5) curse of dimensionality for 3D SRI.

The first challenge was how to resolve isolated contrast agents, and the straightforward solution was using diluted MBs. However, using diluted MBs imposed long data acquisition requirements for full saturation and visualization of the entire vessel bed. It was shown that there is a compromise between the spatial resolution and acquisition time that is imposed by the microvascular flow (Hingot et al. 2019).

Moving from *in vitro* to *in vivo* studies revealed also the second challenge of ultrasound SRI. Motion in the *in vivo* data was inevitable, and therefore, many early *in vivo* studies where focused on a fixated object, e.g. mouse-ear (Christensen-Jeffries, Browning, et al. 2015) and rat brain (Errico et al. 2015). However, in real clinical application, it is not always possible to fixate internal organs like kidneys, and the overall motion could be larger than the size of vessels. Therefore, some motion correction methods were developed to cope with scanning moving objects. Hansen et al. (2016) showed that motion correction of data from a rat kidney could increase precision from 22 to 8 μm for a single vessel. In (Foiret et al. 2017), the effect of motion was reduced by excluding frames with a high motion from breathing, yielding a resolution of 2.1 μm in the axial direction and 6.1 μm in the lateral direction. Two-stage motion correction was applied in Harput, Christensen-Jeffries, Brown, et al. (2018) with a combination of affine registration for the global motion and nonrigid registration for estimation of the local deformation of tissue. This required a nonrigid transformation estimator and reduced the width of the microvessels by a factor of roughly 1.5. Recently, Kierski et al. (2020) investigated a more advanced imaging technique by combining ultrasound microscopy and dual-frequency imaging technique for obtaining a high signal-to-noise ratio (SNR) and a high frame rate. Segments of 100 contrast images with a frame rate of 500 Hz were acquired, followed by B-mode images with a frame rate of 5 Hz. The B-mode frame rate was only sufficient to capture the motion from breathing, and more rapid movements had to be discarded.

Tracking of MBs is another important part of the ultrasound SRI, as it improves the final quality and sharpness of the SR images. Tracking also enables the estimation of clinically meaningful parameters, such as blood flow velocity. However, tracking performance degrades in the presence of high MB concentrations and localization uncertainty. The third challenge is therefore the development of a high performance tracking algorithm. As ultrasound SRI was primarily inspired by optical microscopy, many of the optical particle tracking methods have the same potentials in ultrasound SRI. These methods range from the simple nearest neighbour (NN) (Crocker and Grier 1996) to multi-frame data structure techniques such as dynamic programming (Geiger et al. 1995; Rink et al. 2005), combinatorial schemes (Sbalzarini and Koumoutsakos 2005; Song et al. 2017), multi hypothesis tracking (Ulman et al. 2017), and using explicit motion models (e.g., Kalman filtering) (Godinez et al. 2009; Ku et al. 2009). These tracking approaches together with different localization methods were objectively compared in (Chenouard et al. 2014), and it was shown that tracking based on the Kalman filtering outperformed other methods in most of the examined scenarios; however, none of the trackers performed best

across all scenarios. In 2015, the first *in vivo* ultrasound SRI with velocity mapping was introduced (Christensen-Jeffries, Browning, et al. 2015). While the approach used basic maximum intensity cross-correlation within a small search window, it revealed the great potential of resolving flow velocities in vessels located close to each other. At the same time, an NN tracker was used for the velocity estimation in ultrasound SRI (Errico et al. 2015). In 2016, a modified version of the Markov chain Monte Carlo data association was implemented for the detection and tracking of MBs. The proposed approach demanded higher computational complexity and was not compared with other tracking algorithms (Ackermann and Schmitz 2016). In 2017, the optimal assignment of distances was used to improve the basic greedy-based NN assignment to achieve total minimum distance (Song et al. 2017). This optimal assignment was based on the Hungarian algorithm (Kuhn 1955). Finally, the Kalman-based trackers were employed in ultrasound SRI and used in very recent works in 2019 and 2020 (Solomon et al. 2019; S. Tang et al. 2020).

In conventional vascular ultrasound imaging, the field of view usually contains a few large vessels, which allows easy classification of the arteries and veins. Such classification is also crucial in SRI, but is more challenging due to the plentiness and complexity of vessels in the image. It brings us to the forth challenge in SRI which is the quantification. Since the resolution of conventional ultrasound has been limited to the macrovasculature, the morphological segmentation has been performed manually by the operator, and the vessels with automatic segmentation have been restricted to the quantification of large vessels in the conventional B-mode images (Amir-Khalili, Hamarneh, and Abugharbieh 2015; Smistad and Løvstakken 2016) or tissue perfusion in contrast enhanced ultrasound (CEUS) (Wei et al. 2001). Entering the microscopic realm demands development of automated or semi-automated vessel segmentation algorithms. Ultrasound SR images are made from an accumulation of hundreds of thousands of MB trajectories, called a track map. Contrary to the conventional vascular imaging, each vessel in an SR image may not appear as a solid structure or get filled completely with MB tracks. Therefore, available segmentation techniques can easily misinterpret individual tracks as an individual vessel or fail to distinguish the structures in the ultrasound SR image. So far, the quantification of ultrasound SR images has been performed manually based on region of interest (ROI) (Andersen, Hoyos, et al. 2019; Andersen, Taghavi, et al. 2020; Lowerison et al. 2020; Ozdemir et al. 2021; Sjøgaard et al. 2020), or a single tube characterization for the validation of the SRI (Harput, Toulemonde, et al. 2020; Jensen et al. 2020).

Last but not least, motion correction and tracking of data using 2D information are challenging since the actual vessel structures are 3D, and motion exists in all three dimensions. The difficulty in the quantification of the projected 3D volumes into 2D images has lit up another necessity in ultrasound SRI, which is the need to move to 3D and volumetric SRI. The increasing number of data channels in 3D SRI imposes higher complexity and dimensionality for both hardware and software, making implementation of 3D SRI challenging. However, 3D SRI has been recently attained using matrix probes (Chavignon et al. 2020; Heiles et al. 2019), 2D sparse array (Harput, Christensen-

Jeffries, Ramalli, et al. 2019), and row-column arrays (Jensen et al. 2020).

1.2 Purpose and Motivation

This PhD project is part of a larger project with collaboration between the Technical University of Denmark, Copenhagen University, Copenhagen University Hospital (Rigshospitalet), and BK Medical ApS. The overall goal of the project was to translate novel new super resolution techniques from research to commercial and clinical use. In particular, this PhD project focused on giving solution to several of the above mention challenges in ultrasound SRI. This was done by development of a super-resolution processing pipeline with the ability to visualize micro vessels from *in vivo* rat kidneys using a commercial ultrasound scanner. Various methods, including tissue motion correction, MB tracking, and quantification of SR images were developed and evaluated. The software and algorithms were primarily developed for a 2D imaging setup. However, the perspective is to extend ultrasound SRI to 3D and use it as a tool for diagnosis of some diseases, including cancer and diabetes. These kinds of diseases might alter the microvasculature in their early stages of development, and quantitative study of microvasculature using ultrasound SRI could be a break-through in clinical diagnostics.

1.3 Scientific Contributions

A list of published and submitted papers during this PhD project is shown below. The contribution to each paper is described. These papers can be found in the appendix.

1.3.1 Journal papers

- **Paper 1:**

I. Taghavi, S.B. Andersen, C.A.V. Hoyos, M.B. Nielsen, C.M. Sørensen, and J.A.Jensen.

”In vivo Motion Correction in Super Resolution Imaging of Rat Kidneys.”

In *IEEE Trans. Ultrason., Ferroelec., Freq. Contr.*, 2021

Contribution: *Development of the SRI processing pipeline with a motion correction algorithm according to the BK5000 imaging sequence. Evaluation of resolution using the Fourier ring correlation.*

- **Paper 2:**

S.B. Andersen, **I. Taghavi**, C.A.V. Hoyos, S.B. Søggaard, F. Gran, L. Lonn, K.L. Hansen, J.A. Jensen, M.B. Nielsen, and C.M. Sørensen.

”Super-resolution imaging with ultrasound for visualization of the renal microvasculature in rats before and after renal ischemia: A pilot study.”

In *Diagnostics*, 2020

Contribution: *Development of Software and SRI processing pipeline. Image processing and quantification of velocities estimates.*

- **Paper 3:**

S.B. Andersen, **I. Taghavi**, H.M. Kjer, S.B. Søjgaard, C. Gundlach, V.A. Dahl, M.B. Nielsen, A.B. Dahl, J.A. Jensen, and C.M. Sørensen.

”Evaluation of 2D super-resolution ultrasound imaging of the rat renal vasculature using *ex vivo* micro-computed tomography.”

In *Scientific Reports*, 2021

Contribution: *Image processing and quantification of structure. Development of software and SRI processing pipeline.*

- **Paper 4:**

I. Taghavi, S.B. Andersen, M. Schou, C.A.V. Hoyos, F. Gran, M.B. Nielsen, C.M. Sørensen, and J.A. Jensen.

”Ultrasound Super-Resolution Imaging with a Hierarchical Kalman Tracker”

In *Ultrasonics*, 2022

Contribution: *Main author of the article. Development of algorithms for tracking, evaluation, and simulation. Image processing and development of SRI processing pipeline.*

- **Paper 5:**

I. Taghavi, S.B. Andersen, S.B. Søjgaard, M.B. Nielsen, C.M. Sørensen, M.B. Stuart, and J. A. Jensen

”Blood Vessel Segmentation in Super-Resolution Ultrasound Imaging of Healthy Rat Kidneys.”

In *IEEE Trans. Ultrason., Ferroelec., Freq. Contr.*, 2022, Submitted/In preparation

Contribution: *Main author of the article. Development of algorithms for quantification and evaluation of statistical significance. Image processing and development of SRI processing pipeline.*

- **Paper 6:**

S.B. Andersen, **I. Taghavi**, S.B. Søjgaard, C.A.V. Hoyos, M.B. Nielsen, J.A. Jensen, and C.M. Sørensen.

”Super-resolution ultrasound imaging can quantify alterations in intrarenal microbubble velocities in rats.”

In *Diagnostics*, 2022, Submitted/In preparation

Contribution: *Image processing and quantification of velocities. Development of software and SRI processing pipeline.*

1.3.1.1 CONFERENCE PAPERS

- **Paper 7:**

S. B. Andersen, C. A. V. Hoyos, **I. Taghavi**, F. Gran, K. L. Hansen, C. M. Sørensen,

J. A. Jensen, and M. B. Nielsen

”Super-Resolution Ultrasound Imaging of Rat Kidneys before and after Ischemia-Reperfusion”

In *Proc. IEEE Ultrason. Symp.*, pp. 1169-1172, 2019.

Contribution: *Image processing and software development.*

- **Paper 8:**

I. Taghavi, S.B. Andersen, C.A.V. Hoyos, M. Schou, S.H. Øygaard, F. Gran, K.L. Hansen, C.M. Sørensen, M.B. Nielsen, M.B. Stuart, and J.A. Jensen

”Tracking Performance in Ultrasound Super-Resolution Imaging.”

In *Proc. IEEE Ultrason. Symp.*, pp. 1-4, 2020.

Contribution: *Main Author*

- **Paper 9:**

S. B. Sørsgaard, S. B. Andersen, **I. Taghavi**, C. A. V. Hoyos, K. L. Hansen, F. Gran, J. A. Jensen, M. B. Nielsen, and C. M. Sørrensen

”Super-resolution Ultrasound Imaging of the Renal Microvasculature in Rats with Metabolic syndrome.”

In *Proc. IEEE Ultrason. Symp.*, pp. 1-4, 2020.

Contribution: *Image processing and software development.*

- **Paper 10:**

I. Taghavi, S.B. Andersen, S.B. Sørsgaard, M.B. Nielsen, C.M. Sørrensen, M.B. Stuart, and J. A. Jensen

”Automatic Classification of Arterial and Venous Flow in Super-resolution Ultrasound Images of Rat Kidneys.”

In *Proc. IEEE Ultrason. Symp.*, pp. 1-4, 2021.

Contribution: *Main Author*

- **Paper 11:**

I. Taghavi, S.B. Andersen, M. Schou, M.B. Nielsen, C.M. Sørrensen, M.B. Stuart, and J. A. Jensen

”Microbubble tracking with a forward-backward strategy.”

In *Proc. SPIE Med. Imag.*, pp. 1-6, 2022.

Contribution: *Main Author*

1.3.2 Publications not included in the thesis

From the above mentioned contributions, papers **2**, **3**, **6**, **7**, and **9** are mainly concentrated on the clinical application of the super-resolution images and can be found in the attachments. Instead, this thesis focused on technical aspects of the super-resolution processing.

1.3.3 List of Presentations

- Artimino 2019 (Ultrasound conference on tissue motion and blood velocity imaging), Nijmegen, Netherlands, *Super-resolution ultrasound imaging of rat kidneys*, oral presentation.
- IEEE International Ultrasonics Symposium 2019 Glasgow, UK, *Super-Resolution Ultrasound Imaging of Rat Kidneys before and after Ischemia-Reperfusion*, oral presentation.
- IEEE International Ultrasonics Symposium 2020, Las Vegas, US (Virtual participation), *Tracking Performance in Ultrasound Super-Resolution Imaging*, oral presentation.
- IEEE International Ultrasonics Symposium 2021, Virtual, *Automatic Classification of Arterial and Venous Flow in Super-resolution Ultrasound Images of Rat Kidneys*, poster presentation.
- SPIE Medical Imaging 2022, San Diego, US (pre-recorded), *Microbubble tracking with a forward-backward strategy*, oral presentation.

1.4 Outline of Thesis

The thesis is written in five chapters as described below:

Chapter 1: provides an introduction to the field and its background. The purpose of this project is stated. Scientific contributions to this project are listed, and finally the outline of the thesis is described.

Chapter 2: presents the methods for data acquisition, including simulations, measurements, and *in vivo* experiments. Also, details regarding the hardware and measurement setups are provided.

Chapter 3: describes the SRI processing pipeline and its different building blocks. The two main challenges of the SRI, including tissue motion correction and MB tracking are addressed and evaluated. These findings are according to the papers 1, 4, 8, and 11.

Chapter 4: presents a method for quantification of SR images, acquired by the SRI processing pipeline. This includes the classification and segmentation of arterial and venous flow in the rat kidneys according to the papers 5 and 10.

Chapter 5: concludes the thesis and provides an outlook and perspective of the project.

CHAPTER 2

Simulations and measurements

One of the most fundamental and important steps in this project was data acquisition. The project was broad and covered a wide range of data collection. The raw data were obtained to investigate SRI and to improve its underlying processing steps. Three different kind of data were collected during this project, including simulations, phantom measurements, and *in vivo* experiments. In this chapter, the simulations and measurement setups are described.

Some parts of this chapter are adopted from paper 1 (Taghavi, Andersen, Hoyos, Nielsen, et al. 2021), paper 4 (Taghavi, Andersen, Hoyos, Schou, et al. 2022), and paper 5.

2.1 Simulations

Three type of simulations were used in this project to evaluate different algorithms in the super-resolution processing pipeline. The simulations were conducted using Field IIpro (Jensen 1996, 2014; Jensen and Svendsen 1992) in Matlab (MathWorks, U.S.) to generate the data, where the positions of scatterers are known. In all simulations, the evolution of scatter positions can be described by

$$\vec{r}_i(t + T_{prf}) = \vec{r}_i(t) + T_{prf}\vec{V}_f(t, \vec{r}_i(t)) + \vec{M}(t, \vec{r}_i(t)), \quad (2.1)$$

where $\vec{r}_i(t)$ is the position of scatterer i at time t , T_{prf} is the time between pulse emissions, $\vec{V}_f(t, \vec{r}_i(t))$ is the velocity of the scatterer due to the blood flow, and $\vec{M}(t, \vec{r}_i(t))$ is the motion of the kidney at the position $\vec{r}_i(t)$.

The simplest phantom contained a matrix of point targets located at a distance of 2 mm from each other in both the axial and lateral direction. The stationary scatterers were obtained by forcing two right terms of the (2.1) to zero, *i.e.* $\vec{V}_f(t, \vec{r}_i(t)) = 0$ and $\vec{M}(t, \vec{r}_i(t)) = 0$. This phantom was used to evaluate the localization precision of individual scatterers without tissue motion and flow present.

Another phantom was designed based on the dimensions of the rat kidney. The kidney phantom is shown in Figure 2.1. It mimics the flow in small arteries and veins, where the arterial flow was toward the perimeter and the return venous flow was in the opposite direction. A sparse distribution of scatterers were located randomly in the individual tubes with parabolic velocity profiles and a Gaussian distributed scattering amplitude. This was set using the $\vec{V}_f(t, \vec{r}_i(t))$ term in (2.1). The scatterers moved along the tube axis and were

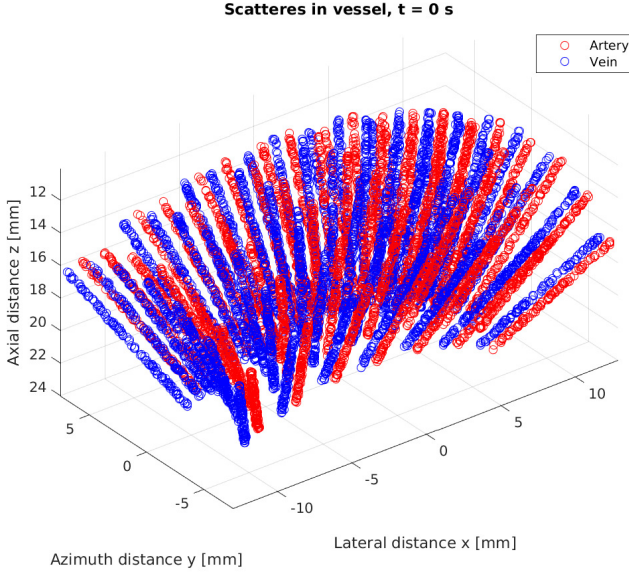


Figure 2.1: The geometry of the *in silico* rat kidney phantom. The red structures have upwards flow and the blue downwards to emulate the arterial and venous flow. *Copyright ©2021, IEEE*

returned in the adjacent tube, when they reached the tube's end. The various dimensions of the phantom are listed in Table 2.1. A slice of the tubes in the elevation direction of the probe was selected in this simulation. The realistic motion from a rat kidney was applied to surrounding stationary scatterers by adding $\vec{\mathcal{M}}(t, \vec{r}_i(t))$ term in (2.1). This ensured that both the stationary tissue and tube locations varied across the heart and breathing cycles for validation of the motion estimation and motion correction algorithms. This phantom was used to evaluate the motion estimation precision in presence of underlying flow.

Lastly, an X-shaped phantom with crossing tubes was simulated. This was made by generating MB positions, each with a known ground truth track and uniformly random lifetime, moving with different velocities. Individual MBs inside the tube were also uniformly distributed with sub-wavelength distance. MB positions were generated according to the ground truth tracks. To simulate uncertainty in MB position estimates, a random Gaussian error was added. Three different trackers' performance was investigated for uncertainties ranging from $\lambda/20$ to $\lambda/2$, where λ is a wavelength. In this study, localization uncertainty refers to the SD of the Gaussian position error. The various parameters of the simulations are listed in Table 2.2. This phantom was used to evaluate the tracking performance under

Table 2.1: Parameters used in the *in silico* rat kidney phantom, Copyright ©2021, IEEE

Parameters	Value
Tube length	10 mm
Tube radius	100 μm
Velocity	2 mm/s
Velocity profile	Parabolic
Number of scatterers	20 per tube
Number of tube pairs	49
Angle between tube pairs	10°
Distance between pairs	1 mm

Table 2.2: Parameters used in the *in silico* X-phantom

Parameters	Value
Tube length	10 mm
Tube radius	250 μm & 125 μm
Peak velocity	10 mm/s & 5 mm/s
Velocity profile	Parabolic
Angle between tubes	15°
Frame-rate (f_r)	55 Hz
Wavelength (λ)	256 μm
Average MB count	17, 31, 51 MB.frame ⁻¹
MB density at phantom center	1.37, 2.46, 4.24 MB. λ^{-2} .frame ⁻¹
Localization uncertainty	$\lambda/20$ to $\lambda/2$

different scenarios of MB concentrations and localization uncertainties.

The low, medium, and high-density scenarios had an average MB count of 17, 31, and 51 MB/frame, corresponding to MB density of 1.37, 2.46, and 4.24 MB/ $(\lambda^2 \cdot \text{frame})$ at the center of the phantom. MB density, calculated based on the size of the vessels and the shape of the phantom, provides an average number of MBs per resolution cell (λ^2). For example, a MB density of 4 MB/ $(\lambda^2 \cdot \text{frame})$ at the center of the phantom means that, on average, we can find 4 MBs in a resolution cell at the center of the phantom. A snapshot of the low, medium, and high density scenarios is shown in Figure 2.2, demonstrating that in the low-density scenario, most of the MBs were not overlapping. In the medium-density scenario, some of the MBs were overlapping, and most of the MBs were overlapping in the high-density scenario. The MB concentration is difficult to control *in vivo* after they

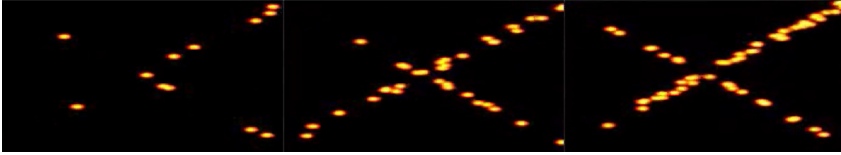


Figure 2.2: An example of low, medium, and high density scenarios. The ground truth MB positions in a random frame were convolved with a Gaussian point spread function for better visualization.

enter the bloodstream; even though the dilution of SonoVue is adjusted to have fewer overlapped MBs, the concentration may vary depending on the vessel structure and blood velocity in specific types of vessels, especially in a complex organ such as kidneys. For this reason, various MB densities were simulated separately, and the aim was to get the best tracking performance in multiple scenarios or most of the individual scenarios.

The above mentioned simulations provide ground truth for evaluation of SRI processing pipeline, which is discussed in Chapter 3.

2.2 Data acquisition

A BK5000 scanner (BK Medical, Herlev, Denmark) and a "hockey stick" X18L5s transducer (BK 9009, BK Medical, Herlev, Denmark) was employed for the data acquisition. The scanner was modified by BK medical with a research interface, which allowed long acquisitions through the live streaming of the data to a disk. The scanner and transducer are shown in Figure 2.3. X18L5s is a linear array probe with 150 elements which covers an imaging width of 24 mm, which was sufficient for scanning a full rat kidney. The height of the aperture was 3.4 mm, and the elevation focus was at 20 mm. Therefore the elevation F-number (depth divided by active aperture width) is 5.9 leading to an imaging plane with varying thickness between 3.4 mm to 1.5 mm.

The scanner acquired two types of images consequently for each frame. First, a contrasted enhanced image based on amplitude modulation was performed (Eckersley, Chin, and Burns 2005). Then, a conventional B-mode image was acquired. Both imaging sequences used a transmit frequency of 6 MHz, equivalent to wavelength of $256 \mu\text{m}$ in the tissue. A sliding aperture of 25 active elements with a focal depth of 10 mm is used for imaging. Each active aperture emitted three times with the pulse repetition frequency f_{prf} of 19.6 kHz, one emission with all elements (full amplitude) and two emissions with even/odd indexed elements (half amplitude). By combining the three emissions, the amplitude-modulated response was calculated as

$$r_{am}(t) = r_{full}(t) - 2r_{half}(t) = r_{all}(t) - r_{even}(t) - r_{odd}(t), \quad (2.2)$$



(a) BK5000 scanner

(b) X18L5s (Hockey stick) transducer

Figure 2.3: The scanner and transducer, used for *in vivo* and *in vitro* measurements

where $r_{am}(t)$ is the amplitude-modulated signal, $r_{full}(t) = r_{all}(t)$ is the received signal when all elements were employed, and $r_{half}(t) = r_{even}(t) = r_{odd}(t)$ is the received signal when half of elements were used. The amplitude-modulated signal contains enhanced non-linear signal from the contrast agents. The active aperture then slid across the array for a total of 91 active sub-apertures, called the contrast sequence. Then, a B-mode image was acquired using the same 91 active sub-apertures, however emitted only once per active sub-aperture with full amplitude, called B-mode sequence. This resulted in $3 \cdot 91 + 91 = 364$ emissions per full sequence. The emissions timeline is shown in Figure 2.4, demonstrating the individual emissions of full sequence over time. Considering the f_{prf} , a full sequence resulted in a frame-rate of 53.85 Hz. To avoid MB disruption, an mechanical index (MI) of 0.2 was used, based on empirical trials.

Three emissions of the contrast sequence corresponded to the same image line as one emission in the B-mode sequence. Considering the emissions timeline, shown in Figure 2.4, one can show that the time difference between the n^{th} line of a contrast image and the m^{th} line of its next B-mode image is

$$t_d(n, m) = \frac{3N_{lines} - 3n + m + 1}{f_{prf}}, \quad (2.3)$$

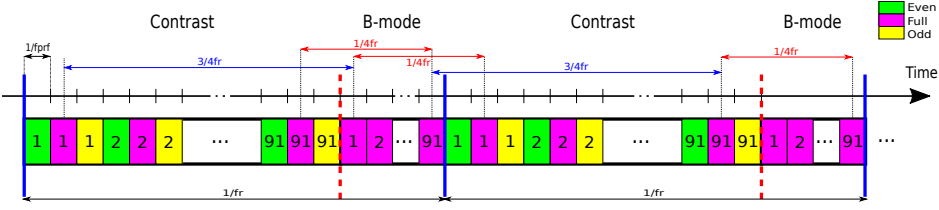


Figure 2.4: BK5000 combined imaging scheme. A contrast sequence is 3×91 emissions followed by a B-mode sequence with 91 emissions. As each image line in the contrast and B-mode images refers to the same lateral position, there is a unique delay between the time of formation of each line in the contrast images to the corresponding line of the B-mode image varying from $f_r/4$ to $3f_r/4$. Copyright ©2021, IEEE

where $n, m \in \{1, 2, \dots, N_{lines}\}$ and N_{lines} is the number of lines in the image. Section 3.2 shows that this time difference has an important role in binding the estimated motion in the B-mode image to the true MB positions in the contrast image.

An example of B-mode and contrast images is shown in Figure 2.5 from BK5000, notice how MBs are visible in the top (CEUS) and not in the bottom (B-mode). The movement of the kidney would be clearly visible in a video stream of B-mode images. In the contrast image, the MBs stand out with a higher contrast. Therefore, the B-mode images can be used to estimate the tissue motion and the contrast images can be used for localization of the contrast agents.

There were two major hardware limitations regarding the data acquisition. The first limitation was low frame-rate due to sliding aperture imaging sequence, and the second limitation was weak contrast signal. For real-time data acquisition purposes, contrast envelope data was calculated in a 16-bit unsigned integer format inside FPGAs. 16 bits are capable of representing $20 \log_{10}(2^{16} - 1) \approx 96$ dB dynamic range of data. However, the extracted MB signals were about 80 dB below the tissue signal level and very close to the system noise floor. This resulted in the contrast data with 16 dB dynamic range and low SNR.

Data acquisition was followed the exact same sequence and parameters for all of the phantom measurements and animal experiments, unless it is mentioned specifically.

2.3 Phantom measurement

In vitro measurement was performed on a 3D printed hydrogel phantom. The setup for the measurement is shown in Figure 2.6.

Measurement Setup: The phantom was mounted inside a water tank using a 3D printed holder. This ensures high acoustical coupling between the fixated probe and phantom, and prevents dehydration of the phantom. The reverberations from the bottom

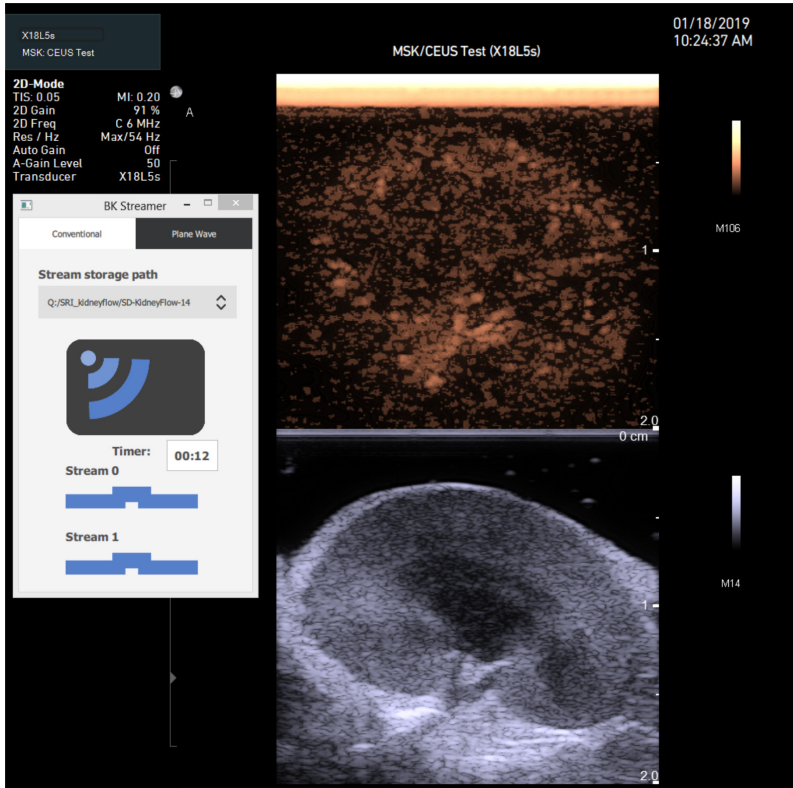


Figure 2.5: A snapshot of streaming the B-mode and CEUS data from BK5000 scanner. The bottom image shows B-mode image of a rat kidney, and the top image shows the CEUS image of that kidney at the same time with some bright MBs.

of the water tank could generate unwanted artifacts and disrupt the image. To prevent these reverberations, rubber sheets were placed beneath the phantom. The water tank was secured on top of a motorized micro-positioning system, which was a combination of 8MTF-75LS05 x-y translation stage with resolution of $0.31\mu\text{m}$ resolution, and an 8MR190-2-28 rotation stage with resolution of 0.01° (Standa, Vilnius, Lithuania). The entire setup was seated on a Newport PG seriesTM optical breadboard (U.S. Patent 6,598,545) and mounted on an IsoStationTM optical table with pneumatic isolation (Irvine, California) to provide a robust vibration performance.

Phantom fabrication: The polyethylene glycol diacrylate (PEGDA) 3D printing technique was recently translated for use in ultrasound imaging (Ommen, Schou, Zhang, et al. 2018). In this technique, stereolithography was employed to build structures with

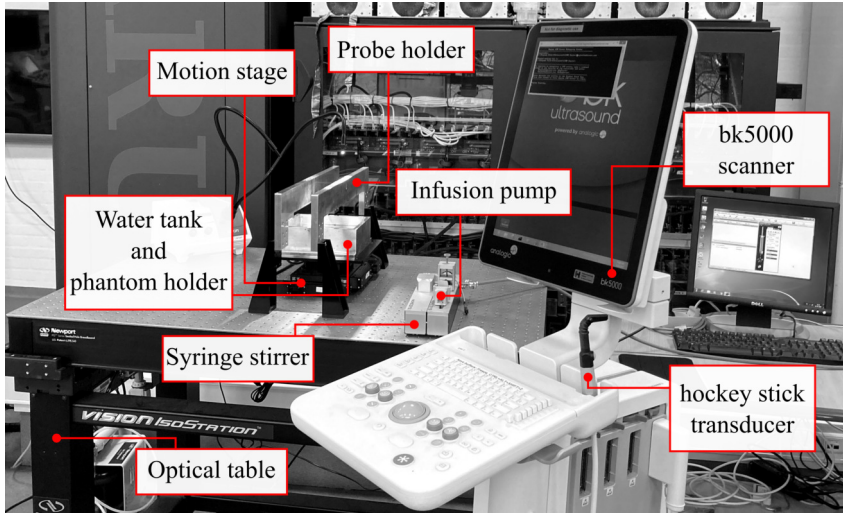


Figure 2.6: Experimental setup for phantom measurement

the scale of 10-200 μm . The delicate structure design based on 3D printing makes this technique favorable for SRI measurements and validation. The phantom was made using hydrogel, a liquid solution of PEGDA (M_n 700 g/mol, 455008, Sigma-Aldrich). In the stereo-lithography, the phantom is 3D printed in a layer by layer fashion using photochemical processes, *i.e.* each layer is locally solidified to build up the desired structure by illuminating the liquid solution. After solidification of a layer, that layer was pulled out of the liquid resin to make a room for a new layer. This process was done using a Digital Mirror Device (DMD, DLP9500UV, Texas Instruments, TX). The experiments showed that using this device, it was possible to make layers with a thickness of 20 μm and separation of 10.8 μm between printed voxels (Ommen, Schou, Beers, et al. 2019, 2021; Ommen, Schou, Zhang, et al. 2018). The technique provides a very flexible phantom design with known structures for validation of the SRI.

The 3D printing nature of the phantom allows implementation of arbitrary 3D structures, however, in our study we worked with a 2D super-resolution imaging and therefore the phantoms with 2D structure were used. The layout of a phantom with several channel pairs is shown in Figure 2.7-a. The flow in the paired channels is opposite to each other and the entire structure can be seen in x-z plane, making it a suitable known structure with low complexity for 2D imaging. The correctness of the channels and the perfusion was tested using fruit dye before usage. This process is shown in Figure 2.7-b (Ommen 2020).

To avoid phantom dehydration, they were kept in the water. Even though the structure and its dimension is known, one should note that this kind of phantoms expands when exposed to the water for a long period of time. It reaches an equilibrium after one day, with

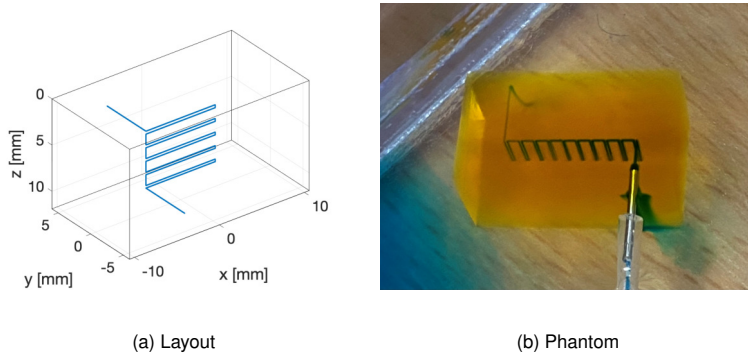


Figure 2.7: (a) Design of channels in the phantom (b) The 3D printed hydro-gel phantom with micrometer size channels during the perfusion testing.

approximately 2.6% (Ommen 2020). This phenomenon should be considered carefully either by compensating for the expansion, or by guiding the expansion in one direction using a confining structure.

Imaging sequence: The B-mode and CEUS imaging sequence, described in Section 2.2, were acquired over 10 minutes for the *in vitro* measurements. The main parameters for the scan are summarized in Figure 2.8.

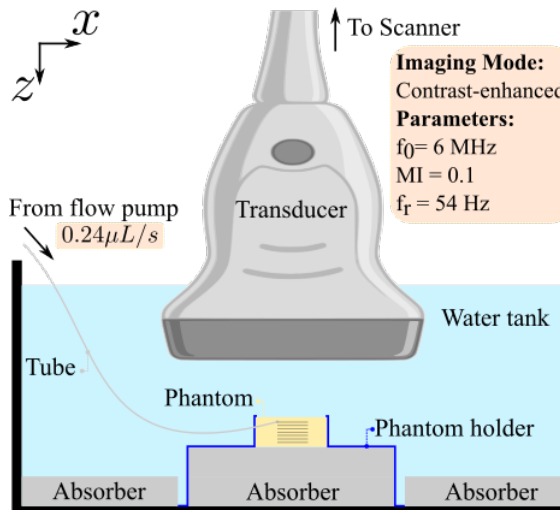


Figure 2.8: Schematic of the measurement setup and important parameters.

In this study, the phantom measurement was merely used for confirmation of the structure that can be obtained by the SRI processing pipeline, discussed in Chapter 3.

2.4 Animal experiments

In the studies of this thesis, the left kidney of 10 healthy male Sprague-Dawley rats (mean weight: 337.3 g, standard deviation (SD) \pm 48.3 g) was scanned. The rats were obtained from Taconic A/S (Lille Skensved, Denmark). The animals were housed at the animal facility at the Department of Experimental Medicine, University of Copenhagen until use. Animal caretakers ensured the rats well being. The rats had standard conditions regarding the water, chow, and 12/12 hours dark/light cycle. The experiments were conducted at the Department of Biomedical Sciences at the University of Copenhagen, and all procedures on the rats agreed with the ethical standards of the university which comply with the EU Directive 2010/63/EU for animal experiments. The protocols for the animal experiments were approved by the Danish Animal Experiments Inspectorate, the Ministry of Environment and Food.

Before the scan: The rats were anesthetized using 5% isoflurane in 65% nitrogen and 35% oxygen; and the anesthesia was maintained with 1–2% isoflurane. The rats lay in the supine position on a heating table to ensure a steady body temperature (37 °C). A ventilator (Ugo Basile, Gemonio, Italy) with 69-72 respirations/min was used for ventilation through a tracheostomy. The left kidney was covered with air-free gel. A "hockey stick" X18L5s transducer (BK 9009, BK Medical, Herlev, Denmark) position was adjusted by looking at the real-time B-mode images on the BK5000 scanner (BK Medical, Herlev, Denmark). At the desired view of the kidney, the probe was fixated using a probe holder.

During the scan: The MBs (SonoVue, Bracco Imaging, Milan, Italy) diluted with isotonic saline were infused in the jugular vein through polyethylene catheters (PE-10). A Statham P23-dB pressure transducer (Gould, Oxnard, CA, USA) through a polyethylene catheter (PE-50) in the left carotid artery was used to measure the mean arterial pressure (MAP). The kidneys were scanned for 10 minutes and the beamformed radio-frequency (RF) data consisted of over 32,000 frames of both B-mode and CEUS images. The setup for scans and experiments is shown in Figure 2.9.

In the laparotomized rats, the left side of the diaphragm was pulled slightly in the cranial direction to reduce the respiratory motion. However, the kidney was still moving with the respiration. The physiological motion induced by heart beating, breathing, and muscle contraction varied among the animals (Taghavi, Andersen, Hoyos, Nielsen, et al. 2021).

The animal experiments were used in the different parts of the thesis including evaluation of the SRI processing pipeline in Chapter 3 and quantification of the SR images in Chapter 4.

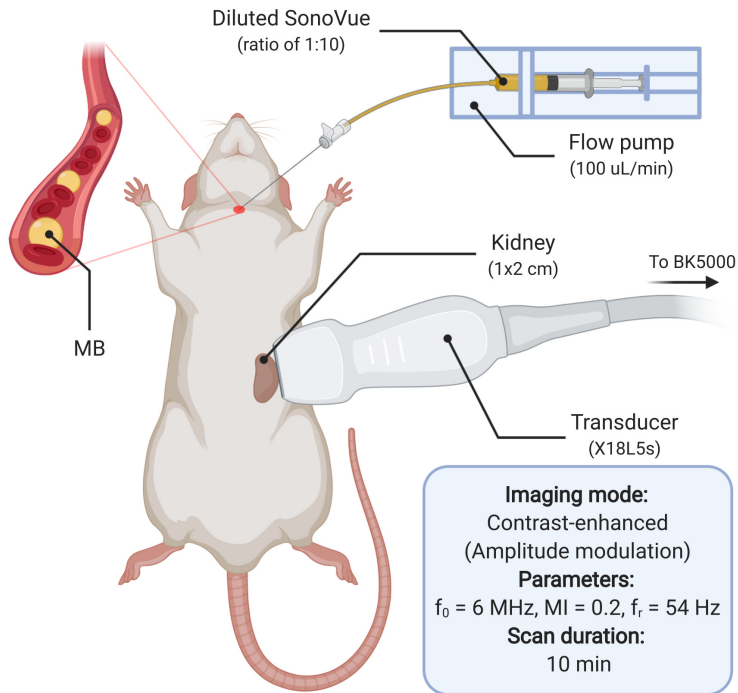


Figure 2.9: Data acquisition setup (Credit: Created with BioRender.com)

Medical terminology: Various terms are used throughout the thesis, referring to specific regions or blood vessels in the kidney. These regions and vessels are defined below and shown in a simplified illustration of the renal anatomy, in Figure 2.10 (Credit: the simplified renal anatomy was drawn based on Figure 1.1 of (Johnson et al. 2018)).

- **Renal:** relating to the kidneys.
- **Cortex:** the outer or superficial part of the kidney.
- **Medulla:** the inner or deep part the kidney. The medulla is divided into two parts, the outer and inner medulla.
- **Renal artery:** the branches of the abdominal aorta which supply the kidneys.
- **Segmental artery:** the secondary branches of the renal arteries that run toward the cortex on the sides of the medulla.

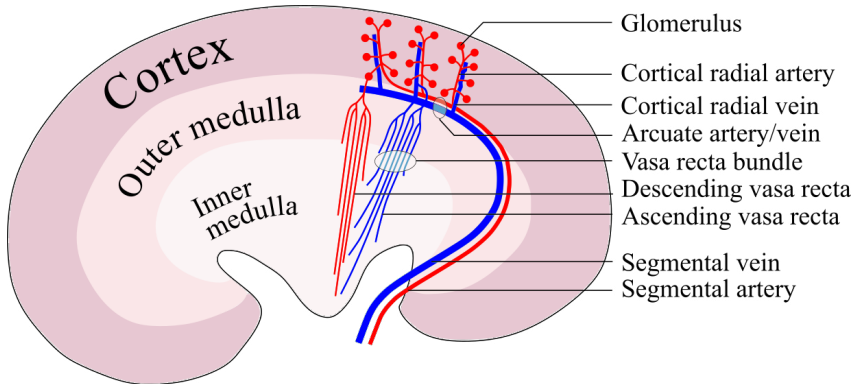


Figure 2.10: A simplified drawing of the rat's renal vasculature (coronal view).

- **Arcuate artery:** the branches of segmental arteries that form arches between cortex and medulla.
- **Cortical radial artery:** the branches of the arcuate arteries that travel toward the renal surface.
- **Afferent arterioles:** the branches of the cortical radial arteries to the glomeruli.
- **Glomerulus:** a small convoluted or intertwined network of capillaries that perform the first step of filtering blood.
- **Vasa recta:** the descending arterioles or ascending venules in the medulla. Vasa recta can be traced within vascular bundles (Ren et al. 2014).

CHAPTER 3

Super-resolution Imaging

Ultrasound super-resolution imaging provides a way to visualize the delicate microvasculature. This visualization is the result of a processing pipeline, shown in Figure 3.1. The processing pipeline includes several processing steps some of them can be performed simultaneously and some can only be used in sequential processing steps. The raw data may be preprocessed before entering the SRI pipeline to enhance the SNR. The three major steps of this processing are as follows:

1. **Detection:** to detect MBs in the CEUS images and extract their positions.
2. **Motion correction:** to compensate MB positions for the tissue motion over time.
3. **Tracking:** to link corrected MB positions and make trajectories of MBs.

After these three steps, a super-resolution image can be created by inserting the MB trajectories in the form of intensity or velocity maps. In this chapter, the processing steps are described in detail. The contribution of the work in thesis is mainly on the motion correction and development of more robust tracking algorithms for the super-resolution images of rat kidneys.

Some parts of this chapter are adopted from paper 1 (Taghavi, Andersen, Hoyos, Nielsen, et al. 2021), paper 4 (Taghavi, Andersen, Hoyos, Schou, Gran, et al. 2022), paper 8 (Taghavi, Andersen, Hoyos, Schou, Øygaard, et al. 2020), and paper 11. Patent application on the tissue motion correction and tracking algorithm explained in this chapter has been purchased by BK Medical ApS, Herlev, Denmark (US Patent 20210407043A1).

3.1 Detection

Detection is the first and essential step to identify MBs and to extract the centroid of the MB positions from the contrast images. This process consists of two parts:

1) **SNR enhancement:** by simple thresholding, model fitting (Cheezum, Walker, and Guilford 2001), spatial, or spatio-temporal filtering (Furnival, Leary, and Midgley 2017; Lok et al. 2020), *e.g.*, singular value decomposition (SVD), Gaussian, Laplacian of Gaussian.

2) **localization:** using peak detection, centroid estimation methods (*e.g.*, weighted centroid) (Bankman 2009; Cheezum, Walker, and Guilford 2001), onset localization (Christensen-

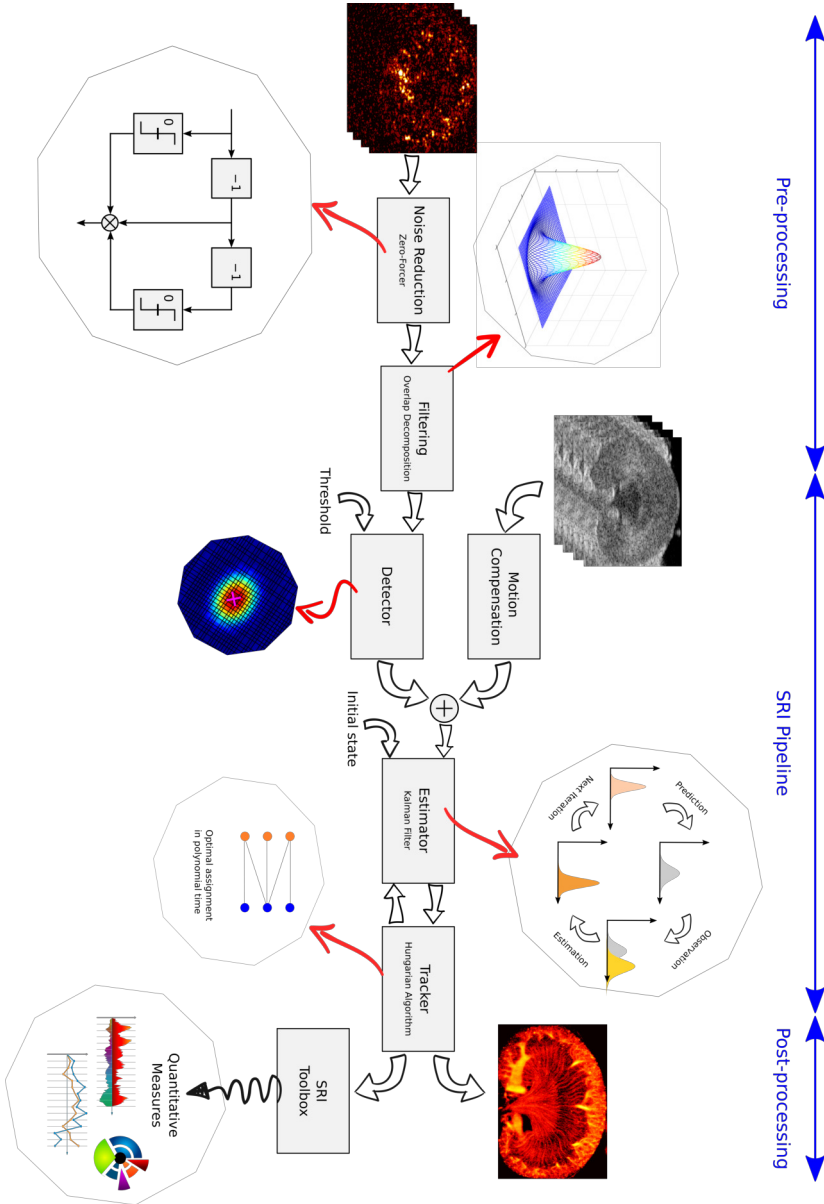


Figure 3. 1.: Super-resolution processing pipeline

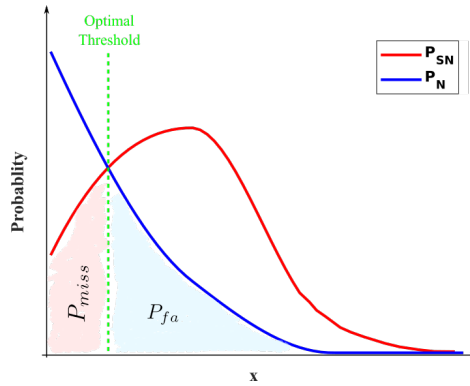


Figure 3.2: Optimal thresholding based on gCNR. $p_{SN}(x)$ and $p_N(x)$ are the probability distribution of pixel values inside and outside ROIs. P_{fa} is probability of false alarm and P_{miss} is the probability of miss-detection.

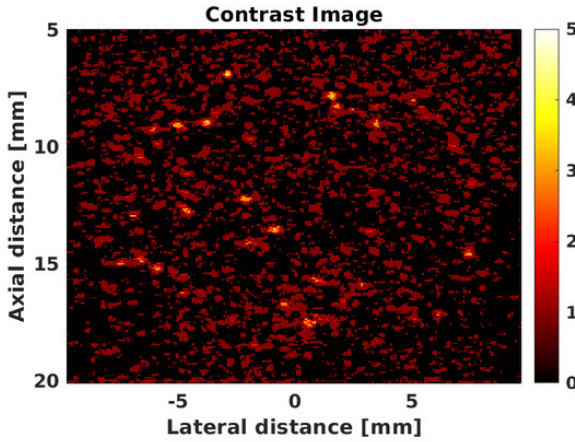
Jeffries et al. 2017), or learning-based methods (Brown, Ghosh, and Hoyt 2020; Liu et al. 2020).

A single or a combination of the above mentioned methods may be used for detection. In this project, the contrast images had only a few quantization levels resulting in a low SNR and the following simple and fast approach was chosen. To improve SNR, a Gaussian filter was applied to the contrast images after thresholding. The symmetric Gaussian filter had a size of 7 pixels with a standard deviation of 1 pixel, where pixel size in the lateral direction was $80 \mu\text{m}$ and $24 \mu\text{m}$ in the axial direction. Then, the weighted-centroid algorithm (Matlab function “*regionprops*”) was used to estimate the centroid of the MBs.

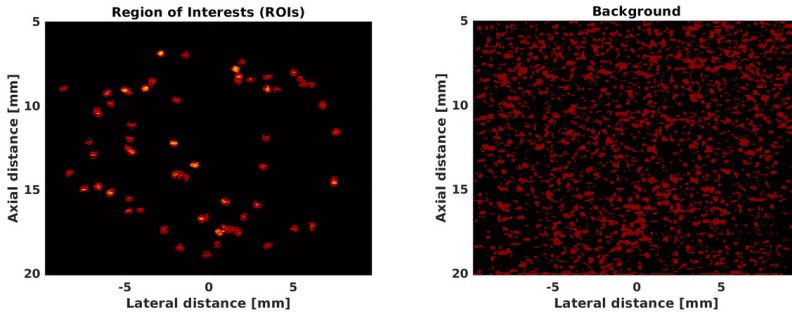
3.1.1 Optimized threshold

A simple and brilliant idea for calculation of contrast-to-noise ratio (CNR), called generalized contrast-to-noise ratio (gCNR), was proposed in (Rodriguez-Molares et al. 2020) to provide a robust calculation of CNR against dynamic range alterations. So no matter how data are beamformed, compressed, and stored, the final metric provides a fair comparison for any kind of scenario. gCNR is calculated based on the probability density function (PDF) of pixel values. The concept can be extended for calculation of the gCNR in CEUS images as described below: Consider the contrast regions are marked in the image as the ROIs. By denoting the PDF of pixels values inside the ROIs as $p_{SN}(x)$, and the PDF of pixel values outside the ROIs as $p_N(x)$, these PDFs can be shown as Figure 3.2. Denoting the overlapping area under the $p_{SN}(x)$ and $p_N(x)$ as OVL , the gCNR is defined as: $gCNR = 1 - OVL$. Since the area under a PDF is always 1, gCNR has a value between 0 and 1.

The gCNR was used as a criteria for optimization of threshold. In the first step, the contrast image shown in Figure 3.3-a is decomposed to ROIs (Figure 3.3-b) and



(a) Contrast Image



(b) ROIs

(c) Background

Figure 3.3: (a) Contrast image decomposed to (b) ROIs and (c) background. Notice the low dynamic range and discrete values of contrast image.

background (Figure 3.3-c). The ROIs were the pixels which were potentially signal plus noise while the background counted as noise.

To decompose the contrast image, the following steps were used:

1. The histogram of all pixel values was calculated.

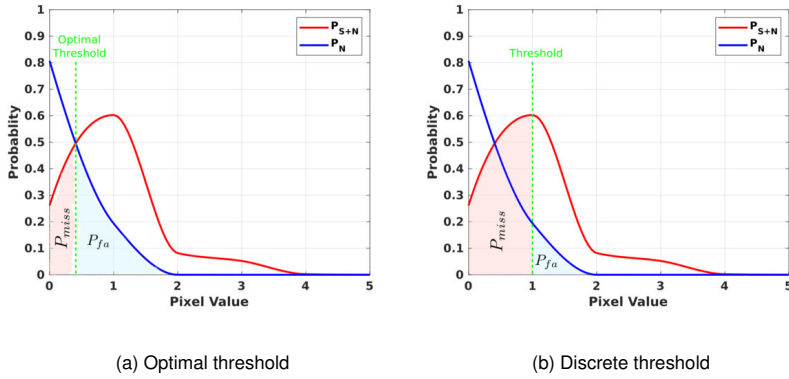


Figure 3.4: Thresholding in theory and practice

2. A simple threshold was applied based on maximum of first derivative of the histogram curve.
3. ROIs were defined with a radius of a wavelength around each the centroid of the remained regions.
4. The ROIs subtracted from the original image forming the background and noise.

The gCNR is defined as

$$gCNR = 1 - \left(\int_{-\infty}^{\epsilon} P_{SN}(x)dx + \int_{\epsilon}^{\infty} P_N(x)dx \right), \quad (3.1)$$

where the first integral is the probability of miss-detection and the second integral is the probability of false alarm. $P_{SN}(x)$ is the PDF of pixel values inside the ROIs (signal + noise) and $P_N(x)$ is the PDF of the pixel values outside the ROIs (noise). The optimal value of threshold at the intersection of $P_{SN}(x)$ and $P_N(x)$, shown in Figure 3.4-a, can maximize the gCNR, however, due to the discretization and low dynamic range of the contrast data, the real threshold was set above the first integer, *i.e.* above the optimal threshold (>1), shown in Figure 3.4-b.

3.1.2 Simulation results

The *in silico* matrix phantom, described in Section 2.1, was used for the investigation of localization precision. Having the ground truth of the point targets, the lateral and axial bias and SD were calculated as $-1.46 \mu\text{m} \pm 20.5 \mu\text{m}$ and $0.48 \mu\text{m} \pm 10.7 \mu\text{m}$.

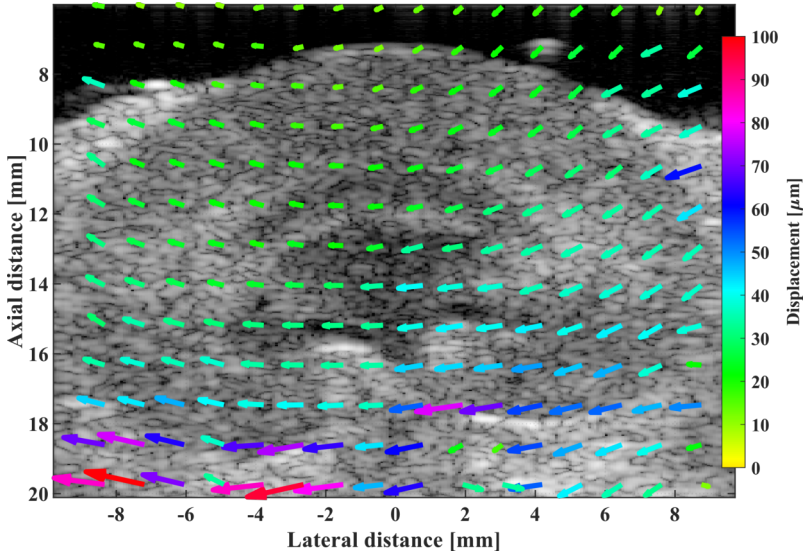


Figure 3.5: Interpolated motion field for a single frame. The arrows indicate direction and magnitude of the motion for a specific time frame. *Copyright ©2021, IEEE*

3.2 Motion Correction

3.2.1 Method

The cross-correlation of the enveloped data in the B-mode images was used for the tissue motion estimation. This technique is primarily called speckle tracking (Trahey, Allison, and Ramm 1987). Regions in the images were correlated to similar regions in a selected reference frame number, and motions in the lateral and axial directions were found. Speckle tracking using the RF data was also tried, but the lateral sampling density was too low to result in an acceptable lateral estimates.

The entire organ was in the field-of-view, and the motion was not uniform across the whole kidney as seen in Figure 3.5. Hence, two different spatial regions do not have the identical displacement, and a single local motion estimation cannot be applied across the whole kidney. Therefore, the B-mode image was divided into smaller spatial blocks (80% overlapped blocks with size of $3 \times 3 \text{ mm}^2$) for block-wise processing. In each block, the estimated motion signal was assigned to the center of that region $\vec{r}_k = (z_k, x_k)$. Putting motion signals at discrete spatial positions and each time frame together forms a discrete motion field, denoted by $\vec{\mathcal{M}}(t_k, \vec{r}_k)$, throughout the entire image. Figure 3.5 illustrates the motion field at specific time frame with arrows on top of the corresponding B-mode frame. In contrast to a rigid structure, notice how the estimated displacements differ spatially.

The motion field was calculated with the following assumptions:

- The local regions were assumed to be small enough so that the motion was spatially invariant within them. Depending on the material and application, this assumption may apply. Kidneys are not rigid, but movements through a small region of local tissue have the same magnitude and direction.
- The frame rate was high enough to capture the fastest varying motion in the temporal domain. The motion variations depend on the source of the motion. In this project, the fastest source of the motion was the heart. According to the Nyquist theorem, the frame rate has to be at least two times the highest frequency in the heartbeat spectrum in order to capture the fastest motion transitions. The motion spectra are investigated in Section 3.2.3.2 below.

The temporal and spatial position of the motion were bound to each other since the image was created by a linear sweep of the beams over time as described in Section 2.2. The motion estimation gives only one estimate per frame. To achieve higher time resolution, the motion time series was upsampled using spline interpolation. Then, the value of the motion at the MB location was calculated by a 2-D spline interpolation over the time interpolated motion field.

Motion estimates for a local part of the renal medulla was used to study the precision and dynamics of the motion estimation algorithm as described in Section 3.2.3.2. The following three scenarios were used to investigate the effect of the motion correction:

1. The SR images were formed directly from the detected positions without motion correction.
2. A small local region was used for the motion correction of the whole image, called a local motion correction.
3. All local regions and motion fields were used for the motion correction of the whole image, called a global motion correction.

Assume a detected MB at the position $\vec{r} = (z_0, x_0)$ in the k^{th} frame, the correct position of that MB, $\hat{\vec{r}} = (\hat{z}_0, \hat{x}_0)$, can be approximated by

$$\hat{\vec{r}} \approx \vec{r} - \vec{\mathcal{M}}\left(\frac{k-1}{f_r} - t_d(m, m), \vec{r}\right), \quad (3.2)$$

where t_d is defined in (2.3), m is the image line that the MB is detected (corresponding to the lateral position of the MB), f_r denotes the frame-rate, and $\vec{\mathcal{M}}(t, \vec{r})$ is the interpolated motion field at time t and position \vec{r} .

Equation (3.2) is an approximation for the motion correction problem, assuming that the motion field is not changing significantly in space and time. In general, the measured

MB location $\vec{r} = (z_0, x_0)$ in k^{th} frame can be written versus the true MB location and the motion field's value at the same temporal and spatial position as

$$\vec{r} = \hat{\vec{r}} + \vec{\mathcal{M}}\left(\frac{k-1}{f_r} - t_d(\hat{n}, m), \hat{\vec{r}}\right), \quad (3.3)$$

where $\hat{\vec{r}} = (\hat{z}_0, \hat{x}_0)$ and \hat{n} are unknown correct MB location and its related image line in the contrast image. The problem of finding $\hat{\vec{r}}$ from the motion field and the measured MB location can be solved similar to a least-squares optimization problem given in

$$[\hat{\vec{r}}, \hat{n}] = \arg \min_{\vec{p}, q} \|\vec{p} - \vec{r} + \vec{\mathcal{M}}\left(\frac{k-1}{f_r} - t_d(q, m), \vec{p}\right)\|_2^2, \quad (3.4)$$

where \vec{p}, q are arguments of the optimization problem.

3.2.2 Evaluation

3.2.2.1 THE PRECISION OF *in vivo* MOTION ESTIMATION

The precision of the motion estimates was investigated in a small region in the outer medulla of the kidney, shown in Figure 3.6. The overall motion was originated from different sources, including motion from the heart beating, the forced ventilation (breathing), smooth muscle contractions, and other movements, which cannot easily be separated out. The three distinct components of the motion signal were separated using Fourier decomposition. Then, the repetitive properties of the breathing and heart beating were used for alignment of all the responses and resulted in a mean response and its precision.

3.2.2.2 RESOLUTION ESTIMATION

The resolution was measured using the Fourier ring correlation (FRC) criterion (Banterle et al. 2013; Hingot et al. 2021; Nieuwenhuizen et al. 2013). Defining the resolution using a simple threshold is controversial (van Heel and Schatz 2005), therefore, in this study a bit-based information threshold was used. Using bit-based information threshold curves for the FRC threshold level is described in (van Heel and Schatz 2005). By inserting each track into a separate image, the SR images were split into two. Matlab's `imhistmatch.m` function was used to equalize the intensity of the split images based on their maximum intensity values. With the two images, FRC curve was calculated based on (Nieuwenhuizen et al. 2013). Then, the resolution was estimated as the inverse spatial frequency at the point where the FRC curve crossed the threshold curve. (van Heel and Schatz 2005).

3.2.3 Results

3.2.3.1 SIMULATION RESULTS

The motion of the *in silico* kidney phantom, described in Section 2.1, has been estimated for the B-mode data and is shown for the first 50 frames in Figure 3.7 in the lateral

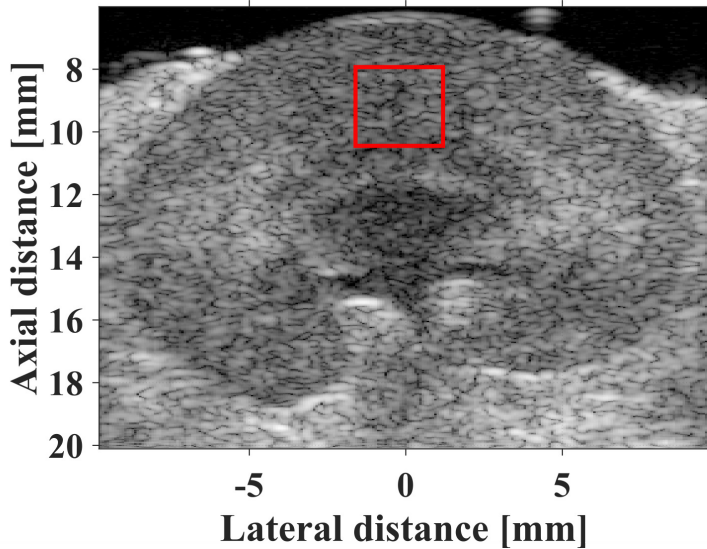


Figure 3.6: The red rectangle in the B-mode image indicates the local region used to estimate the dynamics of the motion.

(bottom) and axial (top) directions, where the blue curve is the estimated motion and the red is the ground truth. The lateral SD was $9.57 \mu\text{m}$ and the axial SD was $1.21 \mu\text{m}$, showing a higher SD for the estimated motion in the lateral direction.

Figure 3.8 shows a non-flowing scatterer (blue cross) in the reference frame and the subsequent corrected positions of this scatterer (red trajectory). These positions were corrected by the motion estimates, resulting in a bias and precision of $10.6 \pm 21.6 \mu\text{m}$ in the lateral and $-10.8 \pm 5.2 \mu\text{m}$ in the axial directions. Similar to the localization step, the axial motion estimations were more precise than the lateral ones.

3.2.3.2 EXPERIMENTAL RESULTS

The motion estimates in both the lateral and axial directions for a single rat are shown in Figure 3.9. A Fourier decomposition of the motion estimates gave the spectra shown in Figure 3.10 with amplitudes in dB, where the lateral spectrum is shown on the bottom and the axial on the top. Both of them exhibited three distinct Fourier series. First, there was a large component around 0 Hz caused by the overall drift of the data. The second series came from the breathing motion. Since the breathing is controlled mechanically by a fixed rate ventilator, the harmonics it produced had a very narrow bandwidth around 70.5 beats per minutes (BPM), with more than 20 harmonics visible on both spectra. Lastly, five harmonics from the heart beating were visible in the lateral motion signal, whose

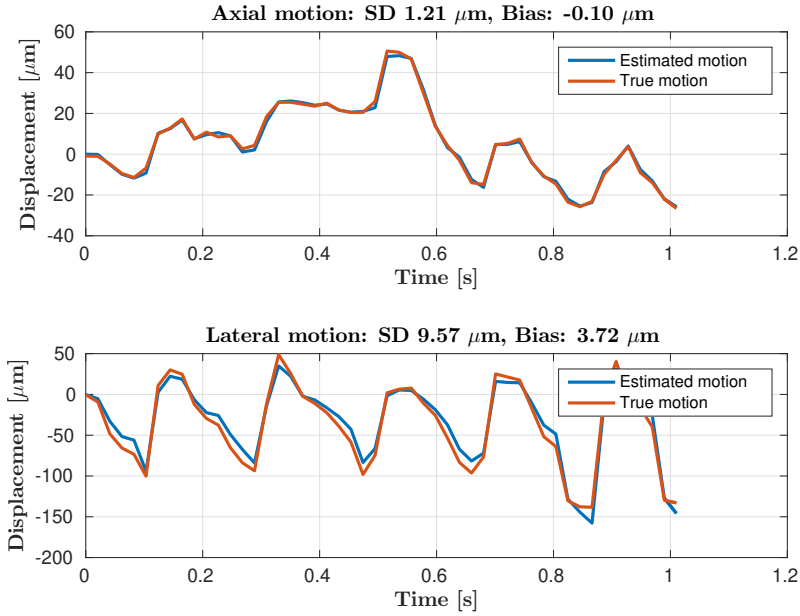


Figure 3.7: The estimated motion from the B-mode image in the lateral (bottom) and axial (top) directions, where the blue curve is the estimated motion and the red is the ground truth. *Copyright ©2021, IEEE*

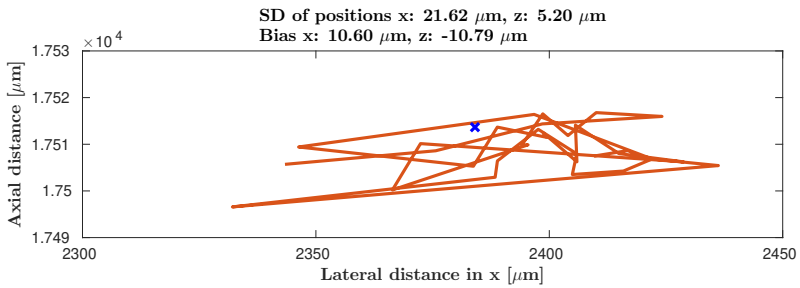


Figure 3.8: Position of a non-flowing scatterer after motion compensation. The blue cross indicates the position in the reference frame and the red trajectory indicate its corrected positions in the subsequent frames. *Copyright ©2021, IEEE*

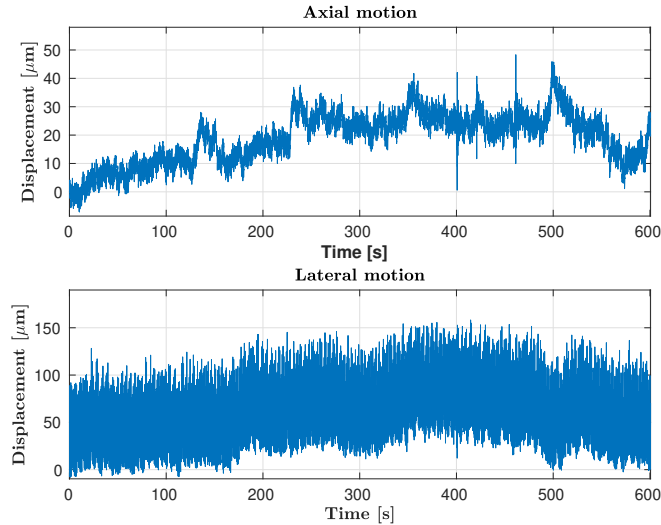


Figure 3.9: Motion in the lateral (bottom) and axial (top) directions during the entire experiment. *Copyright ©2021, IEEE*

amplitude was lower and the components were placed around the harmonics of a heart rate of 353 BPM. The physiological variation of the heart rate causes the harmonics to spread over a larger bandwidth.

Separation of these three Fourier series resulted in the three independent motion signals as shown in Figure 3.11, where the bottom three graphs display the components for the lateral motion. The heartbeat motion series was acquired by filtering the first four harmonics around the heart rate. The breathing motion came from isolation of the first 18 breathing harmonics. Finally, the residual motion was obtained by subtracting two separated series from the motion estimates.

Alignment of repetitive heartbeats and breathing yielded a mean response and its precision. This mean aligned curve and its SD for one of the experiments is shown in Figure 3.12. In this example, the motion estimates for the heart beating, including the physiological variation of the heartbeat, was approximately $\pm 5 \mu\text{m}$ in lateral and $\pm 0.5 \mu\text{m}$ in axial directions. The precisions for these estimates were 0.99 and 0.69 μm , respectively. The breathing motion varied from $-20 \mu\text{m}$ to $+60 \mu\text{m}$ in the lateral and $\pm 4 \mu\text{m}$ axial directions with a precision of 1.64 and 0.22 μm , respectively. The residual motion estimates shown in Figure 3.11 were larger with variations up to nearly 100 μm . Therefore, it is very important to compensate for the overall motion to align up the vessels in a super-resolution image.

The experiment was conducted on the ten different rats and on each rat scanned three times. The experiment setup is explained in Section 2.4. The second scan was done

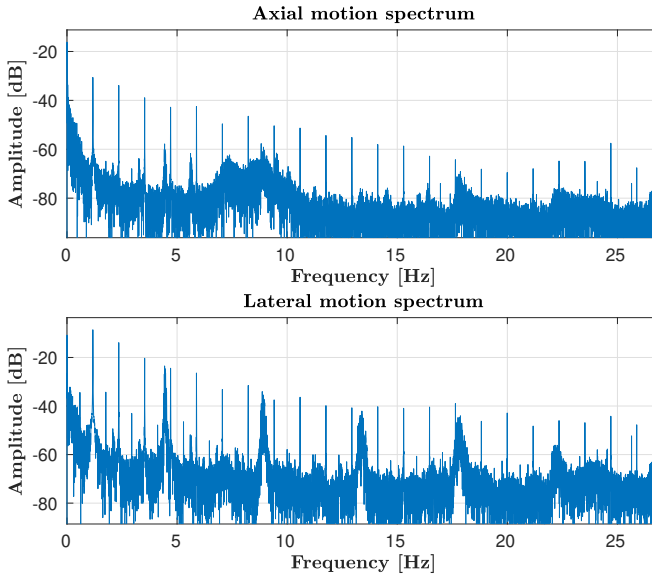


Figure 3.10: Spectral decomposition of the motion signal in the lateral (bottom) and axial directions. *Copyright ©2021, IEEE*

immediately after a clamp on the renal artery or vein was released, and the third scan was performed 1 hour after clamp release*. For each measurement, a similar region and reference frame were selected and the precision of motion estimates were similar to the above example. Figure 3.13 shows this precision for all of the scans and more information about the motion estimates is summarized in Table 3.1. The variation in the precision of motion estimates was quite wide and reached to $20\ \mu\text{m}$. There are several reasons for this. Speckle tracking cannot capture motion in a part of the image that has too large motion or movement in the out-of-plane direction, for example, when the set-up has been touched, which can induce significant kidney motion. However, the motion corrected image has the potential to visualize capillary flow, since the motion estimate's precision is round a factor of two smaller than the $10\ \mu\text{m}$ size of the capillaries and often a factor of 5 smaller.

3.2.3.3 MOTION COMPENSATED IMAGES

The log-scaled intensity maps without motion correction, with local motion correction, and with the motion field correction are shown in first row of the Figure 3.14. The second row of Figure 3.14 shows the corresponding velocity maps, where the color indicates the direction of the blood flow, *e.g.*, a yellow color shows a flow from the left to the right. The

* The purpose of clamping is to model an ischemic disease for a clinical study (Andersen et al. 2020) and is not related to the motion correction

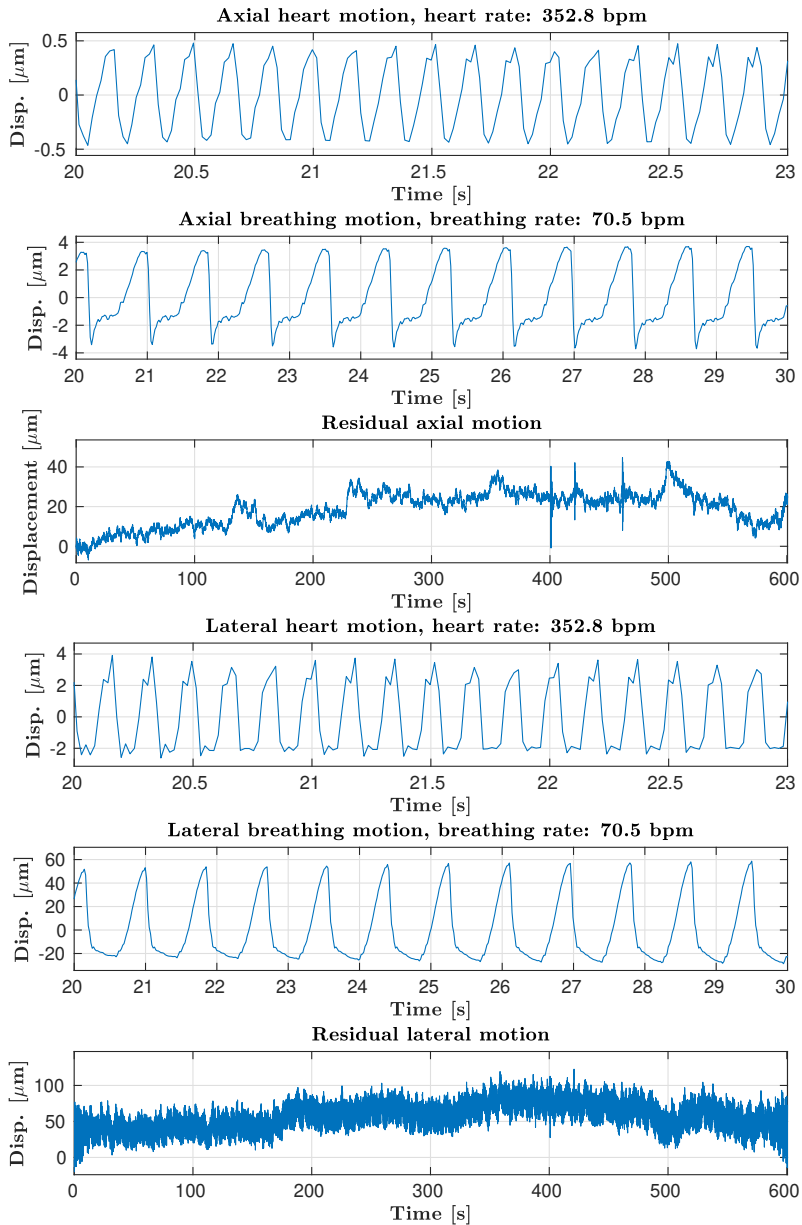


Figure 3.11: Three components of the motion estimates in the lateral (bottom) and axial (top) directions. Copyright ©2021, IEEE

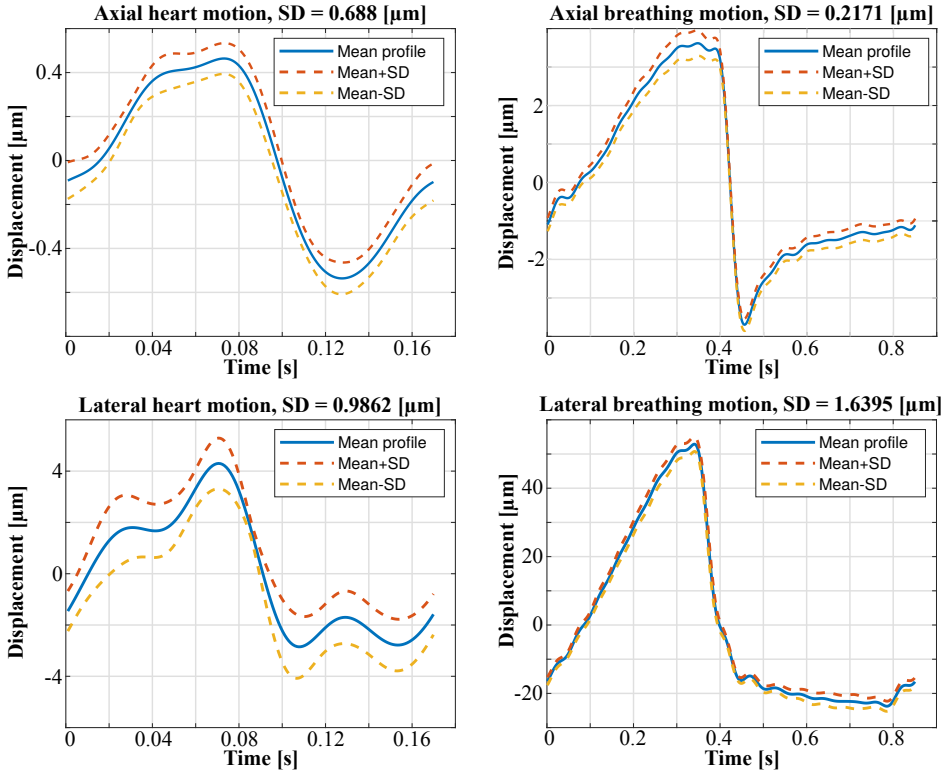


Figure 3.12: Mean and SD of aligned responses for the heart beating (left) and breathing (right) motion in the lateral (bottom) and axial (top) directions. *Copyright ©2021, IEEE*

color wheel on the top right corner of the image demonstrate the direction of color with a range from 0 for the darkest colors to 10 mm/s for the brightest colors. Four rectangles

Table 3.1: Overall precision of motion estimates for all rat experiments. All values in μm . *Copyright ©2021, IEEE*

Motion type	Minimum	Maximum	Mean	SD
Heart, axial	0.069	7.858	1.992	0.945
Breathing, axial	0.062	4.630	1.455	0.858
Heart, lateral	0.431	19.923	6.562	3.254
Breathing, lateral	0.277	20.315	5.438	2.949

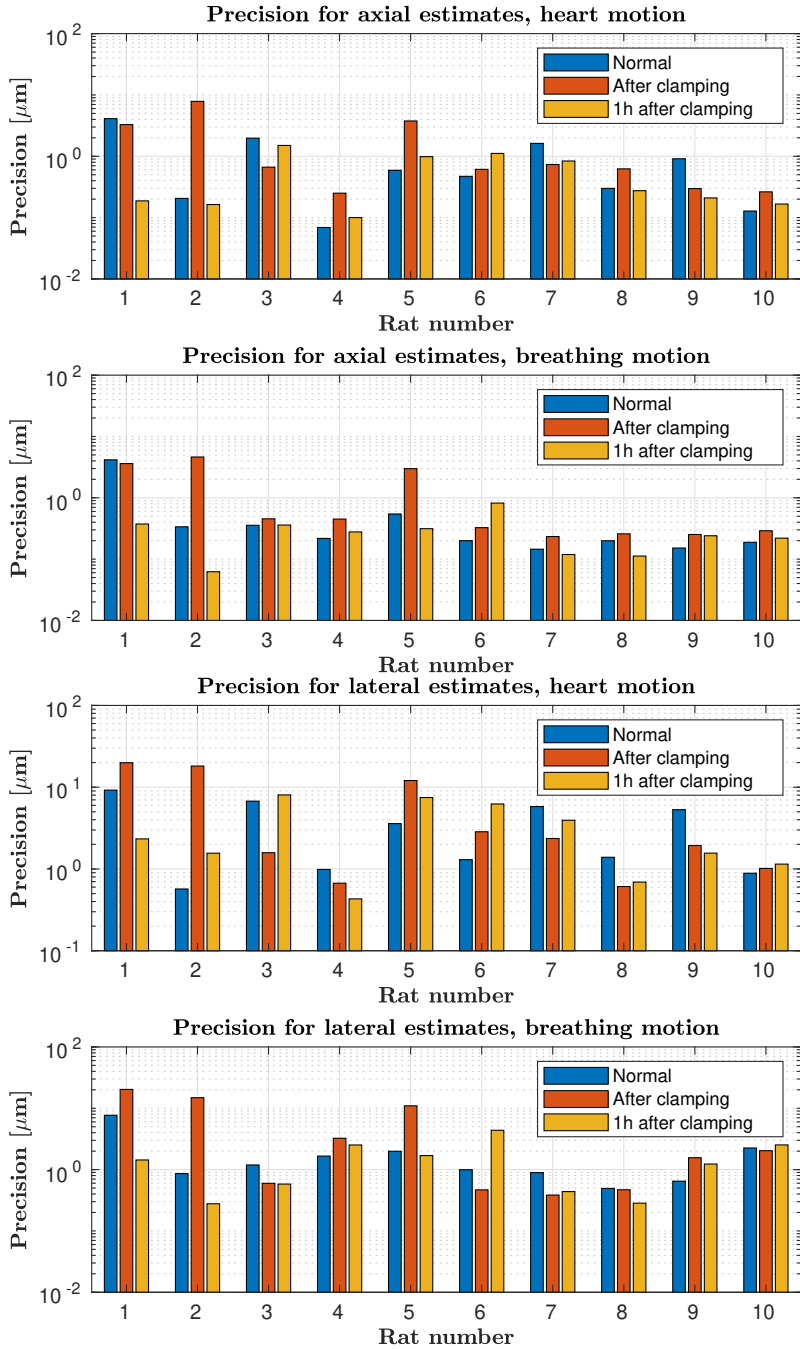


Figure 3.13: Precision of motion estimates for all rat experiments in the lateral (bottom) and axial (top) directions. *Copyright* ©2021, IEEE

on the intensity and velocity maps are zoomed in regions 1-4 in the third row. In each rectangle, line markers were put at the same place to compare the intensity and velocity profiles in these maps. Finally, the polynomial fitted profiles to the pixel values of the intensity and velocity maps are shown in the last row. It can be seen how the velocity maps can differentiate small vessels compared with the intensity maps. Also, the profiles demonstrate that how the profiles without the motion correction can spread out. Having motion correction throughout the entire kidney results in sharper images and more smooth velocity and intensity profiles.

The image was not fully corrected for motion when a local region was used for correction of the whole image. This can be seen from images in rows b and c for the zoomed regions. In the velocity maps, the effect of motion correction on the alignment of small vessels was particularly prominent in the cortical (outer) part of the kidney.

In images without motion correction, the profiles were widely spread, resulting in blurry images. As an example, a reduction in the diameter of a large vessel in the left side of the left side of the kidney from 1.3 mm to 0.7 mm (a factor of 2) was observed after motion correction in both intensity and velocity profile 1. The velocity in this vessel was approximately 8 mm/s. Profile 2 was supposed to show two vessels with a size of about 500 μm , however, it shows that local motion estimation may not be valid for all regions of the kidney. Four smaller vessels with a size of less than 50 μm and less than 250 μm were supposed to show from profiles 3 and 4, respectively. These vessels were only resolved by the velocity profiles. The measured velocity in the medulla was below 1.5 mm/s and 6 mm/s in the cortex. Profiles 3 and 4 are important because they showed that images without proper motion correction could lead to unusually narrow or wide vessels.

The FRC curves for the intensity maps with one-bit and half-bit information threshold curves are demonstrated in Figure 3.15a-c for scenarios with and without motion correction. Figure 3.15-d demonstrates the FRC resolution with one-bit threshold for the first scan of all experiments. An improvement in the image quality after motion correction using the motion field is visible both in terms of the median and inter-quartile range.

3.2.4 Discussion

Motion estimates showed a motion, induced by breathing and heart beating, in the range of the 100-200 μm in the lateral and axial directions. Therefore, uncorrected images would be limited in resolution to 100-200 μm and many of the small vessels would not be resolved. Motion correction with respect to a reference frame improved the resolution. In general, the axial motion was estimated with higher precision than the lateral motion as only the signal envelope was employed. On the other hand, It was impossible to use cross-correlation of RF signals due to the low density of lines. One solution to this problem is to use faster imaging scheme such as plane wave (Tanter and Fink 2014) or synthetic aperture (Jensen, Nikolov, et al. 2006) imaging schemes, which do not have restrictions on the lateral sampling density. Also these imaging methods offer higher frame rates than the conventional sliding aperture technique. One of the main issues

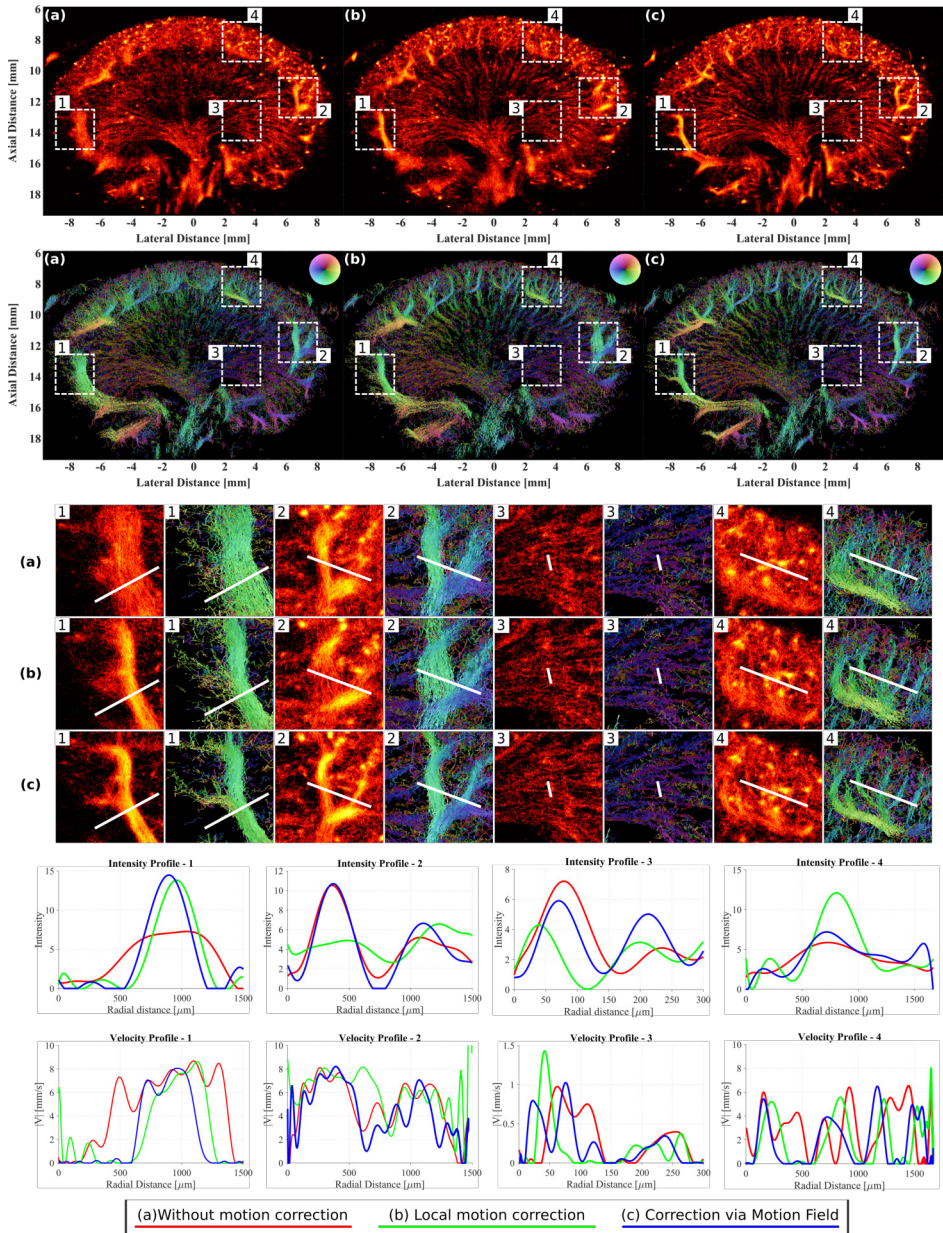


Figure 3.14: Intensity and velocity maps of a rat kidney (a) without motion correction, (b) with local motion correction, and (c) with motion field correction. Four profile markers on the intensity and velocity maps were selected exactly at the same place, in which the polynomial fitted profiles to the pixel values of the maps were obtained. *Copyright* ©2021, *IEEE*

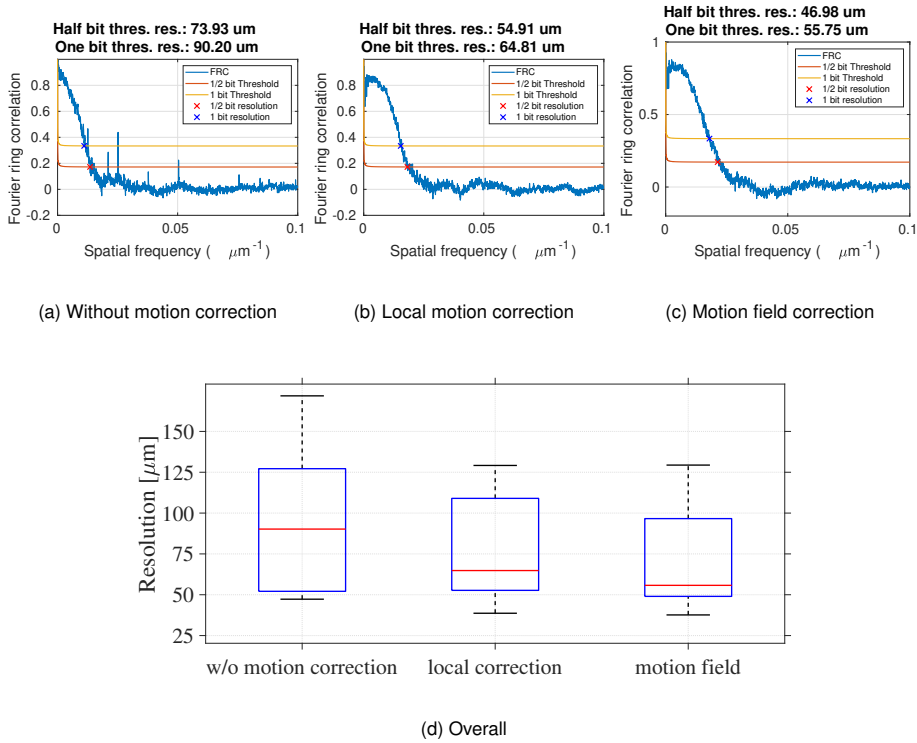


Figure 3.15: (a)-(c): FRC curves and bit-based information threshold for SR images. (d): Box plots of FRC metric with one-bit threshold for 3 scenarios for 10 experiments. Copyright ©2021, IEEE

with the fast imaging techniques is the large amount of the data generated when a long acquisition time is required and the full RF data for a number of elements have to be used. This problem needs to be addressed in future scanners.

In the sequence, shown in Figure 2.4, the frame-rate can be increased by removing the second set of the full emissions if the first set can be stored for the B-mode images. However, this was not possible due to the storage and processing features of the BK5000 scanner.

The precision of the motion estimates for the *in vivo* data was obtained by Fourier decomposition of the motion signal into components from breathing, heartbeat, and residual smooth muscle motion. In general, the motion induced by breathing was larger than the motion from heart beating. The precision of motion estimates from the breathing

was $1.64 \mu\text{m}$ and 217 nm in lateral and axial directions, while the motion from the heart beating with physiological variations had a precision of $0.98 \mu\text{m}$ and 69 nm in the lateral and axial directions. For all of the experiments, the precision of the motion estimates was in the range of 69 nm to $20.3 \mu\text{m}$ with the mean precision of $6.6 \mu\text{m}$ and $2.0 \mu\text{m}$ in lateral and axial directions. In most of the cases, the precision was lower than the capillary size of $10 \mu\text{m}$, making the motion correction precision potentially sufficient for visualization of the capillary flow. In a few rat experiments, the precision was up to $20 \mu\text{m}$. Because parts of the motion estimate were outside the search range, proper motion correction was not possible in these experiments. The degradation in the precision of motion estimates was only observed in experiments 1, 2, and 5 where some parts of the experimental setup must have moved accidentally. Excluding these experiments resulted in a precision always below $10 \mu\text{m}$ and often much lower.

Measuring the microvascular blood flow deep inside organs *in vivo* is a crucial task. In older studies, the mean red blood cell velocity was estimated at about 1 mm/s at the tip of the renal papilla (at the bottom of the medulla) of rat kidneys using video microscopy techniques (Cupples, Sakai, and Marsh 1988; Holliger et al. 1983; Zimmerhackl, Robertson, and Jamison 1985). So, the velocity profile 3 from the medulla, shown in Figure 3.14, corresponded with the previous findings. The other velocity profiles included a combination of arcuate and cortical radial arteries and veins of varying sizes. To validate these velocities, the different types of vessels would need to be separated and classified. Spectral Doppler may help to validate the velocities in the SR velocity maps of the larger vessels. On the contrary, validation of the velocity estimates in the cortical microvasculature is very challenging. To the best of our knowledge, there are no other techniques to estimate the velocity in the *in vivo* cortical microvasculature noninvasively. An *in vitro* study found the blood velocities of about 10 mm/s in the afferent arterioles (Takenaka et al. 1994). Another study noted velocities ranging from 0.5 to 65 mm/s in different renal arteries and arterioles of a split hydronephrotic kidney, however, the relationship between the velocities and vessel sizes was not addressed (Vriese et al. 2000). Hence, if SRI provide can precise estimations of blood flow velocity in various vessels of the kidney, it may fulfill an unmet need and allow evaluation of intrarenal blood flow under various physiological and pathological conditions.

The FRC resolution metric is controversial because of its dependency on threshold criteria, pixel values, and splitting the SR image. Due to the fact that the images of 10 rat kidneys were thresholded, scaled, and split in the exact same way, the metric is still useful for assessing quality even though it may not reflect the actual resolution. A large improvement in the metric was seen when the motion corrections were incorporated.

The motion correction method presented in this Section assumes a negligible out-of-plane motion. The F-number of the transducer is approximately 6 at the depth of 20 mm . This gives the elevation slice thickness greater than 1.2 mm , which is noticeably above the lateral and axial motion of $100\text{-}200 \mu\text{m}$. Thus, the change in motion amplitude in and out of the imaging plane will be negligible and will not affect detection. All in all, to also have super-resolution in the elevation direction, a 3-D data acquisition is required which

can be attained using sparse array (Harput et al. 2019), matrix probes (Chavignon et al. 2020; Heiles et al. 2019), or row-column addressed probes (Jensen, Ommen, et al. 2020; Jensen, Schou, et al. 2019).

3.3 Tracking

3.3.1 Tracking algorithms

3.3.1.1 NEAREST-NEIGHBOR

The simplest and most basic form of tracking is the NN tracker. In NN, the unlabeled MBs from one frame get connected to the MBs in the next frame with minimum euclidean distance. Although the NN tracker is simple and fast, it uses uncertain localization directly. The NN tracker has only one important parameter, called maximum linking distance, which is a criteria on how far two positions can be from each other to be linked from one frame to another frame. In this study, the maximum linking distance was set to $250 \mu\text{m}$. This means that in a system with frame rate of 55 Hz, the fastest trackable MBs had a velocity 13.75 mm/s, otherwise, they violated the criteria of maximum displacement or maximum linking distance.

3.3.1.2 KALMAN FILTER

In engineering, Kalman filters have a long history of reducing measurement uncertainty. Here, a general and simple Kalman model for MB tracking is explained. To use a Kalman filter, the physics of the system must be somehow modeled. A simple flow model implies that MBs in the blood vessels follow the bloodstream and therefore, cannot jump in random directions. This prior state information can be embedded in the Kalman filter structure to form a more robust form of tracking (Solomon et al. 2019; Tang et al. 2020). A linear model for the flow can be formulated as $\vec{r}(n) = \vec{r}(n-1) + d\vec{r}(n) + \epsilon(n)$ where $\vec{r}(n) = (r_z(n), r_x(n))$ is the correct MB location at frame index n , $d\vec{r}(n) = (dr_z(n), dr_x(n))$ is the displacement of the MB from frame index $n-1$ to frame index n , and $\epsilon(n)$ is the error term for this model. This equation literally says that the new position of a MB is the result of previous position of that MB in addition to its displacement and an error. The error comes from the fact that no matter how accurate we want to try to model the entire system, there is always a place for miss modeling and error. The above equation assumes that MB positions are completely accurate and precise which forms the prediction state of the Kalman filter. However, the observation or measurement always comes with some noise and uncertainty. These observations can be seen as $\vec{r}(n) + \nu(n)$, where $\nu(n)$ is a random noise signal.

The above prediction and observation states can be written in the Kalman framework as:

$$\begin{cases} \text{Prediction State:} & \vec{a}(n) = \mathbf{F}\vec{a}(n-1) + \epsilon(n) \\ \text{Observation State:} & \vec{b}(n) = \mathbf{H}\vec{a}(n) + \nu(n), \end{cases} \quad (3.5)$$

where $\vec{a}(n) = [\vec{r}(n), d\vec{r}(n)]^T = [r_z(n), r_x(n), dr_z(n), dr_x(n)]^T$, $\vec{b}(n)$ is the uncertain position, $\epsilon(n) \sim \mathcal{N}(0, \sigma_\epsilon^2)$ is the error for the flow model, where $\mathcal{N}(0, \sigma_\epsilon^2)$ is zero mean Gaussian distribution with standard deviation of σ_ϵ , and $\nu(n) \sim \mathcal{N}(0, \sigma_\nu^2)$ is the measurement noise, which has a standard deviation of σ_ν . According to the linear model of $\vec{r}(n) = \vec{r}(n-1) + d\vec{r}(n) + \epsilon(n)$ and measurement model $\vec{r}(n) + \nu(n)$, \mathbf{F} and \mathbf{H} are

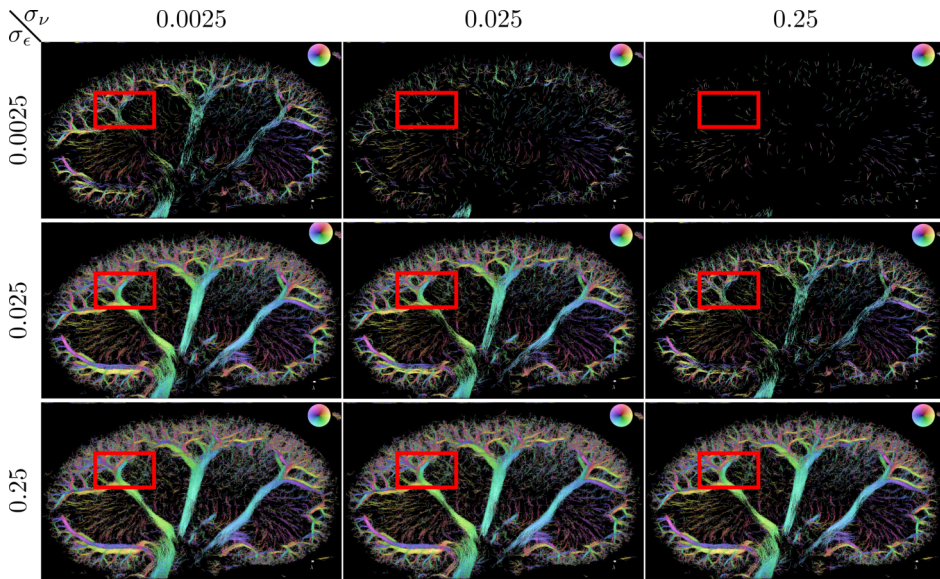
$$\mathbf{F} = \begin{bmatrix} 1 & 0 & 1 & 0 \\ 0 & 1 & 0 & 1 \\ 0 & 0 & 1 & 0 \\ 0 & 0 & 0 & 1 \end{bmatrix}, \quad \mathbf{H} = \begin{bmatrix} 1 & 0 & 0 & 0 \\ 0 & 1 & 0 & 0 \end{bmatrix}.$$

The Kalman filter tries to estimate the true position of MBs using both prediction and observation states. When the true MB positions were estimated, they were linked to the estimated positions for the next frame in a similar fashion to the NN tracker. Therefore, one can see a Kalman (K) tracker as an location estimator using a Kalman filter followed by linking stage.

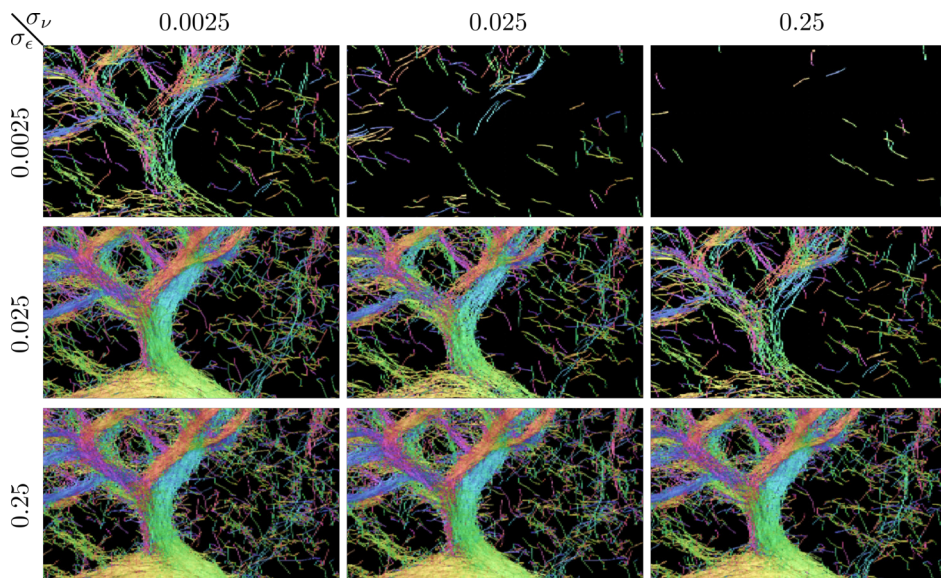
For the maximum linking distance, the same parameter as the NN tracker (250 μm) was used. The σ_ϵ and σ_ν are two parameters, also known as the initial conditions of the Kalman filter, that their adjustment are quite tricky and may vary from one application to another. In this study, the initial conditions of the Kalman filter were determined experimentally by processing *in vivo* data by coarse steps of initial conditions in which the values of σ_ϵ and σ_ν were tested for all combinations of 0.0025, 0.025, and 0.25 m. There reason that *in vivo* data were used for the parameters tuning was because *in vivo* data contained a combination of multiple scenarios, including different MB densities and velocities as well as overlapping and non-overlapping MBs. Also, the ultimate goal was to optimize the processing to get better *in vivo* data and do not over-fit the tracker to a specific simulation. The results for each pair of the selected parameters are shown in Figure 3.16 and the visual effects are listed in Table 3.2. According to these results, the Kalman filter parameters were chosen empirically with a medium σ_ϵ (0.025) and a small σ_ν (0.0025) to retain both small and large vessels with less uncertain tracks.

3.3.1.3 HIERARCHICAL STRATEGY

It is unlikely that having similar initial conditions for all MBs will be beneficial, because MBs are localized with unknown uncertainties and have different speeds. Moreover, the MB lifetimes are related to the number of Kalman filter iterations. Our method proposed using a hierarchical structure of Kalman filters with various initial conditions for different velocity ranges. The flowchart for a hierarchical Kalman (HK) tracker with 5 levels is represented in Figure 3.17. Initially, the tracking was constrained to the low speed range (0 – 3 mm/s) and then increased velocity range at each level (up to 12 – 15 mm/s). From the coarse tuning, described in Figure 3.16 and Table 3.2, with smaller σ_ϵ and larger σ_ν , the slow flows were tracked better and vice versa. Therefore, the initial condition



(a)



(b)

Figure 3.16: Kalman parameters coarse tuning. (a) shows the full view and the red rectangles are the zoomed regions shown in (b). The *in vivo* data were processed using the Kalman filter with various parameters σ_ϵ and σ_ν .

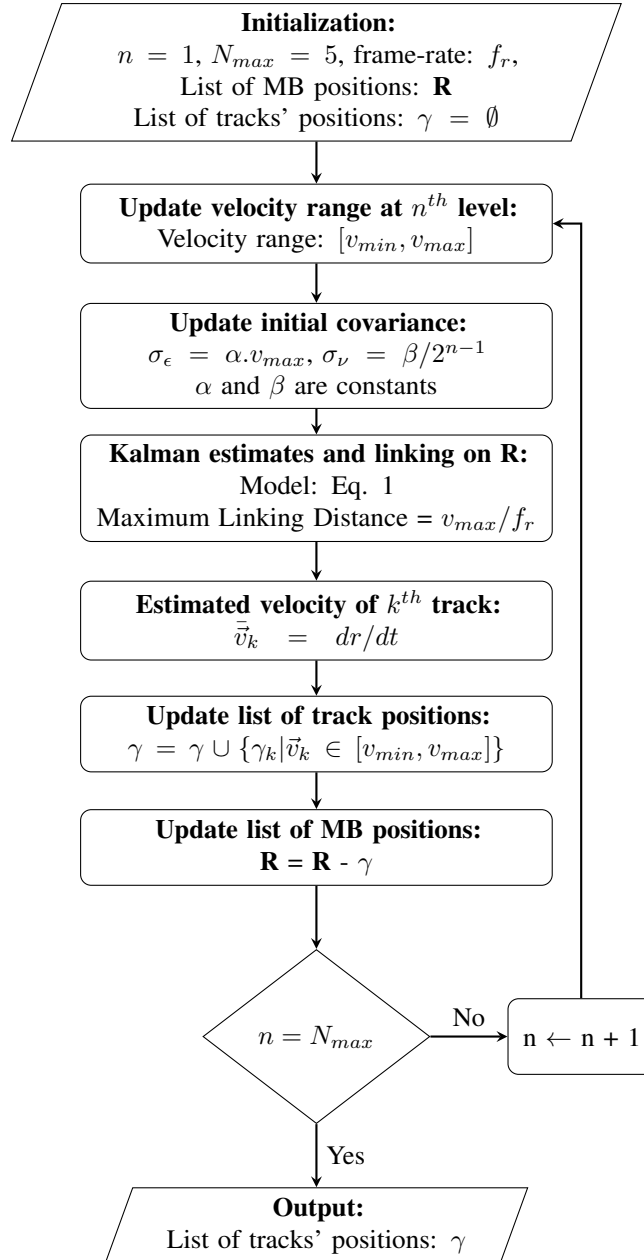


Figure 3.17: Hierarchical Kalman tracker flowchart

σ_ϵ was weighted proportional to the maximum velocity at each level with a constant coefficient of α . While, the σ_ν was treated inversely proportional to the trackers level with a constant coefficient of β . The constant values of $\alpha = 0.001$ and $\beta = 0.025$ were also set experimentally.

At each level, a Kalman filter similar to what is described in (3.5) was used, while the initial conditions were updated at each level. The linking between the estimated positions of the current frame and detections of next frame with the maximum linking distance criteria was performed using the Hungarian algorithm (Kuhn 1955). The linked positions were the new observation of the Kalman filter. The maximum linking distance criteria was also varied at each level. This parameter was set to v_{max}/f_r , where f_r is the system frame-rate and v_{max} is the maximum velocity range of a specific level. When a track of a MB was formed, the MB's velocity was estimated. Defining a MB track γ_k as a set of N_k MB locations at specific times as

$$\gamma_k = \{(x_i, y_i, z_i), t_i\}_{i=1}^{N_k} = \{(\vec{r}_i, t_i)\}_{i=1}^{N_k}, \quad (3.6)$$

the mean velocity of the track γ_k is

$$\vec{v}_k = \frac{\vec{r}_{N_k} - \vec{r}_1}{t_{N_k} - t_1}, \quad (3.7)$$

and its instantaneous velocity at i^{th} position is

$$\vec{v}_{ik} = \frac{\vec{r}_{i+1} - \vec{r}_i}{t_{i+1} - t_i}. \quad (3.8)$$

If the estimated velocity for a track was above the tracker's velocity range, the track was removed from the list of valid tracks. Finally, the MB positions of valid tracks were removed from the list of MB positions. Similarly, the remaining untracked MBs were processed at the next level.

Table 3.2: Observations regarding large and small values of σ_ν and σ_ϵ

	Small σ_ϵ	Large σ_ϵ
Small σ_ν	Unable to track fast flows (large vessels)	Uncertain tracks linking (wavy and squiggly tracks)
Large σ_ν	Unable to track fast flows (large vessels) Generate short and sparse tracks	Unable to track fast flows (large vessels) Increase uncertain track linking (wavy and squiggly tracks)

3.3.2 Evaluation

The performance of tracking was evaluated from a variety of perspectives using various metrics.

3.3.2.1 ASSIGNMENT-BASED METRICS

Estimated tracks were paired with ground-truth tracks using their minimum distances as described in (Chenouard et al. 2014). Based on a gate distance with the size of a wavelength, the true positive (TP), false positive (FP), and false negative (FN) tracks and positions were determined (Chenouard et al. 2014). Jaccard similarity was then calculated as follows

$$JSC = \frac{TP}{TP + FP + FN}. \quad (3.9)$$

The Jaccard similarity coefficient (JSC) has a value between 0 and 1 and represents the similarity between the estimated tracks and the ground-truth tracks. The root mean square error (RMSE) of the TP positions were calculated as a measure of the sub-wavelength accuracy. This study extended the assignment-based metrics to the velocity vectors. A paired velocity vector with an angle error less than 45 degrees and a magnitude error less than 20% was considered as a TP vector. As with tracks and positions, the JSC and RMSE of velocity vectors were evaluated for similarity and accuracy.

3.3.2.2 PROFILE-BASED METRICS

Based on the known ground truth for the velocity profile and the geometry of the tube, the velocity profiles of the SR images were compared with the ground truth. The same parabolic profiles across the tubes were expected, so the relative bias (RB) and relative standard deviation (RSD) were calculated over several cross-sections of the tubes. The velocity profiles were derived using spline interpolation of the velocity maps. Table 3.3 lists the profile-based metrics. A similar method was used to estimate intensity profile values over intensity maps. To assess the diameter (D) of vessels, the 90% width of the profile was calculated. Using the 90% width, it can be seen that different trackers can generate spurious tracks outside the vessel. In addition, the full width at half maximum (FWHM) of the profiles was determined for comparison purposes.

3.3.3 Simulation results

The images obtained by NN, K, and HK trackers for a medium MB density scenario with localization uncertainty of $\lambda/5$ as well as the image from the ground-truth tracks are shown in Figure 3.18. The cross-sections from which the profiles were calculated are shown by the green dashed lines in this Figure.

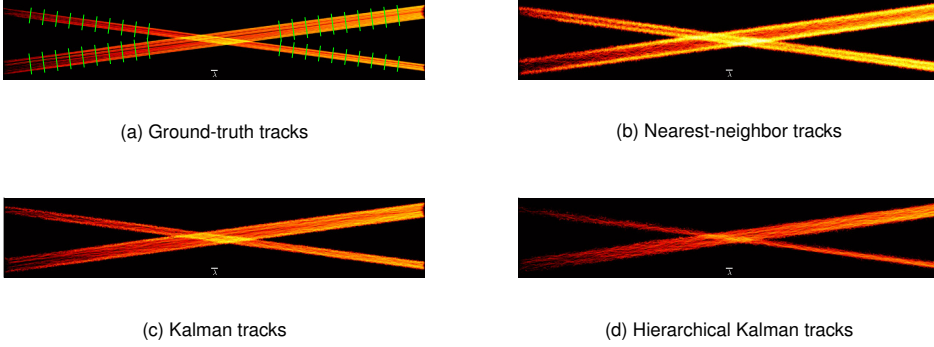


Figure 3.18: (a) The ground truth tracks marked by several green cross-sections over which the velocity and intensity profiles were calculated. SR images attained by (b) nearest-neighbor, (c) Kalman, and (d) hierarchical Kalman trackers in a scenario with an uncertainty of $\lambda/5$ and medium MB density.

3.3.3.1 ASSIGNMENT-BASED METRICS

A summary of all the assignment-based metrics for different scenarios is shown in Table 3.4 which shows the best trackers according to the performance metrics (JSC and glsmse).

In terms of ground truth similarity, the HK tracker performed better in all the high-density scenarios. This tracker also had a lower RMSE in 75% of scenarios. Only in low and medium density scenarios with low localization uncertainty, the NN tracker was competitive with the K and HK trackers (0.05λ and 0.10λ). Reducing the gate size led to similar trends in performance metrics. However, it is worth to mention that the results were worse when smaller gate sizes were used, particularly for scenarios with high uncertainty, and the RMSE estimates were less accurate. More detailed performance metrics for extra scenarios as well as the effect of the gate sizes on these performance

Table 3.3: Definition of profile-based metrics.

Ground truth	$\vec{v}_g(r) = V_p \left(1 - \left(\frac{r}{R}\right)^2\right)$
Estimations	$\{\vec{v}_i(r)\}_{i=1}^N$
Mean Profile	$\bar{\vec{v}}(r) = \mathbb{E}\{\vec{v}_1(r), \vec{v}_2(r), \dots, \vec{v}_N(r)\}$
Standard Deviation Profile	$\vec{v}_{SD}(r) = \sum_{i=1}^N (\vec{v}_i(r) - \bar{\vec{v}}(r))^2 / N$
Relative Bias	$\mathbb{E}\{\bar{\vec{v}}(r) - \vec{v}_g(r)\} / V_p$
Relative Standard Deviation	$\sqrt{\mathbb{E}\{ \vec{v}_{SD}(r) \}} / V_p$

metrics can be found in the supplementary document for the paper 4 (Taghavi, Andersen, Hoyos, Schou, Gran, et al. 2022).

Table 3.4: Assignment-based ranking for Nearest-Neighbor (NN), Kalman (K), and Hierarchical Kalman (HK) trackers using 100 independent simulations for each scenario. The tracker with the best metric for various uncertainty ($\lambda/20 \sim \lambda/2$) and MB density (low, medium, high) scenarios is included in the Table. In scenarios where the best tracker was not significantly superior, the other trackers with relative metric difference less than 2% are included as well.

SD of Localization Uncertainty		0.05 λ			0.10 λ			0.20 λ			0.50 λ		
MB density		Low	Medium	High	Low	Medium	High	Low	Medium	High	Low	Medium	High
Track Level	JSC	NN	NN/HK	HK	NN	NN/HK	HK	K	K	HK	HK	HK	HK
Position Level	JSC	HK	HK	HK	HK/K	HK	HK	K	K	K/HK	K	K	HK
	RMSE	HK	HK	HK	HK	HK	HK	HK/K	HK/K	HK	K	K	K
Mean Velocity	JSC	HK/K	HK	HK	HK/K	HK	HK	HK	HK	HK	HK	HK	HK
	RMSE	HK	HK	HK	HK	HK	HK	HK	HK	HK/K	K	K	K
Inst. Velocity	JSC	HK	HK	HK	HK/K	HK	HK	K	K	K/HK	K/HK	HK/K	HK
	RMSE	K/HK	K/HK	K/HK	K/HK	K/HK	K/HK	HK/K	HK/K	HK/K	HK/K	HK/K	HK/K

3.3.3.2 PROFILE-BASED METRICS

The mean intensity profiles across two vessels are represented in Figure 3.19. In comparison with the HK tracker, both the NN and K trackers showed larger vessel diameters. Table 3.5a summarizes the estimated diameters in this scenario. The estimated diameters were closer to the ground truth when the HK tracker was used. The small vessel diameter was estimated 2.8% larger by the HK, while the it was estimated 31.6% and 55.6% greater than its actual size by the K and NN trackers. These values for the large vessel were 12.6%, 17.2%, and 37.6% when the HK, K, and NN tracker were used.

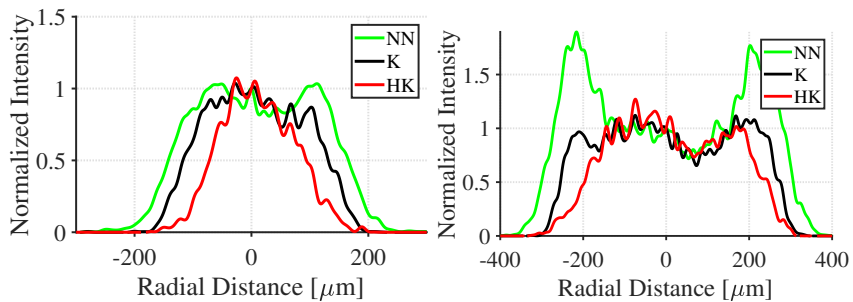


Figure 3.19: Intensity profiles for large (right) and small (left) vessels in a scenario with localization uncertainty of $\lambda/5$ and medium MB density. Each intensity profile is normalized to the value of the intensity at the center of the vessel.

Figure 3.20 shows the mean and instantaneous velocity profiles with statistics listed in Table 3.5b and 3.5c. In the NN tracker, the RSD was higher, while both K and HK trackers showed a noticeable improvement. In contrast to the intensity profiles, the velocity profile statistics showed a small degradation in RSD, when the HK tracker was used.

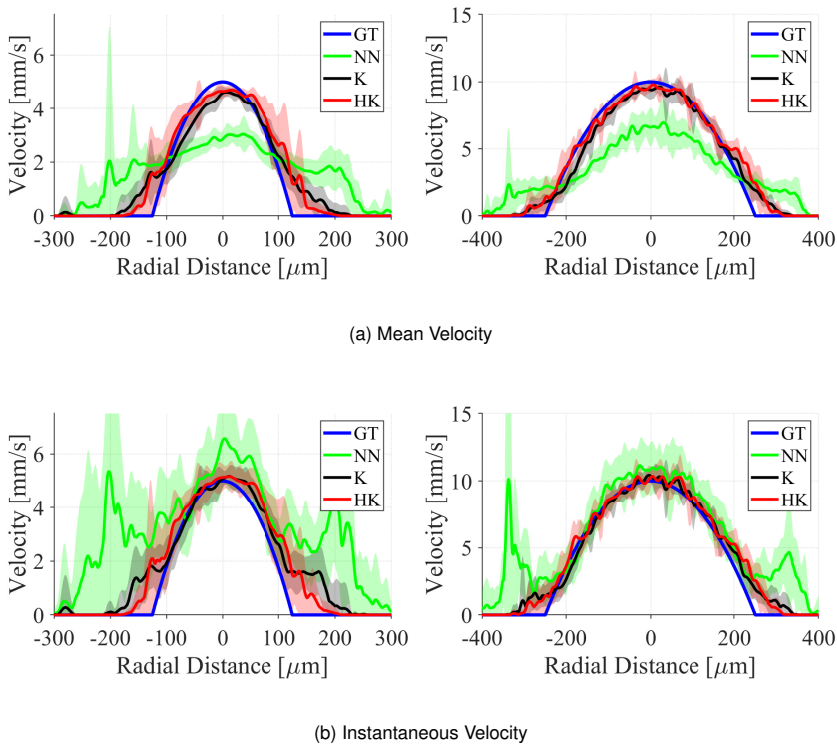


Figure 3.20: (a) Mean and (b) instantaneous velocity profiles for large (right) and small (left) vessels. The ground truth (GT) is the blue parabolic profile. The shaded region indicates the standard deviation.

The functionality of the three trackers in the presence of higher peak velocities is shown in Figure 3.21, which depicts the reduction in the performance of the trackers for tracking higher velocities at a given frame-rate. The profile-based metrics for these simulations are summarized in Table 3.6 and show this performance degradation.

3.3.4 Measurement results

The phantom measurement was only used for the confirmation of the structure. Figure 3.22 shows the known structure of the phantom was realized by the scan and pipeline setup. The visual comparison of a pair of tubes in Figure 3.22, shows that the K and HK trackers produced more straight tracks complying with realistic flow streamlines. Even though

Table 3.5: Profile-based metrics for a medium density scenario with localization uncertainty of $\lambda/5$.

(a) Intensity Profiles						
	Small vessel ($250\mu m$)			Large vessel ($500\mu m$)		
	NN	K	HK	NN	K	HK
D (μm)	389	329	257	688	586	563
FWHM (μm)	307	247	164	607	531	441

(b) Mean Velocity Profiles						
	Small vessel (5 mm/s)			Large vessel (10 mm/s)		
	NN	K	HK	NN	K	HK
RB (%)	4.99	2.61	4.27	-8.25	-0.77	1.69
RSD (%)	17.29	8.90	12.88	10.03	7.01	8.34

(c) Instantaneous Velocity Profiles						
	Small vessel (5 mm/s)			Large vessel (10 mm/s)		
	NN	K	HK	NN	K	HK
RB (%)	35.71	8.70	7.98	16.06	3.26	4.45
RSD (%)	41.77	12.94	16.07	31.73	9.00	9.84

Table 3.6: Statistics of the instantaneous velocity profiles for a medium density scenario with localization uncertainty of $\lambda/5$.

Tracker	Metric	Peak Velocity			
		5 mm/s	10 mm/s	15 mm/s	20 mm/s
NN	RB (%)	28.29	13.36	-3.98	-8.76
	RSD (%)	40.34	23.65	26.96	15.91
K	RB (%)	14.69	8.78	-2.55	-8.94
	RSD (%)	21.26	14.64	15.91	14.89
HK	RB (%)	8.02	8.12	5.95	-1.98
	RSD (%)	16.62	14.67	14.6	17.78

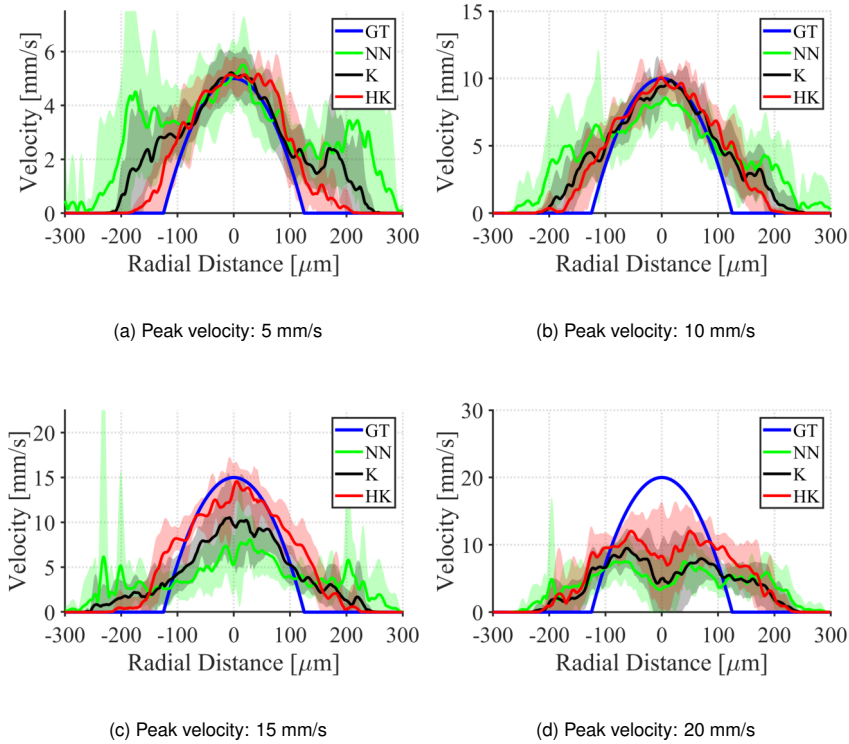


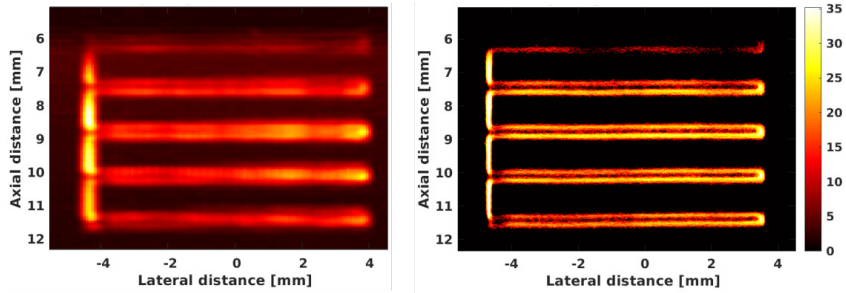
Figure 3.21: Instantaneous velocity profiles of small vessel with different peak velocities for a scenario with localization uncertainty of $\lambda/5$ and medium MB density.

the structure of the phantom was known in this measurement, the casting dimensions of the tubes were not usable as a geometric ground truth as the phantom was exposed to an uncontrolled expansion during its maintenance.

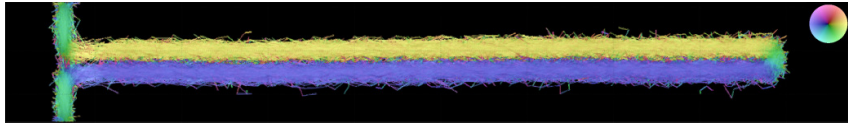
3.3.5 In vivo results

In the proposed HK tracker, Kalman filters with varying initial and linking conditions were applied to the different ranges of blood velocities. Figure 3.23 shows that the slow blood flow was reconstructed in the first level, and then faster flows were recovered in the next levels. The small arteries (red tracks with arrows pointing to them) near the veins appeared at level 4, while they were mostly hidden in the previous levels.

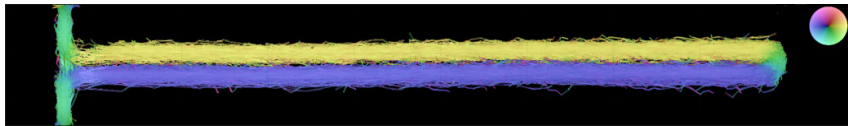
The overall visual enhancement using the HK tracker compared with the NN and K trackers is depicted in Figure 3.24 and Figure 3.25. One region in the medulla and one



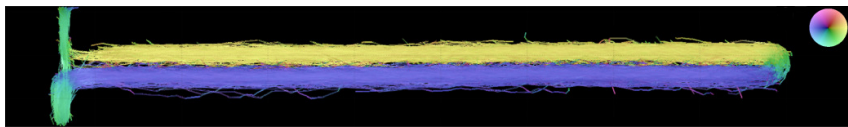
(a) Power map vs. SR intensity map



(b) Nearest-neighbor (NN)



(c) Kalman (K)



(d) Hierarchical Kalman (HK)

Figure 3.22: The structure of the tubes inside the phantom is shown in (a) by accumulated CEUS images (left) and SR intensity map (right). The zoomed on the fourth pair of tubes with (b) NN, (c) K, and HK (d) trackers. The flow direction is encoded by colors corresponding to the color wheel (*e.g.*, a vessel with flow from left to the right is shown in yellow).

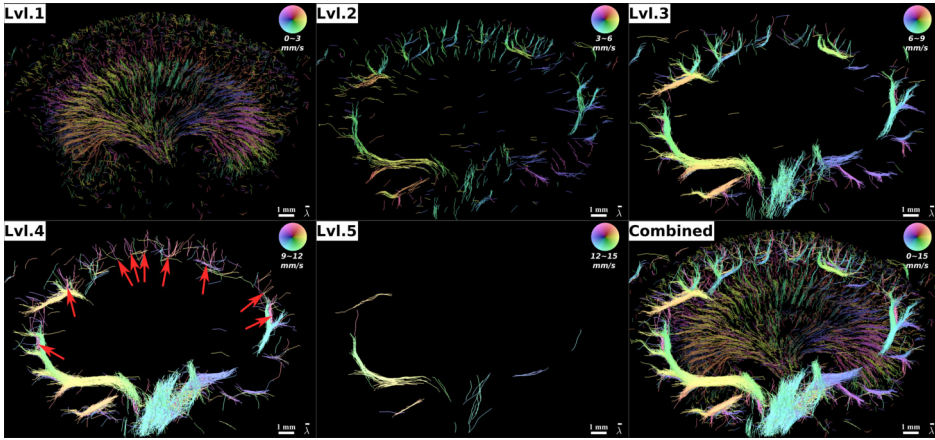
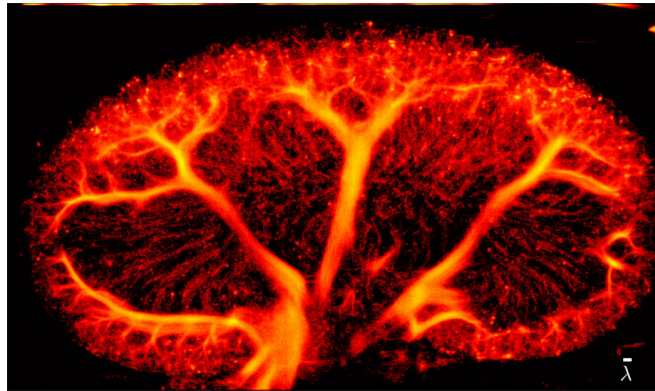


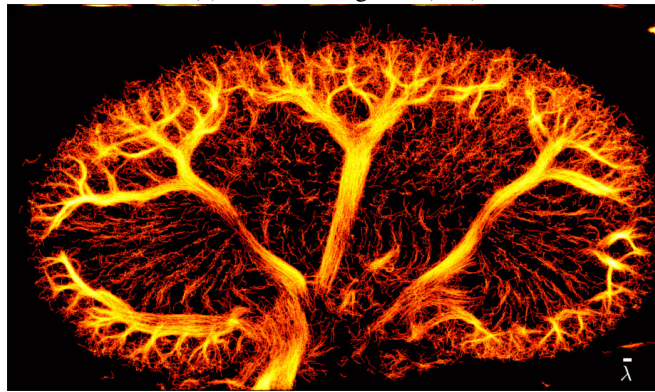
Figure 3.23: The reconstructed tracks at different levels using the proposed hierarchical Kalman (HK) tracker. The Images show a coronal view of the first kidney in a velocity map. The maximum velocities are corresponded to the maximum velocity range at each level of HK tracker, *i.e.* 3, 6, 9, 12, and 15 mm/s. Small arteries with faster flows are indicated by arrows.

region in the cortex in all velocity maps were selected and zoomed in Figure 3.26. In these regions, the diameters of four marked vessels are reported in Table 3.7. In line with the simulations, the estimated diameters from the HK results were smaller than the values from two other trackers. Marker 4 shows a vein example where only part of the vessel was in the imaging plane. It seems that the vein was not fully filled with tracks in this example. The same effect can occur in any other region if the vessel is not completely in the 2-D imaging plane, resulting in an insufficient detection of MBs during the acquisition time. Since there is not ground-truth for the *in vivo* data, only the distributions of the velocities in these regions were investigated and not the profiles. It can be seen from Figure 3.27 that the majority of MBs tracked in both the cortex and medulla had relatively slow velocities of less than 2 mm/s. Using 98% of the cumulative density functions for the peak velocity, the peak velocity in the medulla was estimated to be 1.65 mm/s, while the peak velocity was estimated 3 to 4 times higher by the NN and HK trackers. The peak velocities in the cortical region were 5.05 mm/s, 8.25 mm/s, and 9.90 mm/s for the HK, K, and NN trackers.

The computation time of the three trackers for the *in vivo* data with 3 million MB positions over 32362 frames, using an identical processing unit (Intel® Core™ i7-8700 CPU @ 3.20GHz), was 3.22, 33.71, and 35.70 minutes for the NN, K, and HK trackers, respectively. This indicates that a 5 level HK tracker had roughly the same computation time as the simple K tracker, and both were 10 times slower than the NN tracker.



(a) Nearest-Neighbor (NN)

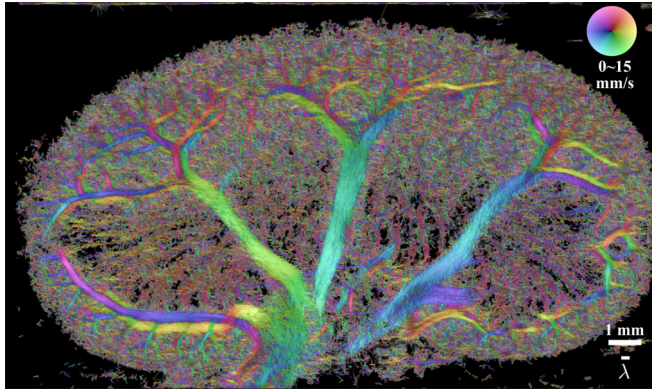


(b) Kalman (K)

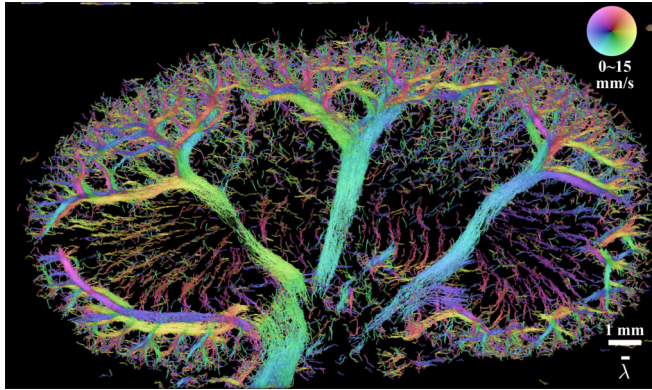


(c) Hierarchical Kalman (HK)

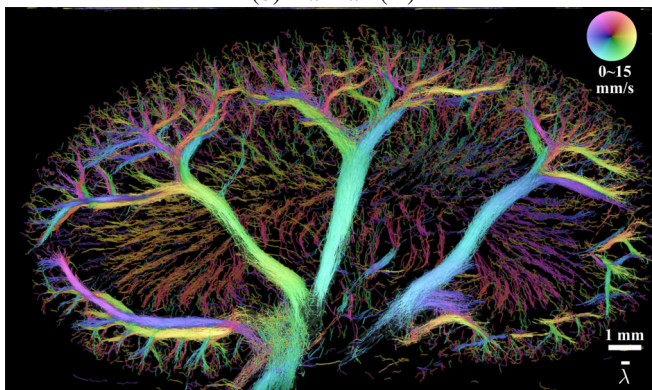
Figure 3.24: Intensity maps of the renal vessels, constructed by (a) NN (b) K and (c) HK trackers. The dynamic range in all images is 60 dB.



(a) Nearest-Neighbor (NN)



(b) Kalman (K)



(c) Hierarchical Kalman (HK)

Figure 3.25: Velocity maps of the renal vessels, constructed by (a) NN (b) K and (c) HK trackers. The flow direction is encoded by colors corresponding to the color wheel (*e.g.*, a vessel with flow from left to the right is shown in yellow). The velocity magnitude from 0 to 15 mm/s are also encoded by color brightness.

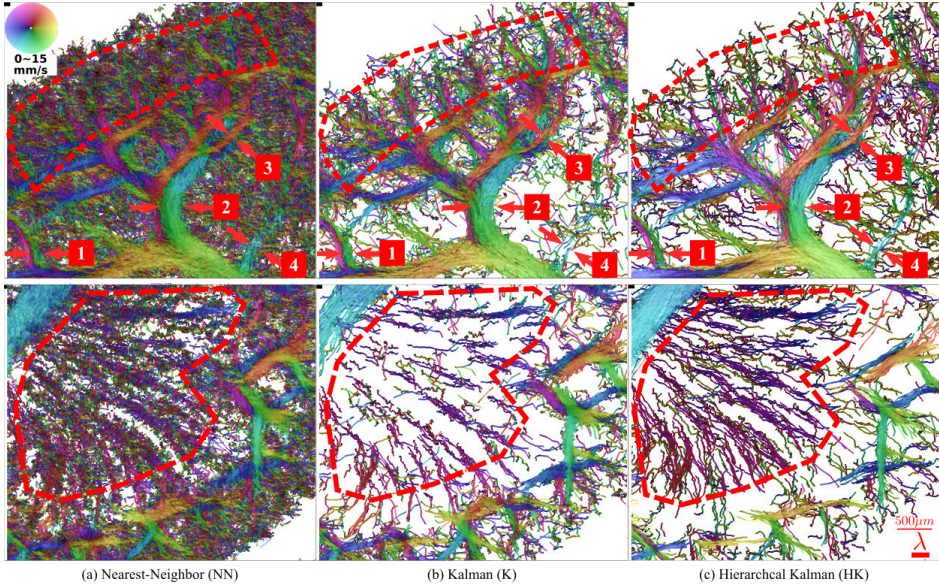


Figure 3.26: Zoomed-in cortical (top) and medullary (bottom) regions of velocity maps, constructed by (a) NN (b) K, and (c) HK trackers. The red markers shows the vessels selected for diameter estimation and the red dashed regions shows the area for calculation of velocity distribution.

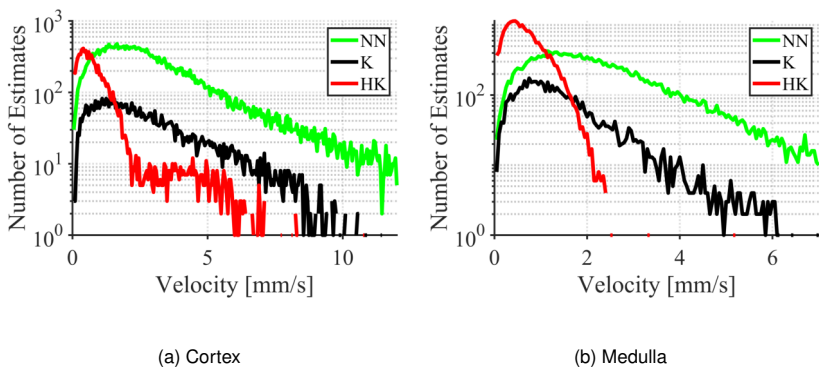


Figure 3.27: Distribution of velocity in the (a) cortical and (b) medullary regions.

Table 3.7: Diameters of the four marked vessels in Figure 3.26.

Marker	Nearest-Neighbor	Kalman	Hierarchical Kalman
(1)	150.40 μm	107.41 μm	79.62 μm
(2)	382.54 μm	311.42 μm	231.75 μm
(3)	131.66 μm	127.01 μm	79.10 μm
(4)	155.61 μm	not saturated	113.37 μm

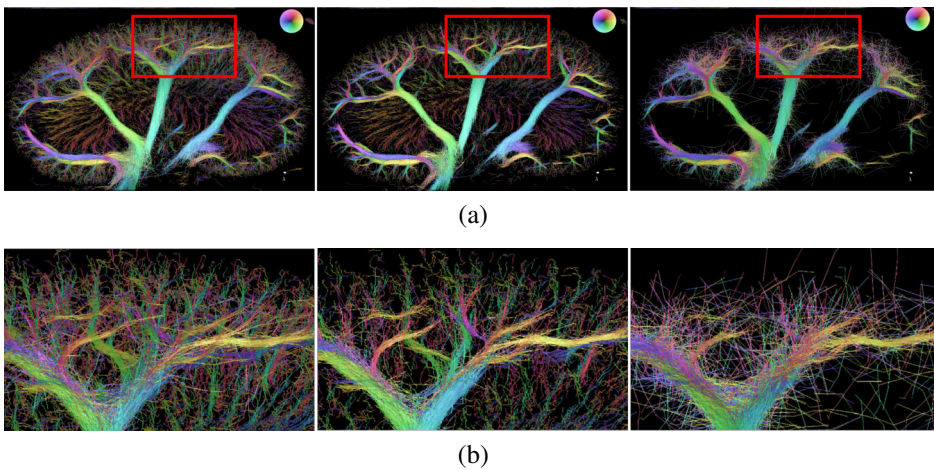


Figure 3.28: Comparison of 3-lvl (left), 5-lvl (middle), and 15-lvl (right) HK trackers. The entire kidney is shown in (a) including red rectangles which are zoomed in (b).

The HK trackers with different number of levels were also qualitatively compared in Figure 3.28, demonstrating that a 3-lvl HK tracker can generate obvious spurious tracks while a 15-lvl HK tracker can miss many of the slowly flowing MBs as it has a much smaller velocity range window at each level.

3.3.6 Forward-backward tracker

So far, the MBs were tracked conventionally from the first frame to the last frame. But what will happen if we track the MBs from the last frame to the first frame?

The block diagram for tracking MBs with a forward-backward configuration is shown in Figure 3.29. In the forward-backward configuration a same kind of tracker simultaneously tracks MBs from the last-frame to the first frame. The direction of tracked MBs in the backward tracks was reversed, and then inserted into an image together with the forward tracks, forming forward-backward tracks. Tracking was done using the three

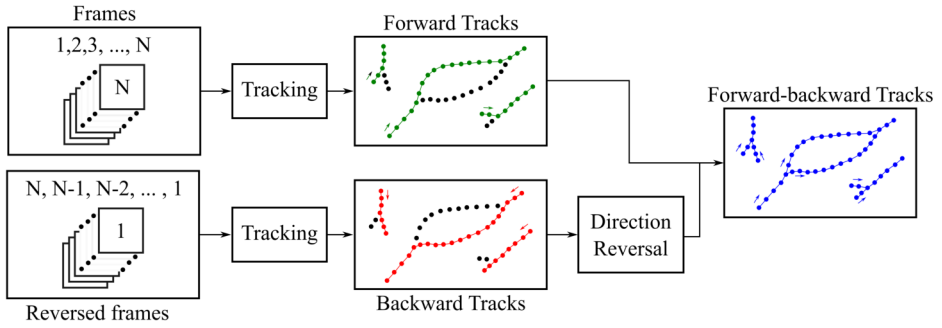


Figure 3.29: Block diagram for tracking MBs in a forward-backward manner

trackers introduced earlier, *i.e.*, NN, K, and HK. To assess the new unique track positions, forward and backward tracks were inserted into two high resolution images. Then, the percentage of the new backward track positions compared with the forward tracks was calculated as

$$P_{new} = \frac{\sum_{i=1}^n \sum_{j=1}^m I_b(i, j) \bar{I}_f(i, j)}{\sum_{i=1}^n \sum_{j=1}^m I_f(i, j)} \times 100, \quad (3.10)$$

where I_f and I_b are the binary images of forward and backward tracks with the image dimensions of $n \times m$, and $\bar{I}_f(i, j) = 1 - I_f(i, j)$.

The velocity profiles of tracked MBs in simulations with known ground-truth profiles are shown in Figure 3.30. The RSD of the profiles remained unchanged, when the NN tracker was employed. On the other hand, the improvement of RSD was between 28% to 40%, when the forward-backward strategy was employed with the K and HK trackers.

The SR images of the cortical region of a rat kidney, shown in Figure 3.31, demonstrates some differences between the two strategies. Figure 3.31.b includes roughly double the amount of tracks in comparison with Figure 3.31.a (28,681 tracks vs. 14,510 tracks). It seems that the cortical radial veins (green) and arteries (red) were filled better with MB trajectories in Figure 3.31.b. Calculating new track positions in backward tracks using (3.10), showed 35% additional positions that were not found in the forward tracks.

3.3.7 Discussion

In this section, a new HK tracker was introduced and its performance was compared with the K and NN trackers in various scenarios and using a several performance metrics. A detector-independent simulation setup with known ground truth tracks was used to evaluate tracking algorithms. According to the benchmark, reported in Table 3.4, the HK tracks were more similar to the ground truth in 38 out of 48 cases, especially in scenarios with a high level of uncertainty and a high density of MB positions. The HK

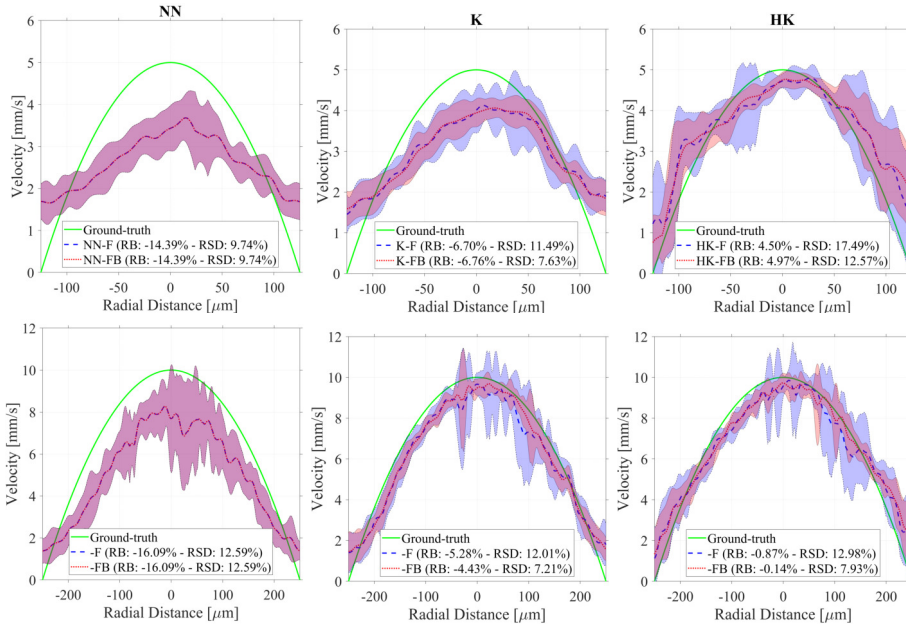


Figure 3.30: Relative bias (RB) and relative standard deviation (RSD) of velocity profiles of small (top) and large (bottom) tubes. The velocity is estimated using the nearest-neighbor (NN), Kalman (K), and hierarchical Kalman (HK) trackers with forward (F) and forward-backward (FB) configurations. Dashed lines shows the mean profile and shaded area is the standard deviation around the mean value.

tracker also achieved the lowest RMSE in 26 out of 36 scenarios. The velocity profiles from the HK tracker were roughly similar to those estimated by the K tracker, however, the intensity profiles showed a better estimation of diameter and, therefore, a better structure improvement by the HK tracker. In the presence of higher MB concentrations and higher uncertainty, the performance of all three trackers degraded. Nevertheless, it was anticipated from the simulations that the HK tracker would outperform the two other trackers under the same conditions.

Interestingly, the *in vivo* SR images showed a visual enhancement in image quality when the proposed HK tracker was used. This could be seen both from more delicate microvascular structures, such as the vasa recta in the medulla[†], as well as neatly streamlined MB trajectories in large vessels. In Figure 3.25a, the dense vessel structures of the cortex were reconstructed with almost random flow directions. These structures were more

[†] see demonstration of vasa recta structures in a postmortem rat kidney filled with microfil silicon rubber in Figure 10 of (Bankir, Bouby, and Trinh-Trang-Tan 1989)

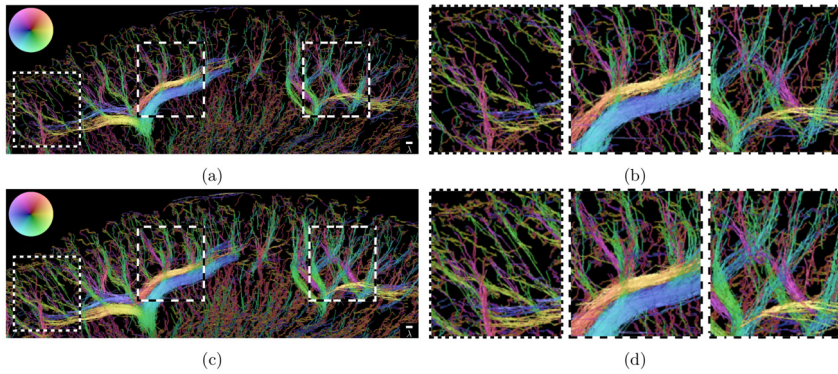


Figure 3.31: Super-resolved velocity map of the cortical region of a rat kidney with a hierarchical Kalman tracking in (a) forward and (c) forward-backward manner. The scale bar in the bottom right is a wavelength. Three regions of (a) and (c), marked by rectangles, are zoomed in (b) and (d).

distinguishable in Figure 3.25b. However, the vasa recta structures with slow flow looked much sparser compared with the same region in Figure 3.25a. In Figure 3.25c, a distinct vessel structure and flow direction could be observed in both the cortical and medullary regions. Moreover, the smooth streamlines of the MB trajectories from HK tracker were noticeable in the vasa recta bundles in medulla (bottom) and the arcuate veins and arteries (top) in Figure 3.26. The marked *in vivo* vessel diameters also had the same trend as the simulations. In Figure 3.25, the velocity maps appeared sparser from Figure 3.25-a to Figure 3.25-c. This is because the NN had more overlapping tracks and more linked MBs. Although the NN tracker generated a greater number of tracks, but based on the JSC and RMSE, we speculate that most of these tracks were not TP.

A direct measurement from decades ago, estimated a velocity less than 2 mm/s in the medulla at the apex of inner medulla, known as the renal papilla (Holliger et al. 1983). This finding is in line with the velocity estimates by the HK tracker, shown in Figure 3.27b. It is worth mentioning that direct measurement of blood flow velocity in the microvasculature is quite challenging, and no imaging modality has been proven to measure these velocities deeper inside an organ.

In a study using nano computed tomography (CT), the dense and complex vascular structure of rat kidney cortex was demonstrated (Wagner et al. 2010). The renal cortex vessel network appears to be better visualized in Figure 3.24a, and it seems that some of the information is missing from the K and HK. This is because the Kalman filter, discussed in Section 3.3.1.2, attempts to predict linear motion models for the MBs. Additionally, many of the cortical vessels do not completely fit within the imaging plane. Consequently, the many MBs passing through the imaging plane shortly do not fit the

flow model. Moreover, these projected vectors into the 2D imaging plane could lead to unreliable displacement and velocity estimations. A better example of unreliable tracks in this region is shown in Figure 3.25a, where velocity vectors moving in all directions obscured the data from in-plane vessels. A 3D ultrasound imaging, using a 2D sparse array (Harput et al. 2019), row-column addressed arrays (Jensen, Ommen, et al. 2020), or matrix probes (Chavignon et al. 2020; Heiles et al. 2019), is needed to capture full MBs displacements reliably.

In the simulated phantom, the diameter of the small vessel is equal to the wavelength (λ). MB trajectories within each vessel, however, were separated by a sub-wavelength. These closely placed streamlines can be perceived as several microvessels. By adding uncertainty to the MB positions, solving a tracking problem becomes more challenging. Similarly, velocity profiles must be estimated with sub-wavelength resolution in the velocity maps.

A tracking algorithm's computational complexity depends on the number of MB positions (inputs) and the generated tracks (outputs). Depending on localization uncertainty, MB lifetime, and structure complexity, one or both could be stochastic. The HK tracker uses multiple Kalman filters, but the number of MB positions processed at each level is reduced relative to the previous level.

Ultrasound contrast data usually suffer from low SNR, since the voltage needs to be low (corresponding to low MI) to avoid disrupting all the MBs, but high enough to capture their non-linear response. The low SNR could produce residual clutter which generates false detections or miss detections. This effect can be added to the simulations by generating or removing random MB positions while keeping the ground-truth tracks the same as before.

The maximum velocity of the velocity maps can be increased by using fast imaging sequences (Jensen, Nikolov, et al. 2006; Tanter and Fink 2014). In addition, higher frame rates allow for more accurate tracking with fewer linking errors, since a shorter linking distance (v_{max}/fr) is needed to reconstruct a velocity map with the same maximum velocity.

MB infusion allows for greater control over the amount of MBs during scan. Thus, the doses of MBs used in the experiments on rats were considerably lower than those given as bolus injections to humans for the examination of, say, tumors or liver. Infusion and bolus injection are not comparable. Based on pre-trials in which different concentrations and infusion rates of MBs were tested, the infusion settings were selected. Other settings will probably be needed for another organ, whether it be in an animal or a human, depending on the vascularity and flow of the organ and the size of the animal/human. Even though the SonoVue is not yet FDA-approved for infusion in human, several studies have worked with MB infusion in humans, and it does not appear to change the safety profile of the drug. So, clinical translation of human SRI using infusion is achievable. In humans, larger out-of-plane motion may pose challenges, so going from 2D to 3D would be beneficial. Clinical implications for SRI of a kidney would include, for example, finding out whether microvascular changes in structure or flow precede microalbuminuria in individuals with

diabetes. As a result, renal involvement could be diagnosed earlier and microvascular effects of renoprotective drugs could be monitored more easily. Another large field where the technique may improve diagnosis and treatment effectiveness is cancer. For example, SRI could be used to differentiate malignant lymph nodes from healthy ones non-invasively.

CHAPTER 4

Blood Vessel Segmentation

So far the various part of SR processing pipeline, shown in Figure 4.1, has been explained. The resulted SR images contain a lot of information with potential clinical applications. In this chapter, a way for quantification of the vessel structured in these images is discussed.

This chapter is adopted form paper 5 (Taghavi et al. 2022), and paper 10 (Taghavi et al. 2021).

4.1 Method

4.1.1 Vessel Classification

Figure 4.1 (bottom right) illustrates a velocity map accumulating more than 30,000 tracks. Although the flow direction is encoded by colors in the velocity map, a specific color may indicate to both venous and arterial flows in different regions of the image. It is shown better in Figure 4.2, where red colors in the velocity map indicate both some arteries and veins.

Considering track definition in equation (3.6) and the velocity of the MB in equation (3.8), the MB locations (\vec{r}_i) and directions ($\angle \vec{v}_{ik}$) are known at any time. In the following, these information are used to make vessel classification and to separate veins and arteries from each other. This process was implemented semi-automated. First, an expert in renal anatomy labeled the inner medulla (IM), outer medulla (OM), and cortex (CO). Additionally, arterial flow direction was drawn for these regions. This was a relatively easy task since the arterial blood in the kidney follows a specific pattern. Upon entering the kidney, the blood flows through the renal artery, distributes through the segmental arteries, and then divides into smaller branches of the arcuate arteries that run along the cortex and medulla borders. Cortical radial arteries travel toward the renal surface, while juxtamedullary efferent vessels enter the vasa recta and travel toward the renal papilla in the medulla. A similar pattern also exist for the veins, since veins and arteries run parallel to one another with opposite flow direction*. Figure 4.3 shows the arterial flow direction in different regions.

The MB trajectories were filtered based on the MBs' positions (\vec{r}_i) and their flow directions ($\angle \vec{v}_{ik}$). With this filtering, particular tracks in specific regions could be included

* The parallel nature of arteries and veins in the renal vasculature is discussed and described more in (Nordsletten et al. 2006)

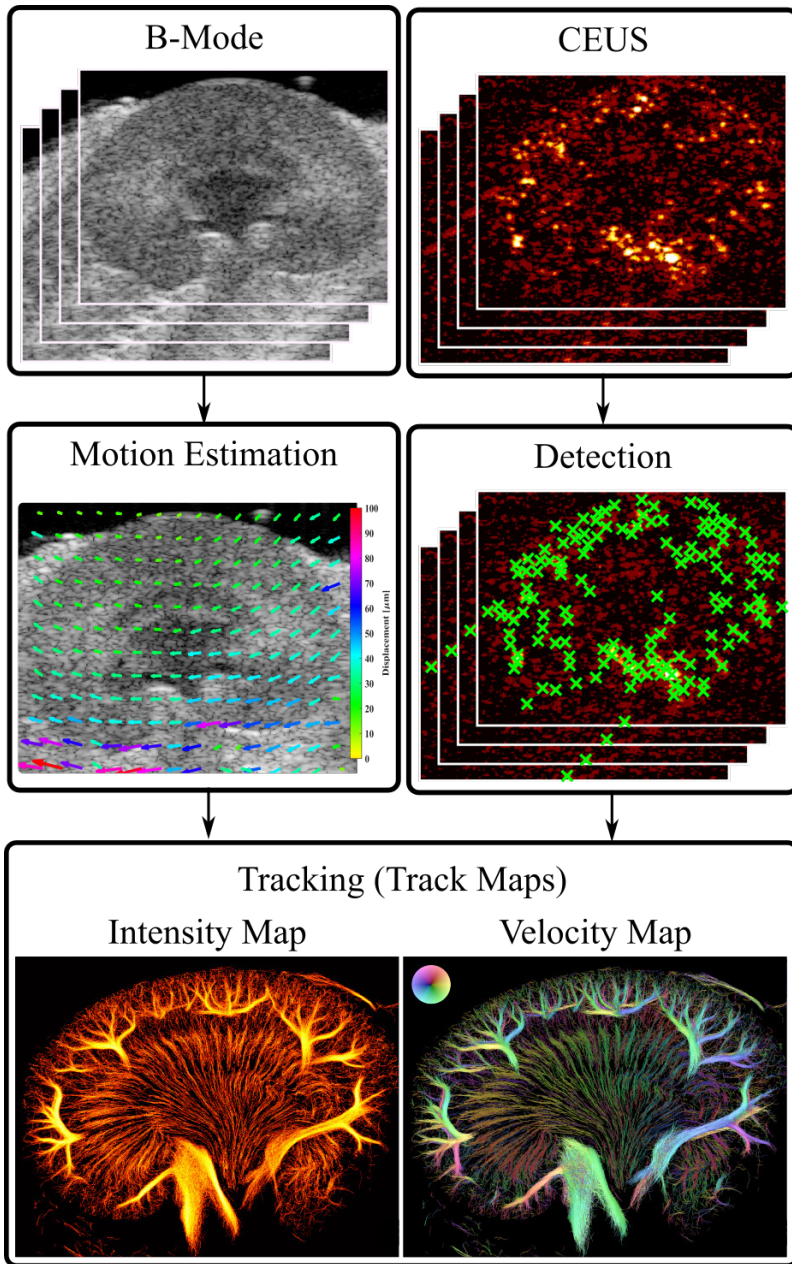


Figure 4.1: Super-resolution ultrasound image processing scheme

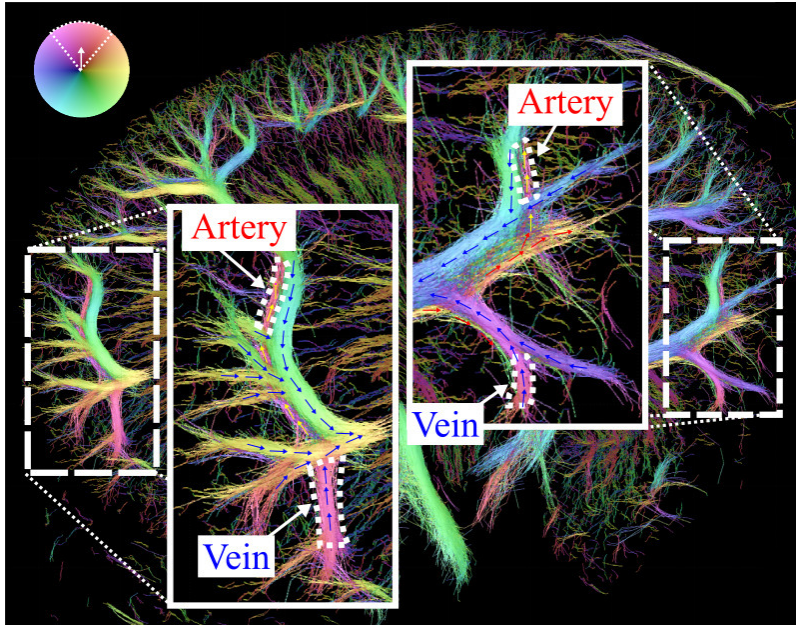


Figure 4.2: Zoom in regions of a velocity map demonstrating unclassified vessels. For example, a red color can represent a vein in a region and at the same time an artery in another region.

or excluded. In a ROI where arterial flow direction has an angle of θ_a , a track position was classified as arterial track position if \vec{r}_i exists in that ROI and $\theta_a - \angle \vec{v}_{ik} < \Delta\theta/2$. With the last term, tracks that had an angular deviation greater than $\Delta\theta$ with respect to the labeled arterial flow were excluded. In the medullary regions, $\Delta\theta$ was set at 90° , and in the cortex, it was set at 125° . Considering the fact that venous flows almost always oppose arterial flows, venous tracks can be classified on the basis of the same constraint with $\theta_v = \theta_a + 180^\circ$ rather than θ_a .

4.1.2 Vessel Segmentation

4.1.2.1 PREPROCESSING

Interesting objects to segment in the track maps are the small vessels rooted into the cortex and bundles of tiny vessels, called ascending vasa recta (AVR) and descending vasa recta (DVR), in the medulla. Assuming that the majority of MB trajectories are estimated inside the vessels, a mask was designed for the isolation of tracks. The mask was created from track maps with the following steps. First, the track maps were convolved with a Gaussian filter with the size of $500 \mu m$ and standard deviation of $25 \mu m$ to give a higher

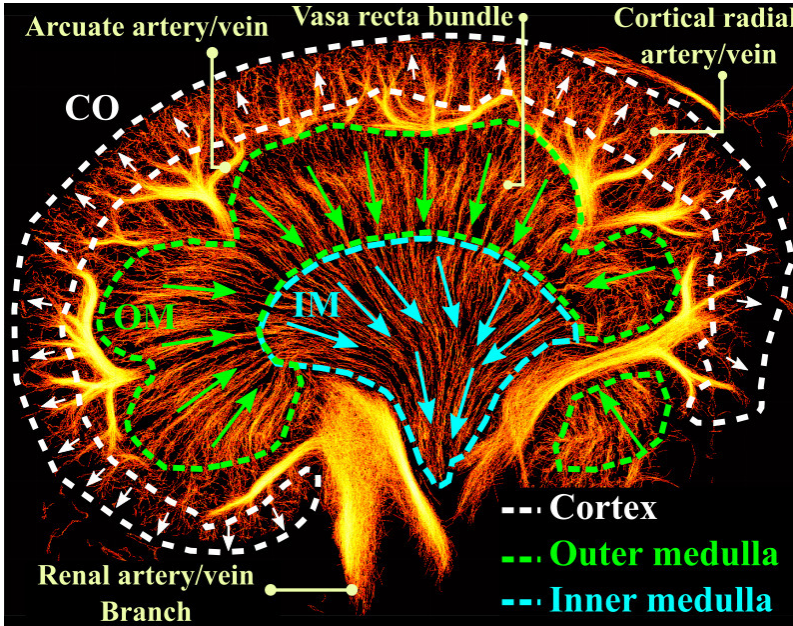


Figure 4.3: Manual labeling of different regions (dashed lines) and arterial flow direction in each region (arrows) based on the anatomical information.

weight to a denser subset of tracks and lower weight to more sparse tracks. Second, a mask with isolated solid structures was created by applying an adaptive threshold based on the local mean values to the filtered image, using the “*adaptthresh*” function in Matlab. The local window size and sensitivity of the adaptive threshold were $500 \mu\text{m}$ and 0.5. This procedure is shown for three different regions of the kidney in Figure 4.4. Lastly, the isolated regions with an area smaller than 0.06 mm^2 were considered noise and removed from the data using “*regionprops*” function in Matlab. The remained isolated regions in the mask were used individually to extract centerlines of the potential vessels.

4.1.2.2 CENTERLINE EXTRACTION

The isolated tracks were obtained by masking the track map. Isolated tracks inside a region of the binary mask are shown in Figure 4.5-a. The isolated tracks were dilated with a disk element of radius $25 \mu\text{m}$ and closed immediately with a disk of $50 \mu\text{m}$, using the “*imdilate*” and “*imclose*” functions in Matlab (Figure 4.5-b). The skeleton of the dilated region was extracted using “*bwmorph*” function (Figure 4.5-c). All vertices and edges of the skeleton were determined by pixel tracing (Figure 4.5-d). Edges with a smaller length than $125 \mu\text{m}$ were removed (Figure 4.5-e). The skeleton was branched by removing the

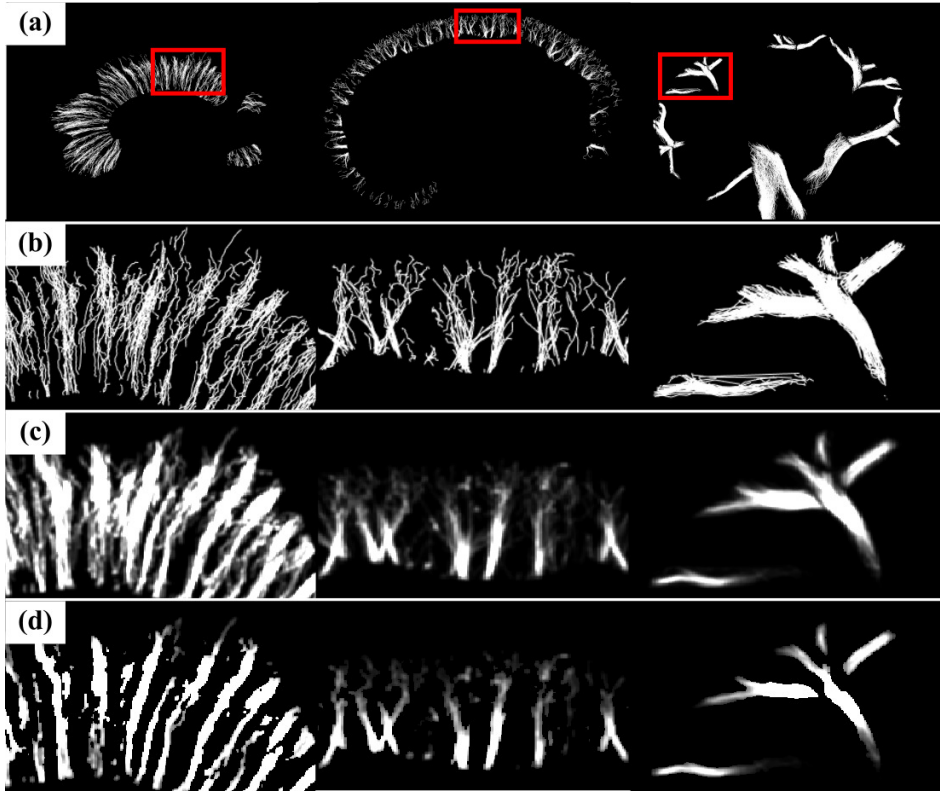


Figure 4.4: Preprocessing steps for track isolation. (a) shows three examples of classified tracks in the outer medulla (left), cortex (middle), and larger vessels (right) with red regions, zoomed in (b). (c): Gaussian filtering. (d): adaptive thresholding.

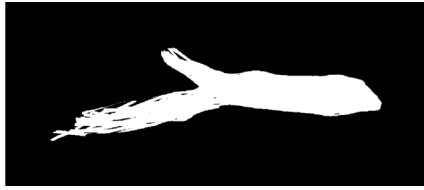
vertices with a degree higher than one (Figure 4.5-f). The process of removing the vertices and short edges was continued until all branches of the skeleton only had pedant vertices (Figure 4.5-g).

4.1.3 Characterization

With the estimated centerline and isolated tracks, different features of the segments and tracks were quantified. These features are described below:

4.1.3.1 VELOCITY

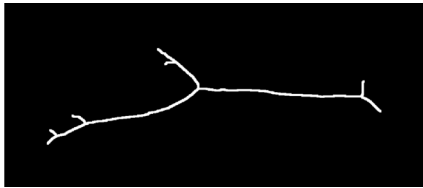
The distribution of the estimated velocities (\vec{v}_{ik}), defined in (3.8), in different regions and different classes of vessels were calculated. The peak velocity was measured as 98% of



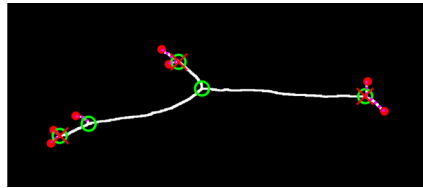
(a) Isolated tracks



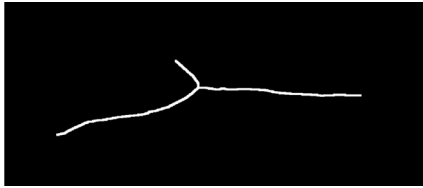
(b) Dialation



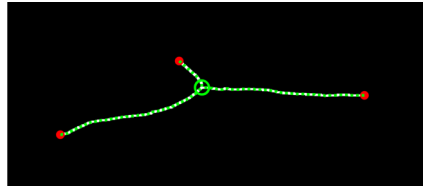
(c) Skeleton



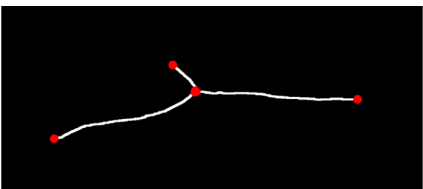
(d) Graph of skeleton



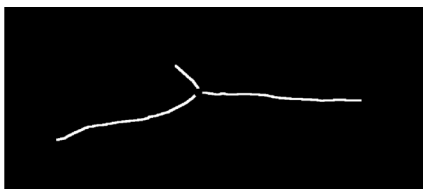
(e) Removing short edges



(f) New graph



(g) Branching



(h) Centerlines

Figure 4.5: Steps from isolated tracks to extraction of centerlines in the isolated area. Red dots in the graph show pendant vertices, and green circles are vertices with higher degrees.

the cumulative distribution function (CDF) of the estimated velocities.

4.1.3.2 DIAMETER

Assuming that uncertain MB positions have normal distribution around vessel's centerline, over 95% of positions would be within 2σ distance of the centerline, where σ is the standard deviation of MBs' distances from the centerline. Therefore, 4σ was considered as the vessel diameter (Figure 4.6-a).

4.1.3.3 LENGTH

Indicating the length of each centerline (Figure 4.6-a).

4.1.3.4 TORTUOSITY

The centerline tortuosity was calculated as the ratio between the centerline's length to the distance between two ends of the centerline. The tortuosity of a straight line is 1 and increases by the degree of curvatures and bends in the centerline (Figure 4.6-b).

4.1.3.5 TRACK DENSITY

The ratio of non-zero pixels to all pixels in a local region was defined as the structure density. Since the density may differ in different local regions, the entire ROI was divided into 50% overlapped 2×2 mm local regions, and the structure density was calculated for each (Figure 4.6-c).

4.1.3.6 INTERSEGMENT DISTANCE

The mean of distances from a segment to its adjacent segments (Figure 4.6-d).

Of the above-mentioned features, velocity, diameter, and track density were calculated based on the individual tracks, while the other features were calculated based only on the extracted segments.

A Wilcoxon signed-rank test was performed to compare features of two classes of vessels, *i.e.* arteries and veins. The p -value of the test was used to assess how the difference between quantified features of classified vessels was statistically significant in the different regions of the kidneys. Considering the small sample size of the study (10 kidneys) and assuming that data had a t -distribution, 95% confidence interval of the median and interquartile range (IQR) of the quantified features were also reported. Finally, the distribution of significant features was shown in the form of box plots.

4.2 Results

Over 300,000 tracks in different regions of 10 kidneys were classified, and 5,606 segments were extracted in total. Figure 4.7 shows the classified artery and vein tracks, demon-

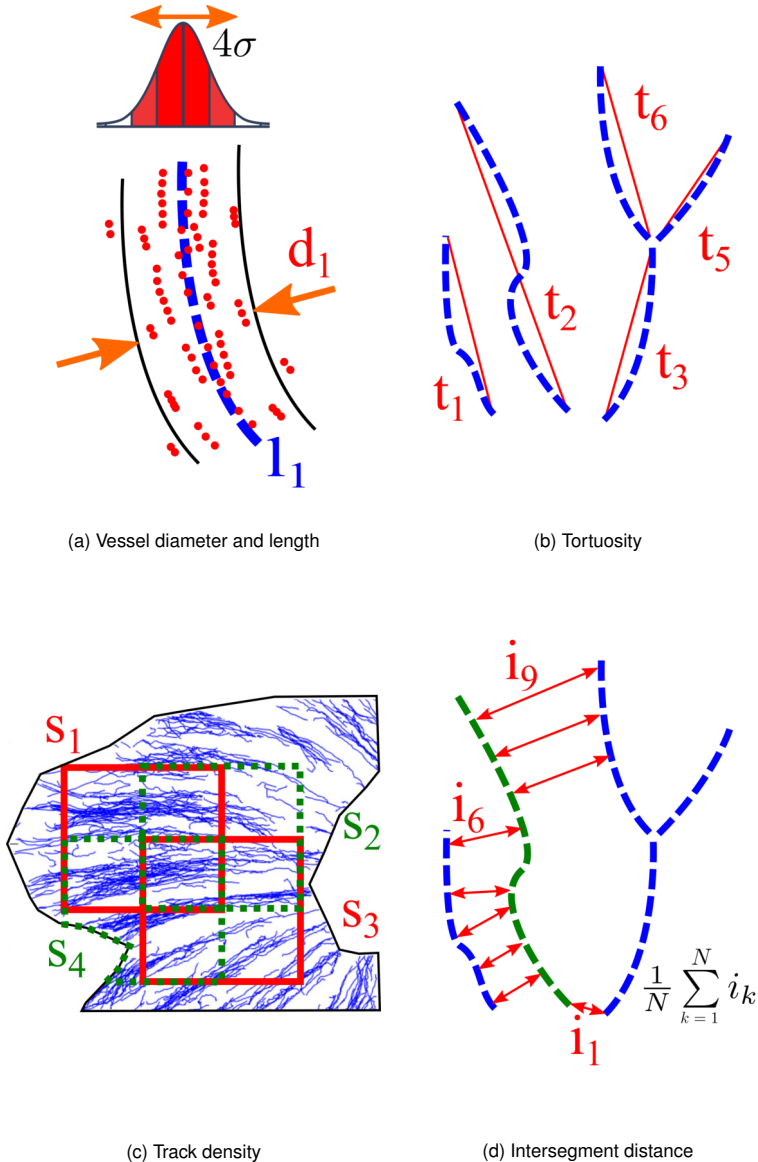


Figure 4.6: Examples of different morphological quantification metrics. Dashed lines are estimated centerlines. (a) diameter and length, (b) tortuosity: ratio of length over distance, (c) Track density: measuring track density in overlapped patches, and (d) Intersegment distance: average distance of a centerline to its adjacent centerlines.

strating the separated arterial and venous flow in the kidney. Sparser artery tracks in the cortical region (dashed oval) and existence of many arteries behind the veins (dashed rectangles) were noticeable. Examples of automated segments from classified artery and vein tracks are shown in Figure 4.8, visualizing the estimated centerlines and the potential vessel walls for the group of tracks.

The statistics of the quantified tracks and segmented data, including t -distribution of median and IQR with 95% confidence interval and the p -value of the Wilcoxon signed-ranked test on these metrics, are summarized in Table 4.1.

Table 4.1: Median and inter-quartile range of estimated features for the classified arteries/DVR bundles (red) and veins/AVR bundles (blue) in three regions. The 95% confidence interval and p -value for each metric are reported. The gray highlighted metrics were considered statistically significant by the Wilcoxon signed-rank test ($p \leq 0.006$).

Feature	Metric	IM Vasa recta bundles	OM Vasa recta bundles	CO
Velocity [mm/s]	Median	0.87 ± 0.07 0.63 ± 0.03 } $p = 0.002$	0.84 ± 0.03 0.68 ± 0.03 } $p = 0.002$	1.87 ± 0.33 1.63 ± 0.26 } $p = 0.695$
	IQR	0.06 ± 0.02 0.04 ± 0.01 } $p = 0.065$	0.04 ± 0.01 0.03 ± 0.01 } $p = 0.193$	0.48 ± 0.15 0.24 ± 0.08 } $p = 0.002$
	Peak (CDF-98%)	2.06 ± 0.15 1.56 ± 0.05 } $p = 0.002$	1.98 ± 0.07 1.61 ± 0.04 } $p = 0.002$	13.89 ± 0.92 9.05 ± 1.60 } $p = 0.002$
Diameter [μm]	Median	178.68 ± 10.18 167.18 ± 15.21 } $p = 0.232$	187.60 ± 5.51 168.80 ± 19.50 } $p = 0.084$	163.09 ± 19.48 173.26 ± 8.52 } $p = 0.275$
	IQR	101.40 ± 16.73 84.91 ± 13.73 } $p = 0.193$	75.44 ± 7.57 103.06 ± 6.45 } $p = 0.002$	97.83 ± 6.08 96.68 ± 12.52 } $p = 1$
Length [mm]	Median	0.88 ± 0.06 0.68 ± 0.14 } $p = 0.006$	1.01 ± 0.08 0.88 ± 0.13 } $p = 0.002$	0.69 ± 0.05 0.74 ± 0.06 } $p = 0.193$
	IQR	0.75 ± 0.05 0.51 ± 0.07 } $p = 0.049$	75.44 ± 7.57 0.47 ± 0.05 } $p = 0.002$	0.41 ± 0.04 0.47 ± 0.08 } $p = 0.131$
Tortuosity	Median	1.11 ± 0.01 1.12 ± 0.00 } $p = 0.027$	1.11 ± 0.00 1.14 ± 0.01 } $p = 0.002$	1.13 ± 0.01 1.13 ± 0.01 } $p = 0.492$
	IQR	0.06 ± 0.01 0.08 ± 0.01 } $p = 0.084$	0.05 ± 0.01 0.09 ± 0.01 } $p = 0.002$	0.11 ± 0.02 0.12 ± 0.02 } $p = 0.625$
Track Density	Median	0.30 ± 0.06 0.22 ± 0.07 } $p = 0.006$	0.30 ± 0.05 0.16 ± 0.04 } $p = 0.002$	0.10 ± 0.03 0.17 ± 0.03 } $p = 0.002$
	IQR	0.09 ± 0.02 0.08 ± 0.01 } $p = 0.557$	0.12 ± 0.02 0.09 ± 0.02 } $p = 0.002$	0.07 ± 0.02 0.11 ± 0.02 } $p = 0.014$
Segment Density	Median	142.63 ± 87.94 183.70 ± 87.47 } $p = 0.275$	202.19 ± 97.16 123.43 ± 90.07 } $p = 0.049$	163.09 ± 19.48 169.00 ± 104.75 } $p = 0.275$
	IQR	50.88 ± 33.83 85.92 ± 37.58 } $p = 0.084$	94.39 ± 25.37 74.26 ± 34.19 } $p = 0.557$	95.06 ± 45.44 101.97 ± 62.73 } $p = 1$

In all regions the median velocity was predicted higher in the arteries compared with the veins. However, the difference between median velocities was only statistically significant in the IM and OM regions ($p = 0.002$). In the CO, the IQR metric showed a statistically significant difference between arteries and veins ($p = 0.002$), however, the test on the median velocity did not reveal significantly higher values for the median of arterial blood velocity ($p = 0.695$). The distribution of velocity estimates in different

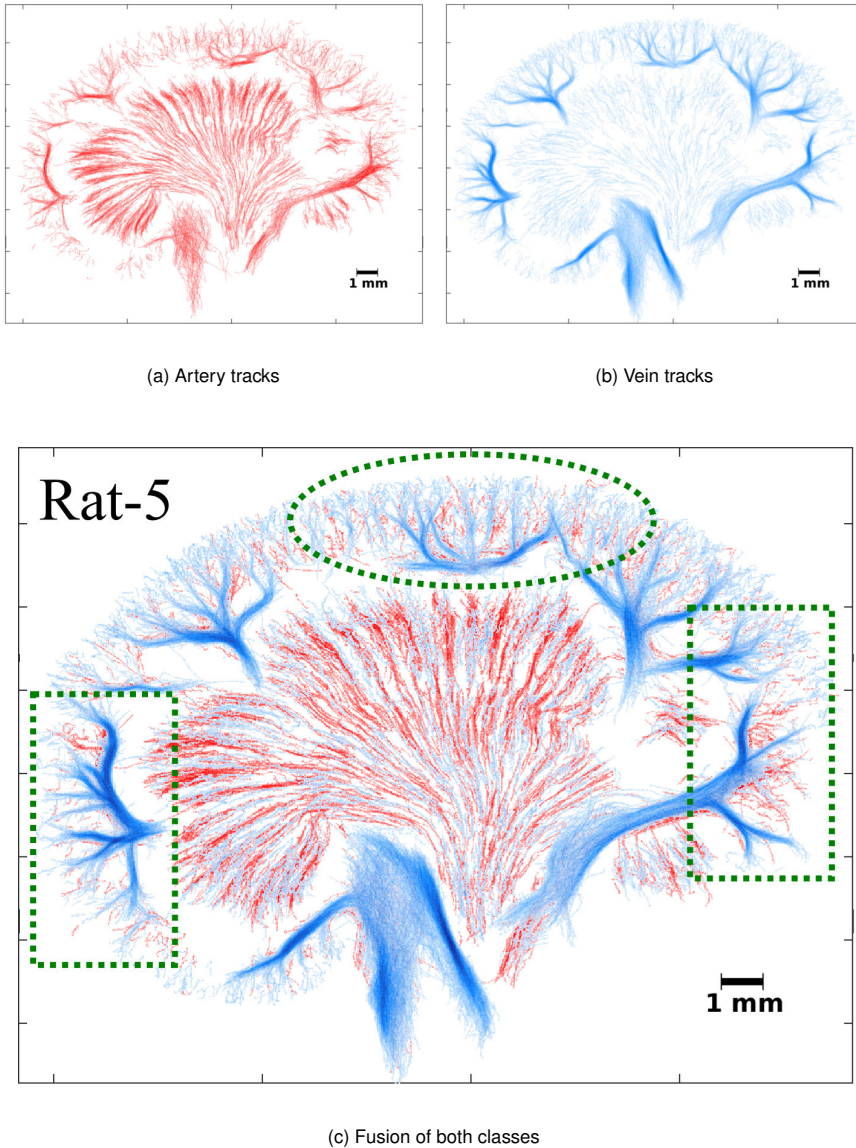


Figure 4.7: Classified tracks into groups of arteries and veins. (a) classified arteries (b) classified veins, and (c) combination of arteries and veins after classification. Comparing (c) with (a) and (b), the dashed oval region shows a noticeable sparser arteries compared with veins in the cortex, and the dashed rectangles show two example of the region with many arteries behind the veins.

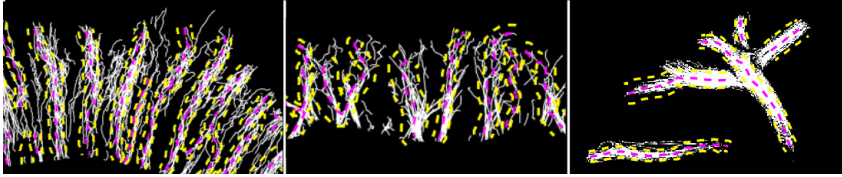


Figure 4.8: Automatic segmentation of examples in Figure 4.4 (left: outer medulla, middle: cortex, right: larger vessels). Red dashed lines are the estimated centerlines, and yellow dashed lines are estimated vessel walls.

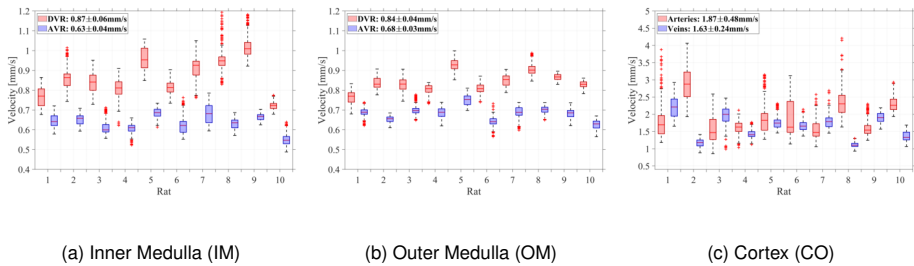


Figure 4.9: Velocity distribution in different regions of the kidney

regions of the rat kidneys are shown in Figure 4.9, demonstrating that blood velocities in the arterioles of the medullary regions (DVR in the IM and OM) were consistently estimated higher than the blood velocities in the venules.

The CDF plots of the velocity estimates and the corresponding peak velocities are shown in Figure 4.10. The statistics of the peak velocities in different regions, summarized as the last metric for velocity in Table 4.1, indicated that the difference between peak velocities of blood in the arteries and veins were statistically significant in the three regions.

The diameter of the bundles of DVR was larger than the groups of AVR in the OM and IM. In the cortical region, a larger median diameter was estimated for the veins. Even though the diameter estimates correspond to the visual appearance in Figure 4.7, only the IQR of the bundle diameters for the AVR and DVR in the OM was statistically significantly different. The distribution of estimated DVR and AVR bundle diameters in the OM region is shown in Figure 4.11.

The segments of the DVR bundles were consistently estimated longer than those from the segments AVR bundles. The artery tracks in the CO were shorter than those from the veins; however, the comparison of this feature in this region did not show a significant difference ($p = 0.193$). The distributions of the segment length in the regions with a significant difference are shown in Figure 4.12.

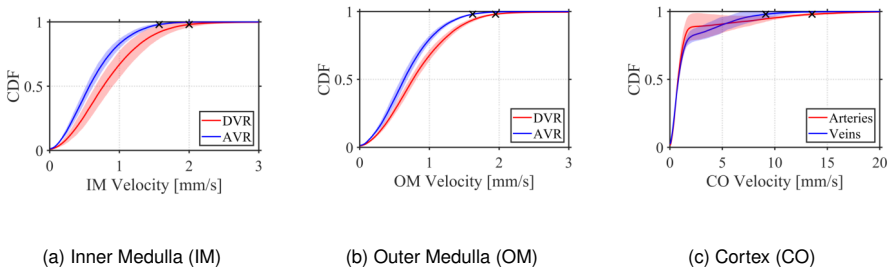


Figure 4.10: CDF plots of velocity estimates in the arteries (red) and veins (blue) in various regions for 10 rat kidneys. Solid line is the mean CDF plot and the shadow area is the standard deviation of the CDFs for 10 rats. Peak velocity is marked by \times .

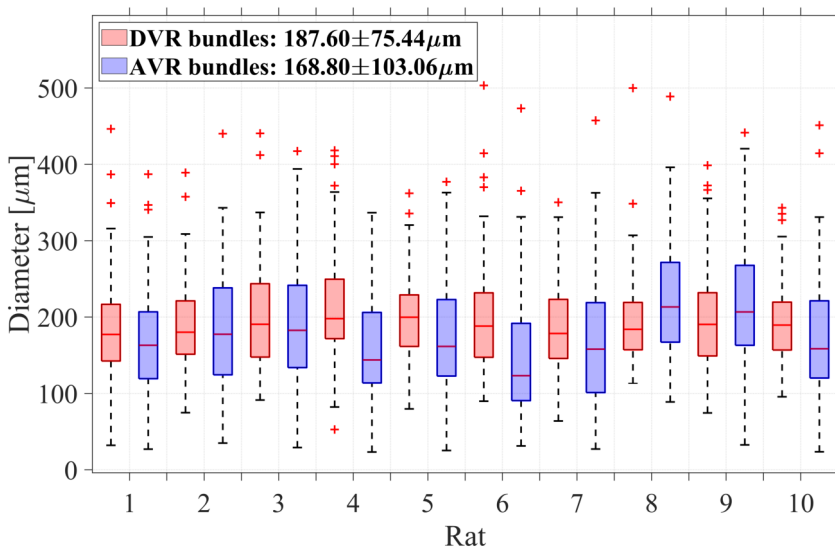
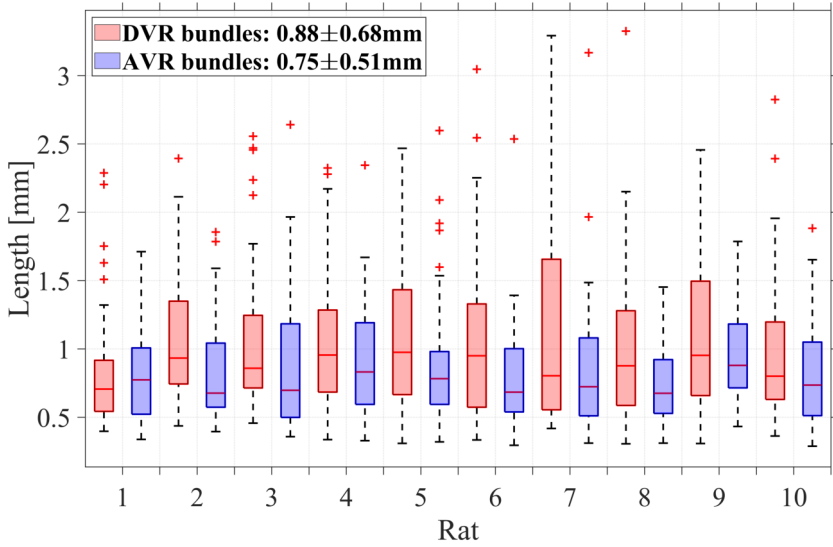
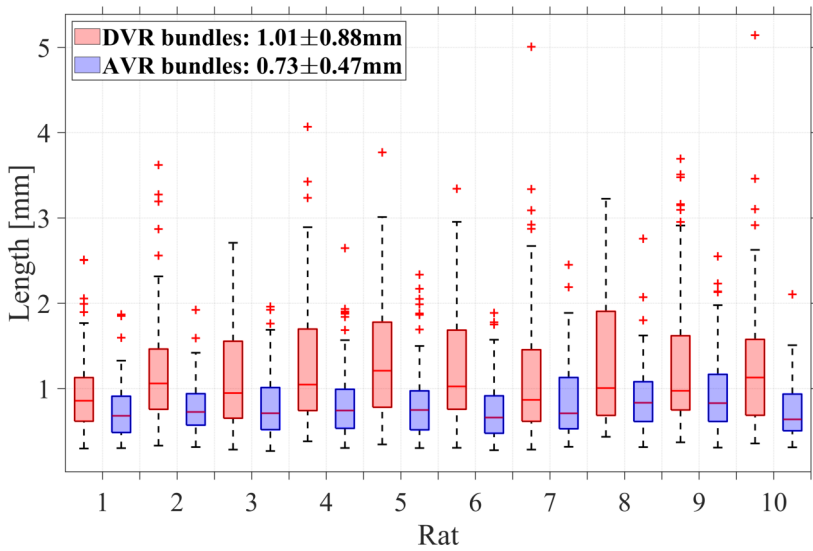


Figure 4.11: Distribution of estimated diameters in the outer medulla



(a) Inner Medulla (IM)



(b) Outer Medulla (OM)

Figure 4.12: Segment lengths distribution in the IM and OM regions.

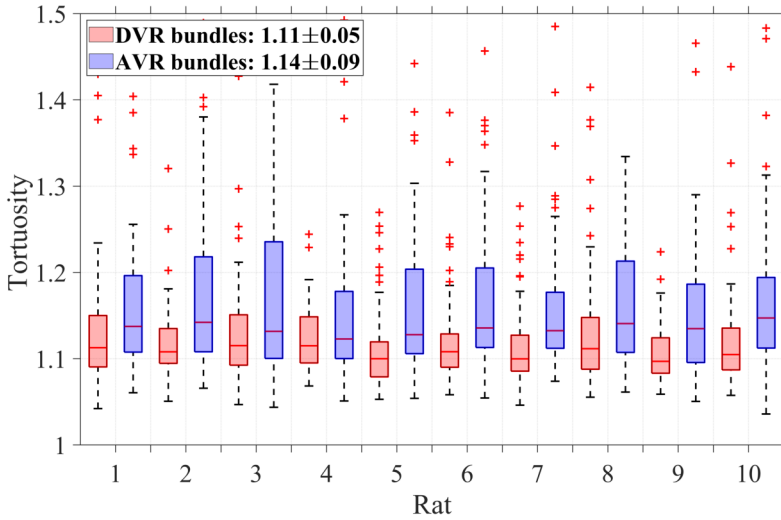
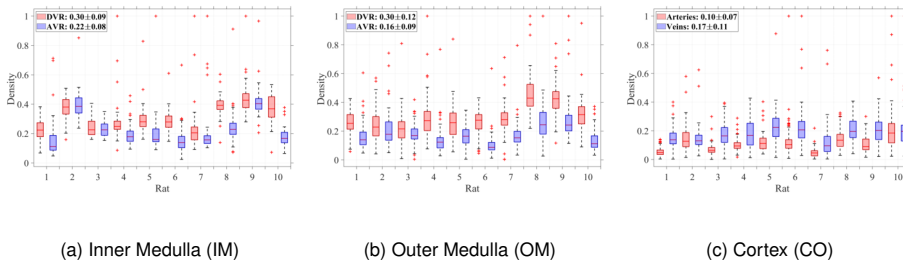


Figure 4.13: Distribution of tortuosity in the outer medulla



(a) Inner Medulla (IM)

(b) Outer Medulla (OM)

(c) Cortex (CO)

Figure 4.14: Track density distribution in different regions of the kidney

The segments of AVR bundles were consistently more tortuous than the segments of the DVR bundles in the OM ($p = 0.002$). The tortuosity distribution of segments in this region is shown in Figure 4.13.

Intersegment distance did not reveal any statistical difference between the two classes; on the other hand, track density showed a consistent pattern of denser DVR in the IM and OM and denser veins in the CO ($p = 0.002$). The distribution of the track densities in all regions is shown in Figure 4.14.

Moving average of the blood velocity in the OM region of 10 kidneys are shown in Figure 4.15. A lower flow in the venules were observed regardless of uncertainties in the velocity estimation and this result were consistent among all rats. The classified images of 9 other kidneys are shown in Figure 4.16.

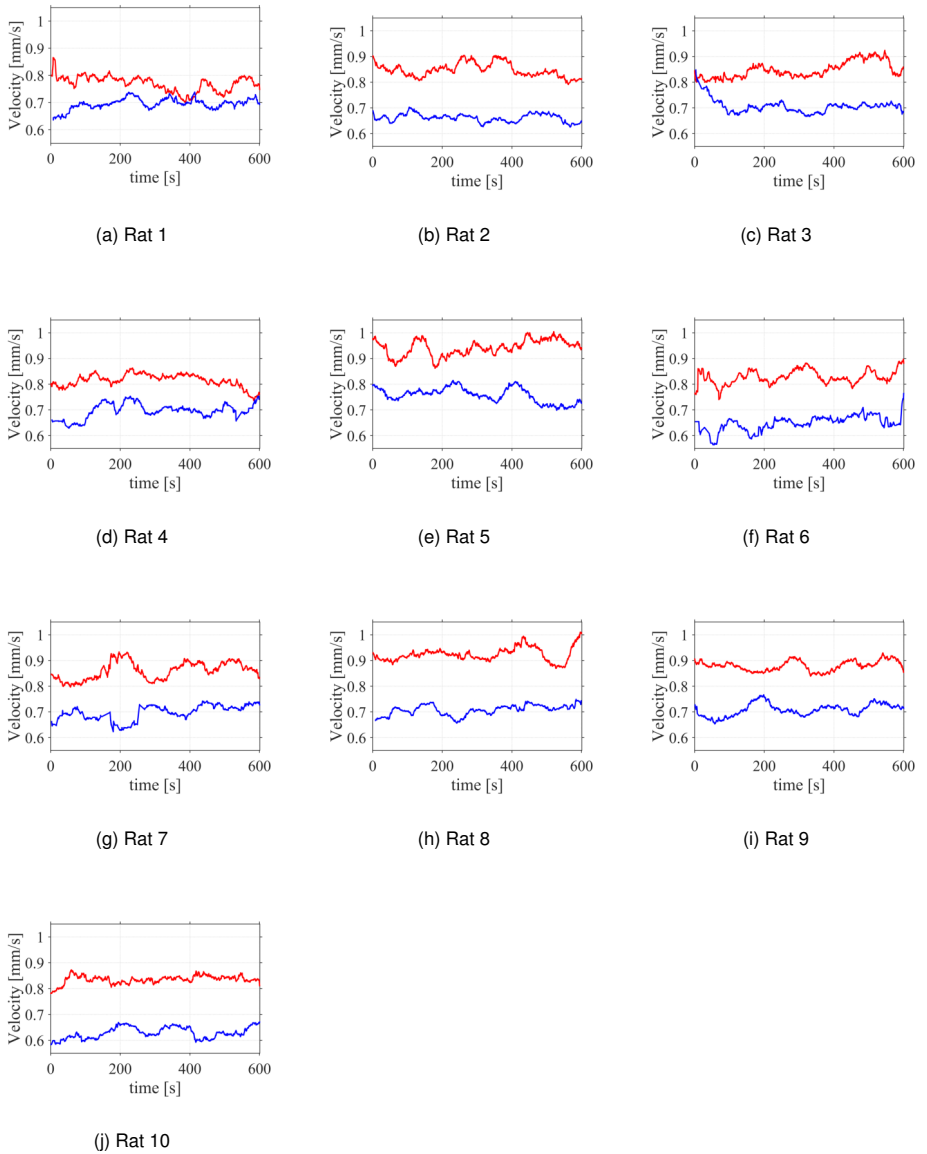


Figure 4.15: The moving average blood velocity in the DVR (red) and AVR (blue) of the outer medulla in 10 healthy kidneys. The moving average window size is 1 minute. In all the cases, a lower velocity in the AVR was observed.

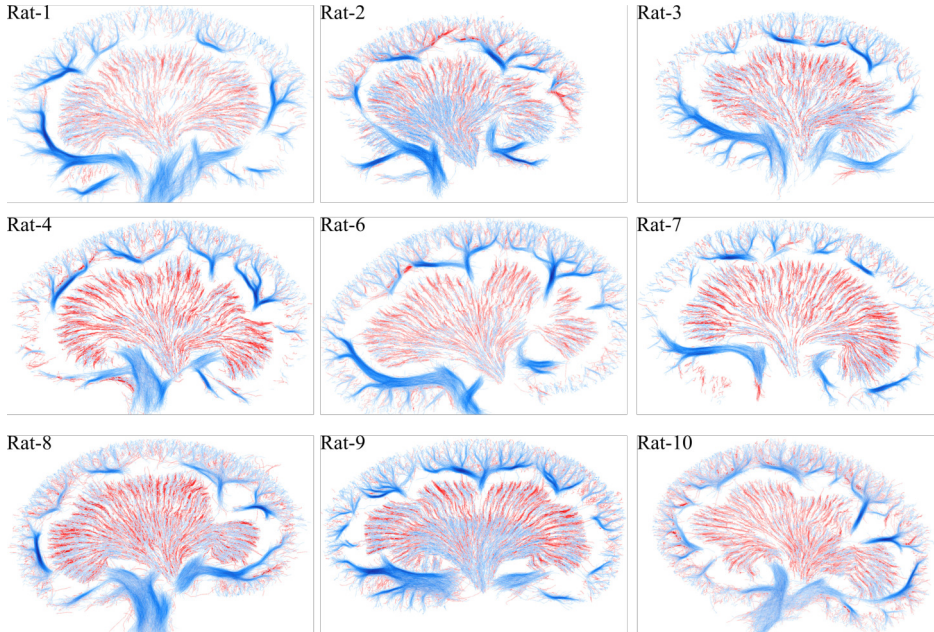


Figure 4.16: SR images of the classified vessels on the other 9 kidneys. Arterioles are shown in red and venules in blue. The kidney for rat 5 is shown in Fig 4.7.

4.3 Discussion

This is the first time a study has investigated an automatic vessel segmentation and characterization of 10 healthy rat kidneys in SRI. The velocity map was employed for separation of arterial and venous flow inside the kidneys. The characterized arteries and veins were compared statistically in three different anatomical regions of the kidneys using the t -distribution confidence intervals and Wilcoxon signed-rank test. The statistics showed a clear differentiation between arterial and venous segments both in morphology and flow dynamics. The arteries and veins of the 10 kidneys were classified in a semi-automated manner, *i.e.*, the procedures required manual labeling of regions and general arterial flow directions in the labeled regions as prior information. However, the individual 300,000 tracks were classified automatically based only on the defined anatomical regions and arterial flow determination in each region.

Several features from the classified tracks and their segments were investigated and compared statistically. It was shown that the difference in the velocity estimates of the classified tracks was statistically significant in the IM and OM regions between arteries and veins. However, these trends were not seen in the CO. Several factors may contribute to the lower performance of velocity estimates in the cortical regions. First, the 3D

complex structure of these rich vascular regions are projected in a 2D imaging plane, and sometimes, the arteries are sandwiched by veins (Andersen et al. 2021). Second, the blood flow in the larger arterial branches is pulsatile, and the peak velocity can reach several cm/s ; nonetheless, the velocity estimation using particle tracking in SRI is limited to the order of 10 mm/s . Tracking algorithms may still under-perform in the presence of a high density of particles, the complex flow pattern of pulsatility, and the ambiguity of 3D to 2D projection. The average number of arterial tracks in CO was 55% lower than the venous tracks, depicting the difficulty of MB tracking in cortical arteries.

Most of the extracted features were statistically significant in the OM region. Moreover, the velocity and track density were two features that showed the statistical difference in all regions. However, other described features were not statistically significant in all regions. The unique anatomical structure of each kidney and the rats' different sizes and weights may also cause uncorrelated morphological characteristics. Moreover, the complexity of the morphological features in the 2D ultrasound SRI may be misinterpreted, when it is accumulated over a thick slice of 3D structure (Andersen et al. 2021). Therefore, the features calculated for segments, *e.g.*, tortuosity, may not be correspondent to the actual vessel existing in 3D.

Automatic segmentation of vessel structures in ultrasound SRI is still at the beginning of its development and requires more investigations. The segmentation performance must be evaluated using a gold standard. A gold standard requires a rich dataset of ultrasound SR images of kidneys that have been manually segmented by multiple experts and such a dataset are not yet available. At a more advanced level, such a gold standard allows training of deep neural network to extract more accurate and relevant features for blood vessel segmentation of kidneys.

It is also worth comparing and discussing the result from a clinical perspective. Several findings in clinical investigations as well as intrinsic nature of SRI based on ultrasound contrast agents can be used to justify features with insignificant difference. It is shown in (Khan et al. 2018) how the arteries are wrapped by a nearby vein. The difficulties in tracking MBs in the larger arteries could be because of both pulsatility of flow and the phenomenon of venous wrapping of renal arteries. For the same reasons the cortical artery diameters could be overestimated in SRI. Although it was expected to observe larger veins compared with arteries (Nordsletten et al. 2006), the estimated interval for the diameters of arteries (163.09 ± 19.48) were roughly the same as the diameters of the veins (173.26 ± 8.52) and the difference was not statistically significant ($p = 0.275$). The DVR and AVR travel in vascular bundles, primarily in the OM (Ren et al. 2014). It has been shown that the AVR are both wider and more numerous than DVR (Holliger et al. 1983; Zimmerhackl, Robertson, and Jamison 1985), and when estimating the diameter of the bundles, one would anatomically expect the AVR to be wider than the DVR (Ren et al. 2014). However, more MBs are available to track in the DVR compared with the AVR due to decay or burst of the bubbles, when they travel the long way in the vasa recta; therefore, the number of tracks from which the diameters were estimated was higher in the DVR compared with the AVR (the ratio of the number of DVR tracks to the number

of AVR tracks was 2.28 ± 0.46 among all rats). In addition, the diameter of the vasa recta bundles that are measured in 2D SRI could be an overlap of several bundles (Andersen et al. 2021), adding to the outcome of the diameter estimates. The same considerations are applicable for the track densities in the OM and IM, where from an anatomical point of view, the AVR was expected to be denser than the DVR.

On the other hand, there were some features that were not expected to be significantly different, *e.g.*, length of arterioles and veins in the IM and OM. This can also be explained by the nature of the SRI. As mentioned above, it seems that the MBs that are exposed to ultrasound waves for longer periods are more likely to have shorter life. With this hypothesis, the abundance of MBs in the DVR compared with the AVR can be justified as whatever exists in the AVR has passed through the DVR and were more exposed to the ultrasound waves.

It was not expected to see more tortuous AVR compared with DVR in healthy rats. The significant difference in the tortuosity of the centerlines in the outer medulla could be the result of 2D projection of 3D structure that exist in the elevational thickness of the ultrasound imaging plane and could cause a miss interpretation of the actual tortuosity of the vessels.

Some features correspond to the results from previous clinical investigations. The velocity in the arterioles was statistically significantly higher than in the venules. This was in line with the previous findings (Holliger et al. 1983; Zimmerhackl, Robertson, and Jamison 1985). Lastly, it was expected to find a denser structure of the veins in the cortex, as these are larger compared with the arteries, and it was easier to track MBs in them, as mentioned. Nevertheless, it should be noted that track density is pixel based and therefore a relative feature. It can be used for comparison as long as pixel size and track thickness of all images are the same.

The purpose of this PhD project was to develop an SRI processing pipeline with tissue motion correction, robust MB tracking, and image quantification. Producing an SR image of an organ, scanned *in vivo*, is challenging from several aspects. The live organ is prone to motions from different sources, such as heart beating and breathing. Furthermore, the individual MBs should be tracked with a robust tracking algorithm that can cope with a high concentration of MBs in complex structures. Finally, the SR images need to be quantified and interpreted. In this thesis, all of these challenges were addressed by different methods to form an SRI processing pipeline with motion correction, robust tracking, and some quantifiable outputs.

Tissue motion correction

An SRI processing pipeline with tissue motion correction was presented in Chapter 3. The *in vivo* data from the left kidney of Sprague-Dawley rats were processed using the proposed approach. The result showed that tissue motion could be reliably measured with micrometer precision. It could be used to compensate for the motion caused by breathing, heartbeats, and muscle contractions.

Robust MB tracking

A HK tracker was proposed in Chapter 3. The HK tracker attempts to track MBs with different ranges of velocity with corresponding initial conditions and linking distances. The proposed tracker was compared with the NN and K trackers and evaluated using several assignment-based and profile-based performance metrics with challenging scenarios of varying MB density and uncertainty. The results indicate that the proposed HK tracker outperforms the NN and K trackers for many metrics and in different scenarios, especially in high concentration and high uncertainty of MB positions. The method also improved the *in vivo* image quality. The *in vivo* results showed noticeable improvement with trends similar to the simulations, including more accurate diameter estimations. The tracking algorithm was further extended, and it was shown that having a Kalman-based tracker with a forward-backward configuration enhanced the tracker performance and improved the velocity estimation.

Blood vessel segmentation

The MB track segmentation, described in Chapter 4, presented a procedure to classify arteries and veins in the ultrasound SR images of the rat kidneys, automatically segment the blood vessels, and extract several features of each class of vessels such as velocity, diameter, length, tortuosity, and density. The t -distribution of each feature with a 95% confidence interval was reported, and it was shown that track density and velocity estimates of the arteries and veins were statistically significant in the different regions of the kidney. Finally, the challenges of vessel characterization using MB tracks in 2D SRI and its comparison with a priori anatomical and physiological knowledge were discussed.

Clinical application

One of the main goals of the SRI project was to investigate the feasibility of using SRI for diagnosing diseases, such as ischemia, diabetes, and cancer. The clinical investigations were conducted in parallel to the development of the SRI processing pipeline and evolved during this project. The clinical studies are out of scope of this thesis and the results related to the clinical application can be found in paper 2 (Andersen, Taghavi, Hoyos, et al. 2020), paper 3 (Andersen, Taghavi, Kjer, et al. 2021), paper 6, paper 7 (Andersen, Hoyos, et al. 2019), and paper 9 (Søgaard et al. 2020).

Perspective and Outlook

From this Ph.D. project, it has been shown that better SR images of rat kidneys can be produced using an SRI processing pipeline with tissue motion correction and robust tracking. More efficient and fast algorithms need to be investigated for implementing the SRI processing pipeline in real-world applications. For the moment, most of the processing is performed offline, as it takes a long time for both motion correction and tracking. The advanced methods in parallel processing and GPU computing will decrease the processing time and enable real-time SRI. Another critical challenge that remains is to extend the developed processing pipeline to 3D data. 2D projection of a 3D structure was one of the fundamental limitations in motion correction, MB tracking, and quantification. The motion in elevation direction (out-of-plane) cannot be captured from the 2D ultrasound images. Projection of the 3D vessel structure to a 2D plane can create very challenging scenarios for MB tracking. Lastly, many features of the projected 3D structure could be miss interpreted by quantification of a 2D SR image.

Bibliography

References from Chapter 1

- Ackermann, D. and G. Schmitz (2016). “Detection and Tracking of Multiple Microbubbles in Ultrasound B-Mode Images”. In: *IEEE Trans. Ultrason., Ferroelec., Freq. Contr.* 63.1, pp. 72–82 (cit. on p. 3).
- Amir-Khalili, A., G. Hamarneh, and R. Abugharbieh (2015). “Automatic vessel segmentation from pulsatile radial distension”. In: *International Conference on Medical Image Computing and Computer-Assisted Intervention*. Springer, pp. 403–410 (cit. on p. 3).
- Andersen, S. B., C. A. V. Hoyos, I. Taghavi, F. Gran, K. L. Hansen, C. M. Sørensen, J. A. Jensen, and M. B. Nielsen (2019). “Super-Resolution Ultrasound Imaging of Rat Kidneys before and after Ischemia-Reperfusion”. In: *Proc. IEEE Ultrason. Symp.* Pp. 1–4 (cit. on p. 3).
- Andersen, S. B., I. Taghavi, C. A. V. Hoyos, S. B. Sjøgaard, F. Gran, L. Lonn, K. L. Hansen, J. A. Jensen, M. B. Nielsen, and C. M. Sørensen (2020). “Super-Resolution Imaging with Ultrasound for Visualization of the Renal Microvasculature in Rats Before and After Renal Ischemia: A Pilot Study”. In: *Diagnostics* 10.11, p. 862 (cit. on p. 3).
- Barnett, F. D. S. B. and M. Ziskin (2007). “Recommendations on the safe use of ultrasound contrast agents”. In: *Ultrasound Med. Biol.* 33.2, pp. 173–174 (cit. on p. 1).
- Chavignon, A., B. Heiles, V. Hingot, and O. Couture (2020). *3D Transcranial Ultrasound Localization Microscopy in Rat with a Multiplexed Matrix Probe*. Presentation at IEEE Ultrason. Symp. (Cit. on p. 3).
- Chenouard, N., I. Smal, F. De Chaumont, M. Maška, I. F. Sbalzarini, Y. Gong, J. Cardinale, C. Carthel, S. Coraluppi, M. Winter, et al. (2014). “Objective comparison of particle tracking methods”. In: *Nat. Methods* 11.3, pp. 281–290 (cit. on p. 2).
- Christensen-Jeffries, K., R. J. Browning, M. Tang, C. Dunsby, and R. J. Eckersley (2015). “In Vivo Acoustic Super-Resolution and Super-Resolved Velocity Mapping Using Microbubbles”. In: *IEEE Trans. Med. Imag.* 34.2, pp. 433–440 (cit. on pp. 2, 3).
- Christensen-Jeffries, K., O. Couture, P. A. Dayton, Y. C. Eldar, K. Hynynen, F. Kiessling, M. O’Reilly, G. F. Pinton, G. Schmitz, M. Tang, et al. (2020). “Super-resolution ultrasound imaging”. In: *Ultrasound Med. Biol.* 46.4, pp. 865–891 (cit. on p. 1).
- Couture, O., B. Besson, G. Montaldo, M. Fink, and M. Tanter (2011). “Microbubble ultrasound super-localization imaging (MUSLI)”. In: *Proc. IEEE Ultrason. Symp.* Pp. 1285–1287 (cit. on p. 1).

- Couture, O., V. Hingot, B. Heiles, P. Muleki-Seya, and M. Tanter (2018). “Ultrasound Localization Microscopy and Super-Resolution: A State of the Art”. In: *IEEE Trans. Ultrason., Ferroelec., Freq. Contr.* 65.8, pp. 1304–1320. DOI: 10.1109/TUFFC.2018.2850811 (cit. on p. 1).
- Couture, O., M. Tanter, and M. Fink (2010). “Method and device for ultrasound imaging”. In: *Patent Cooperation Treaty (PCT)/FR2011/052810* (cit. on p. 1).
- Crocker, J. C. and D. G. Grier (1996). “Methods of digital video microscopy for colloidal studies”. In: *J. Colloid* 179.1, pp. 298–310. DOI: 10.1006/jcis.1996.0217 (cit. on p. 2).
- Errico, C., J. Pierre, S. Pezet, Y. Desailly, Z. Lenkei, O. Couture, and M. Tanter (2015). “Ultrafast ultrasound localization microscopy for deep super-resolution vascular imaging”. In: *Nature* 527, pp. 499–502 (cit. on pp. 2, 3).
- Fink, M. and M. Tanter (2010). “Multiwave imaging and super resolution”. In: *Phys. Today* 63.2, pp. 28–33 (cit. on p. 1).
- Foiret, J., H. Zhang, T. Ilovitsh, L. Mahakian, S. Tam, and K. W. Ferrara (2017). “Ultrasound localization microscopy to image and assess microvasculature in a rat kidney”. In: *Scientific Reports* 7.1, 13662:1–12. DOI: 10.1038/s41598-017-13676-7 (cit. on p. 2).
- Geiger, D., A. Gupta, L. Costa, and J. Vlontzos (1995). “Dynamic programming for detecting, tracking, and matching deformable contours”. In: *IEEE Trans. Pattern Anal. Mach. Intell.* 17.3, pp. 294–302. DOI: 10.1109/34.368194 (cit. on p. 2).
- Godinez, W. J., M. Lampe, S. Worz, B. Muller, R. Eils, and K. Rohr (2009). “Deterministic and probabilistic approaches for tracking virus particles in time-lapse fluorescence microscopy image sequences”. In: *Med. Image Anal.* 13.2, pp. 325–342. DOI: 10.1016/j.media.2008.12.004 (cit. on p. 2).
- Hansen, K. B., C. A. Villagomez-Hoyos, J.C. Brasen, K. Diamantis, V. Sboros, C. M. Sørensen, and J. A. Jensen (2016). “Robust Microbubble Tracking for Super Resolution Imaging in Ultrasound”. In: *Proc. IEEE Ultrason. Symp.* Pp. 1–4 (cit. on p. 2).
- Harput, S., K. Christensen-Jeffries, J. Brown, Y. Li, K. J. Williams, A. H. Davies, R. J. Eckersley, C. Dunsby, and M. Tang (2018). “Two-Stage Motion Correction for Super-Resolution Ultrasound Imaging in Human Lower Limb”. In: *IEEE Trans. Ultrason., Ferroelec., Freq. Contr.* 65.5, pp. 803–814. DOI: 10.1109/TUFFC.2018.2824846 (cit. on p. 2).
- Harput, S., K. Christensen-Jeffries, A. Ramalli, J. Brown, J. Zhu, G. Zhang, C. H. Leow, M. Toulemonde, E. Boni, P. Tortoli, R. J. Eckersley, C. Dunsby, and M. Tang (2019). “3-D Super-Resolution Ultrasound (SR-US) Imaging with a 2-D Sparse Array”. In: *arXiv preprint*, p. 1902.01608v1 (cit. on p. 3).
- Harput, S., M. Toulemonde, A. Ramalli, K. Christensen-Jeffries, E. Boni, P. Tortoli, C. Dunsby, and M. Tang (2020). “Quantitative Microvessel Analysis with 3-D Super-Resolution Ultrasound and Velocity Mapping”. In: *Proc. IEEE Ultrason. Symp.* Pp. 1–4 (cit. on p. 3).

- Heiles, B., M. Correia, V. Hingot, M. Pernot, J. Provost, M. Tanter, and O. Couture (Sept. 2019). “Ultrafast 3D Ultrasound Localization Microscopy Using a 32 x 32 Matrix Array”. In: *IEEE Trans. Ultrason., Ferroelec., Freq. Contr.* 38.9, pp. 2005–2015 (cit. on p. 3).
- Hess, S. T., T. P. K. Girirajan, and M. D. Mason (2006). “Ultra-high resolution imaging by fluorescence photoactivation localization microscopy”. In: *Biophysical Journal* 91.11, pp. 4258–4272 (cit. on p. 1).
- Hingot, V., C. Errico, B. Heiles, L. Rahal, M. Tanter, and O. Couture (2019). “Microvascular flow dictates the compromise between spatial resolution and acquisition time in Ultrasound Localization Microscopy”. In: *Scientific Reports* 9.1, pp. 1–10. DOI: 10.1038/s41598-018-38349-x (cit. on p. 2).
- Jensen, J. A., M. L. Ommen, S. H. Øygaard, M. Schou, T. Sams, M. B. Stuart, C. Beers, E. V. Thomsen, N. B. Larsen, and B. G. Tomov (2020). “Three-Dimensional Super Resolution Imaging using a Row-Column Array”. In: *IEEE Trans. Ultrason., Ferroelec., Freq. Contr.* 67.3, pp. 538–546. DOI: 10.1109/TUFFC.2019.2948563 (cit. on pp. 3, 4).
- Kierski, T. M., D. Espindola, I. G. Newsome, E. Cherin, J. Yin, F. S. Foster, C. E. M. Demore, G. F. Pinton, and P. A. Dayton (2020). “Superharmonic Ultrasound for Motion-Independent Localization Microscopy: Applications to Microvascular Imaging From Low to High Flow Rates”. In: *IEEE Trans. Ultrason., Ferroelec., Freq. Contr.* 67.5, pp. 957–967. DOI: 10.1109/tuffc.2020.2965767 (cit. on p. 2).
- Ku, T. C., L. S. Kao, C. C. Lin, and Y. S. Tsai (2009). “Morphological filter improve the efficiency of automated tracking of secretory vesicles with various dynamic properties”. In: *Microsc. Res. Tech.* 72.9, pp. 639–649. DOI: 10.1002/jemt.20711 (cit. on p. 2).
- Kuhn, H. W. (1955). “The Hungarian method for the assignment problem”. In: *Naval research logistics quarterly* 2.1-2, pp. 83–97 (cit. on p. 3).
- Lockwood, G. R., P-C. Li, M. O’Donnell, and F. S. Foster (1996). “Optimizing the Radiation Pattern of Sparse Periodic Linear Arrays”. In: *IEEE Trans. Ultrason., Ferroelec., Freq. Contr.* 43, pp. 7–14 (cit. on p. 1).
- Lowerison, M. R., C. Huang, F. Lucien, S. Chen, and P. Song (2020). “Ultrasound localization microscopy of renal tumor xenografts in chicken embryo is correlated to hypoxia”. In: *Scientific reports* 10.1, pp. 1–13 (cit. on p. 3).
- Ozdemir, I., K. Johnson, S. Mohr-Allen, K. E. Peak, V. Varner, and K. Hoyt (2021). “Three-dimensional visualization and improved quantification with super-resolution ultrasound imaging-validation framework for analysis of microvascular morphology using a chicken embryo model”. In: *Phys. Med. Biol.* 66.8, p. 085008 (cit. on p. 3).
- Rink, J., E. Ghigo, Y. Kalaidzidis, and M. Zerial (2005). “Rab conversion as a mechanism of progression from early to late endosomes”. In: *Cell* 122.5, pp. 735–749. DOI: 10.1016/j.cell.2005.06.043 (cit. on p. 2).

- Rust, M. J., M. Bates, and X. Zhuang (2006). “Sub-diffraction-limit imaging by stochastic optical reconstruction microscopy (STORM)”. In: *Nat. Methods* 3.10, pp. 793–795 (cit. on p. 1).
- Sbalzarini, I. F. and P. Koumoutsakos (2005). “Feature point tracking and trajectory analysis for video imaging in cell biology”. In: *J. Struct. Biol.* 151.2, pp. 182–195. DOI: 10.1016/j.jsb.2005.06.002 (cit. on p. 2).
- Shekhawat, G. S. and V. P. Dravid (2005). “Nanoscale imaging of buried structures via scanning near-field ultrasound holography”. In: *Science* 310.5745, pp. 89–92 (cit. on p. 1).
- Siepmann, M., G. Schmitz, J. Bzyl, M. Palmowski, and F. Kiessling (2011). “Imaging tumor vascularity by tracing single microbubbles”. In: *Proc. IEEE Ultrason. Symp.*, pp. 6293297, 1906–1908. DOI: 10.1109/ULTSYM.2011.0476 (cit. on p. 1).
- Smistad, E. and L. Løvstakken (2016). “Vessel detection in ultrasound images using deep convolutional neural networks”. In: *Deep Learning and Data Labeling for Medical Applications*. Springer (cit. on p. 3).
- Søgaard, S. B., S. B. Andersen, I. Taghavi, C. A. V. Hoyos, K. L. Hansen, F. Gran, J. A. Jensen, M. B. Nielsen, and C. M. Sørensen (2020). “Super-resolution Ultrasound Imaging of the Renal Microvasculature in Rats with Metabolic syndrome”. In: *Proc. IEEE Ultrason. Symp.* Pp. 1–4 (cit. on p. 3).
- Solomon, O., R. J. G. van Sloun, H. Wijkstra, M. Misch, and Y. C. Eldar (2019). “Exploiting flow dynamics for super-resolution in contrast-enhanced ultrasound”. In: *IEEE Trans. Ultrason., Ferroelec., Freq. Contr.* 60.10, pp. 1573–1586 (cit. on p. 3).
- Song, P., J. D. Trzasko, A. Manduca, R. Huang, R. Kadirvel, D. F. Kallmes, and S. Chen (2017). “Improved super-resolution ultrasound microvessel imaging with spatiotemporal nonlocal means filtering and bipartite graph-based microbubble tracking”. In: *IEEE Trans. Ultrason., Ferroelec., Freq. Contr.* 65.2, pp. 149–167 (cit. on pp. 2, 3).
- Tang, S., P. Song, J. D. Trzasko, M. Lowerison, C. Huang, P. Gong, U. Lok, A. Manduca, and S. Chen (2020). “Kalman Filter-Based Microbubble Tracking for Robust Super-Resolution Ultrasound Microvessel Imaging”. In: *IEEE Trans. Ultrason., Ferroelec., Freq. Contr.* 67.9, pp. 1738–1751 (cit. on p. 3).
- Ulman, V., M. Maška, K. E. Magnusson, O. Ronneberger, C. Haubold, N. Harder, P. Matula, P. Matula, D. Svoboda, M. Radojevic, et al. (2017). “An objective comparison of cell-tracking algorithms”. In: *Nat. Methods* 14.12, p. 1141 (cit. on p. 2).
- Viessmann, O. M., R. J. Eckersley, K. Christensen-Jeffries, M. X. Tang, and C. Dunsby (2013). “Acoustic super-resolution with ultrasound and microbubbles”. In: *Phys. Med. Biol.* 58, pp. 6447–6458 (cit. on p. 1).
- Wei, K., E. Le, J. Bin, M. Coggins, J. Thorpe, and S. Kaul (2001). “Quantification of renal blood flow with contrast-enhanced ultrasound”. In: *Journal of the American College of Cardiology* 37.4, pp. 1135–1140 (cit. on p. 3).

References from Chapter 2

- Eckersley, R. J., C. T. Chin, and P. N. Burns (2005). “Optimising phase and amplitude modulation schemes for imaging microbubble contrast agents at low acoustic power”. In: *Ultrasound Med. Biol.* 31.2, pp. 213–219 (cit. on p. 12).
- Jensen, J. A. (1996). “Field: A Program for Simulating Ultrasound Systems”. In: *Med. Biol. Eng. Comp.* 10th Nordic-Baltic Conference on Biomedical Imaging, Vol. 4, Supplement 1, Part 1, pp. 351–353 (cit. on p. 9).
- (2014). “A Multi-threaded Version of Field II”. In: *Proc. IEEE Ultrason. Symp.* Pp. 2229–2232 (cit. on p. 9).
- Jensen, J. A. and N. B. Svendsen (1992). “Calculation of Pressure Fields from Arbitrarily Shaped, Apodized, and Excited Ultrasound Transducers”. In: *IEEE Trans. Ultrason., Ferroelec., Freq. Contr.* 39.2, pp. 262–267 (cit. on p. 9).
- Johnson, R., J. Feehally, J. Floege, and M. Tonelli (2018). *Comprehensive Clinical Nephrology*. 6th Edition. Elsevier (cit. on p. 19).
- Ommen, M. L. (2020). “Micromachined 2D Transducers and Phantoms for 3D Super-Resolution Ultrasound Imaging”. PhD thesis. Denmark Technical University (cit. on pp. 16, 17).
- Ommen, M. L., M. Schou, C. Beers, J. A. Jensen, N. B. Larsen, and E. V. Thomsen (2019). “3D Printed Calibration Micro-phantoms for Validation of Super-Resolution Ultrasound Imaging”. In: *Proc. IEEE Ultrason. Symp.* Pp. 1–4 (cit. on p. 16).
- (2021). “3D Printed Calibration Micro-Phantoms for Super-Resolution Ultrasound Imaging Validation”. In: *Ultrasonics* 114, p. 106353. DOI: 10.1016/j.ultras.2021.106353 (cit. on p. 16).
- Ommen, M. L., M. Schou, R. Zhang, C. A. V. Hoyos, J. A. Jensen, N. B. Larsen, and E. V. Thomsen (2018). “3D Printed Flow Phantoms with Fiducial Markers for Super-Resolution Ultrasound Imaging”. In: *Proc. IEEE Ultrason. Symp.* Pp. 1–4 (cit. on pp. 15, 16).
- Ren, H., L. Gu, A. Andreassen, J. S. Thomsen, L. Cao, E. I. Christensen, and X. Zhai (2014). “Spatial organization of the vascular bundle and the interbundle region: three-dimensional reconstruction at the inner stripe of the outer medulla in the mouse kidney”. In: *American Journal of Physiology-Renal Physiology* 306.3, F321–F326 (cit. on p. 20).
- Taghavi, I., S. B. Andersen, C. A. V. Hoyos, M. B. Nielsen, C. M. Sørensen, and J. A. Jensen (2021). “In Vivo Motion Correction in Super Resolution Imaging of Rat Kidneys”. In: *IEEE Trans. Ultrason., Ferroelec., Freq. Contr.* 68.10, pp. 3082–3093 (cit. on pp. 9, 18).
- Taghavi, I., S. B. Andersen, C. A. V. Hoyos, M. Schou, F. Gran, K. L. Hansen, M. B. Nielsen, C. M. Sørensen, M. B. Stuart, and J. A. Jensen (2022). “Ultrasound super-resolution imaging with a hierarchical Kalman tracker”. In: *Ultrasonics* 122, p. 106695. DOI: <https://doi.org/10.1016/j.ultras.2022.106695> (cit. on p. 9).

References from Chapter 3

- Andersen, S. B., I. Taghavi, C. A. V. Hoyos, S. B. Søgaaard, F. Gran, L. Lonn, K. L. Hansen, J. A. Jensen, M. B. Nielsen, and C. M. Sørensen (2020). “Super-Resolution Imaging with Ultrasound for Visualization of the Renal Microvasculature in Rats Before and After Renal Ischemia: A Pilot Study”. In: *Diagnostics* 10.11, p. 862 (cit. on p. 32).
- Bankir, L., N. Bouby, and M. Trinh-Trang-Tan (1989). “2 The role of the kidney in the maintenance of water balance”. In: *Bailliere’s clinical endocrinology and metabolism* 3.2, pp. 249–311 (cit. on p. 58).
- Bankman, I. N. (2009). *Handbook of Medical Image Processing and Analysis*. Elsevier Inc. DOI: 10.1016/b978-0-12-373904-9.x0001-4 (cit. on p. 21).
- Banterle, N., K. H. Bui, E. A. Lemke, and M. Beck (2013). “Fourier ring correlation as a resolution criterion for super-resolution microscopy”. In: *J. Struct. Biol* 183.3, pp. 363–367 (cit. on p. 28).
- Brown, K. G., D. Ghosh, and K. Hoyt (2020). “Deep learning of spatiotemporal filtering for fast super-resolution ultrasound imaging”. In: *IEEE Trans. Ultrason., Ferroelec., Freq. Contr.* PP.99, pp. 1–1. DOI: 10.1109/tuffc.2020.2988164 (cit. on p. 23).
- Chavignon, A., B. Heiles, V. Hingot, and O. Couture (2020). *3D Transcranial Ultrasound Localization Microscopy in Rat with a Multiplexed Matrix Probe*. Presentation at IEEE Ultrason. Symp. (Cit. on pp. 40, 60).
- Cheezum, M. K., W. F. Walker, and W. H. Guilford (2001). “Quantitative comparison of algorithms for tracking single fluorescent particles”. In: *Biophys. J.* 81.4, pp. 2378–2388 (cit. on p. 21).
- Chenouard, N., I. Smal, F. De Chaumont, M. Maška, I. F. Sbalzarini, Y. Gong, J. Cardinale, C. Carthel, S. Coraluppi, M. Winter, et al. (2014). “Objective comparison of particle tracking methods”. In: *Nat. Methods* 11.3, pp. 281–290 (cit. on p. 45).
- Christensen-Jeffries, K., S. Harput, J. Brown, P. N. T. Wells, P. Aljabar, C. Dunsby, M. Tang, and R. J. Eckersley (2017). “Microbubble Axial Localization Errors in Ultrasound Super-Resolution Imaging”. In: *IEEE Trans. Ultrason., Ferroelec., Freq. Contr.* 64.11, pp. 1644–1654. DOI: 10.1109/TUFFC.2017.2741067 (cit. on p. 21).
- Cupples, W. A., T. Sakai, and D. J. Marsh (1988). “Angiotensin II and prostaglandins in control of vasa recta blood flow”. In: *Am.J. Phys.-renal Phys.* 254.3, F417–F424. DOI: 10.1152/ajprenal.1988.254.3.F417 (cit. on p. 39).
- Furnival, T., R. K. Leary, and P. A. Midgley (2017). “Denoising time-resolved microscopy image sequences with singular value thresholding”. In: *Ultramicroscopy* 178, pp. 112–124. DOI: 10.1016/j.ultramicro.2016.05.005 (cit. on p. 21).
- Harput, S., K. Christensen-Jeffries, A. Ramalli, J. Brown, J. Zhu, G. Zhang, C. H. Leow, M. Toulemonde, E. Boni, P. Tortoli, R. J. Eckersley, C. Dunsby, and M. Tang (2019). “3-D Super-Resolution Ultrasound (SR-US) Imaging with a 2-D Sparse Array”. In: *arXiv preprint*, p. 1902.01608v1 (cit. on pp. 40, 60).

- Heiles, B., M. Correia, V. Hingot, M. Pernot, J. Provost, M. Tanter, and O. Couture (Sept. 2019). “Ultrafast 3D Ultrasound Localization Microscopy Using a 32 x 32 Matrix Array”. In: *IEEE Trans. Ultrason., Ferroelec., Freq. Contr.* 38.9, pp. 2005–2015 (cit. on pp. 40, 60).
- Hingot, V., A. Chavignon, B. Heiles, and O. Couture (2021). “Measuring image resolution in Ultrasound Localization Microscopy”. In: *IEEE Trans. Med. Imag.* (cit. on p. 28).
- Holliger, C., K. V. Lemley, S. L. Schmitt, F. C. Thomas, C. R. Robertson, and R. L. Jamison (1983). “Direct determination of vasa recta blood flow in the rat renal papilla.” In: *Circ. Research* 53.3, pp. 401–413 (cit. on pp. 39, 59).
- Jensen, J. A., S. Nikolov, K. L. Gammelmark, and M. H. Pedersen (2006). “Synthetic Aperture Ultrasound Imaging”. In: *Ultrasonics* 44, e5–e15 (cit. on pp. 36, 60).
- Jensen, J. A., M. L. Ommen, S. H. Øygaard, M. Schou, T. Sams, M. B. Stuart, C. Beers, E. V. Thomsen, N. B. Larsen, and B. G. Tomov (2020). “Three-Dimensional Super Resolution Imaging using a Row-Column Array”. In: *IEEE Trans. Ultrason., Ferroelec., Freq. Contr.* 67.3, pp. 538–546. DOI: 10.1109/TUFFC.2019.2948563 (cit. on pp. 40, 60).
- Jensen, J. A., M. Schou, M. L. Ommen, S. H. Øygaard, T. Sams, M. B. Stuart, E. V. Thomsen, N. B. Larsen, C. Beers, and B. G. Tomov (2019). “3-D Super Resolution Imaging using a 62+62 Elements Row-Column Array”. In: *Proc. IEEE Ultrason. Symp.* Pp. 1–4 (cit. on p. 40).
- Kuhn, H. W. (1955). “The Hungarian method for the assignment problem”. In: *Naval research logistics quarterly* 2.1-2, pp. 83–97 (cit. on p. 44).
- Liu, X., T. Zhou, M. Lu, Y. Yang, Q. He, and J. Luo (2020). “Deep Learning for Ultrasound Localization Microscopy”. In: *IEEE Trans. Med. Imag.* 39.10, pp. 3064–3078. DOI: 10.1109/tmi.2020.2986781 (cit. on p. 23).
- Lok, U. W., P. Song, J. D. Trzasko, R. Daigle, E. A. Borisch, C. Huang, P. Gong, S. Tang, W. Ling, and S. Chen (2020). “Real time SVD-based clutter filtering using randomized singular value decomposition and spatial downsampling for micro-vessel imaging on a Verasonics ultrasound system”. In: *Ultrasonics* 107, p. 106163. DOI: 10.1016/j.ultras.2020.106163 (cit. on p. 21).
- Nieuwenhuizen, R. P., K. A. Lidke, M. Bates, D. L. Puig, D. Grunwald, S. Stallinga, and B. Rieger (2013). “Measuring image resolution in optical nanoscopy”. In: *Nat. Methods* 10.6, pp. 557–562 (cit. on p. 28).
- Rodriguez-Molares, A., O. M. H. Rindal, J. D’Hooge, S. E. Masoy, A. Austeng, M. A. Lediju Bell, and H. Torp (2020). “The Generalized Contrast-to-Noise Ratio: A Formal Definition for Lesion Detectability”. In: *IEEE Trans. Ultrason., Ferroelec., Freq. Contr.* 67.4, pp. 745–759. DOI: 10.1109/tuffc.2019.2956855 (cit. on p. 23).
- Solomon, O., R. J. G. van Sloun, H. Wijkstra, M. Mischi, and Y. C. Eldar (2019). “Exploiting flow dynamics for super-resolution in contrast-enhanced ultrasound”. In: *IEEE Trans. Ultrason., Ferroelec., Freq. Contr.* 60.10, pp. 1573–1586 (cit. on p. 40).
- Taghavi, I., S. B. Andersen, C. A. V. Hoyos, M. B. Nielsen, C. M. Sørensen, and J. A. Jensen (2021). “In Vivo Motion Correction in Super Resolution Imaging of Rat

- Kidneys”. In: *IEEE Trans. Ultrason., Ferroelec., Freq. Contr.* 68.10, pp. 3082–3093 (cit. on p. 21).
- Taghavi, I., S. B. Andersen, C. A. V. Hoyos, M. Schou, F. Gran, K. L. Hansen, M. B. Nielsen, C. M. Sørensen, M. B. Stuart, and J. A. Jensen (2022). “Ultrasound super-resolution imaging with a hierarchical Kalman tracker”. In: *Ultrasonics* 122, p. 106695. DOI: <https://doi.org/10.1016/j.ultras.2022.106695> (cit. on pp. 21, 47).
- Taghavi, I., S. B. Andersen, C. A. V. Hoyos, M. Schou, S. H. Øygaard, F. Gran, K. L. Hansen, C. M. Sørensen, M. B. Nielsen, M. B. Stuart, and J. A. Jensen (2020). “Tracking Performance in Ultrasound Super-Resolution Imaging”. In: *Proc. IEEE Ultrason. Symp.* Pp. 1–4 (cit. on p. 21).
- Takenaka, T., L. M. Harrison-Bernard, E. W. Inscho, P. K. Carmines, and L. G. Navar (1994). “Autoregulation of afferent arteriolar blood flow in juxtamedullary nephrons”. In: *Am. J. Physio.* 267.5, F879–87. DOI: 10.1152/ajprenal.1994.267.5.F879 (cit. on p. 39).
- Tang, S., P. Song, J. D. Trzasko, M. Lowerison, C. Huang, P. Gong, U. Lok, A. Manduca, and S. Chen (2020). “Kalman Filter–Based Microbubble Tracking for Robust Super-Resolution Ultrasound Microvessel Imaging”. In: *IEEE Trans. Ultrason., Ferroelec., Freq. Contr.* 67.9, pp. 1738–1751 (cit. on p. 40).
- Tanter, M. and M. Fink (Jan. 2014). “Ultrafast imaging in biomedical ultrasound”. In: *IEEE Trans. Ultrason., Ferroelec., Freq. Contr.* 61.1, pp. 102–119. DOI: 10.1109/TUFFC.2014.6689779 (cit. on pp. 36, 60).
- Trahey, G. E., J. W. Allison, and O. T. von Ramm (1987). “Angle independent ultrasonic detection of blood flow”. In: *IEEE Trans. Biomed. Eng.* BME-34.12, pp. 965–967 (cit. on p. 26).
- van Heel, M. and M. Schatz (2005). “Fourier shell correlation threshold criteria”. In: *J. Struct. Biol.* 151.3, pp. 250–262 (cit. on p. 28).
- Vriese, A. S. D., T. J. Verbeuren, M. O. Vallez, N. H. Lameire, M. D. Buyzere, and P. M. Vanhoutte (2000). “Off-line analysis of red blood cell velocity in renal arterioles”. In: *J. Vasc. Research* 37.1, pp. 26–31. DOI: 10.1159/000025710 (cit. on p. 39).
- Wagner, R., V. Denis, F. Hossler, K. Czymmek, E. Pauwels, and L. Van Hoorebeke (Dec. 2010). “High-Resolution Imaging of Kidney Vascular Corrosion Casts with Nano-CT”. In: *Microscopy and microanalysis* 17, pp. 215–9 (cit. on p. 59).
- Zimmerhackl, B., C. R. Robertson, and R. L. Jamison (1985). “Fluid uptake in the renal papilla by vasa recta estimated by two methods simultaneously”. In: *Am. J. Physio.* 248.3, F347–53. DOI: 10.1152/ajprenal.1985.248.3.F347 (cit. on p. 39).

References from Chapter 4

- Andersen, S. B., I. Taghavi, H. M. Kjer, S. B. Sjøgaard, C. Gundlach, V. A. Dahl, M. B. Nielsen, A. B. Dahl, J. A. Jensen, and C. M. Sørensen (2021). “Evaluation of 2D

- super-resolution ultrasound imaging of the rat renal vasculature using ex vivo micro-computed tomography”. In: *Scientific Reports* 11.1, p. 24335. DOI: 10.1038/s41598-021-03726-6 (cit. on pp. 79, 80).
- Holliger, C., K. V. Lemley, S. L. Schmitt, F. C. Thomas, C. R. Robertson, and R. L. Jamison (1983). “Direct determination of vasa recta blood flow in the rat renal papilla.” In: *Circ. Research* 53.3, pp. 401–413 (cit. on pp. 79, 80).
- Khan, Z., J. P. Ngo, B. Le, R. G. Evans, J. T. Pearson, B. S. Gardiner, and D. W. Smith (2018). “Three-dimensional morphometric analysis of the renal vasculature”. In: *American Journal of Physiology-Renal Physiology* 314.5, F715–F725 (cit. on p. 79).
- Nordsletten, D. A., S. Blackett, M. D. Bentley, E. L. Ritman, and N. P. Smith (2006). “Structural morphology of renal vasculature”. In: *Am. J. Physiol. Heart Circ. Physiol.* 291.1, pp. 296–309 (cit. on pp. 63, 79).
- Ren, H., L. Gu, A. Andreasen, J. S. Thomsen, L. Cao, E. I. Christensen, and X. Zhai (2014). “Spatial organization of the vascular bundle and the interbundle region: three-dimensional reconstruction at the inner stripe of the outer medulla in the mouse kidney”. In: *American Journal of Physiology-Renal Physiology* 306.3, F321–F326 (cit. on p. 79).
- Taghavi, I., S. B. Andersen, S. B. Søgaaard, M. B. Nielsen, C. M. Sørensen, M. B. Stuart, and J. A. Jensen (2021). “Automatic Classification of Arterial and Venous Flow in Super-resolution Ultrasound Images of Rat Kidneys”. In: *Proc. IEEE Ultrason. Symp.* Pp. 1–4 (cit. on p. 63).
- (2022). “Blood Vessel Segmentation in Super-Resolution Ultrasound Imaging of Healthy Rat Kidneys”. In: *IEEE Trans. Ultrason., Ferroelec., Freq. Contr.*, (submitted) (cit. on p. 63).
- Zimmerhackl, B., C. R. Robertson, and R. L. Jamison (1985). “Fluid uptake in the renal papilla by vasa recta estimated by two methods simultaneously”. In: *Am. J. Physiol.* 248.3, F347–53. DOI: 10.1152/ajprenal.1985.248.3.F347 (cit. on pp. 79, 80).

References from Chapter 5

- Andersen, S. B., C. A. V. Hoyos, I. Taghavi, F. Gran, K. L. Hansen, C. M. Sørensen, J. A. Jensen, and M. B. Nielsen (2019). “Super-Resolution Ultrasound Imaging of Rat Kidneys before and after Ischemia-Reperfusion”. In: *Proc. IEEE Ultrason. Symp.* Pp. 1–4 (cit. on p. 82).
- Andersen, S. B., I. Taghavi, C. A. V. Hoyos, S. B. Søgaaard, F. Gran, L. Lonn, K. L. Hansen, J. A. Jensen, M. B. Nielsen, and C. M. Sørensen (2020). “Super-Resolution Imaging with Ultrasound for Visualization of the Renal Microvasculature in Rats Before and After Renal Ischemia: A Pilot Study”. In: *Diagnostics* 10.11, p. 862 (cit. on p. 82).
- Andersen, S. B., I. Taghavi, H. M. Kjer, S. B. Søgaaard, C. Gundlach, V. A. Dahl, M. B. Nielsen, A. B. Dahl, J. A. Jensen, and C. M. Sørensen (2021). “Evaluation of 2D

super-resolution ultrasound imaging of the rat renal vasculature using ex vivo micro-computed tomography”. In: *Scientific Reports* 11.1, p. 24335. DOI: 10 . 1038 / s41598-021-03726-6 (cit. on p. 82).

Søgaard, S. B., S. B. Andersen, I. Taghavi, C. A. V. Hoyos, K. L. Hansen, F. Gran, J. A. Jensen, M. B. Nielsen, and C. M. Sørensen (2020). “Super-resolution Ultrasound Imaging of the Renal Microvasculature in Rats with Metabolic syndrome”. In: *Proc. IEEE Ultrason. Symp.* Pp. 1–4 (cit. on p. 82).



Paper 1

In vivo Motion Correction in Super Resolution Imaging of Rat Kidneys

Iman Taghavi, Sofie Bech Andersen, Carlos Armando Villagómez Hoyos, Michael Bachmann Nielsen, Charlotte Mehlin Sørensen, and Jørgen Arendt Jensen

Name of journal:

IEEE Transactions on Ultrasonics, Ferroelectrics, and Frequency Control

Document Version:

Published

DOI:

10.1109/TUFFC.2021.3086983

General rights

Copyright and moral rights for the publications made accessible in the public portal are retained by the authors and/or other copyright owners and it is a condition of accessing publications that users recognise and abide by the legal requirements associated with these rights.

- Users may download and print one copy of any publication from the public portal for the purpose of private study or research.
- You may not further distribute the material or use it for any profit-making activity or commercial gain
- You may freely distribute the URL identifying the publication in the public portal

If you believe that this document breaches copyright please contact us providing details, and we will remove access to the work immediately and investigate your claim.

In Vivo Motion Correction in Super-Resolution Imaging of Rat Kidneys

Iman Taghavi, Sofie Bech Andersen¹, Carlos Armando Villagómez Hoyos, Michael Bachmann Nielsen, Charlotte Mehlin Sørensen², and Jørgen Arendt Jensen³, *Fellow, IEEE*

Abstract—Super-resolution (SR) imaging has the potential of visualizing the microvasculature down to the 10- μm level, but motion induced by breathing, heartbeats, and muscle contractions are often significantly above this level. This article, therefore, introduces a method for estimating tissue motion and compensating for this. The processing pipeline is described and validated using Field II simulations of an artificial kidney. *In vivo* measurements were conducted using a modified bk5000 research scanner (BK Medical, Herlev, Denmark) with a BK 9009 linear array probe employing a pulse amplitude modulation scheme. The left kidney of ten Sprague-Dawley rats was scanned during open laparotomy. A 1:10 diluted SonoVue contrast agent (Bracco, Milan, Italy) was injected through a jugular vein catheter at 100 $\mu\text{l}/\text{min}$. Motion was estimated using speckle tracking and decomposed into contributions from the heartbeats, breathing, and residual motion. The estimated peak motions and their precisions were: heart: axial— $7.0 \pm 0.55 \mu\text{m}$ and lateral— $38 \pm 2.5 \mu\text{m}$, breathing: axial— $5 \pm 0.29 \mu\text{m}$ and lateral— $26 \pm 1.3 \mu\text{m}$, and residual: axial— $30 \mu\text{m}$ and lateral— $90 \mu\text{m}$. The motion corrected microbubble tracks yielded SR images of both bubble density and blood vector velocity. The estimation was, thus, sufficiently precise to correct shifts down to the 10- μm capillary level. Similar results were found in the other kidney measurements with a restoration of resolution for the small vessels demonstrating that motion correction in 2-D can enhance SR imaging quality.

Index Terms—High-resolution imaging, motion estimation, super resolution (SR), ultrasound.

Manuscript received March 25, 2021; accepted May 31, 2021. Date of publication June 7, 2021; date of current version September 27, 2021. This work was supported in part by the Danish National Advanced Technology Foundation under Grant 82-2014-4, in part by the Innovation Fund Denmark under Grant 7050-00004B, and in part by BK Medical, Herlev, Denmark. (Corresponding author: Jørgen Arendt Jensen.)

This work involved human subjects or animals in its research. Approval of all ethical and experimental procedures and protocols was granted by the National Institutes of Health and the Danish National Animal Experiments Inc.

Iman Taghavi and Jørgen Arendt Jensen are with the Center for Fast Ultrasound Imaging, Department of Health Technology, Technical University of Denmark, 2800 Kongens Lyngby, Denmark (e-mail: jaje@dtu.dk).

Sofie Bech Andersen and Michael Bachmann Nielsen are with the Department of Biomedical Sciences, University of Copenhagen, 2100 Copenhagen, Denmark, and also with the Department of Diagnostic Radiology, Copenhagen University Hospital, 2100 Copenhagen, Denmark.

Carlos Armando Villagómez Hoyos is with BK Medical, 2730 Herlev, Denmark.

Charlotte Mehlin Sørensen is with the Department of Biomedical Sciences, University of Copenhagen, DK-2100 Copenhagen, Denmark. Digital Object Identifier 10.1109/TUFFC.2021.3086983

I. INTRODUCTION

ULTRASOUND super-resolution (SR) imaging (SRI) has been introduced over the last six years by a number of research groups [1]–[7]. The method uses tracking of microbubble (MB) contrast agents to visualize the microvasculature down to vessel sizes of 2–20 μm and should under ideal circumstances be capable of depicting capillary networks. The images are acquired over several minutes, over which time the object is considered stationary. This is only possible for fixated objects, such as a rat brain [5] or a fixated mouse ear [4]. Motion is induced in the tissue from breathing, beating heart, and muscle contractions [8], and it can be several times larger than the resolution attainable in SRI. The tissue motion is in all directions and also deforms the tissue, so it is both spatially and temporally variant. It is, thus, important to estimate the motion field and accurately time align it at the precise spatial locations.

Lately, a number of groups have also addressed motion correction to relax the requirement on tissue stationarity. Hansen *et al.* [9] showed that motion correction of data from a rat kidney could increase precision from 22 to 8 μm for a single vessel with the motion estimated at a single location and for a single vessel example. In [10], motion effects were reduced by excluding frames with a too high motion from breathing yielding a resolution of 2.1 μm in the axial direction and 6.1 μm in the lateral direction. Rigid motion was assumed throughout the image.

In [11], a rigid motion correction for the whole image was employed based on a phase correlation method, which visually gave sharper images and more narrow vessels. Two-stage motion correction was applied in [8] with a combination of affine registration for the global motion and nonrigid registration for estimating the local deformation of tissue. This reduced the width of the microvessels by a factor of roughly 1.5. The approach was also simulated for three-dimensional motion correction in [12]. Piepenbrock *et al.* [13] used a flow approach to find the velocity field and suppress the influence from the bubble response on the motion estimation. The approach was tried on a single mouse tumor.

Recently, Kierski *et al.* [14] investigated a more advanced imaging technique by combining ultrasound microscopy and dual-frequency imaging technique for obtaining a high signal-to-noise ratio (SNR) and a high frame rate. Segments

of 100 contrast images with a frame rate of 500 Hz were acquired, followed by B-mode images with a frame rate of 5 Hz. The B-mode frame rate was only sufficient to capture the motion from breathing and more rapid movements had to be discarded. None of the previous studies have addressed the importance of the spatial and temporal difference between the motion estimates in B-mode images and the contrast data when the two images are acquired at two different time points.

The approach taken in this article is to estimate the full motion for all frames without restrictions on the motion and then co-register the estimated tracks to a reference frame as described in Section II. This article is an expanded version of the conference article [15] with an optimized processing, motion estimation as a function of both space and time, more comprehensive statistics, and results from ten rats as described in Section III. The major contribution is to demonstrate the importance of the spatial and temporal variation, how it can be properly found through interpolation, and give the precision of the motion components *in vivo*. The kidneys of Sprague-Dawley rats were selected as scan objects, as they both experience motion from breathing, heartbeat, and limited muscular motion making them suitable for controlled, repeatable, and realistic experiments. The kidney is also a highly perfused organ, which roughly receives 20% of the volume flow for the rat with a vascular structure including both large and small vessels, making it ideal for investigating the possibility of identifying the whole vascular tree at all levels.

The SR pipeline is validated on simulated data and on data from the left kidney of Sprague-Dawley rats as explained in Section IV. The final results demonstrate that resolution can be maintained, although the motion is five-to-ten times larger than the precision attained. Finally, the method is discussed in Section V.

II. METHODS

This section introduces the various methods in the motion correction SRI pipeline shown in Fig. 1. The nonlinear imaging scheme is introduced in II-A, and the basic processing pipeline is presented. The method for determining motion and correcting it is explained in Section II-C. Finally, the image formation is presented in Section II-D.

A. Data Acquisition and Imaging Scheme

The data were acquired using a modified bk5000 scanner (BK Medical, Herlev, Denmark) equipped with a research interface, developed specifically for this project, for the live streaming of the data to a disk. This allowed long acquisitions for 10 min of beamformed radio frequency (RF) data. A "hockey stick" X18L5s transducer (BK 9009, BK Medical, Herlev, Denmark) was employed for imaging. This linear array probe with 150 elements covers an imaging width of 24 mm, which was sufficient for scanning a full rat kidney. The height of the aperture was 3.4 mm, and the elevation focus was at

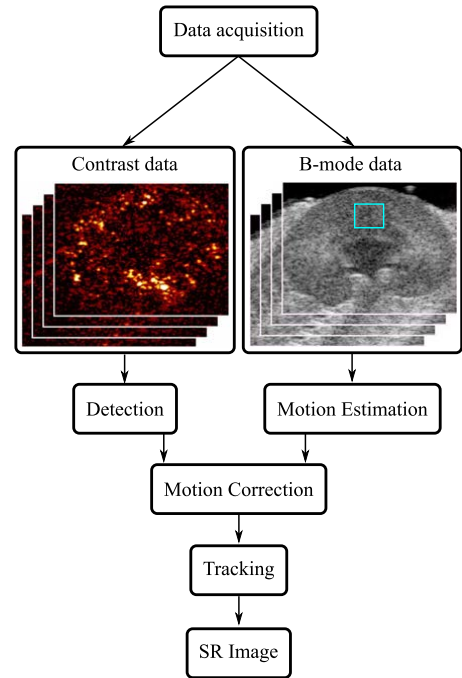


Fig. 1. Block diagram of the processing scheme used in this article. The blue rectangle in the B-mode image indicates a local region used to estimate the dynamics of the motion.

20 mm for an elevation F-number (depth divided by active aperture width) of 5.9.

A pulse amplitude modulation sequence was used for imaging [16] with a transmit frequency of 6 MHz. It employed a sliding aperture approach of 25 elements with a focal depth of 10 mm. Each active aperture emitted three times, one with full amplitude and two with half amplitude. This combination of emissions gave the amplitude-modulated response for enhancing the nonlinear signal from the contrast agent. The active aperture then slid across the array for a total of 91 active subapertures. This is visualized in Fig. 2 and is referred to as the contrast sequence. After this, a B-mode image was acquired. It employed the same 91 active subapertures and, however, emitted only once per active subaperture. This resulted in $3 \cdot 91 + 91 = 364$ emissions per full sequence. The transmit voltage was kept low with a corresponding mechanical index (MI) of 0.2 to avoid disrupting the MBs. The pulse repetition frequency f_{prf} was 19.6 kHz for a frame rate of 53.85 Hz.

The MB dilution of 1:10 was chosen for the individual MBs' point spread function to be distinguishable in each image frame. Due to the contrast dilution, an acquisition time of 10 min was chosen, as pretrials showed this scan duration was needed to sufficiently fill the dense vasculature of the kidney with MBs [17].

Three emissions of the contrast sequence corresponded to the same image line as one emission in the B-mode sequence.

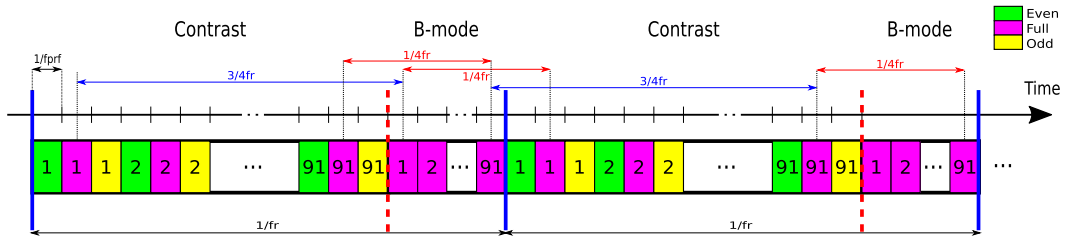


Fig. 2. Imaging scheme used in the *in vivo* studies. Each contrast sequence consisted of 3×91 emissions followed by a B-mode sequence consisting of 91 emissions. While each image line, in the contrast and B-mode images, refers to the same lateral position, there was a unique delay between the time of formation of each line in the contrast images and the corresponding line of the B-mode image varying from $1/(4f_r)$ to $3/(4f_r)$.

The time difference of formation of each line in the contrast image and its next B-mode image is easily measurable from Fig. 2. The time difference between the n th line of a contrast image and the m th line of its next B-mode image is

$$t_d(n, m) = \frac{3N_{\text{lines}} - 3n + m + 1}{f_{\text{prf}}} \quad (1)$$

where $n, m \in \{1, 2, \dots, N_{\text{lines}}\}$ and N_{lines} is the number of lines in the image. This time difference plays an important role in applying the estimated motion to the correct positions in the contrast image.

An example of B-mode and contrast images is shown in Fig. 1. The B-mode image has a poor visualization of the contrast agent but clearly shows how the anatomical structures move during the scans. The contrast image clearly shows the different MBs with a high contrast. Thus, the combination of the two images yields both anatomy motion and contrast agent location.

B. Detection

Detection is required to extract the centroid of the MB's positions from the contrast images. This process consists of two parts: 1) “*SNR enhancement*” by, e.g., simple thresholding, spatial filtering (e.g., Gaussian and Laplacian of Gaussian), spatiotemporal filtering (e.g., singular value decomposition) [18], [19], or model fitting [20] and 2) “*localization*” using peak detection, centroid estimation methods (e.g., weighted centroid) [20], [21] or learning-based methods [22], [23]. A single or a combination of these methods can be employed for detection.

The contrast images only had a few quantization levels yielding a low SNR. The detection threshold was experimentally adjusted to reduce background noise, and the threshold was 1.1 for these datasets, which had only positive integer values up to 5. To improve SNR, a Gaussian filter was applied to the contrast image after thresholding. The kernel size of the symmetric Gaussian filter was 7 pixels with a standard deviation (SD) of 1 pixel, where the pixel sizes in the axial direction and the lateral direction were 24 and 80 μm , respectively. Then, the centroids of the MB positions were estimated using the weighted-centroid algorithm.

C. Motion Estimation and Correction

The tissue motion was estimated from the B-mode image using speckle tracking [24] on the envelope data. Regions in

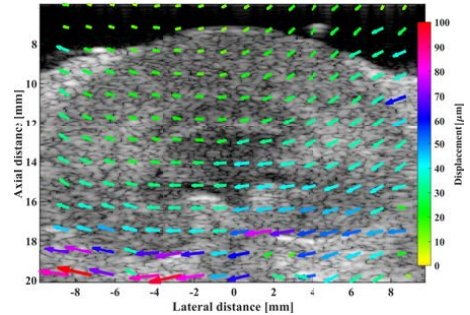


Fig. 3. Estimated motion field for a single frame. The arrows indicate the direction and magnitude of the motion and were found from the interpolated motion field.

the images were correlated with the corresponding regions in a selected reference frame number, and motions in the axial and lateral directions were found. Speckle tracking using the RF data was also attempted, but the lateral sampling density was too low to yield acceptable lateral estimates.

The entire kidney was in the field-of-view, and the motion was not uniform across the whole organ, as shown in Fig. 3. Hence, two different spatial regions do not have the same displacement, and a single local motion estimation cannot be applied across the whole kidney. It was therefore divided into smaller spatial blocks for block-wise processing. The B-mode image was divided into 80% overlapped $3 \times 3 \text{ mm}^2$ local regions, and the estimated motion signal was assigned to the center of each region $\vec{r}_k = (z_k, x_k)$. The collection of all motion signals in the form of $\vec{F}(t_k, \vec{r}_k)$ provided a discrete motion field through the entire image. Fig. 3 shows a snapshot of the motion field with arrows on top of the corresponding B-mode frame. Notice how the estimated displacements vary spatially, as opposed to a rigid structure.

The motion field was calculated with the following assumptions.

- 1) The local regions were assumed small enough so that the motion was spatially invariant inside the regions. This assumption depends on the type of material and application. Although a kidney is not a rigid material, the motion through a small local tissue region has the same magnitude and direction.
- 2) The frame rate was high enough to capture the fastest variation of the motion in the temporal domain.

The acceleration of the motion depends on the source of the motion, and the fastest source for the motion was the heart. According to the Nyquist theorem, the frame rate should be at least two times the maximum frequency in the heartbeat spectrum to capture the fastest transitions in the motion. This was investigated in Section IV-B.

The motion estimates were applied on the MB locations found by the processing pipeline. The time point for the motion depends on the location in the image, as a linear sweep of the beams was conducted from the most positive lateral locations to the most negative location as described in Section II-A. The motion estimation only gave one estimate per frame, and the motion time series was spline interpolated by a factor of 20 to yield a higher time resolution. A linear interpolation between these time points was then made to match the exact time location corresponding to the spatial location of the MB. Motion from one frame to the next easily changes with 100–200 μm , and this time interpolation was therefore essential to attain a co-registration better than 10 μm .

Finally, a 2-D spline interpolation was performed on the time interpolated motion field to yield the exact motion for the spatial position of the detected MB, and this was used in the motion correction to align the positions of the MB to the reference frame. Motion estimates for one of the regions in the medulla were used to study the dynamics and precision of the motion estimation algorithm as described in Section IV-B.

Three different scenarios were investigated for image motion correction: first, no motion correction where the images were formed without compensating for motion, and second local motion correction where a single region was selected for motion estimation. The estimated motion for this region was interpolated in time to account for the different motions at different times. The exact acquisition time for the MB was found, and the estimated motion for this time was used for compensation; third, global motion correction entails the estimation of the motion in all image regions and time interpolation and uses the motion found dependent on the MB image position and thus time for acquisition.

D. Image Formation

The next step was to generate MB tracks. The bubble position was adjusted by the motion estimated in Section II-C, and the motion corrected bubbles in the next frame were found to determine the bubble closest to the current bubble. The search for the next bubble was restricted to the region given by v_s/f_r , where v_s was the maximum allowed MB velocity and f_r was the frame rate of the sequence. The maximum velocity was selected to $v_s = 13.5 \text{ mm/s}$. The selected bubble was then added to the track and removed from the list of bubbles in the frame. The search was continued until no bubble satisfying the criteria was found. Tracks with less than three bubbles were considered noise outliers and were not stored.

Images were then formed from these tracks by inserting the bubble tracks into a high-resolution image with a pixel size of 5 μm . Each track was inserted into the images by drawing an antialiased vector between the different positions

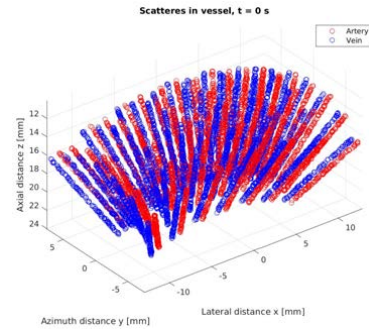


Fig. 4. Geometry of the in silico rat kidney phantom. The red structures have flow upwards and the blue downwards.

in the track using the algorithm developed in [25]. The vector was added to the current content of the image, and this finally yielded a bubble density image. The velocity of the bubbles was found by taking the time derivative of track locations, which yielded both the axial and lateral velocities. The velocity tracks were inserted into an axial and a lateral velocity image by drawing antialiased velocity weighted lines at the track positions. A weighting image was also drawn, and the mean velocity at each pixel in the velocity images was found by dividing with the weighting image if it was different from zero. The axial and lateral velocity images were then combined to yield a vector flow image (VFI) of the bubble velocity. The resulting images are presented in Section IV-C.

E. Resolution estimation

The Fourier ring correlation (FRC) criterion was used to measure the resolution [26], [27]. Using the threshold criteria to define resolution is controversial [28], and this study, therefore, uses a bit-based information threshold curve for the FRC threshold level as discussed in [28]. The SR images are split into two images by inserting every other track into an image. The split images were normalized to their maximum intensity values, and their intensity equalized using the `imhistmatch.m` function in MATLAB. The FRC curve of two images was calculated based on [26] without zero padding, and the resolution was estimated as the inverse spatial frequency, where the one-bit threshold curve crossed the FRC curve [28].

III. EXPERIMENTAL DATA

The motion correction method was investigated using both simulated data as described in Section III-A as well as *in vivo* data from Sprague-Dawley rats as described in Section III-B.

A. Simulation Phantoms

The linear part of the pulse amplitude sequence has been simulated using Field IIpro [29]–[31] to generate reference data, where the positions of the scatterers are known. The first phantom contains a matrix of point targets located at a distance of 2 mm in both the axial and lateral directions.

TABLE I

PARAMETERS USED IN THE IN-SILICON RAT KIDNEY PHANTOM

Parameters	Value
Tube length	10 mm
Tube radius	100 μm
Velocity	2 mm/s
Number of scatterers	20 per tube
Number of tube pairs	49
Angle between tube pairs	10°
Distance between pairs	1 mm

The second phantom was based on the dimensions of a rat kidney and is shown in Fig. 4. It mimics the flow in small arteries and veins, where the arterial flow was toward the perimeter and the return venous flow was in the opposite direction. A sparse distribution of scatterers was located randomly in the individual tubes with parabolic velocity profiles and a Gaussian distributed scattering amplitude. The scatterers moved along the tube axis and were returned to the adjacent tube when they reached the tube's end. The various dimensions of the phantom are listed in Table I. A slice of the tubes in the elevation direction of the probe was selected in this simulation. Stationary scatterers surrounding the tubes were also simulated to mimic the kidney tissue. The evolution of scatterer position was given by

$$\vec{r}(i, t + T_{\text{prf}}) = \vec{r}(i, t) + T_{\text{prf}} \vec{v}_f(\vec{r}(i, t), t) + \Delta \vec{r}_m(t)$$

where $\vec{r}(i, t)$ is the position of scatterer i at time t , T_{prf} is the time between pulse emissions, $\vec{v}_f(\vec{r}(i, t), t)$ is the velocity of the scatterer due to the blood flow, and $\Delta \vec{r}_m(t)$ is the motion of the whole kidney. For the stationary scatterers surrounding the vessel, $\vec{v}_f(\vec{r}(i, t), t) = 0$.

A realistic motion $\Delta \vec{r}_m(t)$ of the whole phantom was introduced from a motion estimation on the *in vivo* measurement. This ensured that both stationary tissue and tube locations varied across the heart and breathing cycles for validation of the motion estimation and motion correction algorithms. Only a linear simulation of the returned signal was conducted, and only the first harmonic was used in processing these data.

B. Animal Preparation and Experiment Setup

The motion study was performed on ten healthy male Sprague-Dawley rats according to protocols approved by the Danish National Animal Experiments Inspectorate. The experiments were conducted at the University of Copenhagen. The ethical standards of the university comply with those of the National Institutes of Health and all procedures were performed accordingly. The animals were housed at the animal facility at the Department of Experimental Medicine. They were held in a 12-/12-h light/dark cycle and could freely access drinking water and a standard chow. Appropriately trained caretakers were responsible for the animal welfare until use.

Induction of anesthesia was done with 5% isoflurane. After tracheotomy, the animals were connected to a ventilator (Ugo Basile, Gemonio, Italy) with a respiration cycle of 72 respirations/minute. An adequate level of anesthesia was maintained with 1%–2% isoflurane, and the muscle relaxant Nimblex (cisatracurium, 0.85 mg/mL, GlaxoSmithKline, London, U.K.) was continuously administered at 20 $\mu\text{L}/\text{min}$.

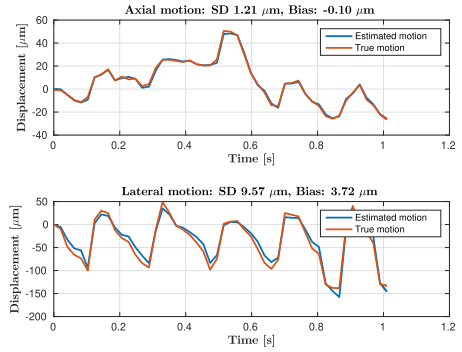


Fig. 5. Estimation of the motion from the B-mode image in the axial (top) and lateral direction (bottom), where the red curve is the true motion and the blue is the estimated motion.

Jugular vein catheterization was done with polyethylene catheters (PE-10), which were then used for infusion of MBs, isotonic saline, and Nimblex. A polyethylene catheter (PE-50) in the left carotid artery and a Statham P23-dB pressure transducer (Gould, Oxnard, CA, USA) was used to monitor the arterial blood pressure. With the animals in the supine position on a heating pad, the left kidney was exposed through open surgery. A metal retractor held the diaphragm to expose the kidney further and reduce respiratory motion. The transducer was placed on the lateral kidney surface and held by a fixated stage. Gel was used for interface coupling. The diluted (1:10) MBs (Sonovue, Bracco Imaging, Milan, Italy) were injected at 100 $\mu\text{L}/\text{min}$, and the 10-min data recording started when the MBs started appearing on the scanner display. Due to the floating of MBs in the syringe, a custom-built device turned the syringe 180° every 60 s.

Each rat was scanned three times. First, a baseline scan was conducted. Thereafter, five rats had the left renal artery clamped, and five rats had the left renal vein clamped for 45 min. A second scan was performed at the onset of reperfusion after the clamp was released. The last scan was performed in a steady state, 1 h after clamp release. The rats were euthanized after the scans. The data have also been used in [32] to characterize the effects of acute renal ischemia on the renal vasculature using SR imaging.

IV. RESULTS

A. Simulation Validation

The basic localization precision of stationary targets was investigated using the matrix phantom. The axial bias is 0.48 μm and the lateral is $-1.46 \mu\text{m}$. The corresponding SDs are 10.7 and 20.5 μm .

The motion of the in silico rat phantom has been estimated for the B-mode data and is shown for the first 50 frames in Fig. 5 in the axial direction (top) and lateral direction (bottom), where the red curve is the true motion and the blue is the estimated motion. The axial SD is 1.21 μm and the lateral is slightly higher at 9.57 μm .

These motion estimates have been used to correct the position of a nonflowing scatterer shown in Fig. 6, where

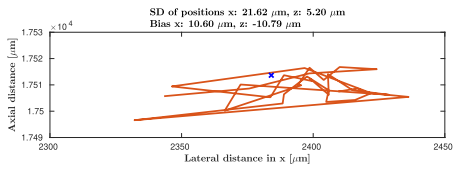


Fig. 6. Localization of a scatterer after motion compensation. The blue cross indicates the true position and the red lines indicate the motion corrected positions.

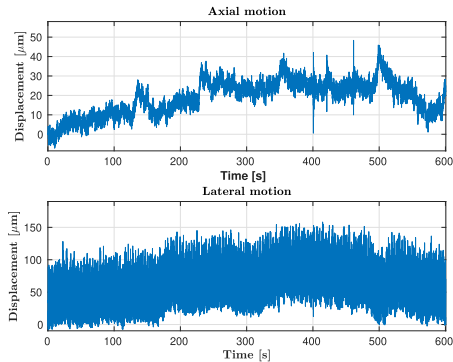


Fig. 7. Motion in the axial direction (top) and lateral direction (bottom) throughout the full experiment.

the blue cross shows the position of the scatterer in the first reference frame. The location in the subsequent frames has been corrected by the estimated motion and this yields the tracks indicated by the red lines. The precision or SD of the target location after correction is then $5.2 \mu\text{m}$ in the axial and $21.6 \mu\text{m}$ in the lateral direction with biases of -10.8 and $10.6 \mu\text{m}$.

B. Precision of In Vivo Motion Estimation

A single region in the top part of the kidney in the medulla was selected for investigating the precision of the motion estimation. The motion in both the axial and lateral directions for all ten minutes of the experiment for a single rat is shown in Fig. 7. This is a combination of motion from the beating heart, the forced ventilation (breathing), smooth muscle contractions, and over all movement, which cannot readily be separated out. A Fourier decomposition gives the spectra shown in Fig. 8 with amplitudes in dB, where the axial spectrum is shown on the top and the lateral on the bottom. Three distinct Fourier series can be seen in both of them. First, a large component around 0 Hz stems from the overall drift in the data. The second series is from the breathing motion. This is controlled mechanically at a fixed rate, and the harmonics of this motion has a very narrow bandwidth around harmonics of 70.5 beats per minute (BPM), and more than 20 harmonics can be seen in both spectra. The last series is from the heart motion, which has a lower amplitude and the components are placed around harmonics of the heart rate of approximately 353 BPM, where five harmonics can be seen in the lateral motion signal. The harmonics are spread over

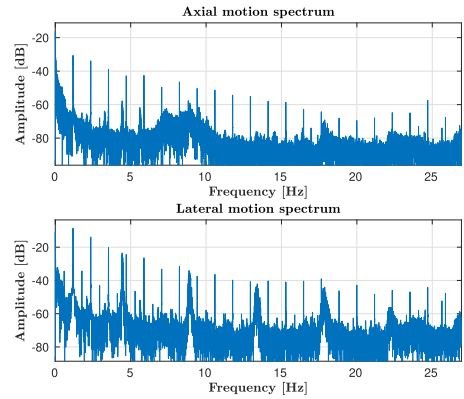


Fig. 8. Spectral decomposition of the motion signal in the axial direction (top) and lateral direction (bottom).

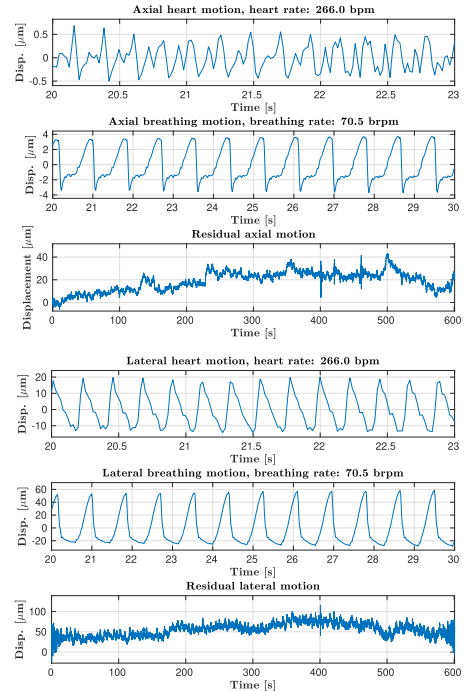


Fig. 9. Separation of the three motion components for the axial motion (top) and the three components for the lateral motion (bottom).

a larger bandwidth, due to the physiological variation of the heart rate.

These three Fourier series can be separated to yield the three independent motion signals as shown in Fig. 9, where the top three graphs display the components for the axial motion. The top graph is when the heartbeat components have been kept by isolating the first four harmonics around the heart rate. The middle graph is when isolating harmonics for breathing for the

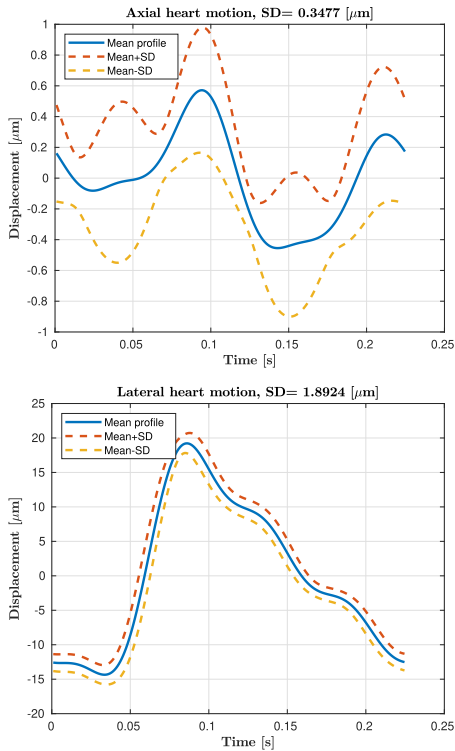


Fig. 10. Mean heartbeat motion for the axial direction (top) and lateral (bottom) direction. The blue solid line denotes the mean value across all cycles and the dashed lines show one SD.

TABLE II

PRECISION ESTIMATES COMBINED FOR ALL RAT EXPERIMENTS.
ALL VALUES IN μm

Motion type	Minimum	Maximum	Mean
Heartbeat, axial	0.069	7.858	1.992
Breathing, axial	0.062	4.630	1.455
Heartbeat, lateral	0.431	19.923	6.562
Breathing, lateral	0.277	20.315	5.438

first 18 harmonics. The lowest graph is for the residual signal, where the two other Fourier series have been subtracted.

The repetitiveness of the heartbeat and the breathing can be used for aligning all the responses and yield a mean response and its precision. This is shown in Fig. 10 for the heartbeat motion and in Fig. 11 for the breathing. In this example, the heart motion is around $\pm 1 \mu\text{m}$ (axial) and -15 to $+20 \mu\text{m}$ (lateral), and the precisions are 0.348 and $1.89 \mu\text{m}$, including the physiological variation of the heartbeat. The breathing motion spans from -20 to $+60 \mu\text{m}$ with precisions of 0.271 and $1.64 \mu\text{m}$. The residual motion shown in Fig. 9 is larger with deviations up to nearly $100 \mu\text{m}$. For vessels to align up and maintain SR, it is, thus, very important to compensate for the combined motion.

The experiment has been repeated for the ten different rats, with three measurements on each rat, as explained in

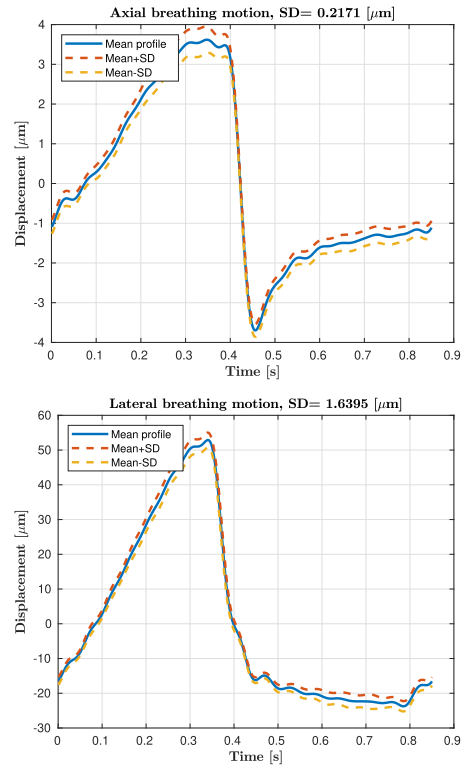


Fig. 11. Mean breathing motion for the axial direction (top) and lateral (bottom) direction. The blue solid line denotes the mean value across all cycles and the dashed lines show one SD.

Section III-B. A similar region and a reference image were selected for each measurement. All precision estimates for all ten rats and all three experiments are shown in Fig. 12 for the four different motion estimates and summarized in Table II. There is a quite wide variation in precision with estimates reaching $20 \mu\text{m}$. This happens in experiments where the motion is too large for the speckle tracking to capture motion in part of the images and can be due to motion in the out-of-plane direction or that the setup has been touched inducing a significant kidney motion. It can, however, be seen that the precision of the motion estimation is around a factor of two lower than the $10 \mu\text{m}$ size of the capillaries and often a factor of 5 lower, indicating that a motion corrected image can potentially visualize the capillary flow.

C. Motion Compensated Images

The log-scaled intensity SR images without motion correction, with local motion correction, and with correction using the motion field are shown in Fig. 13 (top). The corresponding velocity images are shown in the second row with color indicating direction and intensity magnitude, e.g., a yellow color indicates velocity from left to right in the image. The third row shows the zoomed regions 1–4. Four markers on the intensity and velocity images were selected exactly at

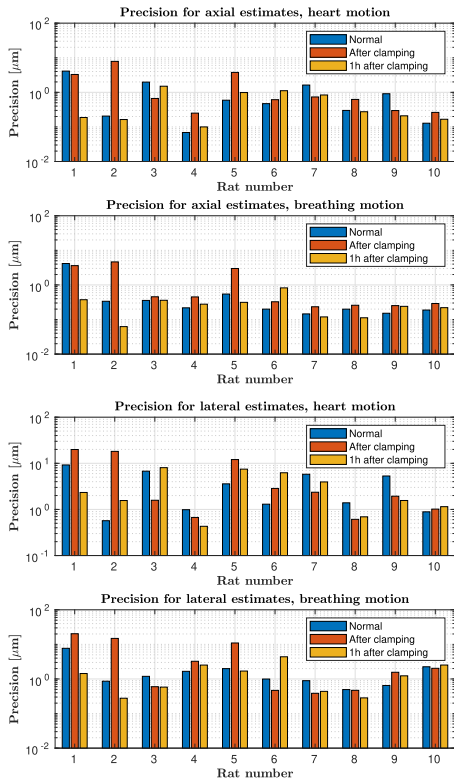


Fig. 12. Precision estimates for the various rat experiments for the axial direction (top) and lateral (bottom) direction.

the same place to compare the intensity and velocity profiles of the SR images. Polynomial fitted profiles to the pixel values of the SR images are shown in the bottom row for comparing diameter and flow velocities of the selected vessels. To remove unrealistic tracks, the MBs that were not traceable for more than five frames as well as those that had an overall displacement less than $200\ \mu\text{m}$ for the whole track (stationary bubbles) were removed. Only tracks with velocities from 0 to $10\ \text{mm/s}$ are shown.

The effect of motion correction was investigated by looking at intensity and velocity profiles over the various cortical and medullary (inner part of the kidney) vessel structures shown in region 1–4 in Fig. 13. The profiles of the exact same regions on the images with and without motion correction are shown in Fig. 13 (bottom).

The FRC curves for the images in Fig. 13 with one-bit and half-bit information threshold curves are shown in Fig. 14, where the left graph is without motion correction, middle is with local motion correction, and right is with global motion correction.

Fig. 15 shows the FRC resolution with one-bit threshold for all ten SR kidney images. It shows an improvement in the image quality after motion correction using the motion field both in the median and interquartile range.

V. DISCUSSION

In vivo measurements have been conducted on ten partly fixated rat kidneys using an amplitude modulation nonlinear imaging scheme. Estimating the motion induced from the forced ventilation and the heartbeating showed that motion in the $100\text{--}200\text{-}\mu\text{m}$ range in both the axial and lateral directions were present. Such motion would limit the resolution in SR imaging to $100\text{--}200\ \mu\text{m}$ and the smallest vessel would not be visible. Compensating the motion in reference to one selected frame reestablishes resolution. In simulations, the precision of the target location after correction is $3.9\ \mu\text{m}$ in the axial direction and $17.7\ \mu\text{m}$ in the lateral direction with biases of -12.4 and $6.5\ \mu\text{m}$. In general, the lateral motion was estimated with a lower precision than the axial motion. This is due to the employment of the signal envelope as the lateral density of lines is too low to employ cross correlation of the RF signals. One obvious choice is to employ fast imaging, such as synthetic aperture [33] or plane wave imaging [34] for high frame rates with no restrictions on the lateral sampling density. The major drawback of this is the increase in the amount of data, as the full RF data for a number of transducer elements have to be employed. This is currently difficult with the long acquisitions used here (10 min) but should be implemented in future scanners. The frame rate could also be increased, if the second set of full emissions in the sequences shown in Fig. 2 could be avoided. This is, however, currently not possible, due to the processing and storage capabilities of the bk5000 scanner. The long acquisition time can potentially be optimized by using the quantitative assessment of vessel reconstruction suggested by Dencks *et al.* [35].

The precision of the *in vivo* motion was also determined by decomposing the motion signal into components from breathing, heartbeat, and residual smooth muscle motion. The breathing motion was in general larger than motion induced by the heart. The precision was $217\ \text{nm}$ (axially) and $1.64\ \mu\text{m}$ (laterally). The heartbeat motion had a precision of $69\ \text{nm}$ (axially) and $0.98\ \mu\text{m}$ (laterally), including physiological variation, and it is a factor of 10 lower than the target of $10\ \mu\text{m}$ for visualizing capillary flow. For all rat experiments, the motion could be estimated with a precision from $69\ \text{nm}$ to $20.3\ \mu\text{m}$ from the linear B-mode image, with a mean axial motion precision of $2.0\ \mu\text{m}$ in the axial direction and $6.6\ \mu\text{m}$ in the lateral direction.

The effect of motion correction is shown in Fig. 13. Using only a single motion correction for the whole image does not fully correct for the motion, which can be seen by comparing images in rows (b) and (c) for the zoomed regions. The effect of motion correction on the alignment of small vessels was especially prominent in the cortical (outer) part of the kidney in the velocity images. The results show that having a motion correction through the entire kidney will provide sharper images and more smooth intensity and velocity profiles.

Both intensity and velocity for Profile 1 show that the diameter of the large vessel in the down-left side of the kidney was reduced from 1.3 to $0.7\ \text{mm}$, and the profiles without motion correction were widely spread, resulting in a blurred image. This shows the reduction in the width of the vessel

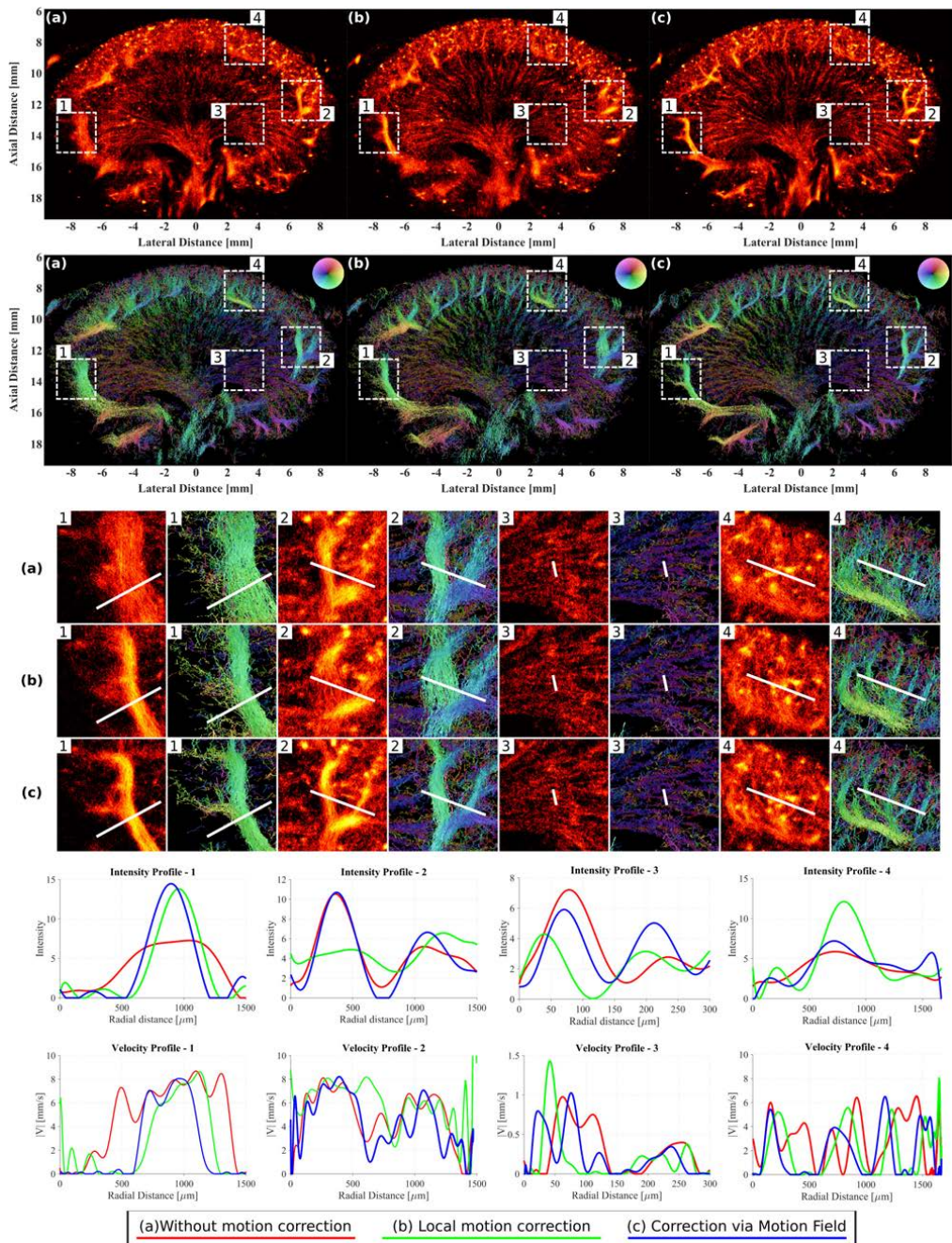


Fig. 13. Intensity and velocity SR images of a rat kidney. (a) Without motion correction. (b) With local motion correction. (c) With correction using the motion field. The intensity images show on the top row which is an accumulation of all bubble positions. The second row shows the velocity images with color-coded traces, where intensity is proportional to MB velocity and direction is shown as the color. Marked regions 1–4 are indicated in the top images and the third row shows the zoomed-in view regions. Four markers on these images were selected exactly at the same place in the third row to compare the intensity and velocity profiles of the SR images. Polynomial fitted profiles to the pixel values of the SR images quantify the diameter and flow velocity of the selected vessels in the bottom row.

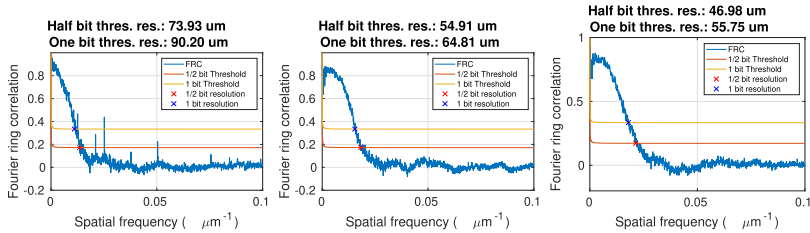


Fig. 14. FRC curves and bit-based information threshold for SR images. (a) Without motion correction. (b) With local motion estimation and global correction. (c) With motion-field estimation and local correction.

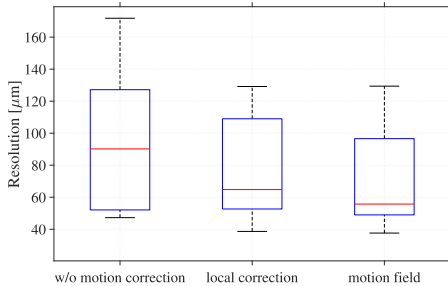


Fig. 15. Box plots of FRC metric with one-bit threshold for three methods and ten SR images of different kidneys.

by a factor of roughly 2. The velocity in this large vessel was around 8 mm/s. Profile 2 was placed over two vessels with a size of 500 μm . Profiles 3 and 4 were calculated over four smaller vessels with a diameter of less than 50 and 250 μm , respectively. The intensity profiles did not show how many vessels existed in the regions. However, the velocity profiles showed the resolved small vessels. The velocity in smaller vessels of the medulla (middle part of the kidney) was measured below 1.5 mm/s, as demonstrated in Profile 3. Profile 4 over a part of the cortical region showed a higher velocity of roughly 6 mm/s. The two last profiles showed how having MB tracks, which are not compensated for the motion appropriately, could lead to unusually narrow or wide vessels.

Estimation of microvascular blood flow deep inside organs is difficult *in vivo*. Older studies using invasive video microscopy techniques have estimated the mean red blood cell velocity in the descending (arterial) vasa recta at the tip of the renal papilla (at the very bottom of the medulla) of rat kidneys to be ≈ 1 mm/s [36]–[38]. This is in the range of the velocity profile 3 from the medulla shown in Fig. 13. The remaining velocity profiles include a mixture of differently sized arcuate and cortical radial arteries and veins. Validation of the velocities in the cortex will require the separation and categorization of the different types of vessels. For larger vessels, spectral Doppler may help validate the SRI-derived velocity estimations. For the cortical microvasculature, validation is very challenging, as no other techniques are available to make it noninvasively and *in vivo*. Different video microscopy approaches have also been used in the cortex. One study *in vitro* blood perfused kidneys from rats found a velocity of ≈ 10 mm/s in the afferent arterioles [39]. Another study estimated blood flow in different renal arteries and arterioles

of varying size in a split hydronephrotic kidney and reported velocities ranging from 0.5 to 65 mm/s but did not describe how the velocities related to vessel size [40]. Therefore, if SRI can provide precise estimations of blood flow velocity in different vascular segments of the kidney, it will fulfill an unmet need and allow evaluation of intrarenal blood flow in various physiological and pathological states.

The FRC resolution metric is shown in Fig. 15. The metric is controversial because of its dependence on splitting the SR image, threshold criteria, and pixel values (or the number of scatterers) in each image. However, since the images from ten rat kidneys were split, scaled, and thresholded the same way, the metric is still helpful for quality assessment even though they may not represent the actual resolution. The metric showed a large improvement in introducing the local motion correction and a less dramatic improvement when employing the global motion field.

The approach assumes that the out-of-plane motion is negligible. The probe used has an elevation F-number of nearly 6 at 20 mm giving that the elevation slice thickness is at least $6\lambda = 1.2$ mm, which is well above the estimated peak axial and lateral motion of 100–200 μm . The change in amplitude of motion in and out of the imaging plane will therefore be negligible and not affect the detection of the bubbles. Also, note that the detection of centroid removes the amplitude of the bubble, so the variation in amplitude will not be seen by the tracking algorithm. Attaining full SR in the elevation direction will necessitate a full 3-D measurements and must employ either sparse 2-D matrix probes [41] or row-column probes [42], [43].

A few rat experiments showed a decreased precision of up to 20 μm . This was due to parts of the estimated motion data being out of the search range precluding motion correction. This was found in three of the early rat experiments and might have been from accidentally moving parts of the experiments and was only seen in experiments 1, 2, and 5. Excluding these always yields a precision below 10 μm and often much lower, indicating that this setup and processing pipeline has the potential of capillary flow visualization.

VI. CONCLUSION

A motion correction SR pipeline has been presented and used on *in vivo* data from the left kidney of Sprague-Dawley rats. It was shown that the tissue motion can be reliably determined with a precision in the μm range and can be used for compensating for the motion from breathing, heartbeating, and muscle contractions.

REFERENCES

- [1] O. M. Viessmann, R. J. Eckersley, K. Christensen-Jeffries, M. X. Tang, and C. Dunsby, "Acoustic super-resolution with ultrasound and microbubbles," *Phys. Med. Biol.*, vol. 58, no. 18, pp. 6447–6458, Sep. 2013.
- [2] M. A. O'Reilly and K. Hynynen, "A super-resolution ultrasound method for brain vascular mapping," *Med. Phys.*, vol. 40, no. 11, pp. 110701-1–110701-7, 2013.
- [3] Y. Desailly, J. Pierre, O. Couture, and M. Tanter, "Resolution limits of ultrafast ultrasound localization microscopy," *Phys. Med. Biol.*, vol. 60, no. 22, pp. 8723–8740, Nov. 2015.
- [4] K. Christensen-Jeffries, R. J. Browning, M.-X. Tang, C. Dunsby, and R. J. Eckersley, "in vivo acoustic super-resolution and super-resolved velocity mapping using microbubbles," *IEEE Trans. Med. Imag.*, vol. 34, no. 2, pp. 433–440, Feb. 2015.
- [5] C. Errico *et al.*, "Ultrafast ultrasound localization microscopy for deep super-resolution vascular imaging," *Nature*, vol. 527, no. 7579, pp. 499–502, Nov. 2015.
- [6] D. Ackermann and G. Schmitz, "Detection and tracking of multiple microbubbles in ultrasound B-mode images," *IEEE Trans. Ultrason., Ferroelectr., Freq. Control*, vol. 63, no. 1, pp. 72–82, Jan. 2016.
- [7] K. Christensen-Jeffries *et al.*, "Super-resolution ultrasound imaging," *Ultrasound Med. Biol.*, vol. 46, no. 4, pp. 865–891, 2020.
- [8] S. Harput *et al.*, "Two-stage motion correction for super-resolution ultrasound imaging in human lower limb," *IEEE Trans. Ultrason., Ferroelectr., Freq. Control*, vol. 65, no. 5, pp. 803–814, May 2018.
- [9] K. B. Hansen *et al.*, "Robust microbubble tracking for super resolution imaging in ultrasound," in *Proc. IEEE Ultrason. Symp.*, Sep. 2016, pp. 1–4.
- [10] J. Foirot, H. Zhang, T. Ilovitsh, L. Mahakian, S. Tam, and K. W. Ferrara, "Ultrasound localization microscopy to image and assess microvasculature in a rat kidney," *Sci. Rep.*, vol. 7, no. 1, pp. 13662:1–13662:12, Dec. 2017.
- [11] V. Hingot, C. Errico, M. Tanter, and O. Couture, "Subwavelength motion-correction for ultrafast ultrasound localization microscopy," *Ultrasonics*, vol. 77, pp. 17–21, May 2017.
- [12] S. Harput *et al.*, "Quantitative microvessel analysis with 3-D super-resolution ultrasound and velocity mapping," in *Proc. IEEE Int. Ultrason. Symp. (IUS)*, Sep. 2020, pp. 1–4.
- [13] M. Piepenbrock, S. Dencks, and G. Schmitz, "Reliable motion estimation in super-resolution US by reducing the interference of microbubble movement," in *Proc. IEEE Int. Ultrason. Symp. (IUS)*, Oct. 2019, Art. no. 8925566.
- [14] T. M. Kierski *et al.*, "Superharmonic ultrasound for motion-independent localization microscopy: Applications to microvascular imaging from low to high flow rates," *IEEE Trans. Ultrason., Ferroelectr., Freq. Control*, vol. 67, no. 5, pp. 957–967, May 2020.
- [15] J. A. Jensen, S. B. Andersen, C. A. V. Hoyos, K. L. Hansen, C. M. Sorensen, and M. B. Nielsen, "Tissue motion estimation and correction in super resolution imaging," in *Proc. IEEE Int. Ultrason. Symp. (IUS)*, Oct. 2019, pp. 1–4.
- [16] R. J. Eckersley, C. T. Chin, and P. N. Burns, "Optimising phase and amplitude modulation schemes for imaging microbubble contrast agents at low acoustic power," *Ultrasound Med. Biol.*, vol. 31, no. 2, pp. 213–219, Feb. 2005.
- [17] V. Hingot, C. Errico, B. Heiles, L. Rahal, M. Tanter, and O. Couture, "Microvascular flow dictates the compromise between spatial resolution and acquisition time in ultrasound localization microscopy," *Sci. Rep.*, vol. 9, no. 1, pp. 1–10, Dec. 2019.
- [18] T. Furnival, R. K. Leary, and P. A. Midgley, "Denoising time-resolved microscopy image sequences with singular value thresholding," *Ultramicroscopy*, vol. 178, pp. 112–124, Jul. 2017.
- [19] U.-W. Lok *et al.*, "Real time SVD-based clutter filtering using randomized singular value decomposition and spatial downsampling for micro-vessel imaging on a verasonics ultrasound system," *Ultrasonics*, vol. 107, Sep. 2020, Art. no. 106163.
- [20] M. K. Cheezum, W. F. Walker, and W. H. Guilford, "Quantitative comparison of algorithms for tracking single fluorescent particles," *Biophys. J.*, vol. 81, no. 4, pp. 2378–2388, Oct. 2001.
- [21] I. N. Bankman, *Handbook of Medical Image Processing and Analysis*. Amsterdam, The Netherlands: Elsevier, 2009.
- [22] K. G. Brown, D. Ghosh, and K. Hoyt, "Deep learning of spatiotemporal filtering for fast super-resolution ultrasound imaging," *IEEE Trans. Ultrason., Ferroelectr., Freq. Control*, vol. 67, no. 9, pp. 1820–1829, Sep. 2020.
- [23] X. Liu, T. Zhou, M. Lu, Y. Yang, Q. He, and J. Luo, "Deep learning for ultrasound localization microscopy," *IEEE Trans. Med. Imag.*, vol. 39, no. 10, pp. 3064–3078, Oct. 2020.
- [24] G. E. Trahey, J. W. Allison, and O. T. von Ramm, "Angle independent ultrasonic detection of blood flow," *IEEE Trans. Biomed. Eng.*, vol. BME-34, no. 12, pp. 965–967, Dec. 1987.
- [25] X. Wu, "An efficient antialiasing technique," *ACM SIGGRAPH Comput. Graph.*, vol. 25, no. 4, pp. 143–152, Jul. 1991.
- [26] R. P. J. Nieuwenhuizen *et al.*, "Measuring image resolution in optical nanoscopy," *Nature Methods*, vol. 10, no. 6, pp. 557–562, Jun. 2013.
- [27] N. Banterle, K. H. Bui, E. A. Lemke, and M. Beck, "Fourier ring correlation as a resolution criterion for super-resolution microscopy," *J. Struct. Biol.*, vol. 183, no. 3, pp. 363–367, Sep. 2013.
- [28] M. van Heel and M. Schatz, "Fourier shell correlation threshold criteria," *J. Struct. Biol.*, vol. 151, no. 3, pp. 250–262, Sep. 2005.
- [29] J. A. Jensen and N. B. Svendsen, "Calculation of pressure fields from arbitrarily shaped, apodized, and excited ultrasound transducers," *IEEE Trans. Ultrason., Ferroelectr., Freq. Control*, vol. 39, no. 2, pp. 262–267, Mar. 1992.
- [30] J. A. Jensen, "Field: A program for simulating ultrasound systems," *Med. Biol. Eng. Comput.*, vol. 4, no. 1, pp. 351–353, 1996.
- [31] J. A. Jensen, "A multi-threaded version of field II," in *Proc. IEEE Int. Ultrason. Symp.*, Sep. 2014, pp. 2229–2232.
- [32] S. B. Andersen *et al.*, "Super-resolution imaging with ultrasound for visualization of the renal microvasculature in rats before and after renal ischemia: A pilot study," *Diagnostics*, vol. 10, no. 11, p. 862, Oct. 2020.
- [33] J. A. Jensen, S. Nikolov, K. L. Gammelmark, and M. H. Pedersen, "Synthetic aperture ultrasound imaging," *Ultrasonics*, vol. 44, pp. e5–e15, Dec. 2006.
- [34] M. Tanter and M. Fink, "Ultrafast imaging in biomedical ultrasound," *IEEE Trans. Ultrason., Ferroelectr., Freq. Control*, vol. 61, no. 1, pp. 102–119, Jan. 2014.
- [35] S. Dencks, M. Piepenbrock, and G. Schmitz, "Assessing vessel reconstruction in ultrasound localization microscopy by maximum likelihood estimation of a zero-inflated Poisson model," *IEEE Trans. Ultrason., Ferroelectr., Freq. Control*, vol. 67, no. 8, 2020, Art. no. 9032203.
- [36] C. Holliger, K. V. Lemley, S. L. Schmitt, F. C. Thomas, C. R. Robertson, and R. L. Jamison, "Direct determination of vasa recta blood flow in the rat renal papilla," *Circulat. Res.*, vol. 53, no. 3, pp. 401–413, Sep. 1983.
- [37] B. Zimmerhackl, C. R. Robertson, and R. L. Jamison, "Fluid uptake in the renal papilla by vasa recta estimated by two methods simultaneously," *Amer. J. Physiol.-Renal Physiol.*, vol. 248, no. 3, pp. F347–F353, Mar. 1985.
- [38] W. A. Cupples, T. Sakai, and D. J. Marsh, "Angiotensin II and prostaglandins in control of vasa recta blood flow," *Amer. J. Physiol.-Renal Physiol.*, vol. 254, no. 3, pp. F417–F424, Mar. 1988.
- [39] T. Takenaka, L. M. Harrison-Bernard, E. W. Inscho, P. K. Carmines, and L. G. Navar, "Autoregulation of afferent arteriolar blood flow in juxtamedullary nephrons," *Amer. J. Physiol.-Renal Physiol.*, vol. 267, no. 5, pp. F879–F887, Nov. 1994.
- [40] A. S. De Vriese, T. J. Verbeuren, M.-O. Vallez, N. H. Lameire, M. De Buyzere, and P. M. Vanhoutte, "Off-line analysis of red blood cell velocity in renal arterioles," *J. Vascular Res.*, vol. 37, no. 1, pp. 26–31, 2000.
- [41] S. Harput *et al.*, "3-D super-resolution ultrasound (SR-US) imaging with a 2-D sparse array," 2019, *arXiv:1902.01608*. [Online]. Available: <http://arxiv.org/abs/1902.01608>
- [42] J. A. Jensen *et al.*, "3-D super resolution imaging using a 62+62 elements row-column array," in *Proc. IEEE Int. Ultrason. Symp. (IUS)*, Oct. 2019, pp. 1–4.
- [43] J. A. Jensen *et al.*, "Three-dimensional super-resolution imaging using a row-column array," *IEEE Trans. Ultrason., Ferroelectr., Freq. Control*, vol. 67, no. 3, pp. 538–546, Mar. 2020.



Iman Taghavi received the B.Sc. and M.Sc. degrees in electrical engineering from the University of Isfahan, Isfahan, Iran, in 2013 and 2016, respectively. He is currently pursuing the Ph.D. degree with Center for Fast Ultrasound Imaging, Technical University of Denmark, Kongens Lyngby, Denmark.

From September 2013 to June 2015, he was a Research Assistant with Isfahan University Advanced Communications Laboratory, Isfahan. His research interests include signal processing and its applications in array sensors, radars, and biomedical imaging.



Sofie Bech Andersen received the master's degree in medicine from the University of Copenhagen, Copenhagen, Denmark, in 2015. She is currently pursuing the Ph.D. degree in preclinical ultrasound superresolution imaging in a collaboration between the Department of Biomedical Sciences, University of Copenhagen, the Department of Radiology, Rigshospitalet, Copenhagen, the Center for Fast Ultrasound Imaging, Technical University of Denmark, Kongens Lyngby, Denmark, and BK Medical, Herlev, Denmark.

She was concluding a year as a Resident (introductory position) in radiology with Rigshospitalet. Her research interest includes the development of diagnostic imaging tools for use in the clinic.



Charlotte Mehlén Sørensen received the B.Sc. degree in biology, the M.Sc. degree in human biology, and the Ph.D. degree in renal physiology from the University of Copenhagen, Copenhagen, Denmark, in 1996, 1999, and 2004, respectively.

She worked as a Drug Discovery Project Leader with Zealand Pharma, Søborg, Denmark. She was employed as an Assistant Professor with the Department of Biomedical Sciences. She has authored or coauthored 52 peer-reviewed articles in international journals. Her research focuses on renal hemodynamics, diabetes, and hypertension. Changes in renal autoregulation and blood flow regulation as a consequence of changes in the topology of the renal vascular tree, intercellular communication, and ion channel expression are investigated *in vivo* in different disease models. She runs a state-of-the-art *in vivo* rodent laboratory for acute and chronic experimental setups.

Dr. Sørensen is a member of the American Physiological Society, Danish Hypertension Society the Scandinavian Physiological Society, and Danish Cardiovascular Academy.



Carlos Armando Villagómez Hoyos was born in 1985. He received the B.Sc. degree in electronics engineering and the M.Sc. degree in digital signal processing from the National Autonomous University of Mexico, Coyoacán, Mexico, in 2008 and 2013, respectively, and the Ph.D. degree in biomedical engineering from the Center for Fast Ultrasound Imaging, Technical University of Denmark, Kongens Lyngby, Denmark, in 2016, with research on optimal synthetic aperture duplex imaging.

He is currently with BK Medical, Herlev, Denmark, as a System Engineer.



Jørgen Arendt Jensen (Fellow, IEEE) received the M.Sc., Ph.D., and Dr.Techn. degrees from the Technical University of Denmark, Lyngby, Denmark, in 1985, 1989, and 1996, respectively.

Since 1993, he has been a Full Professor of biomedical signal processing with the Department of Health Technology, Technical University of Denmark, Kongens Lyngby, Denmark. He has been the Founder and the Head of the Center for Fast Ultrasound Imaging since its inauguration in 1998. CFU has contributed with innovations in transverse oscillation vector flow imaging, synthetic aperture flow imaging in 2-D and 3-D, ultrasound simulation, research scanners, and row-column probes and beamforming. He has authored or coauthored more than 500 journal and conference articles on signal processing and medical ultrasound and the book *Estimation of Blood Velocities Using Ultrasound* (Cambridge University Press, 1996). He is also the Developer and Maintainer of the Field II Simulation Program. He has been a Visiting Scientist with Duke University, Durham, NC, USA, Stanford University, Palo Alto, CA, USA, and the University of Illinois at Urbana-Champaign, Urbana-Champaign, IL, USA. He was the Founder and the Head of the Biomedical Engineering Group Department of Electrical Engineering, Technical University of Denmark, from 2007 to 2010. In 2003, he was one of the founders of the biomedical engineering program in Medicine and Technology, which is a joint degree program between the Technical University of Denmark, Kongens Lyngby, Denmark, and the Faculty of Health and Medical Sciences at the University of Copenhagen, Copenhagen, Denmark. The degree is one of the most sought-after engineering degrees in Denmark. He was a Chairman of the study board from 2003 to 2010 and an Adjunct Professor with the University of Copenhagen from 2005 to 2010. He has given a number of short courses on simulation, synthetic aperture imaging, and flow estimation at international scientific conferences and teaches biomedical signal processing and medical imaging at the Technical University of Denmark. His researches are centered around simulation of ultrasound imaging, synthetic aperture imaging, vector blood flow estimation, 3-D and super-resolution imaging, row-column probes, and construction of ultrasound research systems. He has educated 45 Ph.D. students and currently advises 18 Ph.D. students. He has given more than 60 invited talks at international meetings and received several awards for his research, most recently the Grand Solutions Prize from the Danish Minister of Science, the order of the Dannebrog by his Majesty the Queen of Denmark, and the Rayleigh Award from the UFFC Society in the field of Ultrasonics in 2019.



Michael Bachmann Nielsen received the degree in medicine from the Faculty of Health Science, and the Ph.D. and Dr.Med. Dissertation degrees from the University of Copenhagen, Copenhagen, Denmark, in 1985, 1994, and 1998, respectively.

He is currently a Full Professor of oncoradiology with the University of Copenhagen, and a Consultant with the Department of Radiology, Rigshospitalet, Copenhagen. He has authored over 250 peer-reviewed journal articles on ultra-

sound or radiology. His current research interests include clinical testing of new ultrasound techniques, tumor vascularity, ultrasound elastography, training in ultrasound, and artificial intelligence.



Paper 2

Super-resolution imaging with ultrasound for visualization of the renal microvasculature in rats before and after renal ischemia: A pilot study

Sofie Bech Andersen, **Iman Taghavi**, Carlos Armando Villagómez Hoyos, Stinne Byrholdt Søgaaard, Fredrik Gran, Lars Lönn, Kristoffer Lindskov Hansen, Jørgen Arendt Jensen, Michael Bachmann Nielsen, and Charlotte Mehlin Sørensen

Name of journal in:

Diagnostics

Document Version:

Published

DOI:

10.3390/diagnostics10110862

General rights



Copyright and moral rights for the publications made accessible in the public portal are retained by the authors and/or other copyright owners and it is a condition of accessing publications that users recognise and abide by the legal requirements associated with these rights.

- Users may download and print one copy of any publication from the public portal for the purpose of private study or research.
- You may not further distribute the material or use it for any profit-making activity or commercial gain
- You may freely distribute the URL identifying the publication in the public portal

If you believe that this document breaches copyright please contact us providing details, and we will remove access to the work immediately and investigate your claim.

Article

Super-Resolution Imaging with Ultrasound for Visualization of the Renal Microvasculature in Rats before and after Renal Ischemia: A Pilot Study

Sofie Bech Andersen ^{1,2,3,*}, Iman Taghavi ⁴ , Carlos Armando Villagómez Hoyos ⁵,
Stinne Byrholdt Søgaard ^{1,3}, Fredrik Gran ⁵, Lars Lönn ^{1,3}, Kristoffer Lindskov Hansen ^{1,3},
Jørgen Arendt Jensen ⁴, Michael Bachmann Nielsen ^{1,3}  and Charlotte Mehlin Sørensen ²

¹ Department of Radiology, Rigshospitalet, 2100 Copenhagen, Denmark; stinne.byrholdt.soegaard@regionh.dk (S.B.S.); lars.birger.loenn@regionh.dk (L.L.); Kristoffer.Lindskov.Hansen.01@regionh.dk (K.L.H.); mbn@dadlnet.dk (M.B.N.)

² Department of Biomedical Sciences, University of Copenhagen, 2200 Copenhagen, Denmark; cmehlin@sund.ku.dk

³ Department of Clinical Medicine, University of Copenhagen, 2200 Copenhagen, Denmark

⁴ Center for Fast Ultrasound Imaging, Department of Health Technology, Technical University of Denmark, 2800 Lyngby, Denmark; imat@dtu.dk (I.T.); jaje@dtu.dk (J.A.J.)

⁵ BK Medical ApS, 2730 Herlev, Denmark; choyos@bkmedical.com (C.A.V.H.); fgran@bkmedical.com (F.G.)

* Correspondence: anne.sofie.bech.andersen@regionh.dk

Received: 29 September 2020; Accepted: 21 October 2020; Published: 22 October 2020



Abstract: In vivo monitoring of the microvasculature is relevant since diseases such as diabetes, ischemia, or cancer cause microvascular impairment. Super-resolution ultrasound imaging allows in vivo examination of the microvasculature by detecting and tracking sparsely distributed intravascular microbubbles over a minute-long period. The ability to create detailed images of the renal vasculature of Sprague-Dawley rats using a modified clinical ultrasound platform was investigated in this study. Additionally, we hypothesized that early ischemic damage to the renal microcirculation could be visualized. After a baseline scan of the exposed kidney, 10 rats underwent clamping of the renal vein ($n = 5$) or artery ($n = 5$) for 45 min. The kidneys were rescanned at the onset of clamp release and after 60 min of reperfusion. Using a processing pipeline for tissue motion compensation and microbubble tracking, super-resolution images with a very high level of detail were constructed. Image filtration allowed further characterization of the vasculature by isolating specific vessels such as the ascending vasa recta with a 15–20 μm diameter. Using the super-resolution images alone, it was only possible for six assessors to consistently distinguish the healthy renal microvasculature from the microvasculature at the onset of vein clamp release. Future studies will aim at attaining quantitative estimations of alterations in the renal microvascular blood flow using super-resolution ultrasound imaging.

Keywords: super-resolution ultrasound imaging; rats; Sprague-Dawley; kidney; microcirculation; vasa recta; reperfusion injury

1. Introduction

In vivo visualization of the microvasculature is an important clinical tool. The microvascular networks are fundamental for tissue homeostasis and are altered by diseases such as diabetes, ischemic disease, or cancer as well as normal aging [1–7]. The architectural or functional alterations of the microvasculature can compromise organ function or facilitate tumor growth. Therefore, early and precise diagnosis and monitoring of the microvascular alterations are crucial to detect these unfavorable

microcirculation effects. Super-resolution (SR) ultrasound imaging can depict the vasculature, including the microvasculature, of both superficial and deeper-lying organs and tissues *in vivo* using sparsely distributed microbubbles (MBs) as intravascular tracers. The SR image is obtained over minutes and is an accumulation of thousands of successive image frames in which each MB centroid is detected [8,9]. Furthermore, MB track maps can display estimations of MB velocity and direction based on tracking the MBs between frames. The healthy microvasculature of rodent organs and tissues has been visualized with SR imaging [8–13]. SR imaging can also visualize and quantify the pathological microvascular patterns in rodent and chicken embryo tumors [14–16] and the later stages of acute kidney injury in mice [17]. With a rich and anatomically distinctive vasculature [18], the kidneys are attractive organs for SR imaging. In rodents, ischemia-reperfusion can be used as a model of acute kidney injury, and contrast-enhanced ultrasound studies have shown that the insult causes prolonged reduction of the renal blood flow [19–21], probably due to impaired vascular reactivity and microvascular damage [22].

This study aimed to visualize the renal vasculature in male Sprague-Dawley rats using a modified commercial ultrasound scanner and probe. In addition, to gain initial clinical experience with this SR imaging setup, we investigated whether renal ischemia-reperfusion injuries could be identified using SR images acquired before, immediately after, and one hour after the insult. The SR results were compared with corresponding conventional power Doppler ultrasound scans. We hypothesized that the SR technique would allow us to visualize acute renal microvascular damage *in vivo*. We found that the SR technique revealed consistent and highly detailed depictions of the renal vascular tree, including the ascending vasa recta with a 15–20 μm diameter. The vasa recta were not visible with conventional power Doppler. The SR images alone did not consistently reveal renal blood flow changes after ischemia-reperfusion. Future studies will aim to quantify alterations in the renal microvascular blood flow using MB track maps.

2. Materials and Methods

2.1. Animal Ethics and Preparation

The experiments were performed in accordance with protocols approved by the Danish Animal Experiments Inspectorate under the Ministry of Environment and Food (license number 2015-15-0201-004637, issued on 17 April 2015). The study was performed at the University of Copenhagen, and all procedures agreed with the ethical standards of the university which comply with the EU Directive 2010/63/EU for animal experiments. The animal facility at the Department of Experimental Medicine, University of Copenhagen housed the rats, and animal caretakers were responsible for their wellbeing until use. The rats were held in a 12/12-h light/dark cycle and had free access to water and standard chow. The study was conducted on a total of 15 healthy male Sprague-Dawley rats (mean weight: 322 g, standard deviation (SD) \pm 49 g) obtained from Taconic A/S (Lille Skensved, Denmark). Ten rats underwent ischemia-reperfusion with three consecutive SR scans. Another three rats underwent the same SR protocol as the 10 rats but without ischemia-reperfusion as sham controls for histological evaluation to compensate for the three periods with MB infusion. One rat had an SR scan followed by an *ex vivo* magnetic resonance imaging (MRI) scan. The last rat was included from a pre-trial to show a different imaging plane. Anesthesia was induced with 5% isoflurane in 65% nitrogen and 35% oxygen; 1–2% isoflurane maintained the anesthesia. Ventilation was ensured by tracheotomy with connection to a mechanical ventilator (Ugo Basile, Gemonio, Italy) with 72 respirations/min. Two polyethylene catheters (PE-10) were inserted in the right jugular vein and used for the infusion of MBs (SonoVue, Bracco Imaging, Milan, Italy) and isotonic saline mixed with Nimblex (cisatracurium, 0.85 mg/mL, GlaxoSmithKline, London, UK, 20 $\mu\text{L}/\text{min}$). The mean arterial pressure (MAP) was measured using a polyethylene catheter (PE-50) in the left carotid artery and a Satham P23-dB pressure transducer (Gould, Oxnard, CA, USA). The rats were placed in the supine position on a heating table to ensure a steady body temperature (37 $^{\circ}\text{C}$), and the left kidney was exposed through laparotomy. To further expose the kidney and reduce respiratory motion, a metal

retractor pulled the left side of the diaphragm slightly in the cranial direction. Rat data are available in the Supplementary Materials, Table S1.

2.2. Ultrasound Scanning, Ischemia-Reperfusion Procedure, and Histopathology

An overview of the ischemia-reperfusion experiments is illustrated in Figure 1.

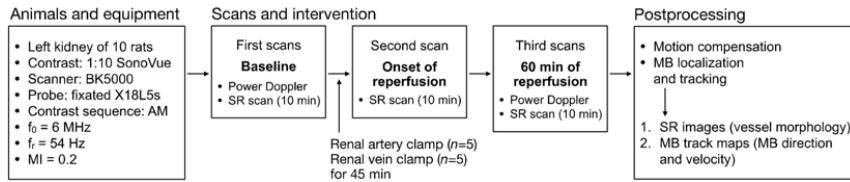


Figure 1. Experiment overview of the ischemia-reperfusion intervention. AM = amplitude modulation, f_0 = center frequency of the probe, f_r = frame rate, MI = mechanical index, SR = super-resolution, MB = microbubble.

Imaging data were obtained using a bk5000 scanner and a fixated X18L5s transducer (BK Medical ApS, Herlev, Denmark). The scanner was modified with a research interface for the live streaming of beamformed radio-frequency data to a disk. The transducer was placed on the lateral surface of the left kidney with gel for coupling. B-mode imaging was used to optimize the imaging plane, making sure both cortical and medullary regions were represented. The MBs were diluted in isotonic saline (1:10) and injected at a rate of 100 $\mu\text{L}/\text{min}$. The MB dilution was made anew before each scan to ensure MB integrity. Data recording was initiated when MBs became visible on the contrast-enhancing sequence display, and the SR data were acquired over 10 min [23]. To ensure a continuous influx of MBs, a custom-built device turned the syringe 180 degrees every 60 s [24]. After a baseline SR scan, five rats had their renal artery clamped, and five rats had their renal vein clamped using a nontraumatic micro-clamp. Both renal vein and artery clamping were included to investigate different severities of tissue damage [25,26]. After 45 min, the clamp was removed and a second SR scan was performed at the onset of reperfusion. The last SR scan was performed in a steadier state, 60 min after clamp release. In between the scans, the kidney was superfused with heated saline (37 $^{\circ}\text{C}$). Before the second and third SR scan, the imaging plane was readjusted with reference to the baseline B-mode image. For comparison, power Doppler ultrasound (PRF: 400 Hz, wall filter cutoff: 80 Hz, center frequency for transmission: 9.5 MHz) was acquired in direct continuation of the baseline and third SR scan, using the same scanner and transducer. All the rats were euthanized in anesthesia immediately after the experiments. The left kidney from the 10 rats that underwent ischemia-reperfusion and both kidneys from the three sham rats were removed and fixated in 4% paraformaldehyde (PFA) for documentation of the tissue damage. The kidneys were embedded in paraffin, cut into 4 μm slices, and stained using a standard hematoxylin and eosin (H&E) protocol. The images were analyzed by a trained anatomist blinded to the intervention category.

2.3. SR Imaging Technique and Data Processing

Contrast images were created using an amplitude modulation sequence (half-power, full-power, half-power) interleaved with B-mode images. Data were acquired using line-per-line focused beam transmission (frame rate: 54 Hz, center frequency for transmission: 6 MHz, mechanical index: 0.2). Off-line processing was conducted using an SR imaging pipeline programmed in MATLAB at the Technical University of Denmark. Nonrigid motion of the kidney was estimated by tissue speckle tracking [27]. The motion was compensated by using the motion estimates to adjust the individual MBs back to their location on the reference image. MBs were localized using thresholding and centroid detection, and tracks were made by connecting the nearest MBs in consecutive frames. Afterward, the tracks were inserted in the high-resolution images to yield SR images and the MB velocities

estimated from the tracks were used to create the MB track maps. A color wheel indicated the MB direction by color and color brightness was proportional to velocity. To highlight specific parts of the vasculature, MB trajectories were classified and shown based on their length, flow direction, velocity, and lifetime index (the number of consecutive frames an MB was tracked). An increase in track length and MB lifetime removed false tracks, leaving the most robust tracks in the images.

2.4. Evaluation of SR Images and Blood Pressure Data

The SR and power Doppler images from the 10 rats that underwent ischemia-reperfusion were independently and blindly evaluated by six of the co-authors. The assessors had different backgrounds qualifying them for SR image assessment: C.M.S. is associate professor in human biology with expertise in renal physiology, M.B.N. is professor in radiology with expertise in vascular ultrasound, L.L. is professor in radiology with expertise in vascular interventional radiology, K.L.H. is a radiologist with expertise in vascular ultrasound, C.A.H.V. is an ultrasound engineer with expertise in vascular ultrasound, and S.B.S. is an M.D. working with SR imaging in a PhD. All assessors had basic knowledge about the SR technique (experience ranging from 6 months to 5 years of working with SR imaging), as well as knowledge about rat kidney vascular anatomy and received written instructions prior to completing the evaluation. The written instructions for each assignment are shown in the Supplementary Materials, Tables S2, S4–S6. The three SR images from each rat were categorized as either baseline (the 10 images the assessors believed look normal based on their basic knowledge about SR imaging and renal vascular anatomy), onset of reperfusion (the 10 images that fit an assumption of low renal blood flow at the onset of reperfusion after a longer period of ischemia) or 60 min of reperfusion (the 10 images that match the assumption that the renal blood flow is restored to some degree). The power Doppler images from each rat were categorized as baseline or 60 min of reperfusion. After this, all scans were categorized as artery or vein clamp intervention, knowing that vein clamping induces most tissue damage [25,26]. The results were calculated as percentages of correct answers from all assessors. Interobserver agreement was tested with a fixed-marginal multi-rater kappa (using the Online Kappa Calculator, available online: <http://justusrandolph.net/kappa/> (accessed on 27 May 2020)). Differences in blood pressure during the scans were tested with a mixed-effects model (REML) with repeated measures with a Greenhouse–Geisser correction using GraphPad Prism 8.0 (version 8.4.3 for mac, GraphPad Software, San Diego, CA, USA).

2.5. Ex Vivo MRI of the Microvasculature

To compare the SR images of the healthy renal microvasculature with another imaging modality, ex vivo MRI was made of a single specimen. The rat was anesthetized and tracheotomized as described above. A polyethylene catheter (PE-25) was placed at the left renal artery through the femoral artery, and the aorta cranially to the left renal artery as well as the right renal artery were closed with sutures. Additional sutures were placed at the left renal artery, left renal vein, and left ureter. The rat was euthanized, and the kidney was perfused with 3 mL of 4% PFA followed by 2 mL containing 1 mL 1:10 diluted GadoSpin P (Viscover, Miltenyi Biotec, Bergisch Gladbach, Germany) and 1 mL 4% PFA. When the injection was completed, the remaining sutures were closed, and the specimen was immersed in 4% PFA. The kidney was scanned for 17 h in a 9.4T preclinical MR scanner (BioSpec 94/30 USR, Bruker BioSpin, Ettlingen, Germany) with a T1 contrast-enhanced 3D spoiled gradient echo sequence (3D Fast Low Angle Shot: 3D-FLASH sequence) [28]. Images were acquired using a 1H cryogenically cooled quadrature-resonator Tx/Rx coil (CryoProbe, Bruker BioSpin). MR image voxel size was 30 μ m isometric. To get a comparable representation of the vasculature, the corresponding 2.5 mm maximum intensity projection MR image slice was reconstructed and compared with the SR images (slice thickness ~0.6–1.2 mm).

3. Results

3.1. The Healthy Renal Microvasculature

In the healthy rat kidneys, a mean of 74 ± 27 MBs/frame was detected during the scans (32,300 frames). The SR images displayed the characteristic anatomical structure of the renal vasculature in the unipapillar rat kidney with the dense cortical vasculature clearly distinguishable from the vasa recta of the medulla (Figure 2A–C). The variations in the images could be caused by a combination of the normal variation in renal artery branching and renal morphology [29] as well as small differences in the imaging plane. The renal vascular structure found with ultrasound SR imaging was comparable to that found with ex vivo MRI (Figure 2D).

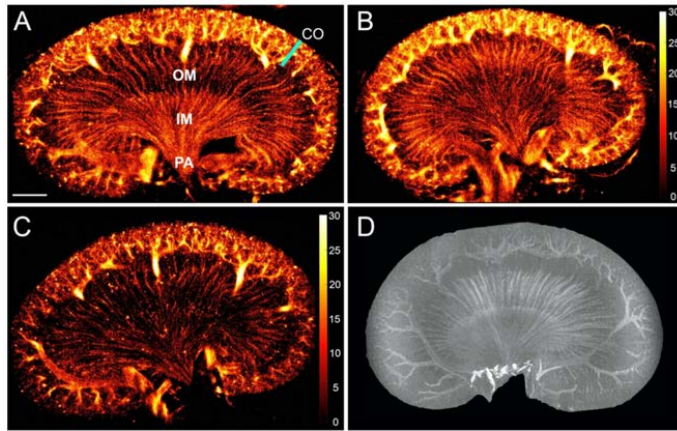


Figure 2. (A–C) Super-resolution images (log-scaled, i.e., color bar shows the value of intensity after logarithmic compression, ranging from 0–30 dB, and intensity corresponds to the number of microbubbles) of the healthy rat renal microvasculature. (A) There is a clear distinction between the dense cortical (CO) microvascular network and the vasa recta of the outer medulla (OM) and inner medulla (IM), leading down to the papilla (PA). Even though the scans were performed under the same conditions, the images show how the number of microbubbles varied between the rats, indicated by the higher intensity on image (B) (average of 117 detected microbubbles/frame) compared with image (C) (average of 70 detected microbubbles/frame). (D) Ex vivo magnetic resonance T1 contrast-enhanced image of another rat kidney for comparison. The kidneys measure approximately 2 cm in craniocaudal length and 1 cm in the medial-lateral direction. Scale bar: 2 mm.

The number of tracks in the MB track maps (Figure 3) ranged from 95,008 to 343,989. These maps allowed further delimitation and characterization of the renal vessels. Using the color wheel, the opposing flow directions in adjacent tracks helped discern arteries from veins (Figure 3A, included tracks with velocities from 0–10 mm/s). Without further image filtering, the MB track maps were difficult to read (Figure 3B, included tracks with velocities from 0–10 mm/s). In Figure 3C, the image from Figure 3B was filtered to include tracks that were longer than 300 μm , with an MB lifetime over 20 frames and a max velocity of 3 mm/s. This filtering highlighted the long straight vasa recta by removing some of the false or short tracks and enabled separation of the descending and ascending vasa recta. Figure 3D was filtered according to the direction and included only flow going from left to right, thereby highlighting the descending vasa recta in the left side and the ascending vasa recta in the right side of the medulla (other filtration parameters: tracks length > 250 μm , MB lifetime > 30 frames, max velocity 3 mm/s).

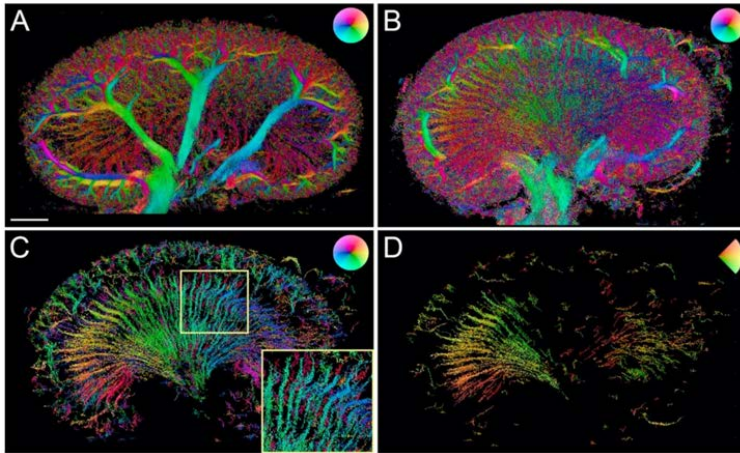


Figure 3. Super-resolution microbubble track maps. (A) Unfiltered microbubble track map. The color of the wheel indicates microbubble flow direction, and the color brightness indicates MB flow velocity. The image shows the opposite flow of the paired arteries and veins of the renal vascular tree. (B) Without filtering, this velocity map (from another rat) contains a high number of tracks (343,939). (C) The microbubble track map from (B) filtered to increase the robustness of the included tracks and highlight the long straight vasa recta, thereby allowing a distinction between the descending (green/blue) and ascending (red) vasa recta (insert). (D) Another way to filter these maps is by direction. This image is filtered to show microbubbles with a direction going from left to right, leaving the descending vasa recta visible on the left side of the medulla, and the ascending visible on the right side. Scale bar: 2 mm.

3.2. The Renal Microvasculature after Ischemia with Reperfusion

At the onset of reperfusion after release of the vein clamp, the SR images depicted the entire renal vasculature poorly perfused with MBs compared with baseline. It was particularly noticeable for the vasa recta, as exemplified in Figure 4A (middle section). The results were subtler at the onset of reperfusion after renal artery clamping where some of the kidneys did not alter from the baseline (Figure 4B, middle section). After 60 min of reperfusion, MBs refilled the microvascular bed in varying degree among the 10 rats. The vasculature appeared more irregular in some samples, while others showed a complete recovery of the microvascular flow after the intervention. All SR images of the 10 rats are available in the Supplementary Materials in Figures S1 and S2.

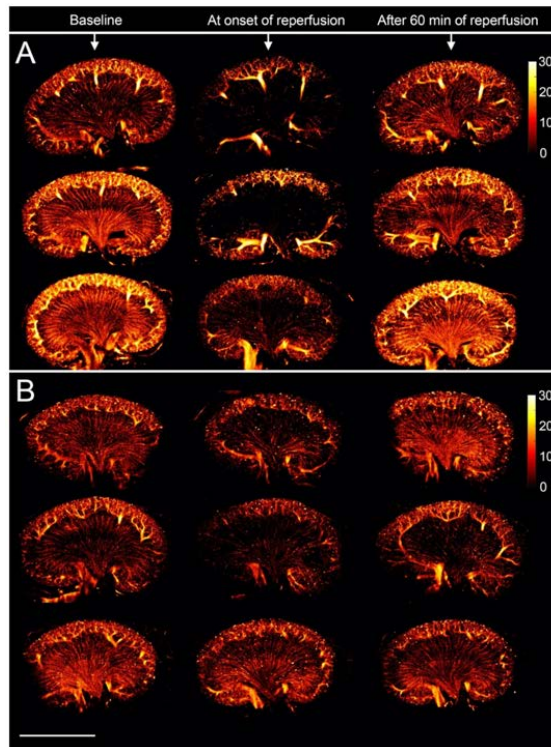


Figure 4. (A) Super-resolution images (log-scaled, i.e., color bar shows the value of intensity after logarithmic compression, ranging from 0–30 dB, and intensity corresponds to the number of microbubbles) of three rat kidneys before and after clamping of the renal vein. (B) Super-resolution images of three rat kidneys before and after clamping of the renal artery. Scale bar: 10 mm.

Six blinded assessors correctly identified the five scans as the onset of reperfusion after vein clamping, while the percentage of correctly identified scans at the onset of reperfusion after artery clamping was only 60%. The assessors were not able to distinguish the baseline scans from the scans after 60 min of reperfusion. For the vein clamping, 63% were correctly identified as baseline or 60 min of reperfusion. For the artery clamping, 40% were correctly identified as baseline and 30% as 60 min of reperfusion. The fixed-marginal kappa was 0.60, showing only moderate agreement among the assessors. When evaluating all the SR scans in the correct order, the assessors correctly identified 67% as either vein or artery clamping. The power Doppler scans visualized only the cortical blood flow. After 60 min of reperfusion, all the power Doppler images showed a decrease in the cortical blood flow compared with baseline (exemplified in Figure 5). The assessors correctly identified all of the 20 power Doppler scans as either baseline or 60 min of reperfusion, and correctly identified 80% as either vein or artery clamping. All power Doppler images as well as the image assessment results are available in the Supplementary Materials in Figures S3 and S4 and Tables S2–S6, respectively.

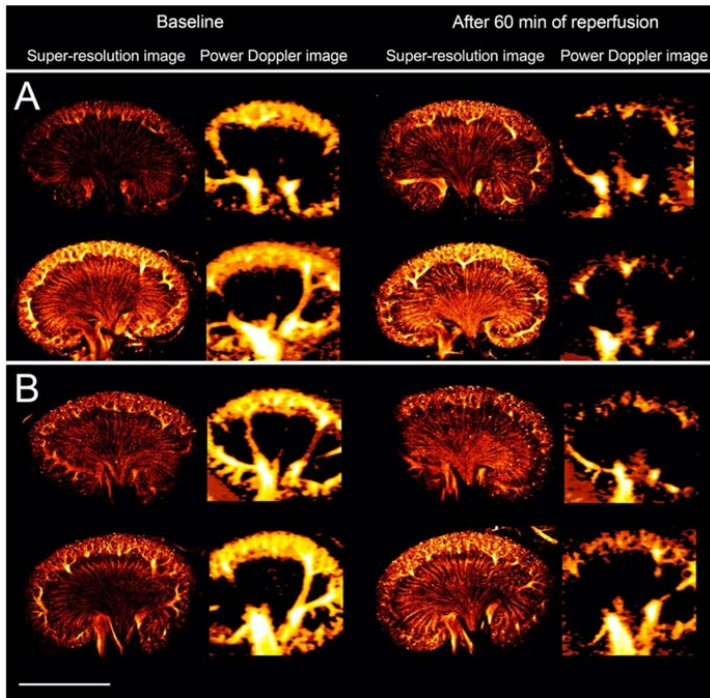


Figure 5. (A) Super-resolution (log-scaled) and power Doppler images of two rat kidneys before and after clamping of the renal vein. (B) Super-resolution (log-scaled) and power Doppler images of two rat kidneys before and after clamping of the renal artery. In these examples, all the super-resolution images showed a complete refilling of the microvascular bed after 60 min of reperfusion. The power Doppler scans from all animals showed a decreased signal in the cortex after 60 min of reperfusion compared with baseline. Scale bar: 10 mm.

There was no statistically significant difference in the MAP measured during the three scans ($p = 0.21$). During the baseline scans, the mean of the MAP for the 10 rats was 109 ± 19 mmHg, and at the onset of reperfusion it was 112 ± 22 mmHg. At 60 min of reperfusion, one rat had missing data, and the MAP was 106 ± 23 mmHg.

3.3. Histopathological Evaluation

Examples of H&E stains from three rats are shown in Figure 6. The five vein clamp specimens were all correctly identified. They revealed a high number of erythrocytes accumulated in the renal interstitial space. Some of the specimens, both after artery and vein clamping, showed intratubular cast formation as a sign of ischemic damage. However, the assessor could not correctly identify all the arterial clamp (60% correctly identified) and sham kidney specimens (67% correctly identified). The results from histopathological evaluation are available in the Supplementary Materials, Table S7.

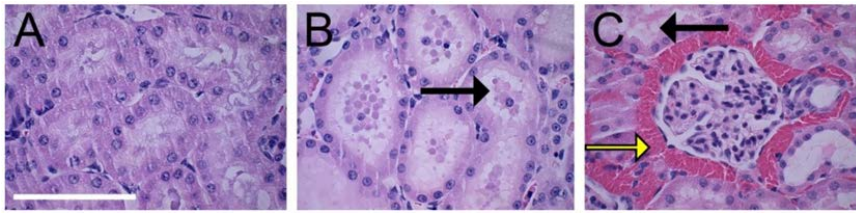


Figure 6. Hematoxylin and eosin staining of the renal cortex from three rats. (A) Control. (B) After renal artery clamping. (C) After renal vein clamping. The black arrows show intratubular cast formation in the tubules. The yellow arrow shows erythrocytes accumulated in the renal interstitial space around a glomerulus. Scale bar: 100 μm .

4. Discussion

We investigated the ability to create SR images of the renal vasculature of healthy Sprague-Dawley rats using a modified clinical ultrasound scanner and probe together with a customized processing pipeline for tissue motion compensation and MB tracking. The SR images revealed a consistent and detailed depiction of the renal vascular tree, including the microvasculature, similar to descriptions from anatomical studies [18,29], to *ex vivo* nano-CT images of mouse kidneys [30], and to the vascular structure of a rat kidney found with *ex vivo* MRI. MBs were tracked in the ascending vasa recta with a diameter of approximately 15–20 μm [31,32]. The descending vasa recta are clustered in vascular bundles and were therefore also visible. Since the sulfur hexafluoride gas in SonoVue is exhaled and MBs act similarly to erythrocytes, the SR images visualize only the renal vasculature and not the tubular system [33,34]. To our knowledge, the presented images reveal the highest level of detail of the renal vascular tree of rats obtained with modified clinical ultrasound platforms. Some studies using ultrasound SR imaging on rodent kidneys have not visualized the vasa recta, which could be due to short scan times or out-of-plane motion [17,35]. SR imaging for visualization of the slowly flowing blood in the vasa recta requires data acquisition to be lengthy to fill as many of the small vessels with MBs as possible for an adequate microvascular representation [23]. As mentioned, the variation in the images of the healthy kidneys may be due to known variations in the renal artery branching and renal morphology [29]. Regarding the microvasculature, it is still not completely clarified how many times the renal cortical radiate arteries branch, and how many afferent arterioles branch from each subsegment of the cortical radiate arteries. Differences in the imaging plane and the detected number of MBs also cause image variations. Hence, these normal variations need to be considered in future studies where different groups of animals and eventually humans with a more complicated multipapillary renal anatomy are investigated and compared.

To gain initial experience with the technique in a clinical setting, the early vascular changes induced by renal ischemia-reperfusion were investigated with SR imaging and compared with power Doppler imaging. Ischemia-reperfusion is known to cause prolonged reductions in renal blood flow [19–22,36–38]. We scanned the kidneys intraabdominally to simplify the SR data by reducing motion from respiration and neighboring bowels that push the kidney out of the imaging plane. This setup confined the study to the very early stages of reperfusion. At the onset of reperfusion after obstructing the renal vein, the SR images showed a more notable reduction in the vascular refilling compared with the renal artery, as demonstrated by the image assessment and as expected, since vein occlusion causes more tissue damage [25,26]. After 60 min of reperfusion, the SR images revealed a varying degree of microvascular MB refilling, while the power Doppler scans showed reduced cortical blood flow in all rats. Power Doppler imaging is used in the clinic for visualization of blood flow but is limited in its ability to detect slow flow. Theoretically, the lowest detectable velocity for the power Doppler in this study was approximately 6.5 mm/s. Therefore, the vasa recta with a blood flow velocity around 1 mm/s were not visualized [10,32]. On the other hand, the velocity cut off for power Doppler enabled the visualization of the decrease in cortical blood flow. The SR images are

accumulations of tracks from the 10 min recording, each track with a specific velocity. Therefore, a decrease in the blood velocity was not visually observable, as indicated by the image assessment. A study that used conventional contrast-enhanced ultrasound to investigate the early response to renal ischemia-reperfusion in mice also found variation in the response to the intervention [20]. Whether this initial degree of MB refilling of the vascular bed influences the outcome after the insult is important to explore [39,40]. Even though the results from this initial pilot study are not ideal yet, they serve as a platform for future experiments. Future work will aim at attaining transcutaneous kidney scans for longitudinal studies with this SR technique. This will allow us to investigate whether SR imaging is able to detect alterations in the microvascular architecture at the early stages of their occurrence. If early or subtle microvascular alterations have a prognostic value and could allow timely initiation or change of treatment, e.g., in persons who are developing diabetic nephropathy but do not yet show other clinical signs of disease [41], or in persons undergoing cancer treatment where early readouts of drug or radiation efficacy are crucial [42], ultrasound SR imaging could fill an unmet need and evolve into a strong tool in the clinical setting.

Other ultrasound techniques and imaging modalities are competing with the SR imaging setup presented in this paper. Ultrasound plane-wave techniques are commonly used to obtain SR images at a higher framerate [8,10–17]. To facilitate a faster implementation of SR imaging in the clinic, we used focused beam transmission which is an established technology in commercial ultrasound platforms. MRI and CT are also clinically relevant modalities for microvascular imaging of deeper-lying structures. We included an ex vivo MR image in this study. Since there are major differences between the in vivo SR imaging and ex vivo MRI, the MR image was included only as a simple reference for the SR images. This could also have been attained with ex vivo μ CT [3,30,43,44]. The downsides of ex vivo imaging are the hour-long scan times, functional investigations are not possible, and the tissue fixation process can shrink the microvascular structures [45,46]. In addition, the number of contrast-filled vessels of the MRI specimen was lower than expected. This inadequate contrast-filling of the vessels is another challenge in ex vivo imaging [44]. In vivo MRI and μ CT can provide maps of tissue oxygenation or perfusion and a relatively high-resolution when applied in small animal research [3,47–49], but also require long scan times and for μ CT a high X-ray exposure. Human clinical scanners have even lower resolution. An advantage of ultrasound SR imaging is the possibility of direct human translation. The current setup with the hockey-stick transducer can be used on humans to achieve images of the same quality as presented here, given the out-of-plane motion is not excessive. The images will be restricted to a relatively small area given the probe's aperture. A target could be superficial lymph nodes. Furthermore, the current scanner settings with a mechanical index of 0.2 and a center frequency of 6 MHz together with dilution of the MBs point to a low risk of adverse bio-effects [50]. If imaging larger organs that span deeper, another probe would be needed, and issues related to, e.g., appropriately high frame rate for MB tracking and differences in MB excitation in shallow vs deeper parts of the organ due to tissue attenuation would have to be addressed. Moreover, acoustic shadowing, associated with massively calcified vessels or kidney stones, is a common problem in ultrasound imaging. Since the performance of SR imaging relies on the echo signals from the MBs, extensive arteriosclerosis may affect MB detection and tracking in the vessels. Accordingly, the efficacy of SR imaging should be addressed when the technique is applied in animals or persons with chronic vascular disease. Nonetheless, compared with MRI and CT, the minutes spent attaining ultrasound images of deeper-lying microvascular structures should be acceptable when applied to the appropriate clinical settings.

This study was limited by the small number of animals. Another limiting factor is the lack of quantitative estimations of microvascular blood flow alterations during reperfusion. In chronic kidney disease the architecture of the vessels changes, resulting in reduced vessel density, decreased branching, or increased tortuosity [2,3,17]. The image assessment of the SR images in this study illustrated how the microvascular flow changes in an acute setup were not detectable by visual image evaluation. Moreover, visual image assessments are often affected by assessor subjectivity,

further strengthening the need for quantitative image analysis strategies. However, to the best of our knowledge, a well-established way of flow quantification at this scale is still a big challenge. The MB number and behavior vary due to differences in anesthesia concentration, blood pressure, body weight, inflammation, and small variances in the handling of the MBs before injection [51], which was confirmed by the range in MB count in the baseline scans. Therefore, the number of MBs as a measure for perfusion is ambiguous, as also indicated by the image assessment. Estimations of MB velocity could reveal microvascular flow alterations. The renal vasculature is densely packed, and the MB track maps are composed of many thousand tracks, each with a unique direction, MB velocity, track length, and lifetime depending on anatomical region and vessel type. In addition, some vascular structures, such as the winding glomerular capillaries, are not possible to visualize with the current SR imaging techniques. Even though filtering allows isolation of specific vessel tracks, estimation of changes in velocities ranging from 1–2 mm/s are affected by even small uncertainties in the location of the MBs. Additionally, the MB tracking in this study was challenged by the relatively low frame rate of 54 Hz. Hence, the complexity of the track information makes quantification of microvascular flow changes an ongoing challenge. We anticipate that microvascular flow changes in the straighter arterioles e.g., the afferent arterioles or the vasa recta will be obtainable with SR imaging in the future. This will give important indirect insight into glomerular blood flow. Another limitation is the differences in the image planes due to probe re-adjustment prior to each scan. When comparing the three scans, anatomical or pathological information outside the imaging plane can be missed or misinterpreted. Studies with 3D reconstructions of 2D ultrasound techniques including SR imaging have been performed in animals including in rodent kidneys, rabbit lymph nodes and different rodent tumors [12,13,15,52,53]. The 3D reconstructions give a more complete morphological examination, but do not allow MB tracking in the elevational plane or motion compensation in all three directions. This could become feasible with other types of probes, e.g., row-column and matrix ultrasound probes that are currently being developed for in vivo SR imaging [54–56].

In conclusion, our study demonstrated that highly detailed ultrasound SR images of the healthy renal vasculature of rat kidneys are obtainable with modified clinical ultrasound equipment. The high level of anatomical detail of both the cortical and medullary vasculature suggests that the method can be applied in the investigation of a broad range of renal diseases. Future studies will aim at achieving quantitative estimations of the renal microvascular blood flow from the MB track maps as well as investigating diseases that disrupt the microvascular architecture to demonstrate the clinical usefulness of the technique.

5. Patents

Patent on the tissue motion correction algorithm by J.A.J. and I.T. used in this study has been purchased by BK Medical ApS, Herlev, Denmark.

Supplementary Materials: The following are available online at <http://www.mdpi.com/2075-4418/10/11/862/s1>, Figure S1: Super-resolution images before and after renal artery clamping, Figure S2: Super-resolution images before and after renal vein clamping, Figure S3: Power Doppler images before and after renal artery clamping, Figure S4: Power Doppler images before and after renal vein clamping, Table S1: Experimental data, Table S2: Image assessment, assignment 1A, Table S3: Assignment 1A, interobserver agreement, Table S4: Image assessment, assignment 1B; Table S5: Image assessment, assignment 2A, Table S6: Image assessment, assignment 2B, Table S7: Assessment of hematoxylin and eosin staining.

Author Contributions: Conceptualization, S.B.A., C.M.S., C.A.V.H., L.L., F.G., K.L.H., J.A.J., M.B.N.; methodology, S.B.A., C.M.S., K.L.H., M.B.N.; software, I.T., J.A.J.; validation, I.T., J.A.J.; formal analysis, I.T., S.B.A.; investigation, S.B.A., S.B.S., C.M.S., C.A.V.H., L.L., K.L.H., M.B.N.; resources, C.M.S., F.G., J.A.J., M.B.N.; data curation, I.T., C.A.V.H., J.A.J.; writing—original draft preparation, S.B.A.; writing—review and editing, S.B.S., I.T., C.M.S., C.A.V.H., F.G., K.L.H., L.L., J.A.J., M.B.N.; visualization, S.B.A., I.T.; supervision, K.L.H., C.M.S., J.A.J., M.B.N.; project administration, S.B.A., F.G., C.M.S., J.A.J., M.B.N.; funding acquisition, F.G., C.M.S., J.A.J., M.B.N. All authors have read and agreed to the published version of the manuscript.

Funding: This research was funded by Innovation Fund Denmark, grant number 7050-00004B.

Acknowledgments: The authors wish to thank Henrik Koch Johansen (former employee at BK Medical ApS, Herlev, Denmark) for constructing the syringe-turning device. We appreciate the technical skills of animal technician Karin Larsen (Department of Biomedical Sciences, University of Copenhagen, Copenhagen, Denmark) who performed the animal surgeries. Thanks to Steen Seier Poulsen (Department of Biomedical Sciences, University of Copenhagen, Copenhagen, Denmark) for assessing the H&E stains. Lastly, thanks to the Panum Preclinical MRI Core Facility, University of Copenhagen, Copenhagen, Denmark for helping create the ex vivo MR image.

Conflicts of Interest: C.A.V.H. and F.G. are employed at BK Medical ApS, Herlev, Denmark. The funders had no role in the design of the study; in the collection, analyses, or interpretation of data; in the writing of the manuscript, or in the decision to publish the results.

References

1. Maric-Bilkan, C.; Flynn, E.R.; Chade, A.R. Microvascular disease precedes the decline in renal function in the streptozotocin-induced diabetic rat. *Am. J. Physiol. Physiol.* **2012**, *302*, F308–F315. [[CrossRef](#)] [[PubMed](#)]
2. Basile, D.P.; Donohoe, D.; Roethe, K.; Osborn, J.L. Renal ischemic injury results in permanent damage to peritubular capillaries and influences long-term function. *Am. J. Physiol. Ren. Physiol.* **2001**, *281*, F887–F899. [[CrossRef](#)]
3. Ehling, J.; Bábíčková, J.; Gremse, F.; Klinkhammer, B.M.; Baetke, S.; Knuechel, R.; Kiessling, F.; Floege, J.; Lammers, T.; Boor, P. Quantitative Micro-Computed Tomography Imaging of Vascular Dysfunction in Progressive Kidney Diseases. *J. Am. Soc. Nephrol.* **2016**, *27*, 520–532. [[CrossRef](#)] [[PubMed](#)]
4. Beckman, J.A.; Duncan, M.S.; Damrauer, S.M.; Wells, Q.S.; Barnett, J.V.; Wasserman, D.H.; Bedimo, R.J.; Butt, A.A.; Marconi, V.C.; Sico, J.J.; et al. Microvascular Disease, Peripheral Artery Disease, and Amputation. *Circulation* **2019**, *140*, 449–458. [[CrossRef](#)] [[PubMed](#)]
5. Ehling, J.; Theek, B.; Gremse, F.; Baetke, S.; Möckel, D.; Maynard, J.; Ricketts, S.A.; Grüll, H.; Neeman, M.; Knuechel, R.; et al. Micro-CT imaging of tumor angiogenesis: Quantitative measures describing micromorphology and vascularization. *Am. J. Pathol.* **2014**, *184*, 431–441. [[CrossRef](#)] [[PubMed](#)]
6. Demidov, V.; Maeda, A.; Sugita, M.; Madge, V.; Sadanand, S.; Flueraru, C.; Vitkin, I.A. Preclinical longitudinal imaging of tumor microvascular radiobiological response with functional optical coherence tomography. *Sci. Rep.* **2018**, *8*, 38. [[CrossRef](#)] [[PubMed](#)]
7. Jonasson, H.; Bergstrand, S.; Fredriksson, I.; Larsson, M.; Östgren, C.J.; Strömberg, T. Normative data and the influence of age and sex on microcirculatory function in a middle-aged cohort: Results from the SCAPIS study. *Am. J. Physiol. Heart Circ. Physiol.* **2020**, *318*, H908–H915. [[CrossRef](#)]
8. Errico, C.; Pierre, J.; Pezet, S.; Desailly, Y.; Lenkei, Z.; Couture, O.; Tanter, M. Ultrafast ultrasound localization microscopy for deep super-resolution vascular imaging. *Nature* **2015**, *527*, 499–502. [[CrossRef](#)]
9. Christensen-Jeffries, K.; Browning, R.J.; Tang, M.X.; Dunsby, C.; Eckersley, R.J. In Vivo Acoustic Super-Resolution and Super-Resolved Velocity Mapping Using Microbubbles. *IEEE Trans. Med. Imaging* **2015**, *34*, 433–440. [[CrossRef](#)]
10. Foiret, J.; Zhang, H.; Ilovitsh, T.; Mahakian, L.; Tam, S.; Ferrara, K.W. Ultrasound localization microscopy to image and assess microvasculature in a rat kidney. *Sci. Rep.* **2017**, *7*, 13662. [[CrossRef](#)]
11. Yu, J.; Lavery, L.; Kim, K. Super-resolution ultrasound imaging method for microvasculature in vivo with a high temporal accuracy. *Sci. Rep.* **2018**, *8*, 13918. [[CrossRef](#)] [[PubMed](#)]
12. Zhu, J.; Rowland, E.M.; Harput, S.; Riemer, K.; Leow, C.H.; Clark, B.; Cox, K.; Lim, A.; Christensen-Jeffries, K.; Zhang, G.; et al. 3D Super-Resolution US Imaging of Rabbit Lymph Node Vasculature in Vivo by Using Microbubbles. *Radiology* **2019**, *291*, 642–650. [[CrossRef](#)]
13. Kierski, T.M.; Espindola, D.; Newsome, I.G.; Cherin, E.; Yin, J.; Foster, F.S.; Demore, C.E.M.; Pinton, G.F.; Dayton, P.A. Superharmonic Ultrasound for Motion-Independent Localization Microscopy: Applications to Microvascular Imaging from Low to High Flow Rates. *IEEE Trans. Ultrason. Ferroelectr. Freq. Control* **2020**, *67*, 957–967. [[CrossRef](#)] [[PubMed](#)]
14. Opacic, T.; Dencks, S.; Theek, B.; Piepenbrock, M.; Ackermann, D.; Rix, A.; Lammers, T.; Stickeler, E.; Delorme, S.; Schmitz, G.; et al. Motion model ultrasound localization microscopy for preclinical and clinical multiparametric tumor characterization. *Nat. Commun.* **2018**, *9*, 1527. [[CrossRef](#)] [[PubMed](#)]
15. Lin, F.; Shelton, S.E.; Espindola, D.; Rojas, J.D.; Pinton, G.; Dayton, P.A. 3-D Ultrasound Localization Microscopy for Identifying Microvascular Morphology Features of Tumor Angiogenesis at a Resolution Beyond the Diffraction Limit of Conventional Ultrasound. *Theranostics* **2017**, *7*, 196–204. [[CrossRef](#)]

16. Lowerison, M.R.; Huang, C.; Lucien, F.; Chen, S.; Song, P. Ultrasound localization microscopy of renal tumor xenografts in chicken embryo is correlated to hypoxia. *Sci. Rep.* **2020**, *10*, 2478. [[CrossRef](#)]
17. Chen, Q.; Yu, J.; Rush, B.M.; Stocker, S.D.; Tan, R.J.; Kim, K. Ultrasound super-resolution imaging provides a noninvasive assessment of renal microvasculature changes during mouse acute kidney injury. *Kidney Int.* **2020**, *98*, 355–365. [[CrossRef](#)]
18. Moffat, D.B.; Fourman, J. A vascular pattern of the rat kidney. 1963. *J. Am. Soc. Nephrol.* **2001**, *12*, 624–632.
19. Cao, W.; Cui, S.; Yang, L.; Wu, C.; Liu, J.; Yang, F.; Liu, Y.; Bin, J.; Hou, F.F. Contrast-Enhanced Ultrasound for Assessing Renal Perfusion Impairment and Predicting Acute Kidney Injury to Chronic Kidney Disease Progression. *Antioxid. Redox Signal.* **2017**, *27*, 1397–1411. [[CrossRef](#)]
20. Fischer, K.; Meral, F.C.; Zhang, Y.; Vangel, M.G.; Jolesz, F.A.; Ichimura, T.; Bonventre, J.V. High-resolution renal perfusion mapping using contrast-enhanced ultrasonography in ischemia-reperfusion injury monitors changes in renal microperfusion. *Kidney Int.* **2016**, *89*, 1388–1398. [[CrossRef](#)]
21. Mahoney, M.; Sorace, A.; Warram, J.; Samuel, S.; Hoyt, K. Volumetric contrast-enhanced ultrasound imaging of renal perfusion. *J. Ultrasound Med.* **2014**, *33*, 1427–1437. [[CrossRef](#)]
22. Yamamoto, T.; Tada, T.; Brodsky, S.V.; Tanaka, H.; Noiri, E.; Kajiya, F.; Goligorsky, M.S. Intravital videomicroscopy of peritubular capillaries in renal ischemia. *Am. J. Physiol. Physiol.* **2002**, *282*, F1150–F1155. [[CrossRef](#)] [[PubMed](#)]
23. Hingot, V.; Errico, C.; Heiles, B.; Rahal, L.; Tanter, M.; Couture, O. Microvascular flow dictates the compromise between spatial resolution and acquisition time in Ultrasound Localization Microscopy. *Sci. Rep.* **2019**, *9*, 2456. [[CrossRef](#)] [[PubMed](#)]
24. Lohmaier, S.; Ghanem, A.; Veltmann, C.; Sommer, T.; Bruce, M.; Tiemann, K. In vitro and in vivo studies on continuous echo-contrast application strategies using SonoVue in a newly developed rotating pump setup. *Ultrasound Med. Biol.* **2004**, *30*, 1145–1151. [[CrossRef](#)]
25. Owji, S.M.; Nikeghbal, E.; Moosavi, S.M. Comparison of ischaemia-reperfusion-induced acute kidney injury by clamping renal arteries, veins or pedicles in anaesthetized rats. *Exp. Physiol.* **2018**, *103*, 1390–1402. [[CrossRef](#)]
26. Park, Y.; Hirose, R.; Dang, K.; Xu, F.; Behrends, M.; Tan, V.; Roberts, J.P.; Niemann, C.U. Increased severity of renal ischemia-reperfusion injury with venous clamping compared to arterial clamping in a rat model. *Surgery* **2008**, *143*, 243–251. [[CrossRef](#)]
27. Jensen, J.A.; Andersen, S.B.; Hoyos, C.A.V.; Hansen, K.L.; Sørensen, C.M.; Nielsen, M.B. Tissue Motion Estimation and Correction in Super Resolution Imaging. In Proceedings of the 2019 IEEE International Ultrasonics Symposium (IUS), Glasgow, UK, 6–9 October 2019; pp. 1–4.
28. Nitta, N.; Takakusagi, Y.; Kokuryo, D.; Shibata, S.; Tomita, A.; Higashi, T.; Aoki, I.; Harada, M. Intratumoral evaluation of 3D microvasculature and nanoparticle distribution using a gadolinium-dendron modified nano-liposomal contrast agent with magnetic resonance micro-imaging. *Nanomed. Nanotechnol. Biol. Med.* **2018**, *14*, 1315–1324. [[CrossRef](#)] [[PubMed](#)]
29. Yoldas, A.; Dayan, M.O. Morphological Characteristics of Renal Artery and Kidney in Rats. *Sci. World J.* **2014**, *2014*, 468982. [[CrossRef](#)]
30. Wagner, R.; Van Loo, D.; Hossler, F.; Czymbek, K.; Pauwels, E.; Van Hoorebeke, L. High-Resolution Imaging of Kidney Vascular Corrosion Casts with Nano-CT. *Microsc. Microanal.* **2011**, *17*, 215–219. [[CrossRef](#)]
31. Yamamoto, K.; Wilson, D.R.; Baumal, R. Blood supply and drainage of the outer medulla of the rat kidney: Scanning electron microscopy of microvascular casts. *Anat. Rec.* **1984**, *210*, 273–277. [[CrossRef](#)]
32. Holliger, C.; Lemley, K.V.; Schmitt, S.L.; Thomas, F.C.; Robertson, C.R.; Jamison, R.L. Direct Determination of Vasa Recta Blood Flow in the Rat Renal Papilla. *Circ. Res.* **1983**, *53*, 401–413. [[CrossRef](#)] [[PubMed](#)]
33. Morel, D.R.; Schwieger, I.; Hohn, L.; Terrettaz, J.; Llull, J.B.; Cornioley, Y.A.; Schneider, M. Human Pharmacokinetics and Safety Evaluation of SonoVue™, a New Contrast Agent for Ultrasound Imaging. *Investig. Radiol.* **2000**, *35*, 80–85. [[CrossRef](#)] [[PubMed](#)]
34. Schneider, M.; Broillet, A.; Tardy, I.; Pochon, S.; Bussat, P.; Bettinger, T.; Helbert, A.; Costa, M.; Tranquart, F. Use of Intravital Microscopy to Study the Microvascular Behavior of Microbubble-Based Ultrasound Contrast Agents. *Microcirculation* **2012**, *19*, 245–259. [[CrossRef](#)] [[PubMed](#)]
35. Yang, Y.; He, Q.; Zhang, H.; Qiu, L.; Qian, L.; Lee, F.-F.; Liu, Z.; Luo, J. Assessment of Diabetic Kidney Disease Using Ultrasound Localization Microscopy: An in Vivo Feasibility Study in Rats. In Proceedings of the 2018 IEEE International Ultrasonics Symposium (IUS), Kobe, Japan, 22–25 October 2018; pp. 1–4.

36. Vetterlein, F.; Pethö, A.; Schmidt, G. Distribution of capillary blood flow in rat kidney during postischemic renal failure. *Am. J. Physiol.* **1986**, *251*, H510–H519. [[CrossRef](#)]
37. Conesa, E.L.; Valero, F.; Nadal, J.C.; Fenoy, F.J.; López, B.; Arregui, B.; Salom, M.G. N-acetyl-L-cysteine improves renal medullary hypoperfusion in acute renal failure. *Am. J. Physiol. Regul. Integr. Comp. Physiol.* **2001**, *281*, R730–R737. [[CrossRef](#)]
38. Regner, K.R.; Zuk, A.; Van Why, S.K.; Shames, B.D.; Ryan, R.P.; Falck, J.R.; Manthathi, V.L.; McMullen, M.E.; Ledbetter, S.R.; Roman, R.J. Protective effect of 20-HETE analogues in experimental renal ischemia reperfusion injury. *Kidney Int.* **2009**, *75*, 511–517. [[CrossRef](#)]
39. Chawla, L.S.; Amdur, R.L.; Amodeo, S.; Kimmel, P.L.; Palant, C.E. The severity of acute kidney injury predicts progression to chronic kidney disease. *Kidney Int.* **2011**, *79*, 1361–1369. [[CrossRef](#)]
40. Wang, H.-J.; Varner, A.; AbouShwareb, T.; Atala, A.; Yoo, J.J. Ischemia/Reperfusion-Induced Renal Failure in Rats as a Model for Evaluating Cell Therapies. *Ren. Fail.* **2012**, *34*, 1324–1332. [[CrossRef](#)]
41. Scurt, F.G.; Menne, J.; Brandt, S.; Bernhardt, A.; Mertens, P.R.; Haller, H.; Chatzikyrkou, C.; Ito, S.; Izzo, J.L.; Januszewicz, A.; et al. Systemic Inflammation Precedes Microalbuminuria in Diabetes. *Kidney Int. Rep.* **2019**, *4*, 1373–1386. [[CrossRef](#)]
42. Kasoji, S.K.; Rivera, J.N.; Gessner, R.C.; Chang, S.X.; Dayton, P.A. Early assessment of tumor response to radiation therapy using high-resolution quantitative microvascular ultrasound imaging. *Theranostics* **2018**, *8*, 156–168. [[CrossRef](#)]
43. Hlushchuk, R.; Zubler, C.; Barré, S.; Correa Shokiche, C.; Schaad, L.; Röthlisberger, R.; Wnuk, M.; Daniel, C.; Khoma, O.; Tschanz, S.A.; et al. Cutting-edge microangiography: New dimensions in vascular imaging and kidney morphometry. *Am. J. Physiol. Physiol.* **2018**, *314*, F493–F499. [[CrossRef](#)] [[PubMed](#)]
44. Perrien, D.S.; Saleh, M.A.; Takahashi, K.; Madhur, M.S.; Harrison, D.G.; Harris, R.C.; Takahashi, T. Novel methods for microCT-based analyses of vasculature in the renal cortex reveal a loss of perfusable arterioles and glomeruli in eNOS^{-/-} mice. *BMC Nephrol.* **2016**, *17*, 24. [[CrossRef](#)] [[PubMed](#)]
45. Kawai, K.; Morikawa, T. The effect of formalin fixation on the size of pelvic sidewall lymph nodes. *Int. J. Colorectal Dis.* **2018**, *33*, 1493–1495. [[CrossRef](#)] [[PubMed](#)]
46. Tran, H.; Jan, N.J.; Hu, D.; Voorhees, A.; Schuman, J.S.; Smith, M.A.; Wollstein, G.; Sigal, I.A. Formalin Fixation and Cryosectioning Cause only Minimal Changes in Shape or Size of Ocular Tissues. *Sci. Rep.* **2017**, *7*, 12065. [[CrossRef](#)]
47. Pöschinger, T.; Renner, A.; Eisa, F.; Dobosz, M.; Strobel, S.; Weber, T.G.; Brauweiler, R.; Kalender, W.A.; Scheuer, W. Dynamic Contrast-Enhanced Micro-Computed Tomography Correlates With 3-Dimensional Fluorescence Ultramicroscopy in Antiangiogenic Therapy of Breast Cancer Xenografts. *Investig. Radiol.* **2014**, *49*, 445–456. [[CrossRef](#)]
48. Pohlmann, A.; Hentschel, J.; Fechner, M.; Hoff, U.; Bubalo, G.; Arakelyan, K.; Cantow, K.; Seeliger, E.; Flemming, B.; Waiczies, H.; et al. High Temporal Resolution Parametric MRI Monitoring of the Initial Ischemia/Reperfusion Phase in Experimental Acute Kidney Injury. *PLoS ONE* **2013**, *8*, e57411. [[CrossRef](#)]
49. Starosolski, Z.; Villamizar, C.A.; Rendon, D.; Paldino, M.J.; Milewicz, D.M.; Ghaghada, K.B.; Annapragada, A.V. Ultra High-Resolution In vivo Computed Tomography Imaging of Mouse Cerebrovasculature Using a Long Circulating Blood Pool Contrast Agent. *Sci. Rep.* **2015**, *5*, 10178. [[CrossRef](#)]
50. Miller, D.L.; Averkiou, M.A.; Brayman, A.A.; Everbach, E.C.; Holland, C.K.; Wible, J.H.; Wu, J. Bioeffects Considerations for Diagnostic Ultrasound Contrast Agents. *J. Ultrasound Med.* **2008**, *27*, 611–632. [[CrossRef](#)]
51. Tang, M.X.; Mulvana, H.; Gauthier, T.; Lim, A.K.P.; Cosgrove, D.O.; Eckersley, R.J.; Stride, E. Quantitative contrast-enhanced ultrasound imaging: A review of sources of variability. *Interface Focus* **2011**, *1*, 520–539. [[CrossRef](#)]
52. Demené, C.; Payen, T.; Dizeux, A.; Barrois, G.; Gennisson, J.-L.; Bridal, L.; Tanter, M. 3-D Longitudinal Imaging of Tumor Angiogenesis in Mice in Vivo Using Ultrafast Doppler Tomography. *Ultrasound Med. Biol.* **2019**, *45*, 1284–1296. [[CrossRef](#)]
53. Huang, C.; Lowerison, M.R.; Lucien, F.; Gong, P.; Wang, D.; Song, P.; Chen, S. Noninvasive Contrast-Free 3D Evaluation of Tumor Angiogenesis with Ultrasensitive Ultrasound Microvessel Imaging. *Sci. Rep.* **2019**, *9*, 4907. [[CrossRef](#)]

54. Jensen, J.A.; Tomov, B.G.; Ommen, M.L.; Øygaard, S.H.; Schou, M.; Sams, T.; Stuart, M.B.; Beers, C.; Thomsen, E.V.; Larsen, N.B. Three-Dimensional Super-Resolution Imaging Using a Row-Column Array. *IEEE Trans. Ultrason. Ferroelectr. Freq. Control* **2020**, *67*, 538–546. [[CrossRef](#)] [[PubMed](#)]
55. Heiles, B.; Correia, M.; Hingot, V.; Pernot, M.; Provost, J.; Tanter, M.; Couture, O. Ultrafast 3D Ultrasound Localization Microscopy Using a 32×32 Matrix Array. *IEEE Trans. Med. Imaging* **2019**, *38*, 2005–2015. [[CrossRef](#)] [[PubMed](#)]
56. Harput, S.; Tortoli, P.; Eckersley, R.J.; Dunsby, C.; Tang, M.X.; Christensen-Jeffries, K.; Ramalli, A.; Brown, J.; Zhu, J.; Zhang, G.; et al. 3-D Super-Resolution Ultrasound Imaging with a 2-D Sparse Array. *IEEE Trans. Ultrason. Ferroelectr. Freq. Control* **2020**, *67*, 269–277. [[CrossRef](#)]

Publisher's Note: MDPI stays neutral with regard to jurisdictional claims in published maps and institutional affiliations.



© 2020 by the authors. Licensee MDPI, Basel, Switzerland. This article is an open access article distributed under the terms and conditions of the Creative Commons Attribution (CC BY) license (<http://creativecommons.org/licenses/by/4.0/>).



Paper 3

Evaluation of 2D super-resolution ultrasound imaging of the rat renal vasculature using *ex vivo* micro-computed tomography

Sofie Bech Andersen, **Iman Taghavi**, Hans Martin Kjer, Stinne Byrholdt Søggaard, Carsten Gundlach, Vedrana Andersen Dahl, Michael Bachmann Nielsen, Anders Bjorholm Dahl, Jørgen Arendt Jensen, and Charlotte Mehlin Sørensen

Name of journal in:

Scientific Reports

Document Version:

Published

DOI:

10.1038/s41598-021-03726-6

General rights

Copyright and moral rights for the publications made accessible in the public portal are retained by the authors and/or other copyright owners and it is a condition of accessing publications that users recognise and abide by the legal requirements associated with these rights.

- Users may download and print one copy of any publication from the public portal for the purpose of private study or research.
- You may not further distribute the material or use it for any profit-making activity or commercial gain
- You may freely distribute the URL identifying the publication in the public portal

If you believe that this document breaches copyright please contact us providing details, and we will remove access to the work immediately and investigate your claim.



OPEN

Evaluation of 2D super-resolution ultrasound imaging of the rat renal vasculature using ex vivo micro-computed tomography

Sofie Bech Andersen^{1,2✉}, Iman Taghavi³, Hans Martin Kjer⁴, Stinne Byrholdt Søgaard^{1,2}, Carsten Gundlach⁵, Vedrana Andersen Dahl⁴, Michael Bachmann Nielsen^{2,6}, Anders Bjorholm Dahl⁴, Jørgen Arendt Jensen³ & Charlotte Mehlin Sørensen¹

Super-resolution ultrasound imaging (SRUS) enables in vivo microvascular imaging of deeper-lying tissues and organs, such as the kidneys or liver. The technique allows new insights into microvascular anatomy and physiology and the development of disease-related microvascular abnormalities. However, the microvascular anatomy is intricate and challenging to depict with the currently available imaging techniques, and validation of the microvascular structures of deeper-lying organs obtained with SRUS remains difficult. Our study aimed to directly compare the vascular anatomy in two in vivo 2D SRUS images of a Sprague–Dawley rat kidney with ex vivo μ CT of the same kidney. Co-registering the SRUS images to the μ CT volume revealed visually very similar vascular features of vessels ranging from ~ 100 to 1300 μ m in diameter and illustrated a high level of vessel branching complexity captured in the 2D SRUS images. Additionally, it was shown that it is difficult to use μ CT data of a whole rat kidney specimen to validate the super-resolution capability of our ultrasound scans, i.e., validating the actual microvasculature of the rat kidney. Lastly, by comparing the two imaging modalities, fundamental challenges for 2D SRUS were demonstrated, including the complexity of projecting a 3D vessel network into 2D. These challenges should be considered when interpreting clinical or preclinical SRUS data in future studies.

Super-resolution ultrasound imaging (SRUS) enables in vivo investigation of the microvasculature at clinically relevant depths^{1–6}. The technique depicts the vascular architecture at levels below 100 μ m, magnitudes lower than the currently available clinical imaging modalities for in-depth imaging, such as CT and MRI. In vivo imaging of the microvasculature at these levels opens new possibilities for investigating disease development and treatment efficacy in, e.g., diabetes or cancer^{7–10}.

The fundamental principle of SRUS is localization and tracking of single intravascular microbubbles (MBs). The final SRUS image is an accumulation of thousands of MB trajectories, each representing one MB's most likely route through the vasculature. More accurate localization and tracking are currently achieved when the MBs are spatially separated in each image frame. Accordingly, dense and well-perfused vascular networks such as the renal vasculature challenge MB tracking, especially since reasonable data acquisition time is critical^{11–14}. In addition, a single vessel is represented by a given number of MB trajectories, making the vessel diameter dependent on the intraluminal distribution and number of MBs that pass through. Lastly, capturing a complex 3D vascular network in 2D is challenging due to overlaying vessels and vessels that traverse the elevational plane. Since the localization and tracking of MBs are subject to uncertainty, it is central to compare the structures depicted in the SRUS images with other modalities. Microphantoms have been used to validate the spatial accuracy and precision of the MB localization^{15,16}. Yet, the phantoms do not reproduce the conditions from in vivo SRUS, where the complex vascular structures, variations in blood flow, and tissue motion complicate SRUS image formation.

¹Department of Biomedical Sciences, University of Copenhagen, 2200 Copenhagen, Denmark. ²Department of Radiology, Rigshospitalet, 2100 Copenhagen, Denmark. ³Center for Fast Ultrasound Imaging, Department of Health Technology, Technical University of Denmark, 2800 Lyngby, Denmark. ⁴Department of Applied Mathematics and Computer Science, Technical University of Denmark, 2800 Lyngby, Denmark. ⁵Department of Physics, Technical University of Denmark, 2800 Lyngby, Denmark. ⁶Department of Clinical Medicine, University of Copenhagen, 2200 Copenhagen, Denmark. ✉email: anne.sofie.bech.andersen@regionh.dk

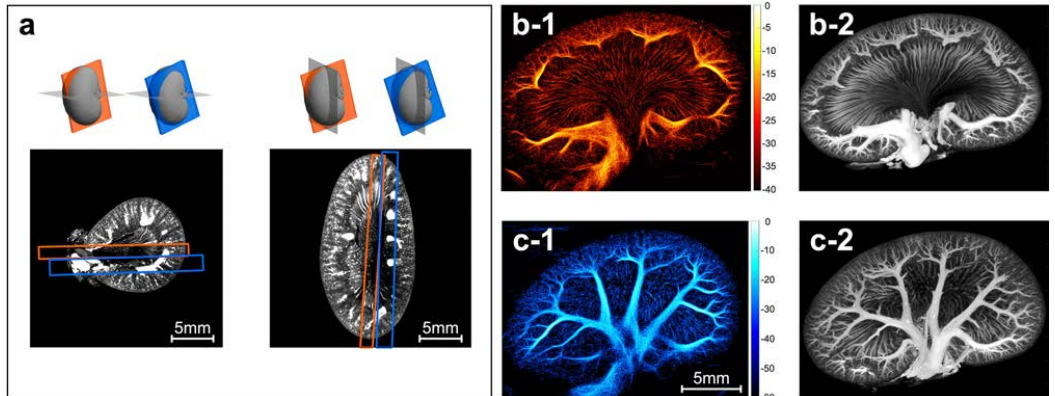


Figure 1. Co-registration of μ CT and super-resolution ultrasound images. (a) Co-registration of the two 2D super-resolution ultrasound images to the μ CT volume. The images show the two ultrasound fields of view in the μ CT coordinate system in an axial μ CT slice to the left and a sagittal μ CT slice to the right. (b-1,c-1) show the two super-resolution ultrasound images (intensity maps). The images are log-scaled with a dynamic range of 40 and 60 dB, respectively. The color bar shows the value of intensity after logarithmic compression. Intensity corresponds to the number of detected microbubbles. (b-2,c-2) show the μ CT maximum intensity projections in the super-resolution ultrasound image overlap.

Studies on cancer models in chick embryos and mice have correlated SRUS results to histological measurements of microvessel density or vessel area fraction^{9,10}. However, it is difficult to co-register the thin histological sections and the SRUS images for comparison of the exact same areas. One of the first studies with SRUS compared an SRUS image of a thin mouse ear with an optical image of the same vessels¹⁷. The chorioallantoic membrane of ex ovo chicken embryos has also been used as an in vivo ‘phantom’ for validation of SRUS; like the mouse ear, the anatomy of the membrane’s thin-layered vascular bed allows co-registration of the SRUS images with optical imaging of the same field-of-view^{18–20}. These approaches have coupled SRUS images directly with accurate images of the microvascular anatomy. The optical imaging techniques are restricted to superficial structures, and can also be limited in providing a ground truth, e.g., due to image contrast. For deeper-lying organs, other approaches are necessary to investigate the accuracy of the vascular anatomy in the SRUS images. The vessel fraction area from SRUS images has been correlated with measures of relative blood volume from ex vivo μ CT of mice tumors¹⁰. In rabbit lymph nodes, the distribution of vessel diameters measured with μ CT and SRUS were in good agreement, with a peak diameter between 10 and 20 μ m²¹. However, in these two studies, the imaging modalities were not directly co-registered and compared. Another study compared SRUS images of the vasa vasorum around rabbit femoral arteries with ex vivo μ CT of the same area and found corresponding results²². Lastly, CT angiography of larger arteries (mostly mm-sized) in the human brain was used for comparison with corresponding transcranial SRUS images²³.

Ex vivo μ CT can also produce detailed images of the dense renal microvasculature in rodents^{24–29}. Therefore, our study aimed to directly compare the vascular anatomy shown in two in vivo 2D SRUS images of a Sprague–Dawley rat kidney with ex vivo μ CT of the same kidney. For this comparison, we aimed at estimating the proportion of vessels in the SRUS images that were also captured in the μ CT. We expected the large vessels to be resolved in both modalities and that the discrepancy between resolved vessels became higher with smaller vessel diameters. Reaching these goals required imaging the same areas of the same rat kidney with both in vivo SRUS and ex vivo μ CT, co-registering the two modalities, segmenting the vessels in each of the modalities, and quantifying the overlap of the two segmentations.

Results

Image co-registration and visual comparison. Maximum intensity projections (MIPs) of the μ CT slices approximately covering the volume depicted in the two SRUS images were created by co-registering the SRUS images to the μ CT volume. In Fig. 1a, the two ultrasound fields of view are shown in the μ CT coordinate system. Figure 1b-1 shows an SRUS image acquired down the center of the kidney (scan 1) to display both the cortical vasculature and the vasa recta of the medulla, and Fig. 1c-1 shows a scan obtained more ventrally (scan 2), showing the segmental and arcuate vessels and their branches. The corresponding μ CT MIPs are shown in Fig. 1b-2,c-2.

Very similar vascular features were evident from visual inspection of the corresponding images from the two imaging modalities. In Fig. 2, some of the similarities are shown in up-scaled examples from the μ CT MIP of scan 1 compared with the corresponding MB track map composed of the MB trajectories, where the color of the trajectories indicates the MB flow direction. For example, both imaging modalities clearly displayed the wavy course of the outer medulla vasa recta and the straighter course of the inner medulla vasa recta (Fig. 2c).

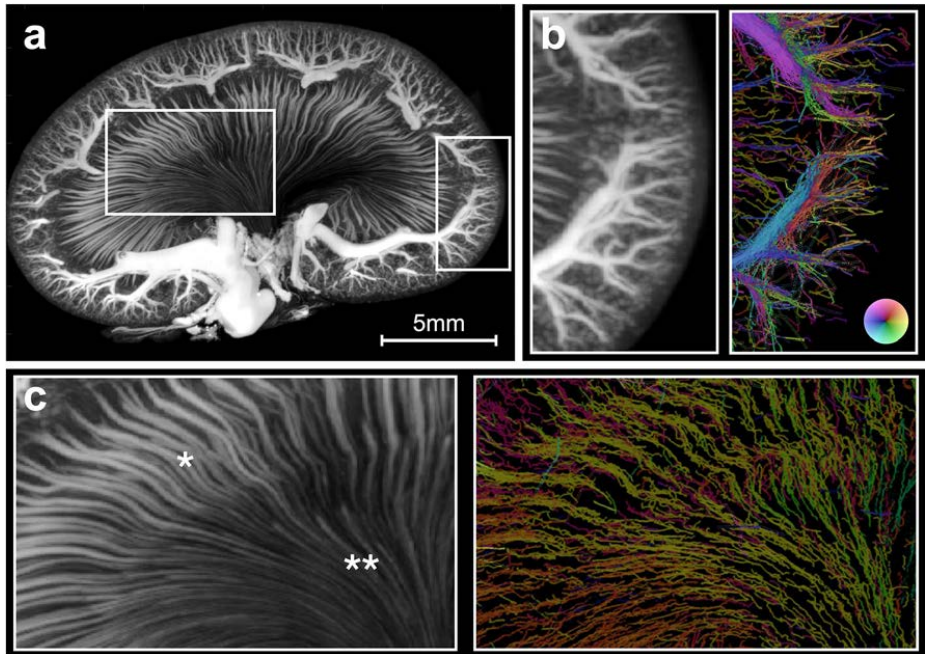


Figure 2. Visual comparison of the μ CT and microbubble track map. (a) μ CT maximum intensity projection in the super-resolution ultrasound image overlap of scan 1. The two marked regions are up-scaled and compared with the corresponding unfiltered microbubble track map in (b) and (c) (for visualization, the color transparency in the microbubble track map is scaled by the intensity map). (b) Shows a part of the renal cortex. (c) Shows a part of the renal medulla with the vasa recta. Notice how the color wheel in the microbubble track map allows separation of arteries and veins according to flow direction, e.g., in (c) with the descending (orange/yellow/green) and ascending (purple/blue) vasa recta of the medulla. * marks outer medulla, ** marks inner medulla.

An advantageous feature of the MB track maps is the immediate distinction between vessels with arterial and venous flow, e.g., the descending and ascending vasa recta: a feature not immediately extractable from the μ CT.

Quantification of similarities between super-resolution ultrasound images and ex vivo μ CT. The proportion of vessels in the SRUS scan 2 that were also captured in the μ CT was assessed by finding the percentage of vessel overlap after vessel segmentation. On the μ CT, the vessel centerlines of the visible, contrast-filled segmental, arcuate, and cortical radial arteries and veins were manually drawn. The majority of the vessels resolved for vessel centerline segmentation in the μ CT were veins (621 vein segments, size range: \sim 80–1400 μ m). Due to the smaller diameter of the arteries, mainly the segmental and arcuate arteries were visible, but even some arcuate arteries had such a small diameter that they were indistinguishable from nearby structures (110 artery segments, size range: \sim 50–500 μ m). The μ CT centerlines were projected into the coordinate system of the 2D SRUS images, and to cover the contrast-filled area, the centerlines were dilated based on approximate expected vessel diameters extracted from examples of diameter measurements of the segmental, arcuate, and cortical radial arteries and veins on the μ CT. This dilation was used only to create two regions of interest (ROIs) for vessel overlap estimation: one for all the vein segments (Fig. 3a-1) and one for all the artery segments (Fig. 3b-1). Dilated volumes were not used for further quantification, so possible biases due to the choice of dilation did not propagate to the rest of the analysis. In these ROIs, we could reasonably expect to observe MB tracks. The MB track map from scan 2 was filtered to include only regions labeled as “segmental or larger arcuate vessels” or “cortex” (see the “Materials and methods” section for clarification). Based on arterial flow direction determination during MB track map filtering, the image was separated into an image displaying only the vein tracks (Fig. 3a-2) and one displaying only the artery tracks (Fig. 3b-2), respectively. Then, the vessel centerlines of well-defined MB trajectories in the filtered MB track map were manually plotted. Of the SRUS vein centerlines, 85% were recovered within the μ CT ROI, while only 65% of the SRUS artery centerlines were recovered (Fig. 3a-3,b-3). Even though the percentage of artery overlap was lower, many of the SRUS artery centerlines had a corresponding μ CT artery ROI in close proximity, as evident from Fig. 3b-3. This illustrates how the discrepancy in vessel overlap becomes higher with smaller vessel diameters.

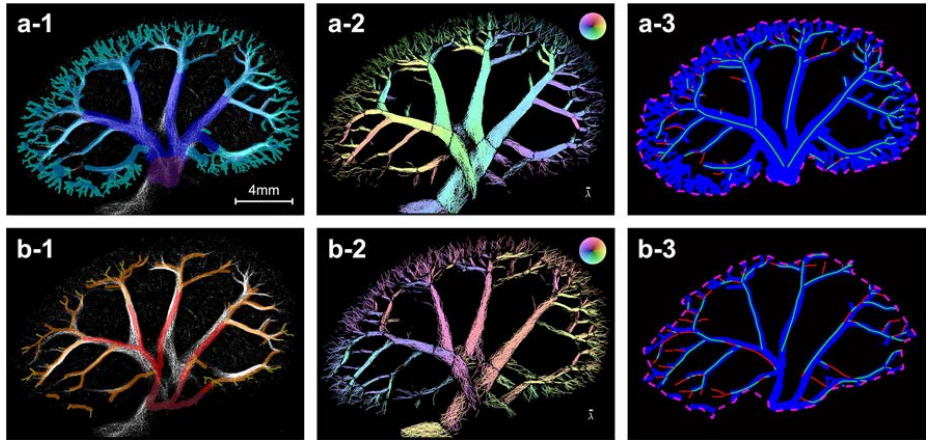


Figure 3. Vessel overlap estimation. **(a)** Veins, **(b)** Arteries. **(a-1,b-1)** Manually drawn veins and arteries on the μ CT in the super-resolution ultrasound scan 2 overlap (the colored μ CT segmentation is displayed on top of a white super-resolution ultrasound image). Purple = renal vein branches, dark blue = segmental veins, blue = arcuate veins, turquoise = cortical radial veins, dark red = renal artery branches, red = segmental arteries, orange = arcuate arteries, yellow = cortical radial arteries. **(a-2,b-2)** Filtered microbubble track maps including only regions labeled as “segmental or larger arcuate vessels” or “cortex” and separated into a map with only vein **(a-2)** and only artery **(b-2)** tracks, respectively. **(a-3,b-3)** Overlap of the manually drawn vessel centerlines in the super-resolution image (green and red lines) and μ CT vessel ROIs (blue) inside the μ CT ROI region (pink dashed line). The green centerlines are overlapping the μ CT ROIs while the red centerlines are not.

The percentage of all the MB tracks (all non-zero pixels in the filtered MB track map) covered by the μ CT ROIs was similar: 77% of the vein MB tracks and 44% of the artery MB tracks were recovered inside the respective μ CT ROIs (Supplementary Fig. S1). As this comparison included more of the smaller arcuate and cortical radial vessels than the centerline comparison, a lower overlap percentage was expected. The reported overlap percentages are difficult to put into context. The vessel structures of the kidney are very densely organized, and some level of spurious overlap can always be expected. As a control, we mirrored the μ CT ROIs along the central axial axis, which resulted in a drop in the overlap percentages to 50% (veins) and 24% (arteries) for the SRUS vessel centerlines and 51% (veins) and 23% (arteries) for the MB tracks (Supplementary Fig. S2). This procedure was considered likely to represent a best-case scenario for spurious overlap, and the percentages would most likely be similar or even smaller for a random match of the SRUS images and μ CT volume.

The segmental and larger arcuate arteries displayed in the SRUS image in Fig. 3b-2 seemed wider than those in the μ CT ROI in Fig. 3b-1. The μ CT demonstrated how these arteries were partially wrapped by their counterpart vein (Fig. 4a,b). Not only are the MBs in the arteries difficult to track due to a pulsating flow with high peak-systolic velocities, but the close proximity with the veins makes it even more challenging; on the unfiltered MB track maps, the artery tracks seemed hidden in the large number of vein tracks surrounding them, as exemplified in Fig. 4c. The MB track map of scan 2 included 4460 segmental/large arcuate artery tracks versus 12,300 segmental/large arcuate vein tracks (number of MB links associated with the arteries: 27,000 vs. number of MB links associated with veins: 83,230). Additionally, the length of tracks associated with the arteries was shorter than the length of tracks associated with the veins (median length of artery tracks: 457 μ m vs. median length of vein tracks: 739 μ m), indicating that it is difficult to link the fast-flowing arterial MBs from frame to frame.

Examples of diameter measurements from two larger, paired arcuate veins and arteries are shown in Fig. 5. The measurements showed a tendency to underestimate the vein diameter and overestimate the artery diameter in the SRUS images relative to the μ CT, when 4 *s.d.* (standard deviation) of the MB position around the centerline was considered the diameter measure in the SRUS data.

The cortical radial arteries with diameters of ~ 50 μ m were found as the limit of structures that could be identified with the μ CT resolution used in our study. At this level, comparison becomes challenging, and discrepancies will arise. To illustrate the challenges with direct comparison of these vessels, three sampled line intensity profiles are shown in Fig. 6. In profile 1, two vessels intertwined in the μ CT MIP (Fig. 6a). When comparing the intensity profiles from the μ CT MIP and SRUS image in Fig. 6c, there seemed to be two vessels with similar size and location in both images. Judging by the direction coloring in Fig. 6b (right) and the flow angles in Fig. 6d, one of the vessels was an artery and the other was a vein. However, the two vessels on the μ CT MIP were both vein branches; this was revealed when inspecting the μ CT volume. The artery or arteries running along these veins were too small to visualize in the μ CT properly but were caught in the ultrasound SRUS image. The size of the artery suggests an overestimation of the artery dimensions in the SRUS images, as was also seen in Fig. 5. Additionally, two separate veins were not readily visible from the SRUS image. This can occur because the veins were closer than the MB localization uncertainty. Profiles 2 and 3 show smaller vessels. The μ CT intensity profile

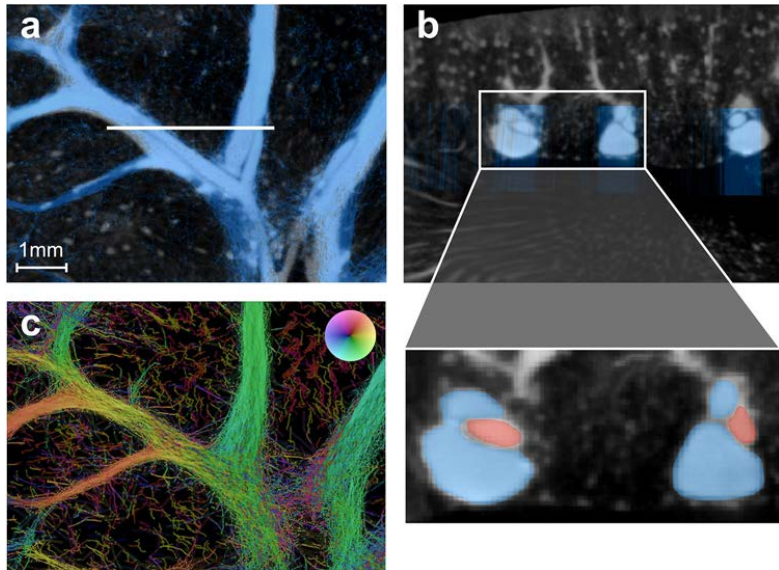


Figure 4. Veins wrapped around their paired artery. (a) Section of a coronal image slice of the μ CT with overlap of super-resolution ultrasound scan 2 (blue). (b) Section of a sagittal image slice of the μ CT with overlap of super-resolution ultrasound scan 2 (blue). The up-scaled content shows how the large segmental veins (blue) wrap around their paired segmental artery (red). (c) Unfiltered microbubble track map of the same slice as (a) (for visualization, the color transparency in the microbubble track map is scaled by the intensity map). The arteries are not readily apparent in the microbubble track maps without filtering and separating the microbubbles with artery and vein flow direction, as shown in Fig. 3b-2.

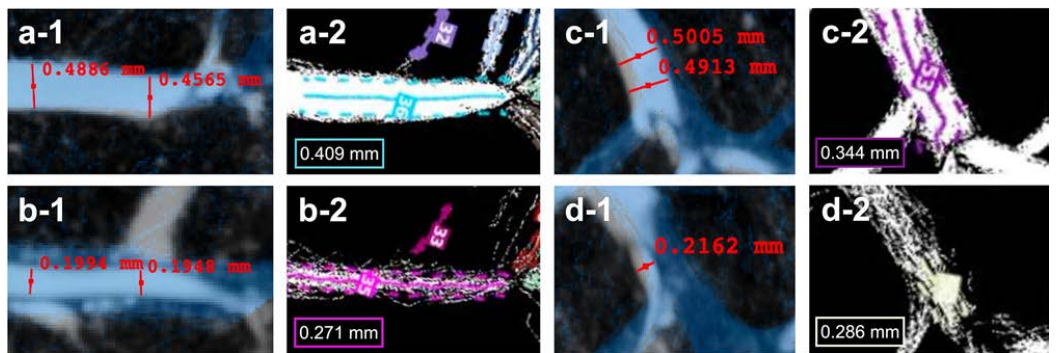


Figure 5. Examples of vessel diameter measurements. (a-1) Arcuate vein in the μ CT with blue super-resolution ultrasound image overlap, shows diameter measurements of 0.489 mm and 0.457 mm. (a-2) Corresponding vessel in the microbubble track map showing a mean diameter, estimated around the turquoise centerline, of 0.409 mm. (b-1) shows the arcuate artery paired with (a-1) with diameter measurements of 0.199 mm and 0.195 mm. (b-2) Corresponding vessel in the microbubble track map showing a mean diameter estimation of 0.271 mm. (c-1) Another example of an arcuate vein in the μ CT with diameter measurements of 0.501 mm and 0.491 mm. (c-2) Corresponding microbubble track map with a mean diameter estimation of 0.344 mm. (d-1) Paired arcuate artery in the μ CT with diameter measurements of 0.216 mm. (d-2) Corresponding artery in the microbubble track map with estimated diameter of 0.286 mm.

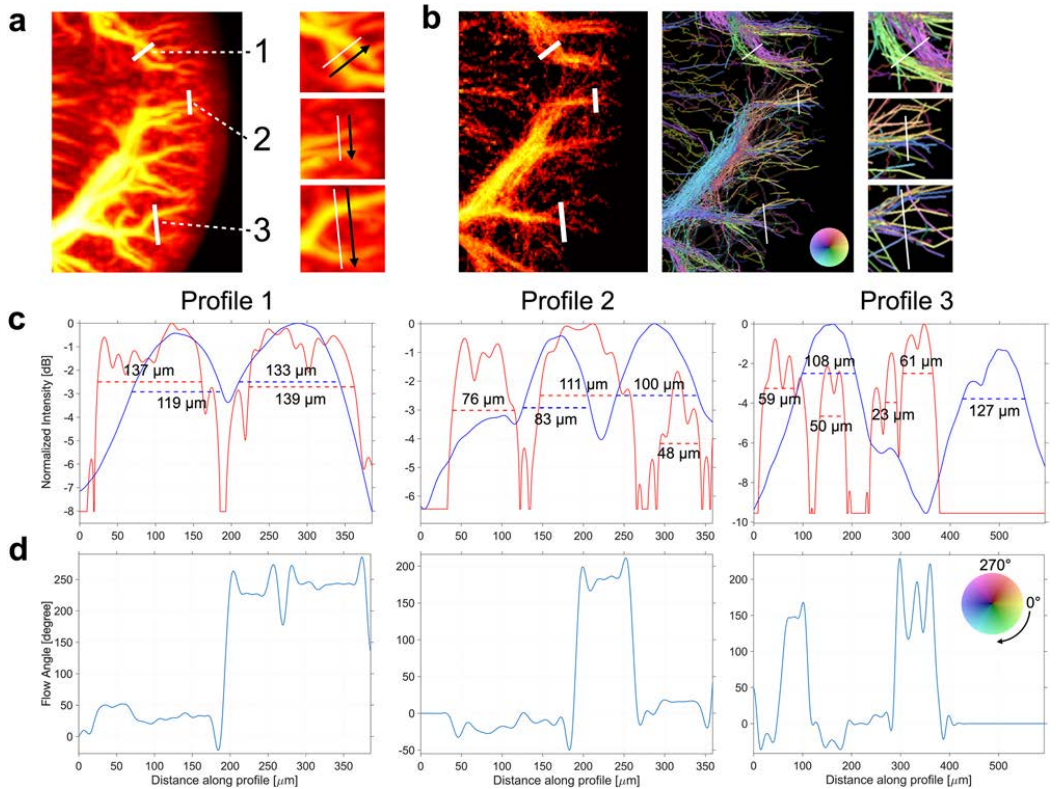


Figure 6. Line intensity profile examples. (a) μ CT maximum intensity projection (MIP) with three lines for profile intensity placed across different vessels. The arrows indicate the direction of the profiles. (b) Corresponding super-resolution ultrasound intensity map (left) and microbubble track map (right). For visualization, the color transparency in the microbubble track map is scaled by the intensity map; this scaling is not applied in the zoomed-in boxes and for the intensity profiles. (c) Shows the three intensity profiles. The blue line is the μ CT MIP intensity profile, the red line is the super-resolution ultrasound intensity profile. The super-resolution ultrasound intensity profile is scaled according to the μ CT intensity. The size shows the -3 dB width of the vessels. (d) Shows the angle of the flow for the super-resolution ultrasound image profiles. This reveals opposite flow directions, separating artery and vein tracks.

2 shows two veins. The corresponding SRUS image profile indicates three arteries and only one vein crossing that same profile line. Again, the veins were not individually resolved in the SRUS image. In addition, it was not possible to verify whether the artery MB tracks represented one or more arteries or whether some were false tracks, again due to the μ CT voxel size. For profile 3, the two veins were spatially further apart and displayed in both intensity profiles, along with arteries in the SRUS intensity profile. Lastly, profiles 2 and 3 also revealed how the global transform-based co-registration led to vessels that did not overlap completely; both μ CT intensity profiles are shifted slightly right to the corresponding SRUS image intensity profiles.

A rotation of the μ CT vessel centerlines revealed the complexity of the 3D vessel structure captured in the 2D SRUS images; Fig. 7 illustrates how multiple vessels lay displaced from each other, winding in the elevational plane of the ultrasound beam, putting further emphasis on the challenge of tracking intravascular MBs in a 2D imaging space.

Figure 7 also demonstrates that not only are the cortical structures difficult to capture in 2D, but vessels that are uniform and placed in parallel, such as the vasa recta, pose certain challenges too. Within the SRUS image and μ CT overlap of scan 1, we found up to nine individual superposed vasa recta bundles in the μ CT that could reasonably contribute with a microbubble track to a single SRUS image pixel (Supplementary Fig. S3). Therefore, the vasa recta depicted in the SRUS images were likely a summation from a couple or more different vasa recta bundles.

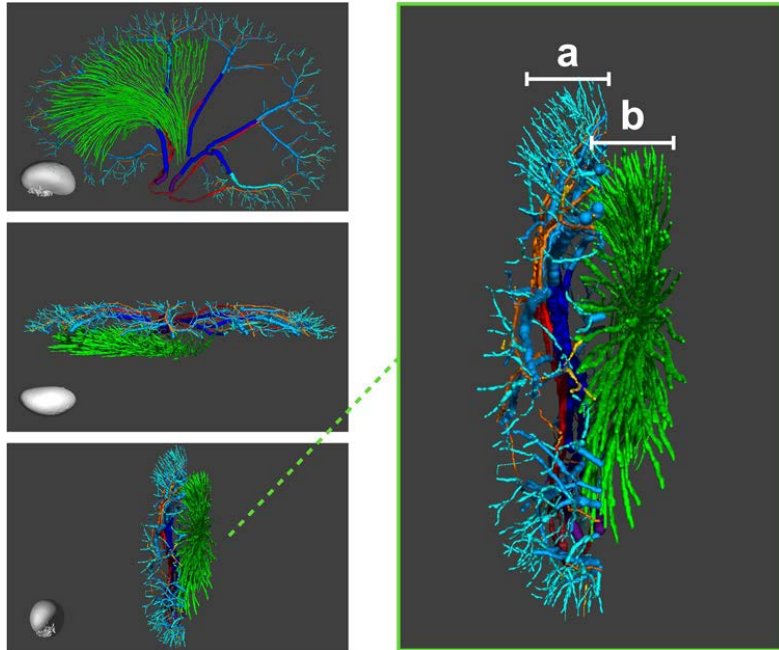


Figure 7. 3D illustration with rotation of the manually drawn vessel centerlines in the μ CT. The 3D illustration shows the vasa recta bundles (green, descending and ascending vasa recta are not distinguishable), and larger arteries and veins (purple = renal vein branches, dark blue = segmental veins, blue = arcuate veins, turquoise = cortical radial veins, dark red = renal artery branches, red = segmental arteries, orange = arcuate arteries, yellow = cortical radial arteries). Insert: (a) shows the μ CT vessel centerlines in super-resolution ultrasound scan 2 overlap. (b) shows approximately half of the well-resolved vasa recta segmented in the μ CT in the super-resolution ultrasound scan 1 overlap.

Discussion

SRUS has been developed for in vivo studies of both the healthy and diseased microvasculature and shows a great clinical potential^{3,9,10,22,23,30,31}. The technique offers a fast investigation of the microvascular architecture, gives quantitative MB velocity estimates as a surrogate measure for microvascular blood flow velocity, and is adaptable to humans. However, due to the high complexity of the microvascular systems³², comparing the structures depicted in the microbubble-based SRUS images with other microvessel imaging modalities and showing their similarities would further support the technique. In this study, we compared two in vivo 2D SRUS images of a rat kidney with the corresponding MIPs from an ex vivo μ CT scan of the same kidney. The two imaging modalities showed visually very similar vascular features, illustrating a high vessel branching complexity captured in the 2D SRUS images. The results also illustrated critical challenges in validating SRUS with ex vivo μ CT at the given resolution quantitatively. In this feasibility study, the presented vessel overlap percentages represent a natural initial attempt. In order to appreciate these scores and their uncertainty, it is important to note the many factors that influence them. Firstly, the comparison included primarily the segmental and larger arcuate vessels, i.e., vessels ranging from ~ 100 to 1300 μ m in diameter. Validating vessels below our ultrasound system's diffraction limit (half the ultrasound wavelength) would mean validating small vessels spatially closer than ~ 125 μ m, which we did not achieve, primarily due to the insufficient resolution of the μ CT used in this study. Secondly, only a single specimen was included. Including more specimens in a larger-scaled study is required to estimate the statistical variation in the overlap measures. Shifting the μ CT ROIs used for comparison could provide some insight into how sensitive the overlap measures are to proper co-registration. However, without a procedure to do this systematically, i.e., having a complete annotation of all vessels in the μ CT, deciding the right kind of ROI displacement type and length is challenging, and it would be hard to draw any conclusions from such an analysis. Therefore, the μ CT ROI mirroring was our only feasible option for this initial study. Lastly, manual labeling is time-consuming and not suited for neither larger-scaled studies nor whole specimen vessel annotation. The lack of automatic approaches for evaluating microvascular network organizations is a bottleneck for taking the SRUS validation to the next level^{33,34}.

For future studies, validating microvascular structures such as afferent arterioles or single vasa recta within the vessel bundles will require optimizing both the SRUS images and the μ CT resolution. The low contrast-to-noise

ratio in our SRUS data resulted in some disorganized trajectories in the unfiltered SRUS images, especially in the renal cortex, as evident from Fig. 1b-1,c-1. Given that the SRUS images were obtained *in vivo* with a modified but commercial ultrasound scanner, this is still a substantial improvement compared with previously available techniques for rodent kidney imaging. However, a higher contrast-to-noise ratio is needed to detect and track the MBs more accurately to improve the image quality for the smaller vessels in the cortex. Since the renal cortex has a high blood flow compared with the medulla, improvements in MB tracking in the cortex could be obtained by, e.g., lowering the MB concentration further or increasing the transmission frequency^{11,12}. Related to the μ CT, we demonstrated the challenging task of capturing the vasculature in a whole organ, as image resolution and field of view are inversely correlated. We chose to include the entire kidney in the μ CT scan to match the SRUS images. Image comparisons can be made at a 5–10 μ m scale using a smaller isometric voxel size in a selected smaller region of the kidney^{24,26}. In Zhu et al.²¹, they used a 4- μ m voxel image to compare vessel size distribution in whole rabbit lymph nodes, which is possible because the lymph nodes are much smaller than the rat kidneys. However, even at this level, the renal cortical arteries and arterioles can still be difficult to dissolve given their small size and often close parallel run with the large veins, as exemplified by Nordsletten et al., where a 4- μ m voxel image was inadequate for resolving all the cortical arteries and arterioles³⁵. Nonetheless, this possibility should still be investigated in future research, and new synchrotron imaging will enable the necessary high resolution in a large volume³⁶. We labeled the vessels in the μ CT in an antegrade manner, starting from the segmental arteries and veins. A commonly used method for organizing the structural information in the vascular networks is the Strahler Ordering, where the vessels are labeled retrogradely, as the resulting vessel categories have shown to correlate well with the vessel radii^{35,37,38}. For our study, the antegrade labeling was considered sufficient, but for future studies with a more detailed categorization of the renal vascular tree, i.e., how the cortical radial arteries branch, a Strahler approach should be considered.

The percentage of image overlap was higher for the veins than the arteries, which a number of factors can explain: Firstly, the veins are voluminous compared with the arteries, and the number of veins segments was six times higher than artery segments. As the μ CT ROIs represent only the well-resolved vessels, the arterial tree was not fully appreciated³⁵. Secondly, the images were manually co-registered with a global similarity transformation. Due to tissue deformation during *ex vivo* specimen preparation, and the fact that the thick SRUS image slices had to fit across roughly 80 thinner μ CT image slices, the overlap was not perfect, as exemplified in Fig. 5c-1. Even a small incongruence in the image registration affects the vessel overlap percentage, although the same vessels are there. Lastly, we compared two fundamentally different imaging modalities. Each of the modalities attained the 2D-projected representations of the 3D vascular structures differently, which inevitably will lead to incomplete vessel overlap³⁹.

We also compared vessel diameter measurements from two larger, paired arcuate arteries and veins, as shown in Fig. 5. These examples pointed toward underestimating the SRUS-derived vein diameters and overestimating the artery diameters compared with those from the μ CT. However, vessel diameters from both imaging modalities are likely to diverge from the actual *in vivo* vessel diameters. For the μ CT images, the *ex vivo* specimen preparation changes vessel proportions due to removing the effect of neural or chemical signals that cause either vessel constriction or dilation. Additional factors such as tissue swelling, perfusion pressure during contrast administration, and the effect of contrast curing and paraffin embedding will affect the vessel dimensions^{40,41}. Moreover, a smaller isometric voxel size is necessary for a more precise vessel delimitation. The dilated vessel centerlines from the μ CT were not used for vessel size estimation but only for creating ROIs in which we expected to find MB tracks. A more systematic direct comparison of specific vessel diameters using μ CT is a more elaborate procedure that would require corresponding branching points and vessel segments to be identified: an arduous task when working with 2D SRUS, where individual vessels overlap. For the SRUS images, when the MB localization is subject to uncertainty, so are the SRUS-derived vessel diameters. Additionally, the diameter of a given vessel relies on the number of MBs passing through^{11–14}. For simplicity, we used *4 s.d.* as a measure for the diameter. Other approaches could be investigated in future studies. In a recent SRUS study, the Euclidean distance from a vessel centerline to the nearest point on the vessel border was used²⁰. The vessel diameter is an essential physiological metric. Using diameters to calculate blood flow metrics such as vascular resistance requires meticulous and accurate measurements, as even minor variations in diameter substantially affect the results. As for now, the diameter measurements from the SRUS images do not seem useful in examining acute and delicate vessel caliber changes but have the potential to give relevant information when examining chronic diseases with vascular alterations together with metrics such as vessel density, branching, or tortuosity^{3,9,10,25,32}. Finally, even though different 2D approaches have been used to examine microvascular alterations^{3,9,10,42,43}, and can give meaningful insight into disease progression and treatment responses, only 3D imaging will truly grasp the pathological alterations that occur in the microvascular anatomy^{25,44}. 3D acquisition of SRUS data will also aid MB tracking by accounting for the elevational dimension of the MB flow^{15,20,21,45,46}. For 2D SRUS used on a microvascular disease model, a great advantage of using 3D μ CT for comparison is the possibility to confirm any 2D-derived pathological microvascular parameters³².

Even if we succeeded with validating vessels below the diffraction limit, these might still be relatively large vessels, such as the cortical radial arteries; however, the medullary and cortical microvasculature comprise the clinically interesting areas of the kidney. The renal microvessels are all in size range of 20 μ m and smaller, and they are densely packed in a complex 3D network, making them very difficult to isolate with SRUS. Our results did show an apparent visual similarity in the vascular patterns of the medullary vasa recta between the two imaging modalities, and SRUS allowed differentiation between the descending and ascending vessels. However, we could not quantify their similarity as described in the “Results” section. The vasa recta are 20- μ m vessels organized in vascular bundles, and they are clinically interesting, as they are central for diluting and concentrating urine. Further, they supply the part of the kidney most vulnerable to ischemic damage: the outer medulla. Thus, they are central in the development of acute and chronic renal failure^{47–49}. Medullary oxygen deficiency is also suspected

to be part of diseases predisposing to renal failure, e.g., diabetes and hypertension. All things considered, further knowledge on medullary perfusion is clinically desirable. It was also clear from the results that tracking MBs from complex 3D vessel networks in 2D is challenging. Studies on optimizing MB tracking to best link the MBs in sequential image frames have been essential for improving the final SRUS image^{19,50–52}. Depending on the elevation depth of the ultrasound beam, the SRUS images will include multiple vessels winding and lying displaced in front of each other in the elevational plane, as shown in Fig. 7. Therefore, when the MB contrast data are processed in a 2D image space, MB trajectories that appear as one vessel can represent a sum of several overlapping vessels, as demonstrated with the vasa recta in Supplementary Fig. S3, or two neighboring vessels, as demonstrated in Fig. 6. Additionally, MBs that traverse in overlapping vessels can be wrongfully linked as a non-existing vessel, especially in areas with dense vasculature and a high MB concentration. Consequently, the challenge in the future is how to grasp the complexity of closely related and intertwined microvessels, such as those in the renal cortical network with the afferent and efferent arterioles entering and exiting the glomerulus and the surrounding densely masked peritubular capillary network^{24,53}. The microvasculature of the renal cortex is—like the vasa recta—essential in the maintenance of various kidney functions, e.g., the afferent and efferent arterioles affect the hydrostatic pressure within the glomerular capillaries and thereby the glomerular filtration; the production of renin from the afferent arterioles helps regulate the arterial blood pressure; and the peritubular capillaries that travel along the renal tubules allow absorption of water and solutes and secretion of organic solutes together with the vasa recta. These cortical vascular components are affected in a range of renal diseases, e.g., diabetic nephropathy^{7,8,54}, hypertensive nephropathy⁵⁵, and arteriosclerosis⁵⁶, ultimately decreasing renal function.

In conclusion, this feasibility study showed that *in vivo* SRUS images correspond visually very well with *ex vivo* μ CT of the same rat kidney. It was also shown that it is challenging to use μ CT data at the chosen resolution to validate the super-resolution capability of ultrasound, i.e., validating vessels in the actual microvasculature of the kidneys. Critical challenges in 2D SRUS were identified, e.g., the complexity of projecting a 3D vessel network into 2D; these challenges should be considered when interpreting clinical or preclinical SRUS data in future studies.

Materials and methods

Ethical considerations. The reporting in this manuscript follows the recommendations in the ARRIVE guidelines. The experiment was conducted in agreement with approved protocols (approval granted from the Danish Animal Experiments Inspectorate under the Ministry of Environment and Food, Denmark). The SRUS scans and μ CT specimen preparation were performed at the University of Copenhagen, and all procedures agreed with the ethical standard of the university, which meets that of the EU Directive 2010/63/EU for animal experiments. The study was conducted on a healthy male Sprague–Dawley rat (weight: 330 g, Janvier Labs, Le Genest-Saint-Isle, France). The rat was housed at the university's animal facility at the Department of Experimental Medicine, where animal caretakers were responsible for its wellbeing. The rat was housed in the company of another rat and held in a 12/12-h light/dark cycle with standard chow and water freely accessible.

***In vivo* super-resolution ultrasound imaging.** The rat was scanned during laparotomy. The rat was anesthetized in a small chamber with 5% isoflurane delivered in 65% nitrogen and 35% oxygen. Ventilation was secured through a tracheostomy tube connected to a mechanical ventilator (Ugo Basile, Gemonio, Italy) with 69 respirations/min. A 2% isoflurane concentration upheld the anesthesia. The left jugular vein was catheterized with two polyethylene catheters (PE-10) for infusion of ultrasound contrast (SonoVue, Bracco Imaging, Milan, Italy) and isotonic saline with the muscle relaxant Nimblex (cisatracurium, 0.85 mg/ml, GlaxoSmithKline, London, United Kingdom, 20 μ l/min). A polyethylene catheter (PE-50) in the left carotid artery and a Satham P23-dB pressure transducer (Gould, Oxnard, CA, USA) ensured continuous monitoring of the mean arterial pressure (MAP). The rat was placed in the supine position on a heating table to ensure a steady body temperature (37 °C). Laparotomy exposed the left kidney, and a metal retractor kept the left side of the diaphragm, ventricle, and spleen away from the kidney. The rat was scanned with a BK5000 scanner and an X18L5s hockey-stick transducer (BK Medical ApS, Herlev, Denmark). The scanner was modified to allow live streaming of beam-formed radio-frequency data to a disk. Two different coronal imaging planes were found with B-mode image guidance: One imaging plane in the renal center showing the medulla's vasa recta (scan 1), and one imaging plane more ventrally showing the segmental and larger arcuate arteries and veins (scan 2). After adjustment of the image plane, the transducer was fixated with a stand. A pump infused the 1:15 dilution of MBs in isotonic saline at 100 μ l/min. The infusion was adjusted to have isolated MBs for localization and tracking (a video of the microbubble signal from SRUS scan 1 can be seen in Supplementary Video S4). Data acquisition started when the MBs reached the renal vasculature. Each SRUS scan was acquired over 10 min. Data were acquired with line-per-line focused beam transmission (frame rate: 54 Hz, center frequency for transmission: 6 MHz, mechanical index: 0.2). An amplitude modulation sequence (half-power, full-power, half-power) generated the contrast images, and interleaved B-mode images were used for motion compensation. Non-rigid motion was estimated with speckle tracking in the renal tissue. The motion was compensated using the displacement estimates to adjust each MB back to its location on a reference image^{57,58}. MBs were localized using thresholding and centroid detection, and MB trajectories were made using a modified Kalman tracker⁵² (maximum linking distance: 278 μ m). Only trajectories of MBs that were observed in at least three consecutive frames were considered a track). Afterward, the trajectories were inserted in high-resolution images to generate the SRUS images. The MB direction was displayed in color-coded MB track maps with a color wheel indicating the direction for a distinction between arterial and venous flow. Brighter colors correspond to faster MB velocities.

Ex vivo μ CT imaging. After SRUS, ligatures were prepared around the left renal artery, renal vein, and ureter as well as the aorta both in the caudal part for catheter fixation and above the left renal artery but below the right renal artery. The rat was heparinized (Heparin “SAD” 1000 IE/ml, Amgros, Copenhagen, Denmark) with 1000 IE/kg intravenously. Once heparinized, the abdominal aorta was catheterized with a PE-50 catheter with the catheter tip placed at the left renal artery, and the ligature around the aorta above the left renal artery was tightened. A ligature near the inferior vena cava occluded the left renal vein, and a small hole cut in the vein allowed the injection media to leave the renal vasculature. The left kidney was perfused with 8 ml heparinized saline (1000 IE/ml heparin diluted 1:100 in isotonic saline) at 2 ml/min. The heparin solution was pre-heated to 40 °C. The flushing continued until only clear saline ran from the renal vein. During the renal vascular flushing, the rat was euthanized by decapitation. Directly after flushing, 3 ml of μ Angiofil contrast agent and hardener mixed according to the manufacturer’s guidelines (Fumedica AG, Muri, Switzerland) was infused at 1 ml/min^{36,40}. The infusion continued until the entire surface of the kidney was blue, and a considerable amount of contrast had left the renal vein. The kidney was left for 30 min, allowing contrast hardening. Afterward, the kidney was excised, decapsulated and fixated in formaldehyde, followed by embedment in paraffin in a custom-made cylinder-shaped holder. The kidney was scanned for 11 h in a ZEISS XRadia 410 Versa μ CT scanner (Carl Zeiss Microscopy GmbH, Jena, Germany) at the following settings: isotropic voxel size 22.6 μ m, 50 kV tube voltage, 0.2 mA current, apertaining LE3 filter, 360° scan around the vertical axis with 3201 different projections (0.112° rotation steps).

Image co-registration and analysis. To obtain images from the μ CT volume with the same vessels as the SRUS images, we made MIPs of the μ CT slices approximately covering the volume depicted in the SRUS images. Prior to co-registration, the 2D SRUS images were assigned a constant elevation depth of 1.8 mm, such that each SRUS image was approximated as a rectangular field-of-view of 15.3 \times 21.5 \times 1.8 mm. The SRUS scans were manually co-registered to the μ CT volume using ITK-SNAP (version 3.8.0)⁵⁹. Due to tissue deformation during μ CT specimen preparation, a local non-rigid registration would be ideal. Differences in resolutions, fields of view, contrast mechanisms and the 2D vs 3D nature of the problem would make this a challenging task, requiring a detailed study on its own. Restricted to a global transformation, we allowed for translation, rotation and scaling to achieve a visually satisfying agreement. From this, we calculated the MIPs of the μ CT within the SRUS overlaps (in the direction of the elevation plane). Afterward, vessel centerlines were manually drawn and labeled in the μ CT in the SRUS image overlaps. The included vessels were the visible, contrast-filled segmental, arcuate and cortical radial arteries and veins found in the SRUS image overlap of scan 2, and the cranial half of the vasa recta visible in the overlap of SRUS scan 1⁶⁰. Each centerline was found manually using the three different imaging planes (coronal, sagittal, and axial). Depending on the orientation of the vessel, the plane where the vessel appeared most circular (in cross section) was used to find the approximate center. The μ CT centerlines were drawn slice by slice starting from the renal artery and vein branches in the hilum in an antegrade manner ending in the cortical radial vessels. The vessels were separated into arteries and veins at this level, based on their size: the veins have a substantially larger diameter than their paired artery (illustrated in Fig. 4b). All the centerlines from the 3D μ CT were projected into the coordinate system of the 2D SRUS images using the inverse similarity transform from the co-registration. To cover the contrast-filled areas, the transformed μ CT centerlines were dilated based on approximate expected vessel diameters. The expected diameters were extracted from selected examples of diameter measurements of the segmental, arcuate, and cortical radial arteries and veins at different branching levels on the μ CT. From this, one ROI with all the arteries and one ROI with all the veins were created for the vessel overlap estimations.

On the SRUS scans, different regions were marked and labeled into either “segmental or larger arcuate vessels”, “cortex” (including all vessels that were located superficially to the larger arcuate vessels that traverse on the border between cortex and medulla; hence, this region could include smaller branches of arcuate vessels, the cortical radial vessels, and possibly also tracks from the renal microvasculature), “outer medulla”, or “inner medulla” using *MATLAB* (Math Works, Inc., version R2020b). Each label consisted of several smaller regions in which the arterial flow direction was determined, which allowed separation of artery and vein MB trajectories. An example of these regions can be seen in Supplementary Fig. S5. In scan 2, the vessel centerlines of well-defined MB trajectories in the filtered MB track maps of the arteries and veins, respectively, were manually plotted.

For scan 2, we compared vessel overlap: Firstly, the percentage of vessel centerlines from the MB track maps that were recovered within the μ CT vessel ROIs was calculated separately for the veins and arteries. Secondly, because the well-defined bundles of MB trajectories in the MB track maps that were used to manually draw the vessel centerlines represented primarily larger vessel, thereby excluding the smaller cortical MB tracks, the percentage of the area with MB tracks (all non-zero pixels in the filtered track map) covered by the μ CT vessel ROIs was also calculated. Additionally, examples of vessel diameters were compared. In the μ CT scan, the diameters were manually measured in ITK-SNAP. For the SRUS images, based on the assumption that vessels have a tubular structure with a Gaussian profile, a simplistic measure for vessel diameter was considered as 4 *s.d.* of the MB’s positions around the centerline for the specific vessel. These centerlines were automatically extracted based on the skeleton of the artery and vein track maps in each of the labeled regions.

Equipment and settings. All the SRUS images in Figs. 1, 2, 3, 4, 5, and 6, the μ CT images in Figs. 1, 2, 3, and 6 (including the μ CT volumes of the kidney in Fig. 1a), and the supplementary figures and video were created in *MATLAB* (version R2019b and R2020b, Mathworks, U.S.). The μ CT images with SRUS image overlap in Figs. 4 and 5 were created in ITK-SNAP (version 3.8.0)⁵⁹. The rendering of the μ CT segmentation in Fig. 7 was done with Blender (version 2.91, www.blender.org). All the figures were gathered, set up, and annotated in Keynote (version 10.3.8, Apple Inc).

Data availability

Raw data and image processing algorithms can be exchanged through a collaboration agreement. Processed data and analysis algorithms can be made available upon request.

Received: 10 May 2021; Accepted: 8 December 2021

Published online: 21 December 2021

References

- Errico, C. *et al.* Ultrafast ultrasound localization microscopy for deep super-resolution vascular imaging. *Nature* **527**, 499–502 (2015).
- Foiret, J. *et al.* Ultrasound localization microscopy to image and assess microvasculature in a rat kidney. *Sci. Rep.* **7**, 13662 (2017).
- Chen, Q. *et al.* Ultrasound super-resolution imaging provides a noninvasive assessment of renal microvasculature changes during mouse acute kidney injury. *Kidney Int.* **98**, 355–365 (2020).
- Kierski, T. M. *et al.* Superharmonic ultrasound for motion-independent localization microscopy: Applications to microvascular imaging from low to high flow rates. *IEEE Trans. Ultrason. Ferroelectr. Freq. Control* **67**, 957–967 (2020).
- Andersen, S. B. *et al.* Super-resolution imaging with ultrasound for visualization of the renal microvasculature in rats before and after renal ischemia: A pilot study. *Diagnostics* **10**, 862 (2020).
- Christensen-Jeffries, K. *et al.* Super-resolution ultrasound imaging. *Ultrasound Med. Biol.* **46**, 865–891 (2020).
- Scurt, F. G. *et al.* Systemic Inflammation precedes microalbuminuria in diabetes. *Kidney Int. Rep.* **4**, 1373–1386 (2019).
- Maric-Bilkan, C., Flynn, E. R. & Chade, A. R. Microvascular disease precedes the decline in renal function in the streptozotocin-induced diabetic rat. *Am. J. Physiol. Physiol.* **302**, F308–F315 (2012).
- Lowerison, M. R., Huang, C., Lucien, F., Chen, S. & Song, P. Ultrasound localization microscopy of renal tumor xenografts in chicken embryo is correlated to hypoxia. *Sci. Rep.* **10**, 1–3 (2020).
- Opacic, T. *et al.* Motion model ultrasound localization microscopy for preclinical and clinical multiparametric tumor characterization. *Nat. Commun.* **9**, 1527 (2018).
- Hingot, V. *et al.* Microvascular flow dictates the compromise between spatial resolution and acquisition time in Ultrasound Localization Microscopy. *Sci. Rep.* **9**, 2456 (2019).
- Christensen-Jeffries, K. *et al.* Poisson statistical model of ultrasound super-resolution imaging acquisition time. *IEEE Trans. Ultrason. Ferroelectr. Freq. Control* **66**, 1246–1254 (2019).
- Lowerison, M. R. *et al.* In vivo confocal imaging of fluorescently labeled microbubbles: Implications for ultrasound localization microscopy. *IEEE Trans. Ultrason. Ferroelectr. Freq. Control* **67**, 1811–1819 (2020).
- Dencks, S., Piepenbrock, M. & Schmitz, G. Assessing vessel reconstruction in ultrasound localization microscopy by maximum likelihood estimation of a zero-inflated poisson model. *IEEE Trans. Ultrason. Ferroelectr. Freq. Control* **67**, 1603–1612 (2020).
- Jensen, J. A. *et al.* Three-dimensional super-resolution imaging using a row-column array. *IEEE Trans. Ultrason. Ferroelectr. Freq. Control* **67**, 538–546 (2020).
- Ommen, M. L. *et al.* 3D printed calibration micro-phantoms for super-resolution ultrasound imaging validation. *Ultrasonics* **114**, 106353 (2021).
- Christensen-Jeffries, K., Browning, R. J., Tang, M. X., Dunsby, C. & Eckersley, R. J. In vivo acoustic super-resolution and super-resolved velocity mapping using microbubbles. *IEEE Trans. Med. Imaging* **34**, 433–440 (2015).
- Huang, C. *et al.* Short acquisition time super-resolution ultrasound microvessel imaging via microbubble separation. *Sci. Rep.* **10**, 1–13 (2020).
- Tang, S. *et al.* Kalman filter-based microbubble tracking for robust super-resolution ultrasound microvessel imaging. *IEEE Trans. Ultrason. Ferroelectr. Freq. Control* **67**, 1738–1751 (2020).
- Ozdemir, I. *et al.* Three-dimensional visualization and improved quantification with super-resolution ultrasound imaging: Validation framework for analysis of microvascular morphology using a chicken embryo model. *Phys. Med. Biol.* **66**, 085008 (2021).
- Zhu, J. *et al.* 3D super-resolution US imaging of rabbit lymph node vasculature in vivo by using microbubbles. *Radiology* **291**, 642–650 (2019).
- Chen, Q. *et al.* Validation of ultrasound super-resolution imaging of vasa vasorum in rabbit atherosclerotic plaques. *IEEE Trans. Ultrason. Ferroelectr. Freq. Control* **67**, 1725–1729 (2020).
- Demené, C. *et al.* Transcranial ultrafast ultrasound localization microscopy of brain vasculature in patients. *Nat. Biomed. Eng.* **5**, 219–228 (2021).
- Wagner, R. *et al.* High-resolution imaging of kidney vascular corrosion casts with nano-CT. *Microsc. Microanal.* **17**, 215–219 (2011).
- Ehling, J. *et al.* Quantitative micro-computed tomography imaging of vascular dysfunction in progressive kidney diseases. *J. Am. Soc. Nephrol.* **27**, 520–532 (2016).
- Hlushchuk, R. *et al.* Cutting-edge microangi-CT: New dimensions in vascular imaging and kidney morphometry. *Am. J. Physiol. Physiol.* **314**, F493–F499 (2018).
- Marsh, D. J. *et al.* Architecture of the rat nephron-arterial network: Analysis with micro-computed tomography. *Am. J. Physiol. Ren. Physiol.* **313**, F351–F360 (2017).
- Xie, L. *et al.* Micro-CT imaging and structural analysis of glomeruli in a model of adriamycin-induced nephropathy. *Am. J. Physiol. Ren. Physiol.* **316**, F76–F89 (2019).
- Vasquez, S. X. *et al.* Optimization of MicroCT imaging and blood vessel diameter quantitation of preclinical specimen vasculature with radiopaque polymer injection medium. *PLoS ONE* **6**, e19099 (2011).
- Yu, J., Lavery, L. & Kim, K. Super-resolution ultrasound imaging method for microvasculature in vivo with a high temporal accuracy. *Sci. Rep.* **8**, 13918 (2018).
- Qian, X. *et al.* Super-resolution ultrasound localization microscopy for visualization of the ocular blood flow. *IEEE Trans. Biomed. Eng.* <https://doi.org/10.1109/TBME.2021.3120368> (2021).
- Corliss, B. A., Mathews, C., Doty, R., Rohde, G. & Peirce, S. M. Methods to label, image, and analyze the complex structural architectures of microvascular networks. *Microcirculation* **26**, e12520 (2019).
- Lee, J., Beighley, P., Ritman, E. & Smith, N. Automatic segmentation of 3D micro-CT coronary vascular images. *Med. Image Anal.* **11**, 630–647 (2007).
- Sled, J. G., Marxen, M. & Henkelman, R. M. Analysis of microvasculature in whole kidney specimens using micro-CT. *Dev. X-Ray Tomography IV* **5535**, 53 (2004).
- Nordsletten, D. A., Blackett, S., Bentley, M. D., Ritman, E. L. & Smith, N. P. Structural morphology of renal vasculature. *Am. J. Physiol. Hear. Circ. Physiol.* **291**, 296–309 (2006).
- Walsh, C. L. *et al.* Imaging intact human organs with local resolution of cellular structures using hierarchical phase-contrast tomography. *Nat. Methods* **18**, 1532–1541 (2021).
- Horsfield, K. Morphometry of the small pulmonary arteries in man. *Circ. Res.* **42**, 593–597 (1978).
- Horsfield, K. Diameters, generations, and orders of branches in the bronchial tree. *J. Appl. Physiol.* **68**, 457–461 (1990).

39. Minnich, B., Bartel, H. & Lametschwandtner, A. Quantitative microvascular corrosion casting by 2D- and 3D-morphometry. *Ital. J. Anat. Embryol.* **106**, 213–220 (2001).
40. Schaad, L. *et al.* Correlative imaging of the murine hind limb vasculature and muscle tissue by MicroCT and light microscopy. *Sci. Rep.* **7**, 1–12 (2017).
41. Ngo, J. P. *et al.* Micro-computed tomographic analysis of the radial geometry of intrarenal artery-vein pairs in rats and rabbits: Comparison with light microscopy. *Clin. Exp. Pharmacol. Physiol.* **44**, 1241–1253 (2017).
42. Zudaire, E., Gambardella, L., Kurcz, C. & Vermeren, S. A computational tool for quantitative analysis of vascular networks. *PLoS ONE* **6**, e27385 (2011).
43. Seaman, M. E., Peirce, S. M. & Kelly, K. Rapid analysis of vessel elements (RAVE): A tool for studying physiologic, pathologic and tumor angiogenesis. *PLoS ONE* **6**, 20807 (2011).
44. Ehling, J. *et al.* Micro-CT imaging of tumor angiogenesis: Quantitative measures describing micromorphology and vascularization. *Am. J. Pathol.* **184**, 431–441 (2014).
45. Harput, S. *et al.* 3-D super-resolution ultrasound imaging with a 2-D sparse array. *IEEE Trans. Ultrason. Ferroelectr. Freq. Control* **67**, 269–277 (2020).
46. Heiles, B. *et al.* Ultrafast 3D ultrasound localization microscopy using a 32×32 matrix array. *IEEE Trans. Med. Imaging* **38**, 2005–2015 (2019).
47. Fischer, K. *et al.* High-resolution renal perfusion mapping using contrast-enhanced ultrasonography in ischemia-reperfusion injury monitors changes in renal microperfusion. *Kidney Int.* **89**, 1388–1398 (2016).
48. Pohlmann, A. *et al.* High temporal resolution parametric MRI monitoring of the initial ischemia/reperfusion phase in experimental acute kidney injury. *PLoS ONE* **8**, e57411 (2013).
49. Munshi, R., Hsu, C. & Himmelfarb, J. Advances in understanding ischemic acute kidney injury. *BMC Med.* **9**, 11 (2011).
50. Solomon, O., Van Sloun, R. J. G., Wijkstra, H., Mischi, M. & Eldar, Y. C. Exploiting flow dynamics for superresolution in contrast-enhanced ultrasound. *IEEE Trans. Ultrason. Ferroelectr. Freq. Control* **66**, 1573–1586 (2019).
51. Song, P. *et al.* Improved super-resolution ultrasound microvessel imaging with spatiotemporal nonlocal means filtering and bipartite graph-based microbubble tracking. *IEEE Trans. Ultrason. Ferroelectr. Freq. Control* **65**, 149–167 (2018).
52. Taghavi, I. *et al.* Tracking performance in ultrasound super-resolution imaging. In *Proc. IEEE Ultrason. Symp.* 1–4 (IEEE, 2020).
53. Bankir, L., Bouby, N. & Trinh-Trang-Tan, M.-M. The role of the kidney in the maintenance of water balance. *Baillière's Clin. Endocrinol. Metab.* **3**(2), 249–311 (1989).
54. Thomas, M. C. *et al.* Diabetic kidney disease. *Nat. Rev. Dis. Primers.* **1**, 1–20 (2015).
55. Cirillo, M. *et al.* Pulse pressure and isolated systolic hypertension: Association with microalbuminuria. *Kidney Int.* **58**, 1211–1218 (2000).
56. Chade, A. R. *et al.* Distinct renal injury in early atherosclerosis and renovascular disease. *Circulation* **106**, 1165–1171 (2002).
57. Jensen, J. A. *et al.* Tissue Motion Estimation and Correction in Super Resolution Imaging. In *Proc. IEEE Ultrason. Symp.* 1–4 (IEEE, 2019).
58. Taghavi, I. *et al.* In vivo motion correction in super resolution imaging of rat kidneys. *IEEE Trans. Ultrason. Ferroelectr. Freq. Control* **68**, 3082–3093 (2021).
59. Yushkevich, P. A. *et al.* User-guided 3D active contour segmentation of anatomical structures: Significantly improved efficiency and reliability. *Neuroimage* **31**, 1116–1128 (2006).
60. Kriz, W. *et al.* A standard nomenclature for structures of the kidney. *Kidney Int.* **33**, 1–7 (1988).

Acknowledgements

We kindly thank BK Medical Aps, Herlev, Denmark, for providing the BK5000 ultrasound scanner and X18L5s probe used in this study. We appreciate the technical skills of animal technician Karin Larsen (Department of Biomedical Sciences, University of Copenhagen, Copenhagen, Denmark) who did the animal surgery. The national research infrastructure DANFIX (NUFI Grant Number 5072-00030B) hosted by the 3D Imaging Center at The Technical University of Denmark is gratefully acknowledged for access to X-ray computed tomography equipment. This study was financially supported by Innovation Fund Denmark (Grant Number 7050-00004B), European Research Council's (ERC) Synergy Grant 854796, and by the Center for Quantification of Imaging Data from MAX IV (QIM) funded by The Capital Region of Denmark.

Author contributions

S.B.A., I.T., H.M.K., S.B.S., C.G., V.A.D., M.B.N., A.B.D., J.A.J., and C.M.S. contributed substantially to the conception and design of this work. S.B.A. performed the SRUS scans and prepared the μ CT specimen along with C.M.S. (and K.L., in acknowledgments). C.G. made the μ CT scan. S.B.A. performed image co-registration and drew vessel centerlines in the μ CT scan with guidance from H.M.K. and C.M.S. S.B.A. did vessel labeling on the SRUS scans. J.A.J. and I.T. developed the super-resolution processing pipeline used for processing the SRUS data, and I.T. processed the SRUS data for this study. I.T. programmed tools for labeling the SRUS images. S.B.A., I.T., and H.M.K. did the analyses and prepared the figures in collaboration. S.B.A. wrote the main manuscript text. I.T., H.M.K., S.B.S., C.G., V.A.D., M.B.N., A.B.D., J.A.J., and C.M.S. substantively revised the manuscript text and figures.

Competing interests

The SRUS images were conducted as part of a jointly funded research collaboration between the Department of Biomedical Sciences at the University of Copenhagen, the Department of Radiology at Rigshospitalet, Center for Fast Ultrasound Imaging at the Technical University of Denmark, and BK Medical ApS, Herlev, Denmark. BK Medical has put the modified ultrasound scanner (BK5000) and the probe (X18L5s hockey-stick) at our disposal and owns a patent for the motion compensation algorithm used in the post-processing of the SRUS images, sold to them by J.A.J. and I.T. BK Medical has had no role in the design, data collection, analysis, decision to publish, or preparation of this manuscript. Aside from this, the authors declare no competing interests.

Additional information

Supplementary Information The online version contains supplementary material available at <https://doi.org/10.1038/s41598-021-03726-6>.

Correspondence and requests for materials should be addressed to S.B.A.

Reprints and permissions information is available at www.nature.com/reprints.

Publisher's note Springer Nature remains neutral with regard to jurisdictional claims in published maps and institutional affiliations.



Open Access This article is licensed under a Creative Commons Attribution 4.0 International License, which permits use, sharing, adaptation, distribution and reproduction in any medium or format, as long as you give appropriate credit to the original author(s) and the source, provide a link to the Creative Commons licence, and indicate if changes were made. The images or other third party material in this article are included in the article's Creative Commons licence, unless indicated otherwise in a credit line to the material. If material is not included in the article's Creative Commons licence and your intended use is not permitted by statutory regulation or exceeds the permitted use, you will need to obtain permission directly from the copyright holder. To view a copy of this licence, visit <http://creativecommons.org/licenses/by/4.0/>.

© The Author(s) 2021



Paper 4

Ultrasound Super-Resolution Imaging with a Hierarchical Kalman Tracker

Iman Taghavi, Sofie Bech Andersen, Carlos Villagómez Hoyos, Mikkel Schou, Fredrik Gran, Kristoffer Lindskov Hansen, Michael Bachmann Nielsen, Charlotte Mehlin Sørensen, Matthias Bo Stuart, and Jørgen Arendt Jensen

Name of journal:

Ultrasonics, Elsevier

Document Version:

Accepted

DOI:

—

General rights

Copyright and moral rights for the publications made accessible in the public portal are retained by the authors and/or other copyright owners and it is a condition of accessing publications that users recognise and abide by the legal requirements associated with these rights.

- Users may download and print one copy of any publication from the public portal for the purpose of private study or research.
- You may not further distribute the material or use it for any profit-making activity or commercial gain
- You may freely distribute the URL identifying the publication in the public portal

If you believe that this document breaches copyright please contact us providing details, and we will remove access to the work immediately and investigate your claim.



Ultrasound super-resolution imaging with a hierarchical Kalman tracker[☆]

Iman Taghavi^{a,*}, Sofie Bech Andersen^{b,c,d}, Carlos Armando Villagómez Hoyos^e, Mikkel Schou^a, Fredrik Gran^e, Kristoffer Lindskov Hansen^{c,d}, Michael Bachmann Nielsen^{c,d}, Charlotte Mehlin Sørensen^b, Matthias Bo Stuart^a, Jørgen Arendt Jensen^a

^a Center for Fast Ultrasound Imaging, Department of Health Technology, Technical University of Denmark, DK 2800, Kgs. Lyngby Denmark

^b Department of Biomedical Sciences, University of Copenhagen, DK 2200, Copenhagen, Denmark

^c Department of Diagnostic Radiology, Rigshospitalet, DK 2100, Copenhagen, Denmark

^d Department of Clinical Medicine, University of Copenhagen, DK 2200, Copenhagen, Denmark

^e BK Medical, DK 2730, Herlev, Denmark

ARTICLE INFO

Keywords:

Super-resolution imaging (SRI)
Ultrasound localization microscopy (ULM)
Contrast-enhanced ultrasound (CEUS)
Microbubble tracking
Microscopy

ABSTRACT

Microbubble (MB) tracking plays an important role in ultrasound super-resolution imaging (SRI) by enabling velocity estimation and improving image quality. This work presents a new hierarchical Kalman (HK) tracker to achieve better performance at scenarios with high concentrations of MBs and high localization uncertainty. The method attempts to follow MBs with different velocity ranges using different Kalman filters. An extended simulation framework for evaluating trackers is also presented and used for comparison of the proposed HK tracker with the nearest-neighbor (NN) and Kalman (K) trackers. The HK tracks were most similar to the ground truth with the highest Jaccard similarity coefficient in 79% of the scenarios and the lowest root-mean-square error in 72% of the scenarios. The HK tracker reconstructed vessels with a more accurate diameter. In a scenario with an uncertainty of 51.2 μm in MB localization, a vessel diameter of 250 μm was estimated as 257 μm by HK tracker, compared with 329 μm and 389 μm for the K and NN trackers. In the same scenario, the HK tracker estimated MB velocities with a relative bias down to 1.7% and a relative standard deviation down to 8.3%. Finally, the different tracking techniques were applied to *in vivo* data from rat kidneys, and trends similar to the simulations were observed. Conclusively, the results showed an improvement in tracking performance, when the HK tracker was employed in comparison with the NN and K trackers.

1. Introduction

Ultrasound super-resolution imaging (SRI) has been introduced over the last five years by a number of research groups [1–7]. The approach employs detection and tracking of microbubble (MB) contrast agents to visualize the microvasculature. Identification of early changes in the vessel structure and flow dynamics of the vessels smaller than 100 μm can potentially be used for early diagnosis or monitoring of diseases like cancer [8], diabetes [9], and atherosclerosis [10].

Various pre-clinical and pilot studies have been conducted with SRI of the microvasculature of the kidneys [11–13], brain [5], tumors [8], and lymph nodes [14]. Although the applications, depths, and wavelengths (λ) are quite diverse in these studies, they all estimate the geometric centroid of the MBs with a sub-wavelength accuracy for

SRI. The validation and quantification of *in vivo* super-resolution (SR) images are still major challenges, as no known imaging modality can yield *in vivo* ground truth for the microvasculature.

Several methods have been introduced to validate ultrasound SRI, including comparison with other imaging modalities, like optical imaging [4,15] and micro-CT [16], correlating the processed ultrasound images with histology and Doppler imaging [17], or using micro-flow phantoms [18–20]. Although these methods provide a method for overall validation for the ultrasound SR images, they cannot be used to evaluate tracking performance independently, as only the structural and overall flow values are provided.

Tracking of MBs is an important part of ultrasound SRI, as it improves the final quality of the SR images. Tracking also enables

[☆] This work was financially supported by grant 82-2014-4 from the Danish National Advanced Technology Foundation, by grant 7050-00004B from Innovation Fund Denmark, and BK Medical, Herlev, Denmark.

* Corresponding author.

E-mail addresses: imat@dtu.dk (I. Taghavi), anne.sofie.bech.andersen@regionh.dk (S.B. Andersen), choyos@bkmedical.com (C.A.V. Hoyos), mschou@dtu.dk (M. Schou), fgran@bkmedical.com (F. Gran), Kristoffer.Lindskov.Hansen.01@regionh.dk (K.L. Hansen), mhn@dadlnet.dk (M.B. Nielsen), cmehlin@sund.ku.dk (C.M. Sørensen), mbst@dtu.dk (M.B. Stuart), jaje@dtu.dk (J.A. Jensen).

<https://doi.org/10.1016/j.ultras.2022.106695>

Received 19 May 2021; Received in revised form 18 November 2021; Accepted 19 January 2022

Available online 4 February 2022

0041-624X/© 2022 The Authors. Published by Elsevier B.V. This is an open access article under the CC BY license (<http://creativecommons.org/licenses/by/4.0/>).

the estimation of clinically meaningful parameters, such as blood flow velocity. However, tracking performance degrades in the presence of high MB concentrations and localization uncertainty. As ultrasound SRI was primarily inspired by optical microscopy, many of the optical particle tracking methods have the same potential in ultrasound SRI. These methods range from simple nearest-neighbor (NN) [21] to more advanced techniques. Many of the tracking methods together with different localization methods were objectively compared for various scenarios in [22], and it was shown that tracking based on the Kalman (K) filtering was among the best methods in most of these scenarios; however, none of the methods performed best across all scenarios. In 2015, the first *in vivo* ultrasound SRI with velocity mapping was introduced [4]. Even though the approach used a basic maximum intensity cross-correlation within a small search window, it revealed great potential of resolving flow velocities in vessels located close to each other. At the same time, another study used an NN tracker for the MB velocity estimation [5]. In 2016, a modified version of the Markov chain Monte Carlo data association was implemented for detection and tracking of MBs [6]. In 2017, a partial assignment tracking based on a bipartite graph was proposed in [23]. This improved image quality in comparison with optimal total distance assignment, based on the Hungarian algorithm [24], and cross-correlation based local tracking. Finally, the Kalman-based trackers were employed in ultrasound SRI and used in very recent works in 2019 and 2020 [15,25].

Even though tracking unlabeled targets is well studied, the trackers' performance in velocity estimation and ultrasound SRI has not been determined. The aforementioned studies either evaluated a combination of detection and tracking methods or compared a number of trackers without a ground truth. Moreover, K trackers with only a single initial condition for all MBs with varying lifetime and uncertainties in their localization might not be beneficial in ultrasound SRI. This paper presents a new hierarchical Kalman (HK) tracker for improving the formation of tracks at different MB velocities. The HK tracker benefits from the robustness of the Kalman filter and the flexibility of tracking MBs differently at separate velocity ranges, each with a different initial condition. Moreover, this paper presents an extended evaluation framework for comparing different trackers' performance using simulations with varying MB concentrations and localization uncertainties. The proposed method was compared with the NN and K trackers using the evaluation framework. Finally, the three trackers were applied to *in vivo* ultrasound data from a rat kidney, and the resulting ultrasound SR images were compared qualitatively and quantitatively to determine the best tracking method.

The rest of the paper is organized as follows. Section 2 describes the methods used in this study. Section 3 presents the simulation and *in vivo* results, and they are discussed in Section 4. Finally, the paper is concluded in Section 5.

2. Methods

2.1. Tracking algorithms

Tracking methods aim to link unlabeled MBs from frame to frame. In the NN tracker, the MBs in the next frame are found to determine the closest MB to the current MB. Although the NN tracker is fast and straightforward, it uses uncertain localizations directly.

Kalman filtering has a long history in engineering and is well known for its ability to reduce the uncertainty in the measurements. Considering that MBs in the blood vessels follow the bloodstream and cannot jump into any direction, a more robust tracking is possible via Kalman filtering and linear motion model, as this method considers the prior state information [15,25]. This consideration can be modeled as $\vec{r}(t) = \vec{r}(t-1) + d\vec{r}(t) + \epsilon(t)$, where $\vec{r}(t) = (r_x(t), r_y(t))$ is the position of the MB at time t , $d\vec{r}(t) = (dr_x(t), dr_y(t))$ is the displacement of the MB,

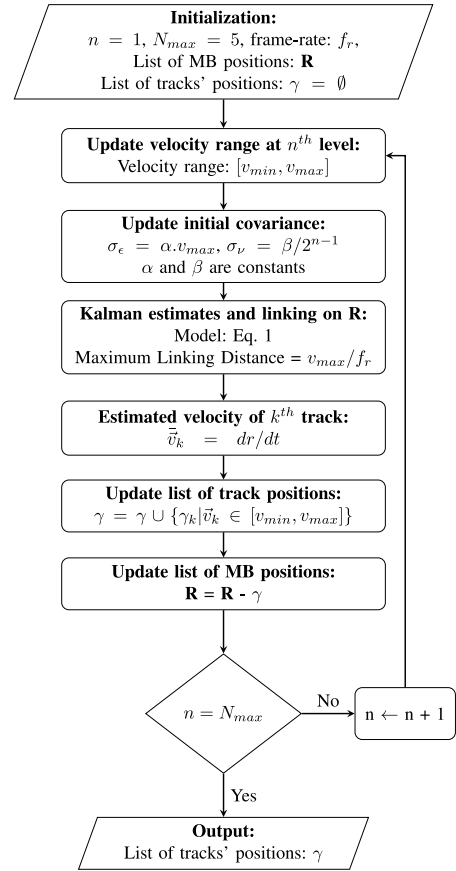


Fig. 1. Hierarchical Kalman tracker flowchart.

and $\epsilon(t)$ is the displacement error. This model is formulated using the Kalman framework as:

$$\begin{cases} \text{Prediction State:} & \bar{x}(t) = \mathbf{F}x(t-1) + \epsilon(t) \\ \text{Observation State:} & \bar{z}(t) = \mathbf{H}\bar{x}(t) + v(t), \end{cases} \quad (1)$$

where $x(t) = [\vec{r}(t), d\vec{r}(t)]^T = [r_x(t), r_y(t), dr_x(t), dr_y(t)]^T$,

$$\mathbf{F} = \begin{bmatrix} 1 & 0 & 1 & 0 \\ 0 & 1 & 0 & 1 \\ 0 & 0 & 1 & 0 \\ 0 & 0 & 0 & 1 \end{bmatrix}, \quad \mathbf{H} = \begin{bmatrix} 1 & 0 & 0 & 0 \\ 0 & 1 & 0 & 0 \end{bmatrix},$$

$\epsilon(t) \sim \mathcal{N}(0, \sigma_\epsilon^2)$, and $v(t) \sim \mathcal{N}(0, \sigma_v^2)$ is the localization uncertainty. In this study, the NN and K trackers used a maximum linking distance of 250 μm , equivalent to a displacement of a MB in a frame with the maximum flow velocity of 13.75 mm/s in a system with a frame-rate of 55 Hz. When entering the bloodstream, the MBs have unknown concentrations, different velocities, and flow dynamics in different anatomical regions. To cover most of these variations, the initial conditions of the K tracker were experimentally set to $\sigma_v = 0.002$ m and $\sigma_\epsilon = 0.025$ m (see Section I in the supplementary document).

Having similar initial conditions for all MBs might not be beneficial, since MBs are localized with unknown uncertainties and have various velocities. Additionally, the different MB lifetimes correspond to the

number of iterations in the Kalman filter. The proposed method uses a hierarchical structure of Kalman filters, which considers different initial conditions for different ranges of velocities. The flowchart for a 5 level HK tracker is shown in Fig. 1. The tracking starts with a constraint on the low velocity range (0–3 mm/s) and increases velocity range at each level (up to 12–15 mm/s). The initial standard deviation of displacement error was considered proportional to the maximum velocity at each level with a constant coefficient of α . The initial standard deviation of uncertainty was set inversely proportional to the level of tracking with a constant coefficient of β . The constant values of $\alpha = 0.001$ and $\beta = 0.025$ were also set experimentally (see Section I in the supplementary document). For each range of velocity, a Kalman filter, described in (1), with updated initial conditions was utilized to estimate more accurate positions of MBs from uncertain positions. The estimated positions were linked and assigned to the next frame positions with a constraint on the maximum linking distance using the Hungarian algorithm [24]. The Hungarian algorithm finds the input of the Kalman filter in its next iteration from the list of MB positions in which the selected positions have the optimal minimum total distance to the Kalman estimates in the previous iteration. The maximum linking distance was v_{max}/f_r , where v_{max} was the maximum velocity in the processing level, and f_r was the system frame-rate. With the formation of the MB trajectory, the velocity of that MB was estimated by knowing the total displacement and time. Considering track γ_k as a set of N_k positions, each observed at a specific time, defined as

$$\gamma_k = \{((x_i, y_i, z_i), t_i)\}_{i=1}^{N_k} = \{(\vec{r}_i, t_i)\}_{i=1}^{N_k}, \quad (2)$$

the mean velocity of the track γ_k is estimated as

$$\vec{v}_k = \frac{\vec{r}_{N_k} - \vec{r}_1}{t_{N_k} - t_1}, \quad (3)$$

and the instantaneous velocity of the track γ_k at its i th position is estimated as

$$\vec{v}_{ik} = \frac{\vec{r}_{i+1} - \vec{r}_i}{t_{i+1} - t_i}. \quad (4)$$

The tracks with estimated velocity beyond the tracker's velocity range were removed from the list of tracks. Finally, the MB positions corresponding to the track positions were removed from the list of MBs, and at the next level, the same procedure was applied to the remaining untracked MBs.

2.2. Simulations

Artificial X-shaped crossing tubes were simulated in Matlab (MathWorks, U.S.). The simulations were made by generating MB positions, each with a known ground truth track and uniformly random lifetime, moving with different velocities. Individual MBs inside the tube were also uniformly distributed with sub-wavelength distance. MB positions were generated according to the ground truth tracks. To simulate uncertainty in MB position estimates, a random Gaussian error was added. The trackers' performance was investigated over uncertainties ranging from $\lambda/20$ to $\lambda/2$. In this study, localization uncertainty refers to the SD of the Gaussian position error. The various parameters of the simulations are listed in Table 1. The low, medium, and high-density scenarios had an average MB count of 17, 31, and 51 MB.frame⁻¹, corresponding to MB density of 1.37, 2.46, and 4.24 MB. λ^{-2} .frame⁻¹ at the center of the phantom. MB density, calculated based on the size of the vessels and the shape of the phantom, provides an average amount of the MBs per resolution cell (λ^2). For example, a MB density of 4 MB. λ^{-2} .frame⁻¹ at the center of the phantom means that, on average, we can find 4 MBs in a resolution cell at the center of the phantom. The low, medium, and high density scenarios were only part of the whole simulated scenarios (See Section II of the supplementary document for extra information). A snapshot of these scenarios is shown in Fig. 2, demonstrating that in the low-density scenario, most of the MBs were

Table 1

Parameters used in the *in silico* X-phantom.

Parameters	Value
Tube length	10 mm
Tube radius	250 μ m & 125 μ m
Peak velocity	10 mm/s & 5 mm/s
Velocity profile	Parabolic
Angle between tubes	15°
Frame-rate (f_r)	55 Hz
Wavelength (λ)	256 μ m
Average MB count	17, 31, 51 MB.frame ⁻¹
MB density at phantom center	1.37, 2.46, 4.24 MB. λ^{-2} .frame ⁻¹
Localization uncertainty	$\lambda/20$ to $\lambda/2$

Table 2

Definition of profile-based metrics.

Ground truth (GT)	$\vec{v}_g(r) = V_p(1 - (\frac{r}{R})^2)$
Estimations	$\{\vec{v}_i(r)\}_{i=1}^N$
Mean Profile	$\vec{v}(r) = \mathbb{E}\{\vec{v}_i(r), \vec{v}_2(r), \dots, \vec{v}_N(r)\}$
Standard Deviation (SD) Profile	$\vec{v}_{SD}(r) = \sum_{i=1}^N (\vec{v}_i(r) - \vec{v}(r))^2 / N$
Relative Bias	$\mathbb{E}\{ \vec{v}(r) - \vec{v}_g(r) \} / V_p$
Relative SD	$\sqrt{\mathbb{E}\{ \vec{v}_{SD}(r) \}} / V_p$

not overlapping. In the medium-density scenario, some of the MBs were overlapping, and most of the MBs were overlapping in the high-density scenario. The MB concentration is not controllable *in vivo* after MB injection; even though the dilution of SonoVue is adjusted to have fewer overlapped MBs, the concentration may vary depending on the vessel structure and blood velocity in specific types of vessels, especially in a complex organ such as kidneys. For this reason, various MB densities were simulated separately, and the aim was to get the most tracking performance in multiple scenarios or most of the individual scenarios.

Various performance metrics were employed to evaluate tracking performance from different aspects.

2.2.1. Assignment-based metrics

The estimated tracks were assigned and paired to the ground truth tracks based on their minimum distance as described in [22]. For the paired tracks, true positive (TP), false positive (FP), and false negative (FN) positions and tracks were determined based on a gate distance with the size of a wavelength [22]. Then, the Jaccard similarity was calculated as

$$JSC = \frac{TP}{TP + FP + FN}, \quad (5)$$

representing similarity to the ground truth. For the sub-wavelength accuracy, the root-mean-square-error (RMSE) of the TP positions were calculated. In this study, the assignment-based metrics were extended for the velocity vectors. A paired velocity vector with a magnitude error less than 20% and angle error less than 45 degrees was counted as a TP vector. In the same way of tracks and positions, the JSC and RMSE of velocity vectors were used for similarity and accuracy evaluation.

2.2.2. Profile-based metrics

Considering the known velocity profile and the geometry of the tube as the ground truth, the velocity profiles of the SR images were compared with the ground truth. As the same parabolic profiles across the tubes were expected, the relative bias (RB) and relative standard deviation (RSD) were calculated over several spatial cross-sections. The velocity profiles were calculated using spline interpolation of velocity map values. Table 2 summaries the metrics calculated using the estimated and ground truth profiles. The intensity profiles were also estimated using the same method over intensity map values. The 90% width of the profile was considered as an estimate for the diameter (D) to show how the different trackers can generate spurious tracks outside the vessel. The full width at half maximum (FWHM) of the profiles was also estimated for comparison.

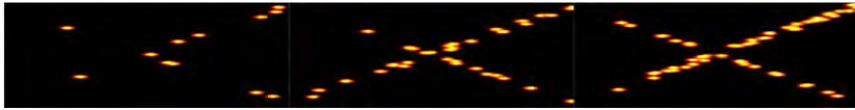


Fig. 2. An example of low, medium, and high density scenarios. The ground truth MB positions in a random frame were convolved with a Gaussian point spread function for better visualization.

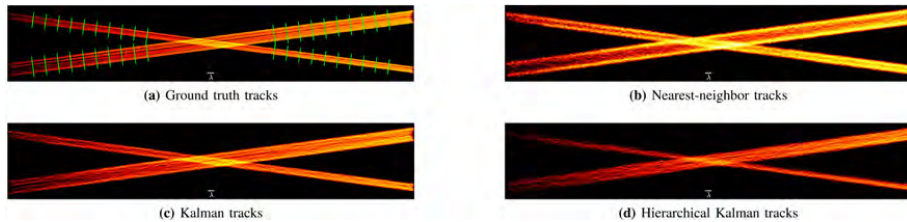


Fig. 3. (a) The ground truth tracks marked by several green cross-sections are used for measuring intensity and velocity profiles. SR images reconstructed using (b) nearest-neighbor, (c) Kalman, and (d) hierarchical Kalman trackers for medium MB density with an uncertainty of $\lambda/5$.

2.3. *In vivo* measurement

The *in vivo* measurements were conducted on two Sprague-Dawley rat kidneys during laparotomy using a modified BK5000 scanner and an X18L5s transducer (BK Medical, Herlev, Denmark). The rats were tracheotomized and ventilated with a mechanical ventilator. A metal retractor pulled the left side of the diaphragm slightly in the cranial direction to make the kidney more accessible for the probe and reduce respiratory motion. However, the kidney was still moving concurrently with the respirations to a certain extent (it varied among the animals how much the respiratory motions pushed the kidney in the lateral image direction, and the value of the motion range were reported in another study [26]). Ten minutes of B-mode and contrast-enhanced images with a frame-rate of 53.85 Hz were recorded. A pulse amplitude modulation sequence was used for imaging with a transmit frequency of 6 MHz ($\lambda = 256 \mu\text{m}$). The transmit voltage was low with a corresponding mechanical index (MI) of 0.2 to prevent bursting of the MBs. The MBs (SonoVue, Bracco, Milan, Italy) were injected with a flow-rate of 100 $\mu\text{l}/\text{min}$ after a 1:10 dilution. During the infusion, a syringe stirrer was used to keep the solution homogeneous and prevent drop in the MB concentration during the scan. The measurement was performed in agreement with protocols approved by the Danish Animal Experiments Inspectorate under the Ministry of Environment and Food. All procedures matched the ethical standard of the University of Copenhagen at which the measurements were performed. The *in vivo* kidney data were collected previously for a pilot pre-clinical study [12].

The motion-field was estimated locally using B-mode images [26, 27], for patches of $3 \times 3 \text{ mm}$ with 80% overlap. The MBs were localized using the weighted-centroid on the Gaussian-filtered contrast images. The localization was compensated for the tissue motion by subtracting the motion-field value at that position and time. Next, the corrected MB positions were tracked using the NN, K, and HK trackers. The estimated tracks were inserted into an image with a pixel size of $5 \mu\text{m}$ to form the final SR images. An intensity map was created when all tracks were inserted into the SR image with each track having the same weight. A velocity map was created by inserting all track velocities into the SR image. The velocity maps were visualized by scaling and remapping of velocity vectors to an RGB color wheel, where color shows flow direction and brightness indicates velocity magnitude.

3. Results

3.1. Simulation results

The ground truth tracks and images with estimated tracks using NN, K, and HK for a medium MB density scenario with a localization

uncertainty of $\lambda/5$ are shown in Fig. 3. The green dashed lines in Fig. 3a are the cross-section position in which the profiles were calculated.

3.1.1. Assignment-based metrics

The overall benchmark of all the assignment-based metrics for different scenarios is summarized in Table 3 (see Section II of the supplementary document for quantitative numbers). The table shows the best trackers by performance metrics (JSC and RMSE). In terms of similarity to the ground truth, the HK tracker was superior in all of the high density scenarios, and it had the lowest RMSE in 75% of scenarios. The NN tracker was only competitive with K and HK in low and medium density scenarios with low localization uncertainty (0.05λ and 0.10λ). Decreasing the value of the gate size also resulted in the same trends in the performance metrics. However, a lower performance was estimated when smaller gate sizes were used, especially for high uncertainty scenarios and less accurate estimates of RMSE were obtained (see Section III of the supplementary document).

3.1.2. Profile-based metrics

The mean intensity profiles for two vessels are shown in Fig. 4. Both the NN and K trackers showed larger vessel diameters compared with the HK tracker. The estimated diameters for this scenario are listed in Table 4a, showing a more accurate diameter estimation (D) for the HK tracker. The small vessel diameter was overestimated 2.8% by the HK, while the vessel was 31.6% and 55.6% wider than its actual size using the K and NN trackers. These numbers for the large vessel were 12.6% (HK), 17.2% (K), and 37.6% (NN).

Mean and instantaneous velocity profiles for two vessels are shown in Fig. 5, where solid lines are mean profiles and shaded areas are the SD of the profiles. The statistics of the estimated profiles, listed in Table 4b and 4c, shows a high RSD, when the NN tracker was used, while both K and HK tracker shows a noticeable improvement in velocity estimation. Unlike the structure, indicated by the intensity profiles, the velocity profile statistics showed a slight degradation in RSD, when the HK tracker was employed.

Fig. 6 shows the instantaneous velocity profiles, estimated by the three trackers, in the small vessel ($250 \mu\text{m}$) with various peak velocities. The tracking performance was degraded at higher peak velocities for the given frame-rate. The statistics of these profiles are listed in Table 5, showing the degradation of the different trackers, when the peak velocity was increased.

Table 3

Assignment-based ranking for Nearest-Neighbor (NN), Kalman (K), and Hierarchical Kalman (HK) trackers using 100 independent simulations for each scenario. The tracker with the best metric for various uncertainty ($\lambda/20 \sim \lambda/2$) and MB density (low, medium, high) scenarios is included in the Table. In scenarios where the best tracker was not significantly superior, the other trackers with relative metric difference less than 2% are included as well.

SD of Localization Uncertainty		0.05 λ			0.10 λ			0.20 λ			0.50 λ		
MB density		Low	Medium	High	Low	Medium	High	Low	Medium	High	Low	Medium	High
Track Level	JSC	NN	NN/HK	HK	NN	NN/HK	HK	K	K	HK	HK	HK	HK
Position Level	JSC	HK	HK	HK	HK/K	HK	HK	K	K	K/HK	K	K	HK
	RMSE	HK	HK	HK	HK	HK	HK	HK/K	HK/K	HK	K	K	K
Mean Velocity	JSC	HK/K	HK	HK	HK/K	HK	HK	HK	HK	HK	HK	HK	HK
	RMSE	HK	HK	HK	HK	HK	HK	HK	HK	HK/K	K	K	K
Inst. Velocity	JSC	HK	HK	HK	HK/K	HK	HK	K	K	K/HK	K/HK	HK/K	HK
	RMSE	K/HK	K/HK	K/HK	K/HK	K/HK	K/HK	HK/K	HK/K	HK/K	HK/K	HK/K	HK/K

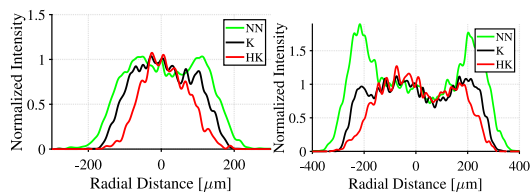


Fig. 4. Intensity profiles for small (left) and large (right) vessels in a medium-density scenario with localization uncertainty of $\lambda/5$. The intensity values were normalized to the intensity at the center of the vessel.

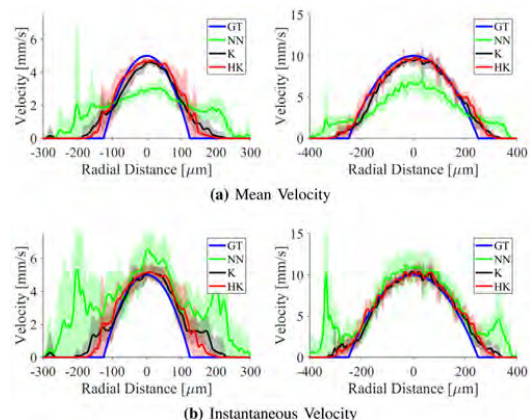


Fig. 5. (a) Mean and (b) instantaneous velocity profiles for small (left) and large (right) vessels. Blue profile is the ground truth (GT) parabolic profile. The shaded area shows the standard deviation.

3.2. In vivo results

In the proposed hierarchical tracker, different ranges of flow velocities were tracked with a corresponding Kalman filter and linking conditions. It is shown in Fig. 7 that the slow flow microvasculature was mapped at the first level, and tracking continued to recover faster flows of the larger vessels at the next levels. Notice how small arteries (red tracks pointed by arrows) close to the veins appeared at level 4, while they were mostly hidden in the previous levels.

Intensity and velocity maps for the entire kidney are shown in Figs. 8 and 9, demonstrating the overall visual improvement when the HK tracker is used compared with the NN and K trackers. Fig. 10 shows two zoomed regions of the velocity maps. Four examples of vessels were selected (arrows), and their diameters are listed in Table 6.

Table 4

Profile-based metrics for a medium density scenario with localization uncertainty of $\lambda/5$.

	Small vessel (250 μm)			Large vessel (500 μm)		
	NN	K	HK	NN	K	HK
D (μm)	389	329	257	688	586	563
FWHM (μm)	307	247	164	607	531	441
(b) Mean Velocity Profiles						
	Small vessel (5 mm/s)			Large vessel (10 mm/s)		
	NN	K	HK	NN	K	HK
RB (%)	4.99	2.61	4.27	-8.25	-0.77	1.69
RSD (%)	17.29	8.90	12.88	10.03	7.01	8.34
(c) Instantaneous Velocity Profiles						
	Small vessel (5 mm/s)			Large vessel (10 mm/s)		
	NN	K	HK	NN	K	HK
RB (%)	35.71	8.70	7.98	16.06	3.26	4.45
RSD (%)	41.77	12.94	16.07	31.73	9.00	9.84

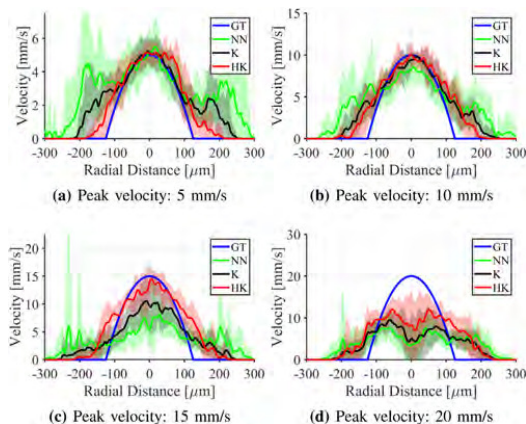


Fig. 6. Instantaneous velocity profiles of small vessel for a medium density scenario with localization uncertainty of $\lambda/5$ for different peak velocities.

Similar to the simulations, the HK tracker had a smaller estimate for the vessel diameter. Marker 4 shows a vein, which is only partly inside the imaging plane. In this example, the vein was not filled completely with tracks, when the K tracker was employed. This effect can easily take place in the cortical and medullary regions and the diameters of unfilled or out-of-plane structures can be misinterpreted. Therefore, only the distribution of velocity estimates in these regions was investigated. Fig. 11 shows that the majority of tracked MBs in

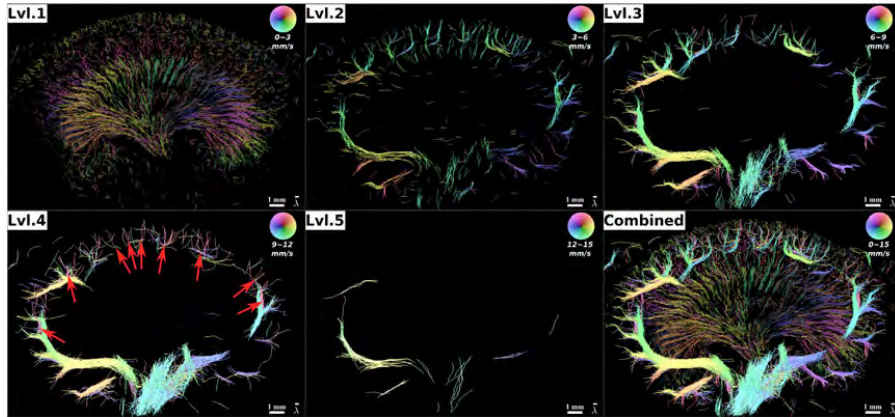


Fig. 7. The reconstructed tracks at different levels of the proposed hierarchical Kalman (HK) tracker. The images are velocity maps showing a coronal view in the center of the first kidney. The maximum velocities are 3, 6, 9, 12, and 15 mm/s, corresponding to the velocity range of the HK tracker at each level. The arrows point to the small arteries with faster flows.

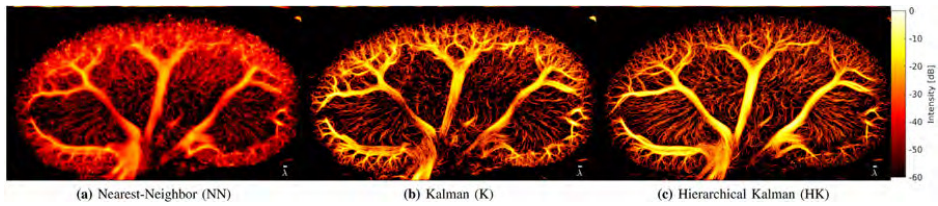


Fig. 8. Intensity maps of the renal vascular tree processed with (a) NN (b) K and (c) HK trackers. All images are log-scaled with a 60 dB dynamic range according to the color bar.

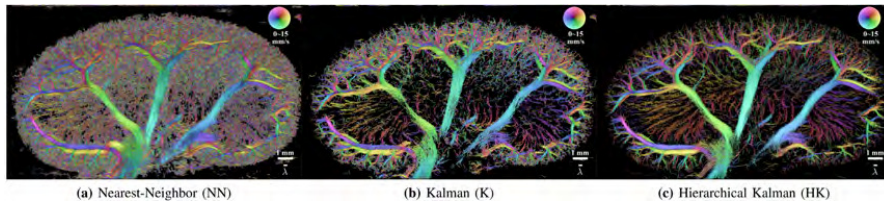


Fig. 9. Velocity maps of the renal vascular tree processed with (a) NN (b) K and (c) HK trackers. Colors indicate the flow direction according to the color wheel in the top-right corner (e.g. yellow color shows a flow from left to right). Brightness corresponds to the magnitude of the velocities (e.g. the darkest is closer to 0 and the brightest is closer to 15 mm/s).

Table 5

Statistics of the instantaneous velocity profiles for a medium density scenario with localization uncertainty of $\lambda/5$.

Tracker	Metric	Peak Velocity			
		5 mm/s	10 mm/s	15 mm/s	20 mm/s
NN	RB (%)	28.29	13.36	-3.98	-8.76
	RSD (%)	40.34	23.65	26.96	15.91
K	RB (%)	14.69	8.78	-2.55	-8.94
	RSD (%)	21.26	14.64	15.91	14.89
HK	RB (%)	8.02	8.12	5.95	-1.98
	RSD (%)	16.62	14.67	14.6	17.78

both the cortex and medulla (outer and inner regions of the kidney) had slow velocities below 2 mm/s. Considering the 98% of the cumulative density functions as the peak velocity, the peak velocity in the medulla

Table 6

Vessel diameter of the four marked vessels in Fig. 10.

Marker	Nearest-Neighbor	Kalman	Hierarchical Kalman
(1)	150.40 μm	107.41 μm	79.62 μm
(2)	382.54 μm	311.42 μm	231.75 μm
(3)	131.66 μm	127.01 μm	79.10 μm
(4)	155.61 μm	not saturated	113.37 μm

was estimated to 1.65 mm/s, while the NN and HK trackers resulted in 3 to 4 times higher peak velocities. These values for the cortex were 5.05 mm/s using the HK tracker compared with 8.25 mm/s and 9.90 mm/s when using the K and NN trackers.

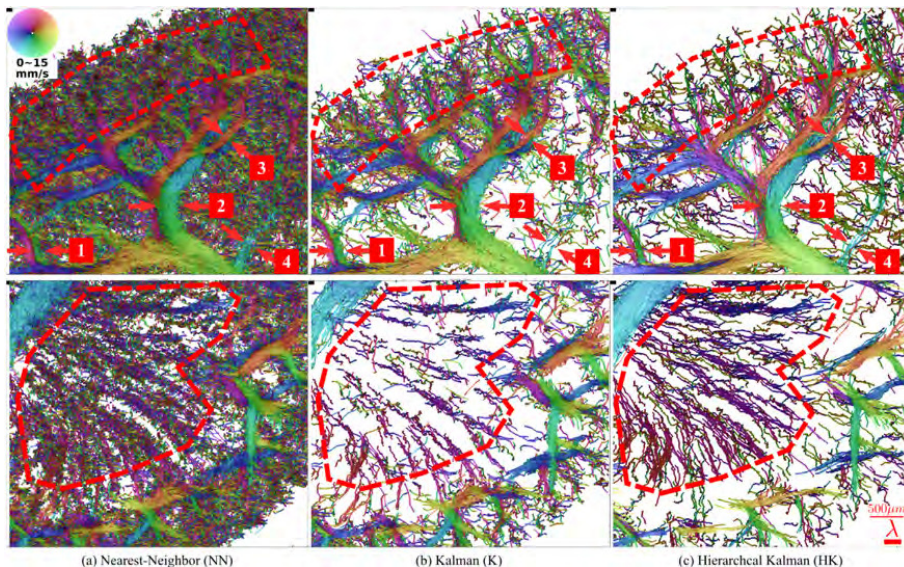


Fig. 10. Zoomed-in regions of velocity maps showing a region of the cortex and major vessel branches (top) and the medulla (bottom) using (a) NN (b) K, and (c) HK trackers. Four major vessel branches were marked for reporting vessel diameter. The red dashed lines show the region of interest where the distribution of velocity estimates were investigated.

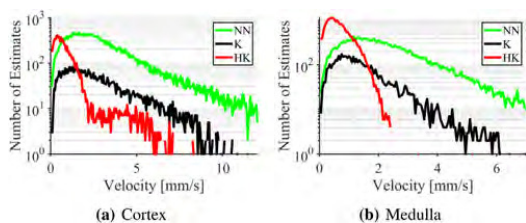


Fig. 11. Distribution of velocity estimates in (a) the cortex and (b) the medulla, used for determining peak and mean velocity.

The computational complexity of the three tracking algorithms were compared based on the processing time for the same problem using the same processor (Intel® Core™ i7-8700 CPU @ 3.20 GHz). The computation time of three different tracking algorithms for solving the *in vivo* tracking of 3 million MB positions over 32362 frames was 3.22 min for the NN tracker, while it was 33.71 min and 35.79 min for the K and HK trackers, indicating that the HK tracker with 5 levels had roughly the same computation time as the simple K tracker, and both trackers were 10 times slower than the NN tracker.

The difference between hierarchical Kalman trackers with different number of levels was also investigated. A 3-lvl hierarchical tracker is qualitatively compared with a 5-lvl and a 15-lvl hierarchical tracker in Fig. 12. Decreasing the number of levels generated obvious spurious tracks. On the other hand, the hierarchical tracker with very small velocity ranges failed to link slow MBs and caused unusual tracks, when the unlinked positions were used at the higher levels.

4. Discussion

This study introduced a new hierarchical Kalman tracker, and its performance was evaluated and compared with the NN and K trackers using a variety of performance metrics and challenging scenarios. The

evaluation of tracking algorithms was based on a detector-independent simulation setup with known ground truth tracks. Summarized in Table 3, the HK tracker had a superior performance in the similarity of generated tracks to the ground truth in 38 out of 48 cases, especially scenarios with a high density and high uncertainty of MB positions. This tracker also showed the lowest RMSE in 26 out of 36 cases. Although the velocity profiles from the HK tracker were not competitive to the ones estimated by the K tracker, the intensity profiles showed a better diameter estimation and therefore structure improvement by the HK tracker. According to the simulations, the performance of all three trackers will drop in the presence of higher MB concentration and higher uncertainty. However, it is anticipated that under the same condition, the HK tracker outperforms the two other trackers.

The *in vivo* ultrasound SR images presented in this study also showed a visual improvement in image quality using the proposed HK tracker, exemplified with more delicate medullary microvasculature called vasa recta (for comparison, see Fig. 10 in [28]), which demonstrates these structures in a postmortem rat kidney with microfil silicone rubber) as well as neat streamlines of MB trajectories in the large vessels. A dense structure with random flow directions can be seen in the cortical regions in Fig. 9a. Fig. 9b shows more distinguishable vessels in the cortical regions. However, vasa recta with slow velocities are sparser in comparison with Fig. 9a. In Fig. 9c, both cortical and medullary regions have distinguishable vessel structures and flow directions. In Fig. 10, notice the smooth streamlines of MBs in the larger arcuate arteries and veins (top) and vasa recta bundles in the medulla (bottom), when the HK tracker was employed. The distinguished vessel diameters also followed the trends observed in the simulations. The velocity maps, shown in Fig. 9, appear to become progressively sparser from Fig. 9-a to Fig. 9-c. This is due to more overlapping tracks and more linked MBs in the NN. Even though the NN tracker generates a considerably higher number of tracks, we speculate on the JSC and RMSE in simulation results that many of the NN tracks are not TP.

Several decades ago, a direct measurement of blood flow in the medulla estimated the velocity below 2 mm/s [29]. This finding corresponds to velocity estimates from the HK tracker, shown in Fig. 11b. It

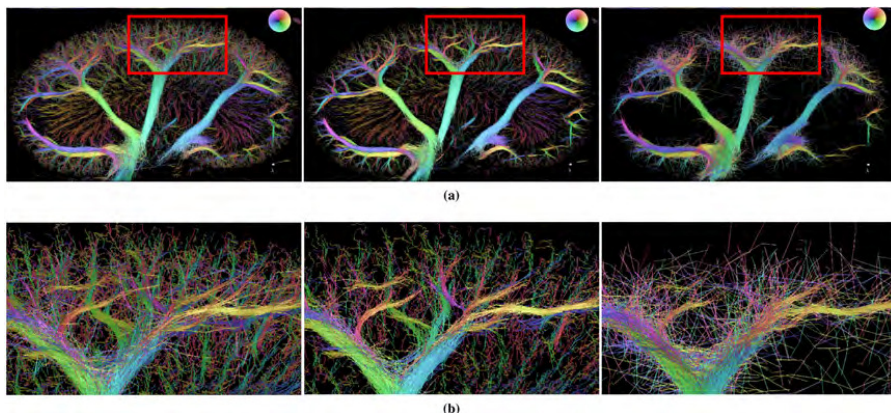


Fig. 12. Hierarchical Kalman with different number of levels (left: 3-lvl, middle: 5-lvl, right: 15-lvl). (a) shows the full view and the red rectangles are the zoomed regions shown in (b).

is worth noting that direct measurement of blood flow in the microvasculature is quite demanding, and no imaging modality has shown the ability to measure velocities deeper inside organs.

A study using nano-CT has demonstrated the dense and complex vascular architecture in the cortex of the rat kidney [30]. The kidney dense vessel structure of the renal cortex seems to be shown better in Fig. 8a, while it seems that the K and HK are missing some of the information. This is due to the Kalman structure, which tries to predict a specific linear motion model for the MBs, as described in Section 2.1. In addition, many of the cortical vessels are not completely inside the imaging plane. Therefore, the many MBs that shortly pass through the imaging plane do not satisfy the flow model. Moreover, these projected vectors into the 2D imaging plane could cause unreliable displacement and velocity estimates. The unreliable tracks in this region are more evident in Fig. 9a, as velocity vectors moving in all directions covered the data from the in-plane vessels. A 3D measurement, using a 2D sparse array [31] or row-column arrays [20], is required to capture MBs movement in all dimensions reliably.

In the simulated phantom, the small vessel diameter is a wavelength (λ). However, the MB trajectories inside each vessel had a sub-wavelength distance from each other. These delicate streamlines can be perceived as several microvessels inside the phantom. Solving a tracking problem in this situation becomes even more cumbersome by adding uncertainty to the MB positions. The same analogy for super-resolved velocity maps exists in which the velocity profiles must be estimated with sub-wavelength resolution.

The computational complexity of a tracking algorithm depends on the number of MB positions (inputs) and the generated tracks (outputs). One or both could be stochastic depending on the localization uncertainty, MB lifetime, and structure complexity. Although the HK tracker employs multiple Kalman filters, the number of MB positions processed at each level is reduced compared with the previous level.

The contrast ultrasound data usually suffer from low SNR (or more specifically contrast-to-noise ratio), as the voltage should be kept low (corresponding to low MI) to do not disrupt all of the MBs and high enough to capture their non-linear response. The low SNR may result in residual clutter. This may also generate false detections or miss detections that can potentially affect the results. This limitation can be added to the current simulation setup by randomly generating or removing MB positions, while keeping the ground truth tracks the same as before.

Imaging sequences with higher frame-rate [32,33] can be employed to increase maximum velocity that can be estimated. Moreover, a higher frame-rate allows more reliable tracking with fewer linking

errors, because a shorter linking distance (v_{max}/fr) is required to reconstruct a velocity map with the same maximum velocity.

The MB infusion is used to have more control on the amount of MBs during the time. Therefore, MB concentrations used for the rat experiments in this study were much lower than those administered in a bolus injection for human examinations of, e.g., liver tumors. The bolus injection and infusion are not comparable. The infusion settings were chosen based on pre-trials where different MB concentrations and infusion rates were tested. For another organ, whether in animals or humans, other settings are probably needed — it depends on the vascularity and flows in the specific organ and size of the animal/human. Clinical translation is possible. SonoVue is not yet FDA-approved for infusion, but many studies worked with human MB infusion (for purposes other than SRI). It does not seem to alter the drug's safety profile. Challenges may arise with larger out-of-plane motion in humans, and therefore, the technique would benefit greatly going from 2D to 3D. For the kidney, clinical implications would be, e.g., investigating whether microvascular alterations in structure or flow velocity precede microalbuminuria in persons with diabetes. This could allow earlier diagnosis of renal involvement and improve the possibility of monitoring the microvascular effects of renoprotective drug treatment. Cancer is another large field where the technique could allow improved diagnostics and treatment effect evaluation. For example, SRI could help with non-invasively distinguishing malignant lymph nodes from healthy or reactive ones.

5. Conclusion

This paper presented a new hierarchical Kalman tracker, which attempts to track MBs with different ranges of velocity with corresponding initial conditions and linking distances. The proposed tracker was compared with the NN and K tracker and evaluated using several assignment-based and profile-based performance metrics with challenging scenarios of varying MB density and uncertainty. The results indicate that the proposed HK tracker outperforms the NN and K trackers for many metrics and in different scenarios, especially in high concentration and high uncertainty of MB positions. The method also improved the *in vivo* image quality. The *in vivo* results showed noticeable improvement with some trends similar to the simulations, including more accurate diameter estimations.

Declaration of competing interest

The authors declare that they have no known competing financial interests or personal relationships that could have appeared to influence the work reported in this paper.

Appendix A. Supplementary data

Supplementary material related to this article can be found online at <https://doi.org/10.1016/j.ultras.2022.106695>.

References

- [1] O.M. Viessmann, R.J. Eckersley, K. Christensen-Jeffries, M.X. Tang, C. Dunsby, Acoustic super-resolution with ultrasound and microbubbles, *Phys. Med. Biol.* 58 (2013) 6447–6458.
- [2] M.A. O'Reilly, K. Hynynen, A super-resolution ultrasound method for brain vascular mapping, *Med. Phys.* 40 (11) (2013) 110701–110707, <http://dx.doi.org/10.1118/1.4823762>.
- [3] Y. Desailly, J. Pierre, O. Couture, M. Tanter, Resolution limits of ultrafast ultrasound localization microscopy, *Phys. Med. Biol.* 60 (22) (2015) 8723–8740.
- [4] K. Christensen-Jeffries, R.J. Browning, M. Tang, C. Dunsby, R.J. Eckersley, In vivo acoustic super-resolution and super-resolved velocity mapping using microbubbles, *IEEE Trans. Med. Imaging* 34 (2) (2015) 433–440.
- [5] C. Errico, J. Pierre, S. Pezet, Y. Desailly, Z. Lenkei, O. Couture, M. Tanter, Ultrafast ultrasound localization microscopy for deep super-resolution vascular imaging, *Nature* 527 (2015) 499–502.
- [6] D. Ackermann, G. Schmitz, Detection and tracking of multiple microbubbles in ultrasound B-mode images, *IEEE Trans. Ultrason. Ferroelec. Freq. Contr.* 63 (1) (2016) 72–82.
- [7] K. Christensen-Jeffries, O. Couture, P.A. Dayton, Y.C. Eldar, K. Hynynen, F. Kieseling, M. O'Reilly, G.F. Pinton, G. Schmitz, M. Tang, et al., Super-resolution ultrasound imaging, *Ultrasound Med. Biol.* 46 (4) (2020) 865–891.
- [8] F. Lin, S.E. Shelton, D. Espindola, J.D. Rojas, G. Pinton, P.A. Dayton, 3-D ultrasound localization microscopy for identifying microvascular morphology features of tumor angiogenesis at a resolution beyond the diffraction limit of conventional ultrasound, *Theranostics* 7 (1) (2017) 196–204, <http://dx.doi.org/10.7150/thno.16899>.
- [9] D. Ghosh, J. Peng, K. Brown, S. Sirsi, C. Mineo, P.W. Shaul, K. Hoyt, Super-resolution ultrasound imaging of skeletal muscle microvascular dysfunction in an animal model of type 2 diabetes, *J. Ultrasound Med.* 38 (10) (2019) 2589–2599.
- [10] J. Yu, L. Lavery, K. Kim, Super-resolution ultrasound imaging method for microvasculature in vivo with a high temporal accuracy, *Sci. Rep.* 8 (1) (2018) 1–11.
- [11] J. Foiret, H. Zhang, T. Ilovitsh, L. Mahakian, S. Tam, K.W. Ferrara, Ultrasound localization microscopy to image and assess microvasculature in a rat kidney, *Sci. Rep.* 7 (1) (2017) 13662:1–12, <http://dx.doi.org/10.1038/s41598-017-13676-7>.
- [12] S.B. Andersen, I. Taghavi, C.A.V. Hoyos, S.B. Sogaard, F. Gran, L. Lonn, K.L. Hansen, J.A. Jensen, M.B. Nielsen, C.M. Sørensen, Super-resolution imaging with ultrasound for visualization of the renal microvasculature in rats before and after renal ischemia: A pilot study, *Diagn.* 10 (11) (2020) 862.
- [13] Q. Chen, J. Yu, B.M. Rush, S.D. Stocker, R.J. Tan, K. Kim, Ultrasound super-resolution imaging provides a noninvasive assessment of renal microvasculature changes during mouse acute kidney injury, *Kidney Int.* (2020) 355–365.
- [14] J. Zhu, E.M. Rowland, S. Harput, K. Riemer, C.H. Leow, B. Clark, K. Cox, A. Lim, K. Christensen-Jeffries, G. Zhang, J. Brown, C. Dunsby, R.J. Eckersley, P.D. Weinberg, M.-X. Tang, 3D Super-resolution US imaging of rabbit lymph node vasculature in vivo by using microbubbles, *Radiology* 291 (3) (2019) 642–650, <http://dx.doi.org/10.1148/radiol.2019182593>.
- [15] S. Tang, P. Song, J.D. Trzasko, M. Lowerison, C. Huang, P. Gong, U. Lok, A. Manduca, S. Chen, Kalman filter-based microbubble tracking for robust super-resolution ultrasound microvessel imaging, *IEEE Trans. Ultrason. Ferroelec. Freq. Contr.* 67 (9) (2020) 1738–1751.
- [16] Q. Chen, J. Yu, L. Lukashova, J.D. Latoche, J. Zhu, L. Lavery, K. Verdelis, C.J. Anderson, K. Kim, Validation of ultrasound super-resolution imaging of vasa vasorum in rabbit atherosclerotic plaques, *IEEE Trans. Ultrason. Ferroelec. Freq. Contr.* 67 (8) (2020) 1725–1729.
- [17] M.R. Lowerison, C. Huang, F. Lucien, S. Chen, P. Song, Ultrasound localization microscopy of renal tumor xenografts in chicken embryo is correlated to hypoxia, *Sci. Rep.* 10 (1) (2020) 1–13.
- [18] M.L. Ommen, M. Schou, C. Beers, J.A. Jensen, N.B. Larsen, E.V. Thomsen, 3D Printed Calibration Micro-phantoms for Validation of Super-Resolution Ultrasound Imaging, in: *Proc. IEEE Ultrason. Symp.*, 1–4, 2019.
- [19] J. Youn, M.L. Ommen, M.B. Stuart, E.V. Thomsen, N.B. Larsen, J.A. Jensen, Detection and localization of ultrasound scatterers using convolutional neural networks, *IEEE Trans. Med. Imaging* 39 (12) (2020) 3855–3867.
- [20] J.A. Jensen, M.L. Ommen, S.H. Øygard, M. Schou, T. Sams, M.B. Stuart, C. Beers, E.V. Thomsen, N.B. Larsen, B.G. Tomov, Three-dimensional super resolution imaging using a row-column array, *IEEE Trans. Ultrason. Ferroelec. Freq. Contr.* 67 (3) (2020) 538–546, <http://dx.doi.org/10.1109/TUFFC.2019.2948563>.
- [21] J.C. Crocker, D.G. Grier, Methods of digital video microscopy for colloidal studies, *J. Colloid* 179 (1) (1996) 298–310, <http://dx.doi.org/10.1006/jcis.1996.0217>.
- [22] N. Chenouard, I. Smal, F. De Chaumont, M. Maška, I.F. Szbalzarini, Y. Gong, J. Cardinale, C. Carthel, S. Coraluppi, M. Winter, et al., Objective comparison of particle tracking methods, *Nature Methods* 11 (3) (2014) 281–290.
- [23] P. Song, J.D. Trzasko, A. Manduca, R. Huang, R. Kadivrel, D.F. Kallmes, S. Chen, Improved super-resolution ultrasound microvessel imaging with spatiotemporal nonlocal means filtering and bipartite graph-based microbubble tracking, *IEEE Trans. Ultrason. Ferroelec. Freq. Contr.* 65 (2) (2017) 149–167.
- [24] H.W. Kuhn, The Hungarian method for the assignment problem, *Nav. Res. Logist. Q.* 2 (1–2) (1955) 83–97.
- [25] O. Solomon, R.J.G. van Sloun, H. Wijkstra, M. Mischi, Y.C. Eldar, Exploiting flow dynamics for super-resolution in contrast-enhanced ultrasound, *IEEE Trans. Ultrason. Ferroelec. Freq. Contr.* 60 (10) (2019) 1573–1586.
- [26] I. Taghavi, S.B. Andersen, C.A.V. Hoyos, M.B. Nielsen, C.M. Sørensen, J.A. Jensen, In vivo motion correction in super resolution imaging of rat kidneys, *IEEE Trans. Ultrason. Ferroelec. Freq. Contr.* 68 (10) (2021) 3082–3093.
- [27] J.A. Jensen, S.B. Andersen, C.A.V. Hoyos, K.L. Hansen, C.M. Sørensen, M.B. Nielsen, Tissue motion estimation and correction in super resolution imaging, in: *Proc. IEEE Ultrason. Symp.*, 1–4, 2019.
- [28] L. Bankir, N. Bouby, M. Trinh-Trang-Tan, 2 The role of the kidney in the maintenance of water balance, *Bailliere's Clin. Endocrinol. Metab.* 3 (2) (1989) 249–311.
- [29] C. Holliger, K.V. Lemley, S.L. Schmitt, F.C. Thomas, C.R. Robertson, R.L. Jamison, Direct determination of vasa recta blood flow in the rat renal papilla, *Circ. Res.* 53 (3) (1983) 401–413.
- [30] R. Wagner, V. Denis, F. Hossler, K. Czymmek, E. Pauwels, L. Van Hoorebeke, High-resolution imaging of kidney vascular corrosion casts with nano-CT, *Microsc. Microanal.* 17 (2010) 215–219.
- [31] S. Harput, K. Christensen-Jeffries, A. Ramalli, J. Brown, J. Zhu, G. Zhang, C.H. Leow, M. Toulemonde, E. Boni, P. Tortoli, R.J. Eckersley, C. Dunsby, M. Tang, 3-D Super-resolution ultrasound (SR-US) imaging with a 2-D sparse array, 2019, *ArXiv Preprint*.
- [32] J.A. Jensen, S. Nikolov, K.L. Gammelmark, M.H. Pedersen, Synthetic aperture ultrasound imaging, *Ultrasonics* 44 (2006) e5–e15.
- [33] M. Tanter, M. Fink, Ultrafast imaging in biomedical ultrasound, *IEEE Trans. Ultrason. Ferroelec. Freq. Contr.* 61 (1) (2014) 102–119, <http://dx.doi.org/10.1109/TUFFC.2014.6689779>.

Supplementary document

1

CONTENTS

I	Parameter selection strategy	1
II	Performance metrics	3
III	Gate size effect	7

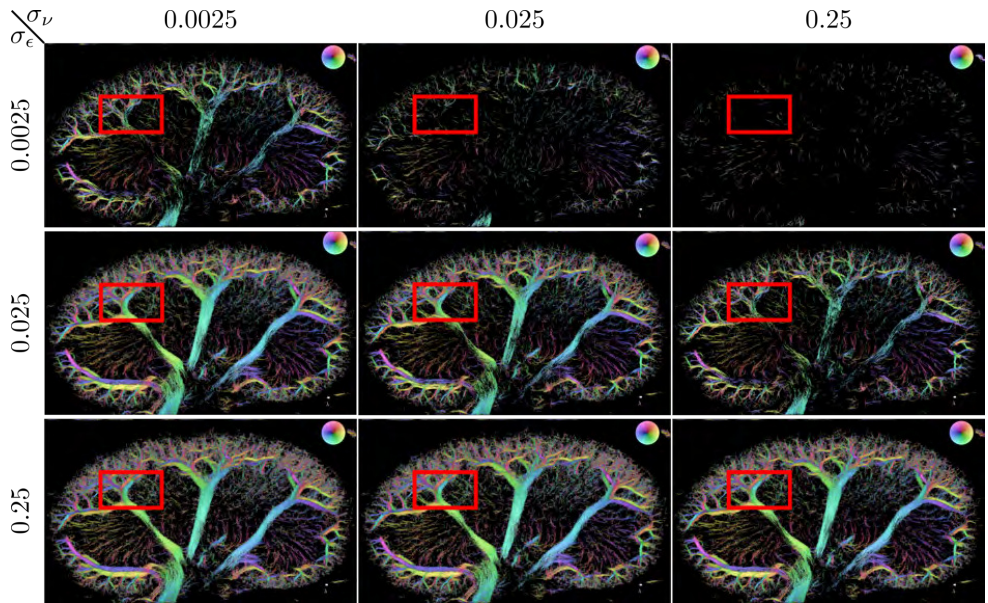
I. PARAMETER SELECTION STRATEGY

The *in vivo* data were tracked with the Kalman tracker with various values of σ_ϵ and σ_v in coarse steps of 0.0025, 0.025, and 0.25 m. The *in vivo* data were used, as they contain a combination of multiple scenarios (low density, high density, overlapping MBs, non-overlapping MBs, low velocities, high velocities). The results are shown in Fig. 1. The visible effects by the selection of each pair of parameters are listed in Table I. Based on these observations, the Kalman parameters were empirically selected with a small σ_v (0.0025) and a medium σ_ϵ (0.025) to have both large and small vessels and less uncertain tracks.

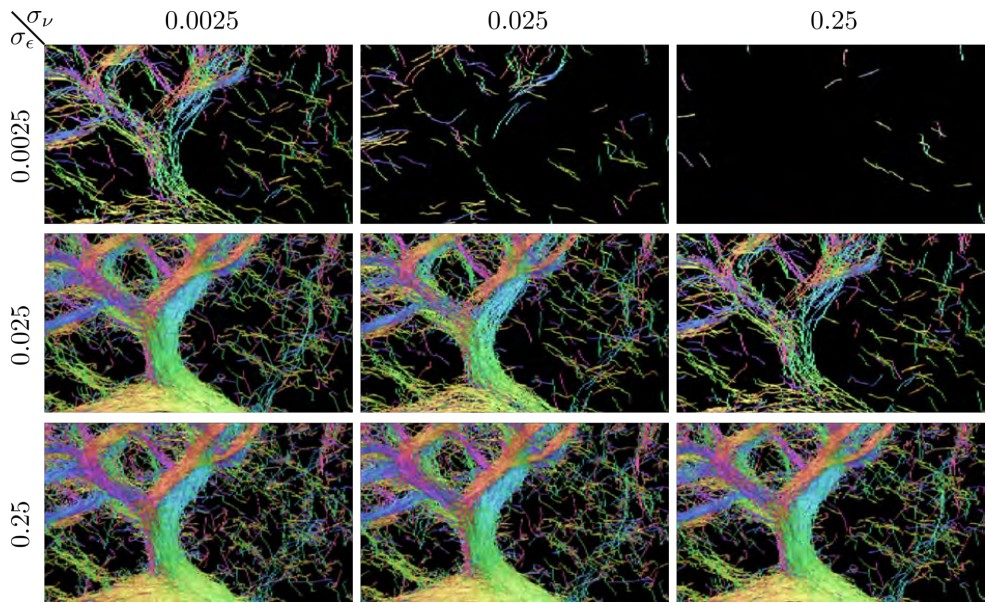
TABLE I: Observation after selecting large and small values of σ_ϵ and σ_v

	Small σ_ϵ	Large σ_ϵ
Small σ_v	Unable to track fast flows (large vessels)	Uncertain tracks linking (wavy and squiggly tracks)
Large σ_v	Unable to track fast flows (large vessels) Generate short and sparse tracks	Unable to track fast flows (large vessels) Increase uncertain track linking (wavy and squiggly tracks)

From the above observation, it can be inferred that faster flows can be tracked better with larger σ_ϵ and smaller σ_v while slower flows can be tracked better with smaller σ_ϵ and larger σ_v . This strategy was used for the adjustment of the parameters at different levels of the hierarchical Kalman tracker.



(a)



(b)

Fig. 1: Kalman parameters coarse tuning. (a) shows the full view and the red rectangles are the zoomed regions shown in (b). The in vivo data were processed using the Kalman filter with coarse steps of the parameters σ_ϵ and σ_ν .

II. PERFORMANCE METRICS

The performance metrics for a larger number of simulations for different density scenarios are listed here (the ranking for only three density scenarios at different uncertainty levels are reported in Table III of the main article). Each set of MB density (row) and standard deviation (SD) of localization error (column) is called a scenario. The performance metrics of the Nearest-neighbor (NN), Kalman (K), and hierarchical Kalman (HK) were reported for each scenario. The performance metrics are also highlighted by colors. The green color represents the best performance metric, and the red color is the worst performance metric. Even though sometimes a method has a better performance compared with another method, the difference between their performance metric is not high. For this reason, in the ranking (Table III of the main article), the methods that had a difference in their performance metrics of less than 2% were also reported. This means that method A with the best performance metric of p_A and method B with the performance metric of p_B would receive the same rank in the ranking table if $|p_A - p_B|/p_A < 0.02$. A JSC of 1 meant the maximum similarity between the ground truth and the estimation. The RMSE for positions was normalized to the wavelength (λ). Velocity error was normalized to the ground-truth velocity, and therefore the relative RMSE for velocity is presented in percentage. All numbers were rounded to two decimal places (in some cases with an insignificant difference, both yellow and green color could have the same round value).

TABLE II: JSC at track level

Average MB count [MB/frame]	SD of localization error											
	0.05 λ			0.10 λ			0.20 λ			0.50 λ		
	NN	K	HK	NN	K	HK	NN	K	HK	NN	K	HK
1	0.72	0.99	0.90	0.71	0.99	0.82	0.72	0.99	0.51	0.14	0.45	0.35
4	0.97	0.98	0.88	0.96	0.97	0.80	0.91	0.97	0.47	0.09	0.40	0.36
9	0.95	0.93	0.84	0.92	0.92	0.76	0.82	0.90	0.45	0.07	0.35	0.36
13	0.93	0.89	0.81	0.88	0.87	0.75	0.73	0.83	0.44	0.06	0.30	0.34
17 (low)	0.90	0.82	0.80	0.83	0.79	0.73	0.64	0.74	0.42	0.05	0.26	0.32
22	0.87	0.75	0.80	0.78	0.70	0.70	0.57	0.65	0.41	0.05	0.23	0.31
26	0.84	0.69	0.80	0.73	0.63	0.68	0.52	0.58	0.40	0.05	0.20	0.30
31 (Medium)	0.80	0.61	0.79	0.70	0.56	0.68	0.47	0.51	0.38	0.04	0.18	0.28
35	0.77	0.56	0.78	0.66	0.50	0.64	0.43	0.45	0.37	0.04	0.17	0.27
39	0.74	0.51	0.76	0.62	0.45	0.62	0.39	0.40	0.36	0.04	0.15	0.26
43	0.71	0.46	0.75	0.58	0.41	0.60	0.36	0.36	0.34	0.03	0.07	0.10
47	0.68	0.42	0.73	0.56	0.37	0.58	0.34	0.33	0.34	0.04	0.14	0.25
51 (High)	0.66	0.39	0.72	0.53	0.34	0.56	0.31	0.30	0.33	0.04	0.12	0.23

TABLE III: JSC at position level

Average	SD of localization error											
MB count	0.05 λ			0.10 λ			0.20 λ			0.50 λ		
[MB/frame]	NN	K	HK	NN	K	HK	NN	K	HK	NN	K	HK
1	0.98	1.00	0.96	0.96	1.00	0.91	0.92	0.99	0.56	0.28	0.65	0.22
4	0.88	0.97	0.88	0.80	0.95	0.80	0.70	0.91	0.56	0.22	0.58	0.20
9	0.80	0.93	0.85	0.69	0.89	0.78	0.57	0.83	0.55	0.19	0.53	0.20
13	0.75	0.84	0.88	0.63	0.82	0.84	0.51	0.78	0.53	0.15	0.46	0.19
17 (low)	0.69	0.83	0.84	0.57	0.76	0.79	0.43	0.72	0.50	0.13	0.41	0.20
22	0.67	0.80	0.83	0.52	0.74	0.75	0.38	0.67	0.48	0.11	0.35	0.20
26	0.63	0.76	0.82	0.48	0.70	0.73	0.34	0.62	0.45	0.10	0.32	0.21
30 (Medium)	0.59	0.73	0.80	0.45	0.67	0.72	0.31	0.57	0.43	0.09	0.27	0.21
35	0.56	0.69	0.80	0.42	0.62	0.70	0.28	0.53	0.42	0.09	0.25	0.21
39	0.54	0.65	0.79	0.39	0.58	0.69	0.25	0.48	0.39	0.08	0.23	0.21
43	0.52	0.62	0.78	0.37	0.54	0.67	0.23	0.44	0.37	0.03	0.04	0.06
47	0.50	0.58	0.77	0.34	0.50	0.65	0.21	0.41	0.36	0.07	0.19	0.20
51 (High)	0.47	0.56	0.76	0.33	0.48	0.64	0.20	0.38	0.35	0.07	0.17	0.20

TABLE IV: Normalized RMSE of estimated positions

Average	SD of localization error											
MB count	0.05 λ			0.10 λ			0.20 λ			0.50 λ		
[MB/frame]	NN	K	HK	NN	K	HK	NN	K	HK	NN	K	HK
1	0.07	0.10	0.06	0.14	0.12	0.09	0.28	0.18	0.19	0.58	0.40	0.50
4	0.09	0.10	0.07	0.15	0.12	0.10	0.29	0.18	0.19	0.59	0.40	0.50
9	0.10	0.10	0.07	0.16	0.13	0.10	0.30	0.19	0.20	0.59	0.41	0.51
13	0.11	0.11	0.08	0.18	0.13	0.11	0.31	0.20	0.20	0.59	0.42	0.51
17 (low)	0.12	0.12	0.08	0.19	0.14	0.12	0.32	0.21	0.21	0.59	0.43	0.52
22	0.13	0.12	0.09	0.20	0.15	0.12	0.33	0.22	0.22	0.59	0.44	0.52
26	0.15	0.13	0.09	0.21	0.16	0.13	0.34	0.22	0.22	0.59	0.45	0.53
30 (Medium)	0.16	0.14	0.10	0.22	0.17	0.13	0.35	0.24	0.23	0.60	0.46	0.53
35	0.17	0.15	0.10	0.23	0.18	0.14	0.36	0.24	0.23	0.60	0.46	0.54
39	0.17	0.16	0.10	0.24	0.19	0.14	0.36	0.25	0.24	0.60	0.47	0.54
43	0.18	0.17	0.11	0.25	0.20	0.15	0.38	0.27	0.25	0.69	0.67	0.68
47	0.19	0.18	0.11	0.26	0.21	0.15	0.38	0.27	0.25	0.60	0.49	0.55
51 (High)	0.20	0.19	0.12	0.27	0.22	0.16	0.39	0.28	0.26	0.61	0.50	0.56

TABLE V: JSC of mean velocity estimates

Average	SD of localization error											
MB count	0.05 λ			0.10 λ			0.20 λ			0.50 λ		
[MB/frame]	NN	K	HK	NN	K	HK	NN	K	HK	NN	K	HK
1	0.99	0.98	0.99	0.97	0.97	0.98	0.94	0.97	0.95	0.83	0.92	0.79
4	0.94	0.98	0.98	0.89	0.97	0.95	0.81	0.95	0.94	0.63	0.84	0.76
9	0.90	0.97	0.96	0.83	0.96	0.95	0.73	0.93	0.93	0.51	0.77	0.73
13	0.88	0.96	0.96	0.79	0.95	0.95	0.69	0.90	0.91	0.41	0.71	0.71
17 (low)	0.85	0.95	0.95	0.76	0.93	0.94	0.66	0.89	0.89	0.35	0.66	0.69
22	0.84	0.94	0.95	0.74	0.91	0.93	0.62	0.86	0.87	0.30	0.60	0.67
26	0.82	0.93	0.94	0.72	0.90	0.92	0.59	0.83	0.85	0.27	0.55	0.65
30 (Medium)	0.81	0.91	0.94	0.70	0.88	0.92	0.56	0.80	0.83	0.23	0.51	0.64
35	0.80	0.89	0.94	0.69	0.85	0.91	0.53	0.77	0.82	0.21	0.47	0.62
39	0.79	0.87	0.93	0.67	0.83	0.90	0.51	0.74	0.79	0.20	0.44	0.60
43	0.78	0.85	0.93	0.66	0.80	0.89	0.47	0.70	0.76	0.06	0.15	0.25
47	0.77	0.83	0.93	0.65	0.77	0.89	0.45	0.67	0.76	0.17	0.37	0.58
51 (High)	0.76	0.81	0.92	0.63	0.74	0.88	0.42	0.64	0.74	0.15	0.35	0.56

TABLE VI: Relative RMSE of mean velocities

Average	SD of localization error											
MB count	0.05 λ			0.10 λ			0.20 λ			0.50 λ		
[MB/frame]	NN	K	HK	NN	K	HK	NN	K	HK	NN	K	HK
1	1.56	1.65	1.26	2.12	2.09	1.74	3.22	2.70	3.21	8.40	4.77	7.35
4	2.58	1.92	1.70	3.35	2.28	2.03	4.31	2.90	3.29	8.43	5.18	7.59
9	3.31	2.13	1.80	4.18	2.49	2.26	5.47	3.27	3.41	8.77	5.77	7.91
13	3.86	2.35	2.13	4.82	2.78	2.51	6.21	3.61	3.61	9.08	6.24	8.15
17 (low)	4.39	2.54	2.32	5.29	3.03	2.78	6.85	3.90	3.85	9.43	6.69	8.29
22	4.72	2.75	2.50	5.72	3.24	2.96	7.37	4.23	4.05	9.72	7.07	8.58
26	5.06	2.97	2.65	6.03	3.48	3.08	7.62	4.54	4.30	9.94	7.47	8.70
30 (Medium)	5.28	3.20	2.83	6.37	3.78	3.32	7.91	4.83	4.51	10.10	7.82	8.93
35	5.57	3.45	2.96	6.70	4.05	3.50	8.26	5.10	4.72	10.29	8.09	8.96
39	5.76	3.74	3.09	6.92	4.35	3.68	8.46	5.40	4.97	10.29	8.45	9.13
43	5.98	3.90	3.23	7.09	4.59	3.82	8.67	5.85	5.35	11.73	11.62	11.44
47	6.19	4.17	3.31	7.32	4.80	3.94	8.85	5.95	5.36	10.66	8.89	9.38
51 (High)	6.31	4.39	3.45	7.42	5.13	4.07	8.98	6.31	5.61	10.55	9.23	9.45

TABLE VII: JSC of instantaneous velocity estimates

Average	SD of localization error											
MB count	0.05 λ			0.10 λ			0.20 λ			0.50 λ		
[MB/frame]	NN	K	HK	NN	K	HK	NN	K	HK	NN	K	HK
1	0.37	0.66	0.69	0.20	0.52	0.53	0.08	0.33	0.30	0.01	0.11	0.07
4	0.32	0.62	0.66	0.17	0.47	0.48	0.07	0.31	0.30	0.01	0.11	0.06
9	0.31	0.60	0.63	0.15	0.45	0.45	0.06	0.29	0.30	0.01	0.11	0.06
13	0.30	0.59	0.62	0.15	0.45	0.47	0.06	0.30	0.29	0.01	0.10	0.06
17 (low)	0.28	0.58	0.61	0.15	0.45	0.47	0.06	0.30	0.27	0.01	0.10	0.07
22	0.28	0.57	0.61	0.14	0.44	0.47	0.05	0.29	0.26	0.01	0.09	0.07
26	0.28	0.56	0.61	0.14	0.43	0.46	0.05	0.28	0.25	0.01	0.08	0.08
30 (Medium)	0.27	0.54	0.60	0.13	0.42	0.47	0.05	0.27	0.24	0.01	0.07	0.08
35	0.26	0.52	0.61	0.13	0.39	0.46	0.04	0.25	0.23	0.01	0.07	0.08
39	0.26	0.50	0.61	0.12	0.38	0.45	0.04	0.24	0.22	0.01	0.06	0.08
43	0.25	0.47	0.61	0.12	0.35	0.45	0.04	0.22	0.20	0.01	0.04	0.05
47	0.24	0.45	0.60	0.11	0.33	0.44	0.04	0.20	0.20	0.01	0.06	0.09
51 (High)	0.24	0.43	0.60	0.11	0.32	0.44	0.04	0.19	0.19	0.01	0.05	0.09

TABLE VIII: Relative RMSE of instantaneous velocities

Average	SD of localization error											
MB count	0.05 λ			0.10 λ			0.20 λ			0.50 λ		
[MB/frame]	NN	K	HK	NN	K	HK	NN	K	HK	NN	K	HK
1	10.49	8.27	8.22	11.15	9.64	10.06	11.46	10.72	10.99	11.58	11.34	11.33
4	10.47	8.34	8.23	11.20	9.63	10.04	11.44	10.73	11.01	11.57	11.32	11.36
9	10.48	8.35	8.23	11.21	9.65	10.06	11.45	10.71	10.99	11.49	11.35	11.32
13	10.46	8.27	8.23	11.21	9.63	10.04	11.45	10.71	10.99	11.50	11.34	11.31
17 (low)	10.48	8.25	8.27	11.21	9.59	10.04	11.44	10.69	10.98	11.50	11.35	11.31
22	10.48	8.18	8.24	11.20	9.55	10.01	11.45	10.68	10.98	11.53	11.36	11.31
26	10.47	8.09	8.18	11.21	9.50	10.00	11.46	10.67	10.97	11.50	11.37	11.32
30 (Medium)	10.47	8.05	8.17	11.22	9.48	9.99	11.47	10.66	10.97	11.51	11.37	11.28
35	10.48	8.01	8.16	11.23	9.47	9.99	11.45	10.66	10.97	11.45	11.38	11.30
39	10.50	8.00	8.13	11.24	9.47	9.98	11.47	10.66	10.97	11.51	11.38	11.31
43	10.50	8.02	8.14	11.24	9.47	9.98	11.48	10.69	10.98	11.51	11.50	11.46
47	10.51	8.02	8.09	11.25	9.47	9.97	11.47	10.68	10.98	11.49	11.41	11.30
51 (High)	10.52	8.04	8.09	11.25	9.49	9.98	11.48	10.71	10.98	11.51	11.42	11.31

III. GATE SIZE EFFECT

The radial gate size of a wavelength (λ) might seem a bit high for the evaluation of super-resolution techniques. The gating can be seen as a coarse criterion for the measurement of JSC. For the accuracy below the gate size, the RMSE was used to reflect how the estimated positions or velocities are close to the ground truth. In this section, the effect of various radial gate sizes, including λ , $\lambda/2$, and $\lambda/4$, and various angular gate sizes, including 45° , 22.5° , and 11.25° , were investigated.

Fig. 2 shows that the JSC of all algorithms drops slightly by decreasing the gate size. However, the trends are preserved. It can be seen that in all high-density situation, the HK tracker outperformed other trackers. In the scenarios with lower localization uncertainty (Fig. 2-a,b,c) and lower MB density, there are situations where the NN or the K tracker perform better than the HK tracker. The K tracker performed very well in the scenarios with SD of localization error equal to 0.20λ and medium to low range MB densities.

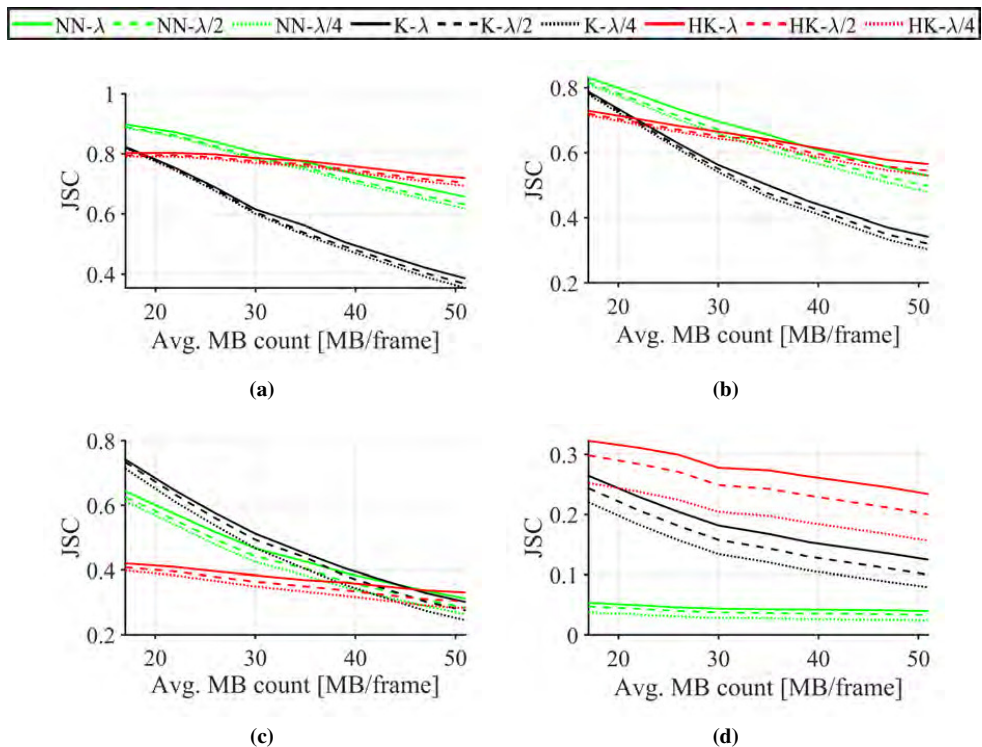


Fig. 2: Gate size effect on JSC of tracks. The JSC is shown versus different MB densities with the SD of localization error equal to (a) 0.05λ , (b) 0.10λ , (c) 0.20λ , and (d) 0.50λ . The gate size is λ for solid lines, $\lambda/2$ for dashed lines, and $\lambda/4$ for dotted lines.

Fig. 3 shows that the JSC of the positions were less dependent on the gate size, when the uncertainties were small (Fig. 3-a,b). The JSC of NN had a larger drop, when the uncertainty of the positions increased to 0.20λ (Fig. 3-c). The JSC of all methods were dropped at smaller gate sizes, when the uncertainty increased to 0.50λ . However, the trends were still comparable.

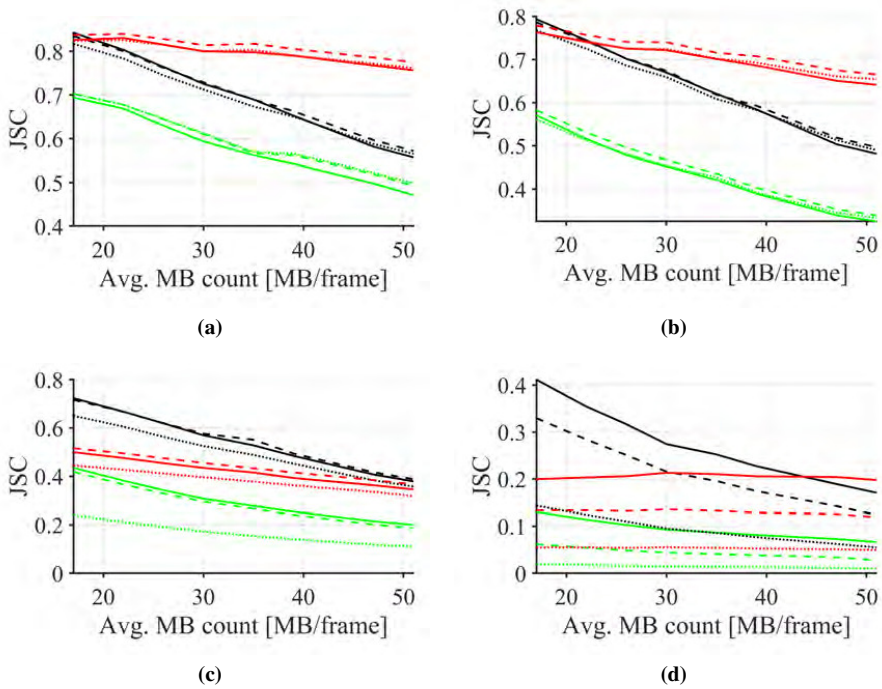


Fig. 3: Gate size effect on JSC of MB positions. The JSC is shown versus different MB densities with SD of localization error equal to (a) 0.05λ , (b) 0.10λ , (c) 0.20λ , and (d) 0.50λ . The gate size is λ for solid lines, $\lambda/2$ for dashed lines, and $\lambda/4$ for dotted lines.

The normalized RMSE was calculated for the positions that were estimated within the radial gate size of the ground-truth positions. Note that the RMSE cannot exceed the radial gate size. Fig. 4 shows the RMSE of the estimated positions from the ground-truth position. It can be seen that RMSE is reduced by decreasing the gate size, and RMSE cannot effectively be compared if the gate size is small. These poor statistics might be due to the smaller amount of the true positions in the smaller gate size. In the main manuscript, a relatively large radial gate size (a wavelength) was selected, and then the RMSE of the positions was used as a finer metric. The same strategy regarding the gate size was used in the following paper:

N. Chenouard et al., "Objective comparison of particle tracking methods," Nature methods, vol. 11, no. 3, pp. 281–290, 2014

Fig. 5 shows the effect of angular gate size smaller than 45° , which resulted in the same relative performance metrics.

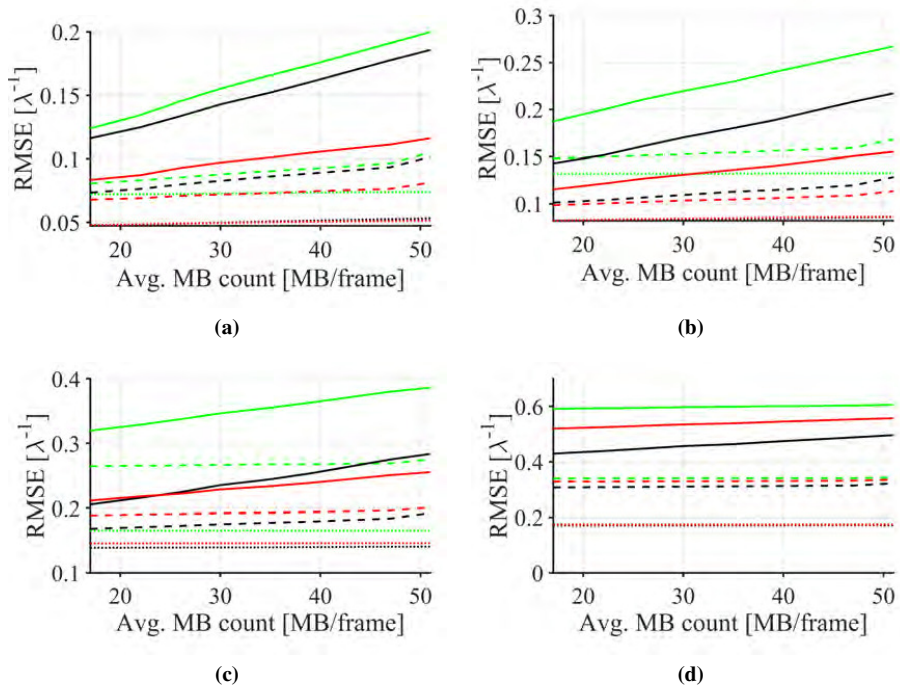


Fig. 4: Gate size effect on normalized RMSE of positions. The normalized RMSE to wavelength is shown versus various MB densities with SD of localization error equal to (a) 0.05λ , (b) 0.10λ , (c) 0.20λ , and (d) 0.50λ . The gate size is λ for solid lines, $\lambda/2$ for dashed lines, and $\lambda/4$ for dotted lines.

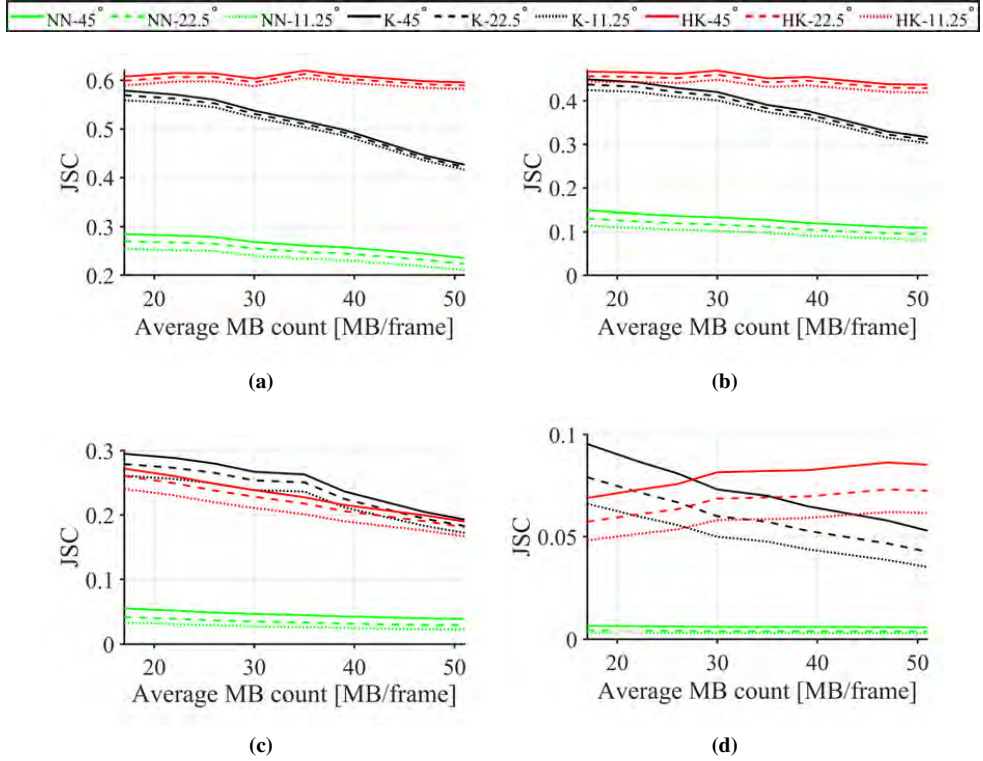


Fig. 5: Angular size effect on JSC of instantaneous velocities. The JSC is shown versus various MB densities with SD of localization error equal to (a) 0.05λ , (b) 0.10λ , (c) 0.20λ , and (d) 0.50λ . The angular gate size is 45° for solid lines, 22.5° for dashed lines, and 11.25° for dotted lines.



Paper 5

Blood Vessel Segmentation in Super-Resolution Ultrasound Imaging of Healthy Rat Kidneys

Iman Taghavi, Sofie Bech Andersen, Stinne Byrholdt Sjøgaard, Michael Bachmann Nielsen, Charlotte Mehlin Sørensen, Matthias Bo Stuart, and Jørgen Arendt Jensen

Name of journal:

IEEE Transactions on Ultrasonics, Ferroelectrics, and Frequency Control

Document Version:

In preparation

DOI:

—

General rights

Copyright and moral rights for the publications made accessible in the public portal are retained by the authors and/or other copyright owners and it is a condition of accessing publications that users recognise and abide by the legal requirements associated with these rights.

- Users may download and print one copy of any publication from the public portal for the purpose of private study or research.
- You may not further distribute the material or use it for any profit-making activity or commercial gain
- You may freely distribute the URL identifying the publication in the public portal

If you believe that this document breaches copyright please contact us providing details, and we will remove access to the work immediately and investigate your claim.

Blood Vessel Segmentation in Super-Resolution Ultrasound Imaging of Healthy Rat Kidneys

Iman Taghavi, Sofie Bech Andersen, Stinne Byrholdt Sogaard, Michael Bachmann Nielsen, Charlotte Mehlin Sørensen, Matthias Bo Stuart, and Jørgen Arendt Jensen

Abstract—Super-resolution ultrasound imaging (SRI) has the potential to visualize the microvasculature. This paper presents a method for semi-automated classification and automated segmentation of blood vessels in 10 super-resolution (SR) images of healthy Sprague-Dawley rat kidneys. The results show classification of the renal vessels into arteries and veins, extraction of vascular features, such as blood velocity, vessel diameter, length, tortuosity, and density in 2D SRI of kidneys, and determine the features with statistically significant difference between arteries and veins. The blood velocity and track density were two features that were statistically significantly different between arteries and veins in the inner medulla (IM), outer medulla (OM), and cortex (CO) of the kidneys, based on the Wilcoxon signed-rank test ($p \leq 0.002$). Considering the t -distribution for 10 samples, the median velocity in the arterioles of the whole medulla was predicted to be 0.84 ± 0.03 mm/s, while the prediction was 0.64 ± 0.03 mm/s for venules. A statistically significant difference between the two classes of vessels (arteries/arterioles vs. veins/venules) was observed in other regions of the kidneys, including a difference in the interquartile range (IQR) of velocities in the CO (0.48 ± 0.15 mm/s vs. 0.24 ± 0.08 mm/s) and median track density in all the regions of the kidney (IM: $30 \pm 3\%$ vs. $22 \pm 7\%$, OM: $30 \pm 5\%$ vs. $16 \pm 4\%$, CO: $10 \pm 3\%$ vs. $17 \pm 3\%$). Other features such as diameter, length, and tortuosity were only statistically significantly different in the arterioles and venules of the OM. In conclusion, it is possible to classify and segment blood vessels in 2D SRI and extract features with statistically significant difference between arteries and veins, especially the velocities of medullary regions and track density in the cortical region.

Index Terms—Super-resolution imaging (SRI), Ultrasound localization microscopy (ULM), Contrast-enhanced ultrasound (CEUS), Vascular imaging, Blood vessel segmentation, Vessel classification, Vessel characterization

I. INTRODUCTION

Blood vessel segmentation is a key element in medical image analysis, and vessel characterization has a significant role in diagnosis and treatment of diseases. Manual vessel segmentation is a demanding task. It usually suffers from poor intra-

“This work was financially supported by grant 82-2014-4 from the Danish National Advanced Technology Foundation, by grant 7050-00004B from Innovation Fund Denmark, and BK Medical”

I. Taghavi, M. B. Stuart, and J. A. Jensen are with the center for fast ultrasound imaging (CFU), Department of Health Technology, Technical University of Denmark (DTU), DK-2800 Denmark (imat@dtu.dk, mbst@dtu.dk, jaje@dtu.dk).

S. B. Andersen, S. B. Sogaard, and C. M. Sørensen are with the Department of Biomedical Sciences, University of Copenhagen, DK-2100, Denmark (anne.sofie.bech.andersen@regionh.dk, sbyrholdt@sund.ku.dk, cmehldin@sund.ku.dk)

S. B. Andersen, S. B. Sogaard, and M. B. Nielsen are with the Department of Diagnostic Radiology, Copenhagen University Hospital, DK-2100, Denmark (anne.sofie.bech.andersen@regionh.dk, sbyrholdt@sund.ku.dk, mbn@dadlnet.dk)

and inter-operator reproducibility and repeatability. Therefore, automated or semi-automated segmentation methods are necessary, especially when it comes to detailed microvascular images. Automated vessel segmentation has a long history and has been employed in different anatomical regions. It is also used for different imaging modalities. However, most studies have been limited to the retina [1], which has a known gold standard for segmentation with a massive public image dataset. There are also studies in other organs, such as the brain [2–5], liver [6–8], heart [9–12], and recently the kidneys [13–15]. These studies used either magnetic resonance imaging (MRI) or computed tomography (CT) technique. In ultrasound imaging, vessel segmentation is still limited to applications such as characterization of the carotid and femoral arteries [16, 17].

Ultrasound is a commonly used imaging modality for non-invasive vascular imaging. Various ultrasound imaging techniques have been designed to visualize the blood flow and vascular structure. These techniques range from color Doppler [18], power Doppler [19], vector flow imaging [20, 21] to contrast-enhanced ultrasound (CEUS) [22], and super-resolution ultrasound imaging (SRI) [23–26]. The resolution of an imaging system can be increased beyond the resolution imposed by the diffraction limit using super-resolution (SR) techniques. Breaking the conventional resolution limit enables deep microvascular imaging [26]. It is worth mentioning that even though the enhancement of spatial resolution in SRI is achieved at the cost of a reduction in temporal resolution [27], SRI is still among the fastest non-invasive medical imaging techniques.

Since the resolution of conventional ultrasound has been limited to the macrovasculature, the morphological segmentation has been performed manually by the operator, and the studies with automatic segmentation have been restricted to the quantification of large vessels in the conventional B-mode images [16, 17] or tissue perfusion in CEUS [28]. Entering the microscopic realm demands development of automated or semi-automated vessel segmentation algorithms. Ultrasound SR images are made from an accumulation of hundreds of thousands of microbubble (MB) trajectories, called a track map. Contrary to the conventional vascular imaging, each vessel in an SR image may not appear as a solid structure or get filled completely with MB tracks. Therefore, available segmentation techniques can easily misinterpret individual tracks as an individual vessel or fail to distinguish the structures in the ultrasound SR image. So far, the quantification of ultrasound SR images has been performed manually based on

regions of interest (ROI) [29–33], or a single tube characterization for the validation of the SRI [34, 35].

In conventional vascular ultrasound imaging, the field of view usually contains a few large vessels, which allows easy classification of the arteries and veins. Such classification is also crucial in SRI, but is more challenging due to the plentiful and complexity of vessels in the image. As arteries and veins are initially unidentified by MB tracking, an easy way to bypass the classification problem is visualizing the flow in 2D using a velocity map with an RGB color wheel. The velocity map was demonstrated for the first time in [24].

In relation to classification and characterization of the vessels in SR images, the following questions arise: How can we easily classify the vessels into arteries and veins in an SR image? Is it possible to characterize the vessels in an SR image in an automated manner? Are the features of the characterized arteries and veins statistically significantly different? The last question is important, when a machine is used to classify the vessels from their features without any supervision. This study aims to answer these questions. Our hypothesis is that automatic classification, segmentation, and characterization of vessels are possible using track maps and knowledge about the anatomy of the organ of interest: here, the kidney. To evaluate this hypothesis, a set of animal experiments on 10 healthy rat kidneys were conducted. The vasculature’s characterization inside the kidneys led to statistically significant quantitative numbers for classified vessels. The paper is an expanded version of the conference paper [36] with added vessel segmentation steps after classification, morphological feature statistics, investigation on two extra regions of the kidneys including inner medulla and cortex, and on a larger group of rats.

The paper is organized as follows. In Section II, the methods used in this study are described, including the data acquisition, SRI processing scheme, vessel classification, segmentation, and characterization. The results are presented in Section III and discussed in Section IV. Finally the paper is concluded in Section V.

II. METHODS

Automated vessel segmentation may include single or multiple processing techniques, including vessel enhancement, learning models, deformable model-based segmentation, and tracking of the vasculature structure [37]. Our method consists of a vessel enhancement technique and a pixel tracking approach for skeletonization and centerline estimation of vessels. This section starts with a brief explanation of the methods for data acquisition and SR processing. Then, the vessel segmentation method using track maps is explained.

A. Data acquisition

The *in vivo* measurements were conducted on 10 male Sprague-Dawley rat kidneys. As described in [30], the animal preparation and experiments were performed in agreement with the approved protocols by the Danish Ministry of Environment and Food and matched the ethical standard of the University of Copenhagen. All rats were healthy and had a

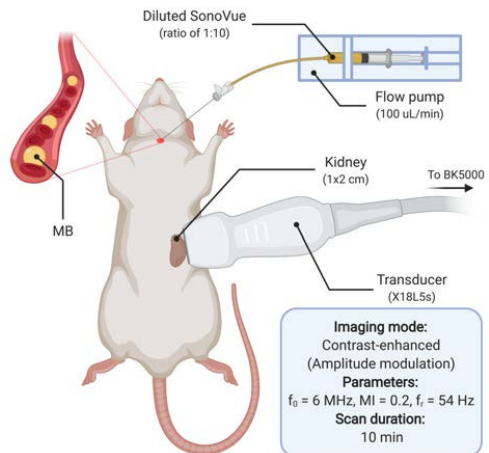


Fig. 1: Data acquisition setup (Credit: Created with BioRender.com)

weight in the range of 337.3 ± 48.3 grams. The left kidneys were scanned intraoperatively for 10 minutes using a BK5000 scanner (BK Medical, Herlev, Denmark) and a “hockey stick” X18L5s transducer (BK 9009, BK Medical, Herlev, Denmark). The beamformed RF data consisted of over 32,000 frames of both B-mode and CEUS images. The scan parameters and experiment setup are summarized in Fig. 1.

B. Super-resolution imaging

After data acquisition, the data were post-processed using a super-resolution processing scheme, demonstrated in Fig. 2. The microbubbles (MBs) were detected by applying a 2D Gaussian filter with a size of 7×7 pixels and a standard deviation of 1 pixel. The pixel size of the CEUS image was $24 \mu\text{m}$ in the axial direction and $80 \mu\text{m}$ in the lateral direction. The MB centroid positions were estimated using the weighted-centroid algorithm (“*regionprops*” function of *Matlab*). The motion field relative to a reference frame was estimated locally over time from 3×3 mm patches of the B-mode images with an 80% overlap, and then, a 3D spline interpolation was used to obtain a continuous motion field at any time and position. The motion-corrected positions were obtained by subtracting the value of the motion field from the positions at the corresponding time and location [38]. Finally, the motion-corrected positions were tracked using a hierarchical Kalman tracker [39]. A track is defined as a set of positions at different time instants that likely belong to a unique MB. Accumulating all of the tracks into an image with a pixel size of $5 \mu\text{m}$ made an intensity map. The tracking algorithm also provided the vector velocity information, which was inserted into a matrix to form a velocity map. The velocity maps were visualized by scaling and remapping velocity vectors to an RGB color wheel, where color shows flow direction and brightness indicates velocity magnitude.

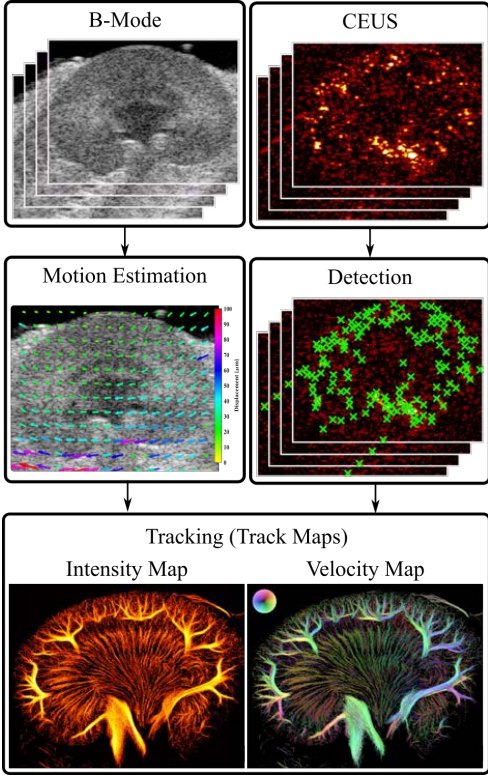


Fig. 2: Super-resolution ultrasound image processing scheme

C. Vessel Classification

The velocity map, shown in Fig. 2 (bottom right), is an accumulation of over 30,000 tracks. In the velocity map, the flow direction is illustrated by the color wheel. However, a unique color can show both arterial and venous flow directions in different areas of the image. This is better shown in Fig. 3, where a red color in the velocity map visualization can be both a vein or an artery. A track γ_k is considered as a set of N_k positions, observed at specific times. This definition can be formulated as

$$\gamma_k = \left\{ \left((x_i, y_i, z_i), t_i \right) \right\}_{i=1}^{N_k} = \left\{ \left(\vec{r}_i, t_i \right) \right\}_{i=1}^{N_k}, \quad (1)$$

where k is the track index, and \vec{r}_i is the position of a MB at the time t_i . The velocity of tracked MB at time t_i is

$$\vec{v}_{ik} = \frac{\vec{r}_{i+1} - \vec{r}_i}{t_{i+1} - t_i}. \quad (2)$$

The tracks were classified into arteries and veins before segmentation. This classification was implemented in a semi-automated manner. Firstly, the large anatomical regions of the kidney, including inner medulla (IM), outer medulla (OM), and cortex (CO), were labeled by an expert in renal anatomy. The arterial flow direction in these regions was also determined. The arterial blood follows a unique pattern in the kidney. The

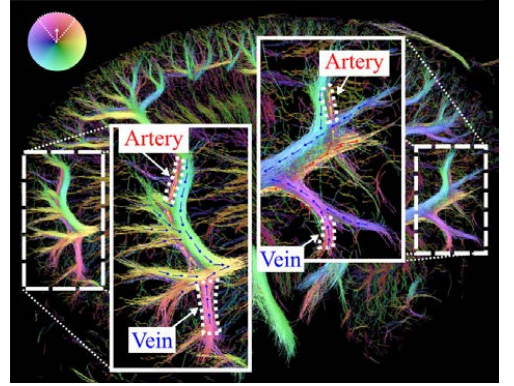


Fig. 3: Zoom in regions of a velocity map demonstrating unclassified vessels. For example, a red color can represent a vein in a region and at the same time an artery in another region.

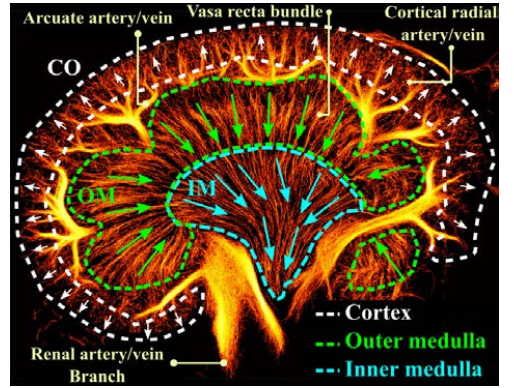


Fig. 4: Manual labeling of different regions (dashed lines) and arterial flow direction in each region (arrows) based on the anatomical information.

blood enters the kidney via the renal artery, distributes through the larger segmental arteries and then splits into smaller branches of the arcuate arteries running on the border between the cortex and medulla. In the cortex, the arterial blood flows toward the renal surface in the cortical radial arteries, while arterial blood to the medulla flows from juxtamedullary efferent arterioles into the vasa recta toward the renal papilla. The veins run in a parallel manner to the arteries. This flow pattern is shown in Fig. 4. The large vessels (LV) in the image were also labeled for visualization of the entire track map, but they were not the subject of this study and therefore, they were not included in the analysis. The MBs' positions (\vec{r}_i) and their movement directions ($\angle \vec{v}_{ik}$) were used for filtering their trajectories. This filtering allowed the inclusion or exclusion of particular types of tracks or tracks in specific regions. Assuming that arterial flow direction in an ROI has the angle of θ_a , a position of a track was classified as arterial track position, if \vec{r}_i exists in that ROI and $|\theta_a - \angle \vec{v}_{ik}| < \Delta\theta$. The last term put a constraint on the exclusion of tracks that had

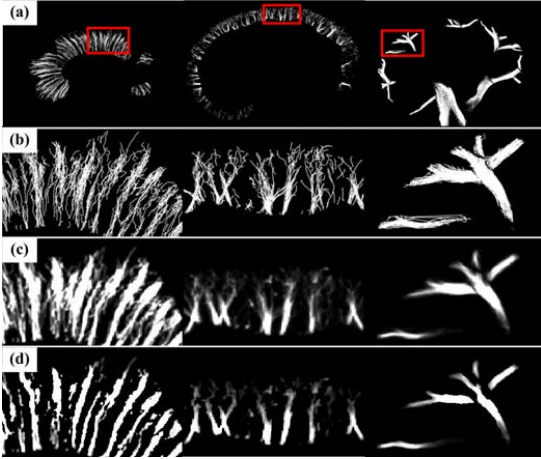


Fig. 5: Preprocessing steps for track isolation. (a) shows three examples of classified tracks in the outer medulla (left), cortex (middle), and larger vessels (right) with red boxes, zoomed in (b). (c): Gaussian filtering. (d): adaptive thresholding.

more angular deviation than $\Delta\theta$ with respect to the labeled arterial flow in that position of ROI. $\Delta\theta$ was set to 90° in the medullary regions and 125° for the cortical region. Noting that the venous flow direction is almost always in the opposite direction of arterial flow, the venous tracks can be classified with the same constraint but $\theta_v = \theta_a + 180^\circ$ instead of θ_a . The last term is according to the parallel nature of arteries and veins in the renal vasculature [40].

D. Vessel Segmentation

1) *Preprocessing:* Interesting objects to segment in the track maps are the small vessels rooted into the cortex and bundles of tiny vessels, called ascending vasa recta (AVR) and descending vasa recta (DVR), in the medulla. Assuming that the majority of MB trajectories are estimated inside the vessels, a mask was designed for the isolation of tracks. The mask was created from track maps with the following steps. First, the track maps were convolved with a Gaussian filter with the size of $500 \mu\text{m}$ and standard deviation of $25 \mu\text{m}$ to give a higher weight to a denser subset of tracks and lower weight to more sparse tracks. Second, a mask with isolated solid structures was created by applying an adaptive threshold based on the local mean values to the filtered image, using the “*adaptthresh*” function in Matlab. The local window size and sensitivity of the adaptive threshold were $500 \mu\text{m}$ and 0.5. This procedure is shown for three different regions of the kidney in Fig. 5. Lastly, the isolated regions with an area smaller than 0.06 mm^2 were considered noise and removed from the data using “*regionprops*” function in Matlab. The remained isolated regions in the mask were used individually to extract centerlines of the potential vessels.

2) *Centerline extraction:* The isolated tracks were obtained by masking the track map. Isolated tracks inside a region of the binary mask are shown in Fig. 6-a. The isolated tracks

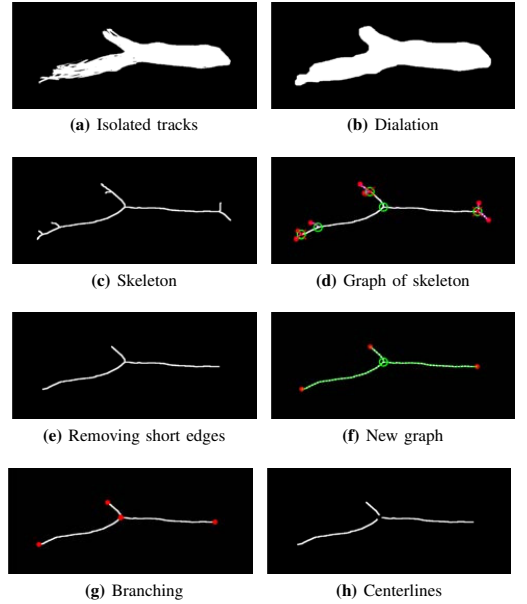


Fig. 6: Steps from isolated tracks to extraction of centerlines in the isolated area. Red dots in the graph show pendant vertices, and green circles are vertices with higher degrees.

were dilated with a disk element of radius $25 \mu\text{m}$ and closed immediately with a disk of $50 \mu\text{m}$, using the “*imdilate*” and “*imclose*” functions in Matlab (Fig. 6-b). The skeleton of the dilated region was extracted using “*bwmorph*” function (Fig. 6-c). All vertices and edges of the skeleton were determined by pixel tracing (Fig. 6-d). Edges with a smaller length than $125 \mu\text{m}$ were removed (Fig. 6-e). The skeleton was branched by removing the vertices with a degree higher than one (Fig. 6-f). The process of removing the vertices and short edges was continued until all branches of the skeleton only had pendant vertices (Fig. 6-g).

E. Characterization

With the estimated centerline and isolated tracks, different features of the segments and tracks were quantified. These features are described below:

1) *Velocity:* The distribution of the estimated velocities (\vec{v}_{ik}), defined in (2), in different regions and different classes of vessels were calculated. The peak velocity was measured as 98% of the cumulative distribution function (CDF) of the estimated velocities.

2) *Diameter:* Assuming that uncertain MB positions have normal distribution around vessel’s centerline, over 95% of positions would be within 2σ distance of the centerline, where σ is the standard deviation of MBs’ distances from the centerline. Therefore, 4σ was considered as the vessel diameter (Fig. 7-a).

3) *Length:* Indicating the length of each centerline (Fig. 7-a).

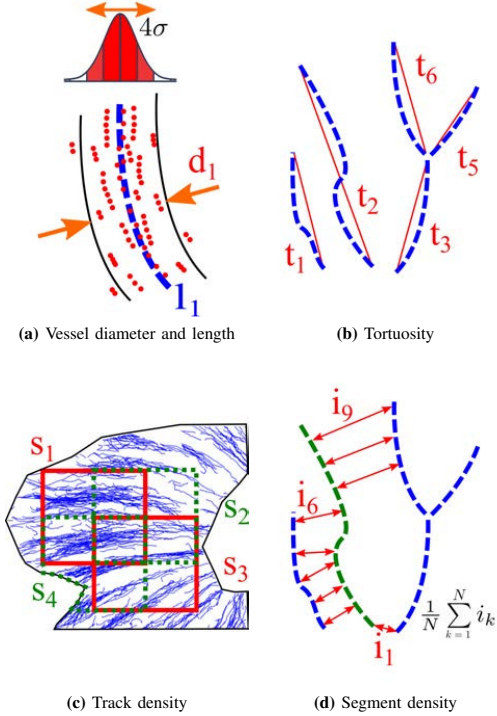


Fig. 7: Examples of different morphological quantification metrics. Dashed lines are estimated centerlines. (a) diameter and length, (b) tortuosity: ratio of length over distance, (c) Track density: measuring track density in overlapped patches, and (d) Segment density: average distance of a centerline to its adjacent centerlines.

4) *Tortuosity*: The centerline tortuosity was calculated as the ratio between the centerline's length to the distance between two ends of the centerline. The tortuosity of a straight line is 1 and increases by the degree of curvatures and bends in the centerline (Fig. 7-b).

5) *Track density*: The ratio of non-zero pixels to all pixels in a local region was defined as the structure density. Since the density may differ in different local regions, the entire ROI was divided into 50% overlapped 2×2 mm local regions, and the structure density was calculated for each (Fig. 7-c).

6) *Segment density*: The mean of distances from a segment to its adjacent segments (Fig. 7-d).

Of the above-mentioned features, velocity, diameter, and track density were calculated based on the individual tracks, while the other features were calculated based only on the extracted segments.

A Wilcoxon signed-rank test was performed to compare features of two classes of vessels, *i.e.* arteries and veins. The p -value of the test was used to assess how the difference between quantified features of classified vessels was statistically significant in the different regions of the kidneys. Considering the small sample size of the study (10 kidneys)

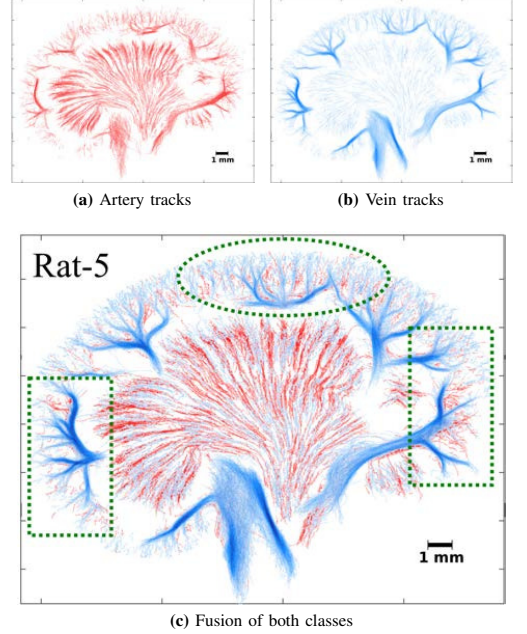


Fig. 8: Classified tracks into groups of arteries and veins. (a) classified arteries (b) classified veins, and (c) combination of arteries and veins after classification. Comparing (c) with (a) and (b), the dashed oval region shows a noticeable sparser arteries compared with veins in the cortex, and the dashed rectangles show two example of the region with many arteries behind the veins.

and assuming that data had a t -distribution, 95% confidence interval of the median and interquartile range (IQR) of the quantified features were also reported. Finally, the distribution of significant features was shown in the form of box plots.

III. RESULTS

Over 300,000 tracks in different regions of 10 kidneys were classified, and 5,606 segments were extracted in total. Fig. 8 shows the classified artery and vein tracks, demonstrating the separated arterial and venous flow in the kidney. Sparser artery tracks in the cortical region (dashed oval) and existence of many arteries behind the veins (dashed rectangles) were noticeable. Examples of automated segments from classified artery and vein tracks are shown in Fig. 9, visualizing the estimated centerlines and the potential vessel walls for the group of tracks.

The statistics of the quantified tracks and segmented data, including t -distribution of median and IQR with 95% confidence interval and the p -value of the Wilcoxon signed-rank test on these metrics, are summarized in Table I.

In all regions the median velocity was predicted higher in the arteries compared with the veins. However, the difference between median velocities was only statistically significant in the IM and OM regions ($p = 0.002$). In the CO, the IQR metric showed a statistically significant difference between arteries and veins ($p = 0.002$), however, the test on the median

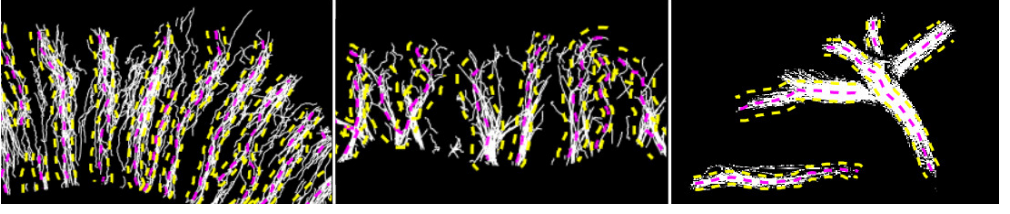


Fig. 9: Automatic segmentation of examples in Fig. 5 (left: outer medulla, middle: cortex, right: larger vessels). Red dashed lines are the estimated centerlines, and yellow dashed lines are estimated vessel walls.

TABLE I: Median and inter-quartile range of estimated features for the classified **arteries** and **veins** in three regions. The 95% confidence interval and p -value for each metric are reported. The gray highlighted metrics were considered statistically significant by the Wilcoxon signed-rank test ($p \leq 0.006$).

Feature	Metric	IM	OM	CO
Velocity [mm/s]	Median	0.87 ± 0.07 0.63 ± 0.03 } $p = 0.002$	0.84 ± 0.03 0.68 ± 0.03 } $p = 0.002$	1.87 ± 0.33 1.63 ± 0.26 } $p = 0.695$
	IQR	0.06 ± 0.02 0.04 ± 0.01 } $p = 0.065$	0.04 ± 0.01 0.03 ± 0.01 } $p = 0.193$	0.48 ± 0.15 0.24 ± 0.08 } $p = 0.002$
	Peak (CDF-98%)	2.06 ± 0.15 1.56 ± 0.05 } $p = 0.002$	1.98 ± 0.07 1.61 ± 0.04 } $p = 0.002$	13.89 ± 0.92 9.05 ± 1.60 } $p = 0.002$
Diameter [um]	Median	178.68 ± 10.18 167.18 ± 15.21 } $p = 0.232$	187.60 ± 5.51 168.80 ± 19.50 } $p = 0.084$	163.09 ± 19.48 173.26 ± 8.52 } $p = 0.275$
	IQR	101.40 ± 16.73 84.91 ± 13.73 } $p = 0.193$	75.44 ± 7.57 103.06 ± 6.45 } $p = 0.002$	97.83 ± 6.08 96.68 ± 12.52 } $p = 1$
Length [mm]	Median	0.88 ± 0.06 0.68 ± 0.14 } $p = 0.006$	1.01 ± 0.08 0.88 ± 0.13 } $p = 0.002$	0.69 ± 0.05 0.74 ± 0.06 } $p = 0.193$
	IQR	0.75 ± 0.05 0.51 ± 0.07 } $p = 0.049$	75.44 ± 7.57 0.47 ± 0.05 } $p = 0.002$	0.41 ± 0.04 0.47 ± 0.08 } $p = 0.131$
Tortuosity	Median	1.11 ± 0.01 1.12 ± 0.00 } $p = 0.027$	1.11 ± 0.00 1.14 ± 0.01 } $p = 0.002$	1.13 ± 0.01 1.13 ± 0.01 } $p = 0.492$
	IQR	0.06 ± 0.01 0.08 ± 0.01 } $p = 0.084$	0.05 ± 0.01 0.09 ± 0.01 } $p = 0.002$	0.11 ± 0.02 0.12 ± 0.02 } $p = 0.625$
Track Density	Median	0.30 ± 0.06 0.22 ± 0.07 } $p = 0.006$	0.30 ± 0.05 0.16 ± 0.04 } $p = 0.002$	0.10 ± 0.03 0.17 ± 0.03 } $p = 0.002$
	IQR	0.09 ± 0.02 0.08 ± 0.01 } $p = 0.557$	0.12 ± 0.02 0.09 ± 0.02 } $p = 0.002$	0.07 ± 0.02 0.11 ± 0.02 } $p = 0.014$
Segment Density	Median	142.63 ± 87.94 183.70 ± 87.47 } $p = 0.275$	202.19 ± 97.16 123.43 ± 90.07 } $p = 0.049$	163.09 ± 19.48 169.00 ± 104.75 } $p = 0.275$
	IQR	50.88 ± 33.83 85.92 ± 37.58 } $p = 0.084$	94.39 ± 25.37 74.26 ± 34.19 } $p = 0.557$	95.06 ± 45.44 101.97 ± 62.73 } $p = 1$

velocity did not reveal significantly higher values for the median of arterial blood velocity ($p = 0.695$). The distribution of velocity estimates in different regions of the rat kidneys are shown in Fig. 10, demonstrating that blood velocities in the arterioles of the medullary regions (DVR in the IM and OM) were consistently estimated higher than the blood velocities in the venules.

The CDF plots of the velocity estimates and the corresponding peak velocities are shown in Fig. 11. The statistics of the peak velocities in different regions, summarized as the last metric for velocity in Table I, indicated that the difference between peak velocities of blood in the arteries and veins were statistically significant in the three regions.

The diameter of the bundles of DVR was larger than the groups of AVR in the OM and IM. In the cortical region, a larger median diameter was estimated for the veins. Even though the diameter estimates correspond to the visual appearance in

Fig. 8, only the IQR of the bundle diameters for the AVR and DVR in the OM was statistically significantly different. The distribution of estimated DVR and AVR bundle diameters in the OM region is shown in Fig. 12.

The segments of the DVR bundles were consistently estimated longer than those from the segments AVR bundles. The artery tracks in the CO were shorter than those from the veins; however, the comparison of this feature in this region did not show a significant difference ($p = 0.193$). The distributions of the segment length in the regions with a significant difference are shown in Fig. 13.

The segments of AVR bundles were consistently more tortuous than the segments of the DVR bundles in the OM ($p = 0.002$). The tortuosity distribution of segments in this region is shown in Fig. 14.

Segment density did not reveal any statistical difference between the two classes; on the other hand, track density showed

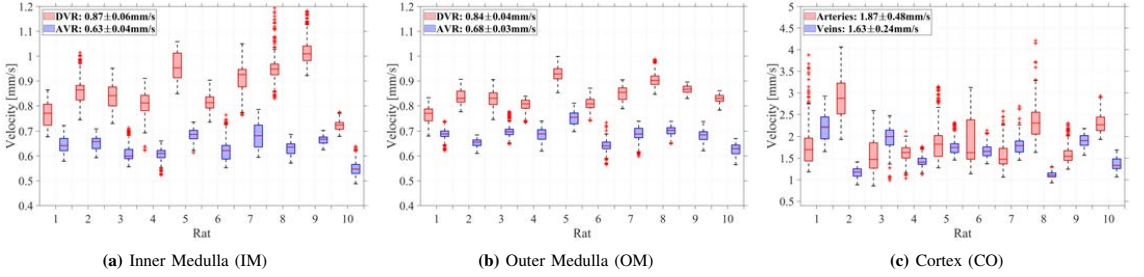


Fig. 10: Velocity distribution in different regions of the kidney

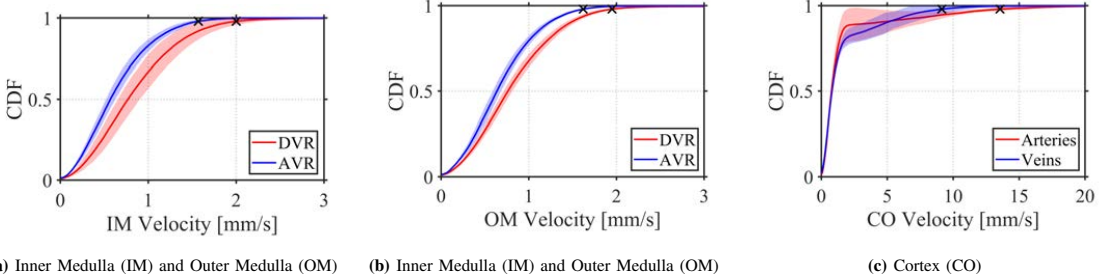


Fig. 11: CDF plots of velocity estimates in the **arteries** and **veins** in various regions for 10 rat kidneys. Solid line is the mean CDF plot and the shadow area is the standard deviation of the CDFs for 10 rats. Peak velocity is marked by \times .

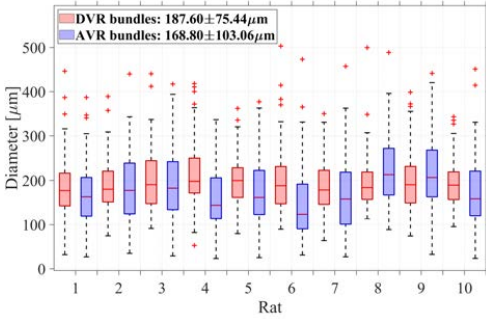


Fig. 12: Distribution of estimated diameters in the outer medulla

a consistent pattern of denser DVR in the IM and OM and denser veins in the CO ($p = 0.002$). The distribution of the track densities in all regions is shown in Fig. 15.

IV. DISCUSSION

This is the first time a study has investigated an automatic vessel segmentation and characterization of 10 healthy rat kidneys in SRI. The velocity map was employed for separation of arterial and venous flow inside the kidneys. The characterized arteries and veins were compared statistically in three different anatomical regions of the kidneys using the t -distribution confidence intervals and Wilcoxon signed-rank test. The statistics showed a clear differentiation between arterial and venous segments both in morphology and flow dynamics. The arteries and veins of the 10 kidneys were

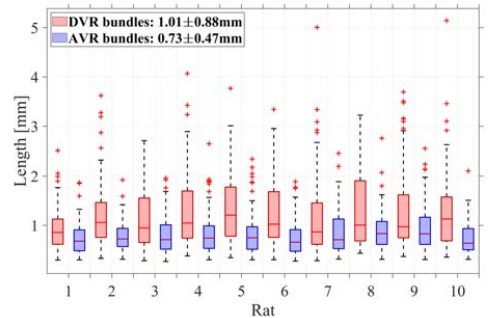
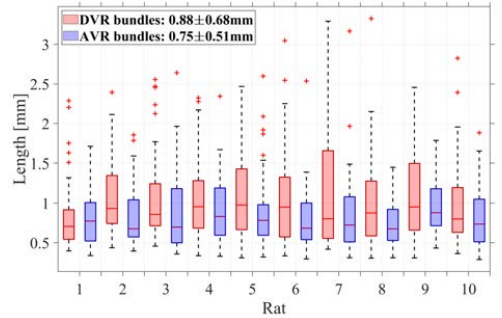


Fig. 13: Segment lengths distribution in the IM and OM regions.

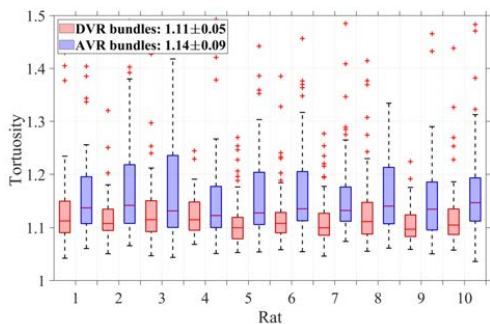
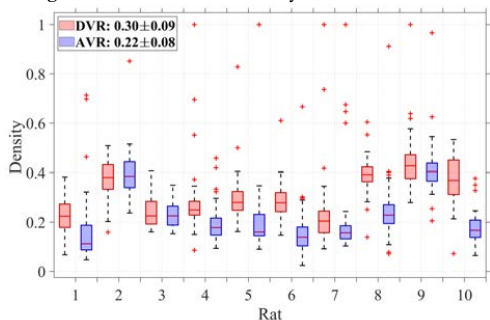
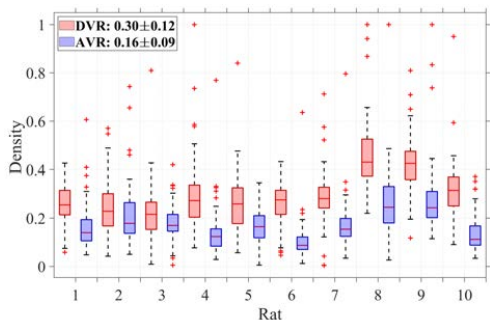


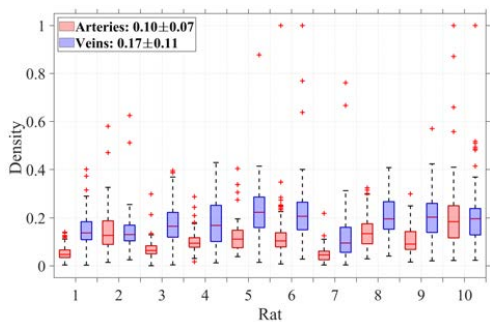
Fig. 14: Distribution of tortuosity in the outer medulla



(a) Inner Medulla (IM)



(b) Outer Medulla (OM)



(c) Cortex (CO)

Fig. 15: Track density distribution in different regions of the kidney

classified in a semi-automated manner, *i.e.*, the procedures required manual labeling of regions and general arterial flow directions in the labeled regions as prior information. However, the individual 300,000 tracks were classified automatically based only on the defined anatomical regions and arterial flow determination in each region.

Several features from the classified tracks and their segments were investigated and compared statistically. It was shown that the difference in the velocity estimates of the classified tracks was statistically significant in the IM and OM regions between arteries and veins. However, these trends were not seen in the CO. Several factors may contribute to the lower performance of velocity estimates in the cortical regions. First, the 3D complex structure of these rich vascular regions are projected in a 2D imaging plane, and sometimes, the arteries are sandwiched by veins [41]. Second, the blood flow in the larger arterial branches is pulsatile, and the peak velocity can reach several *cm/s*; nonetheless, the velocity estimation using particle tracking in SRI is limited to the order of 10 *mm/s*. Tracking algorithms may still under-perform in the presence of a high density of particles, the complex flow pattern of pulsatility, and the ambiguity of 3D to 2D projection. The average number of arterial tracks in CO was 55% lower than the venous tracks, depicting the difficulty of MB tracking in cortical arteries.

Most of the extracted features were statistically significant in the OM region. Moreover, the velocity and track density were two features that showed the statistical difference in all regions. However, other described features were not statistically significant in all regions. The unique anatomical structure of each kidney and the rats' different sizes and weights may also cause uncorrelated morphological characteristics. Moreover, the complexity of the morphological features in the 2D ultrasound SRI may be misinterpreted, when it is accumulated over a thick slice of 3D structure [41]. Therefore, the features calculated for segments, *e.g.*, tortuosity, may not be correspondent to the actual vessel existing in 3D.

Automatic segmentation of vessel structures in ultrasound SRI is still at the beginning of its development and requires more investigations. The segmentation performance must be evaluated using a gold standard. A gold standard requires a rich dataset of ultrasound SR images of kidneys that have been manually segmented by multiple experts and such a dataset are not yet available. At a more advanced level, such a gold standard allows training of deep neural network to extract more accurate and relevant features for blood vessel segmentation of kidneys.

It is also worth comparing and discussing the result from a clinical perspective. Several findings in clinical investigations as well as intrinsic nature of SRI based on ultrasound contrast agents can be used to justify features with insignificant difference. It is shown in [42] how the arteries are wrapped by a nearby vein. The difficulties in tracking MBs in the larger arteries could be because of both pulsatility of flow and the phenomenon of venous wrapping of renal arteries. For the same reasons the cortical artery diameters could be overestimated in SRI. Although it was expected to observe larger veins compared with arteries [40], the estimated interval

APPENDIX

for the diameters of arteries (163.09 ± 19.48) were roughly the same as the diameters of the veins (173.26 ± 8.52) and the difference was not statistically significant ($p = 0.275$). The DVR and AVR travel in vascular bundles, primarily in the OM [43]. It has been shown that the AVR are both wider and more numerous than DVR [44, 45], and when estimating the diameter of the bundles, one would anatomically expect the AVR to be wider than the DVR [43]. However, more MBs are available to track in the DVR compared with the AVR due to decay or burst of the bubbles, when they travel the long way in the vasa recta; therefore, the number of tracks from which the diameters were estimated was higher in the DVR compared with the AVR (the ratio of the number of DVR tracks to the number of AVR tracks was 2.28 ± 0.46 among all rats). In addition, the diameter of the vasa recta bundles that are measured in 2D SRI could be an overlap of several bundles [41], adding to the outcome of the diameter estimates. The same considerations are applicable for the track densities in the OM and IM, where from an anatomical point of view, the AVR was expected to be denser than the DVR.

On the other hand, there were some features that were not expected to be significantly different, *e.g.*, length of arterioles and veins in the IM and OM. This can also be explained by the nature of the SRI. As mentioned above, it seems that the MBs that are exposed to ultrasound waves for longer periods are more likely to have shorter life. With this hypothesis, the abundance of MBs in the DVR compared with the AVR can be justified as whatever exists in the AVR has passed through the DVR and were more exposed to the ultrasound waves.

It was not expected to see more tortuous AVR compared with DVR in healthy rats. The significant difference in the tortuosity of the centerlines in the outer medulla could be the result of 2D projection of 3D structure that exist in the elevational thickness of the ultrasound imaging plane and could cause a miss interpretation of the actual tortuosity of the vessels.

Some features correspond to the results from previous clinical investigations. The velocity in the arterioles was statistically significantly higher than in the venules. This was in line with the previous findings [44, 45]. Lastly, it was expected to find a denser structure of the veins in the cortex, as these are larger compared with the arteries, and it was easier to track MBs in them, as mentioned. Nevertheless, it should be noted that track density is pixel based and therefore a relative feature. It can be used for comparison as long as pixel size and track thickness of all images are the same.

V. CONCLUSION

This paper presented a procedure to classify arteries and veins in the ultrasound SR images of the rat kidneys, automatically segment the blood vessels, and extract several features of each class of vessels such as velocity, diameter, length, tortuosity, and density. The *t*-distribution of each feature with 95% confidence interval was reported, and it was shown that track density and velocity estimates of the arteries and veins were statistically significant in the different regions of the kidney. Finally this paper shed a light on the challenges of vessel characterization in 2D SRI and its comparison with a priori anatomical and physiological knowledge.

Moving average of the blood velocity in the OM region of 10 kidneys are shown in Fig. 16. A lower flow in the venules were observed regardless of uncertainties in the velocity estimation and this result were consistent among all rats. The classified images of 9 other kidneys are shown in Fig. 17.

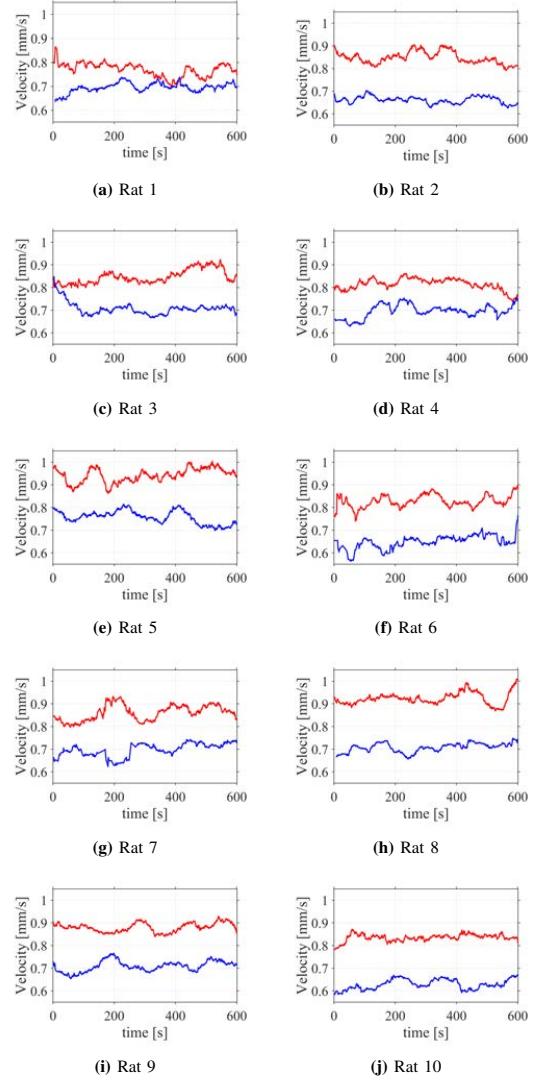


Fig. 16: The moving average blood velocity in the DVR (red) and AVR (blue) of the outer medulla in 10 healthy kidneys. The moving average window size is 1 minute. In all the cases, a lower velocity in the AVR was observed.

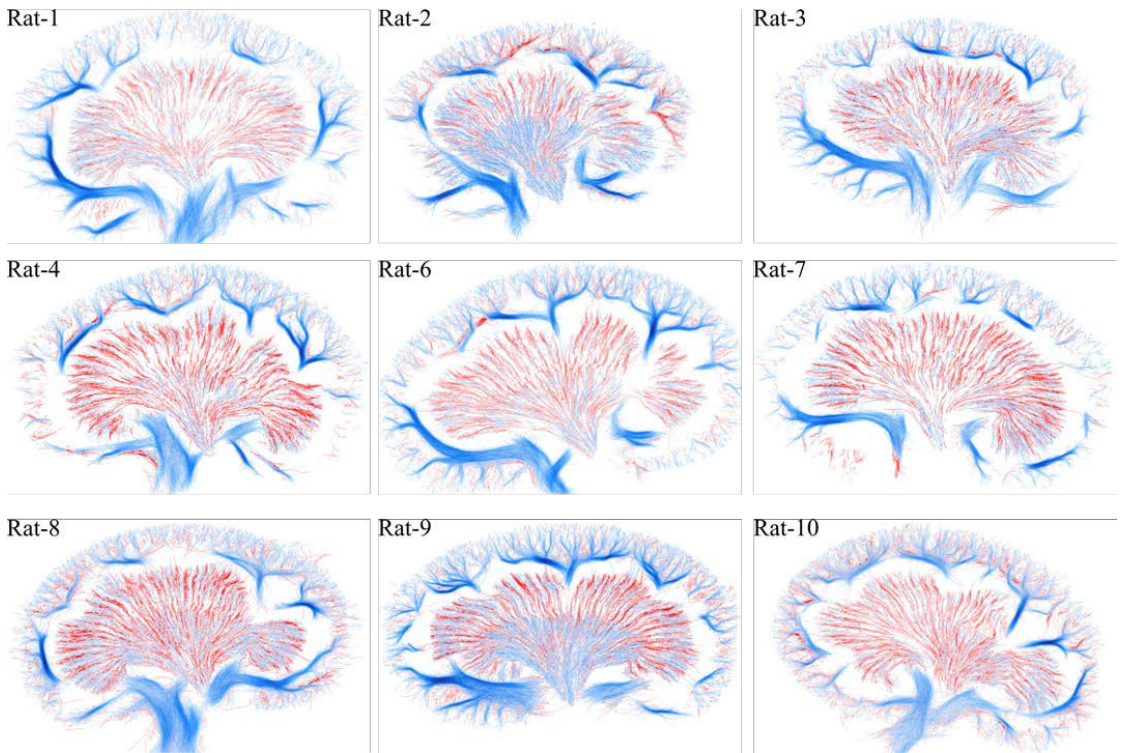


Fig. 17: SR images of the classified vessels on the other 9 kidneys. Arterioles are shown in red and venules in blue. The kidney for rat 5 is shown in Fig 8.

REFERENCES

- [1] M. M. Fraz, P. Remagnino, A. Hoppe, B. Uyyanonvara, A. R. Rudnicka, C. G. Owen, and S. A. Barman, "Blood vessel segmentation methodologies in retinal images - a survey," *Computer methods and programs in biomedicine*, vol. 108, no. 1, pp. 407–433, 2012.
- [2] M. S. Hassouna, A. A. Farag, S. Hushek, and T. Moriarty, "Cerebrovascular segmentation from tof using stochastic models," *Medical image analysis*, vol. 10, no. 1, pp. 2–18, 2006.
- [3] S. Cetin, A. Demir, A. Yezzi, M. Degertekin, and G. Unal, "Vessel tractography using an intensity based tensor model with branch detection," *IEEE Trans. Med. Imag.*, vol. 32, no. 2, pp. 348–363, 2012.
- [4] S. Cetin and G. Unal, "A higher-order tensor vessel tractography for segmentation of vascular structures," *IEEE Trans. Med. Imag.*, vol. 34, no. 10, pp. 2172–2185, 2015.
- [5] A. Klepaczko, P. Szczypiński, A. Deistung, and J. Reichenbach, "Simulation of mr angiography imaging for validation of cerebral arteries segmentation algorithms," *Computer methods and programs in biomedicine*, vol. 137, pp. 293–309, 2016.
- [6] C. Bauer, T. Pock, E. Sorantin, H. Bischof, and R. Beichel, "Segmentation of interwoven 3-D tubular tree structures utilizing shape priors and graph cuts," *Medical image analysis*, vol. 14, no. 2, pp. 172–184, 2010.
- [7] D. A. Oliveira, R. Q. Feitosa, and M. M. Correia, "Segmentation of liver, its vessels and lesions from ct images for surgical planning," *Biomedical engineering online*, vol. 10, no. 1, pp. 1–23, 2011.
- [8] E. Gocer, Z. K. Shah, and M. N. Gurcan, "Vessel segmentation from abdominal magnetic resonance images: adaptive and reconstructive approach," *International journal for numerical methods in biomedical engineering*, vol. 33, no. 4, p. e2811, 2017.
- [9] O. Friman, M. Hindennach, C. Kuhnel, and H. Peitgen, "Multiple hypothesis template tracking of small 3d vessel structures," *Medical image analysis*, vol. 14, no. 2, pp. 160–171, 2010.
- [10] M. Schaap, T. van Walsum, L. Neeffjes, C. Metz, E. Capuano, M. de Bruijne, and W. Niessen, "Robust shape regression for supervised vessel segmentation and its application to coronary segmentation in cta," *IEEE Trans. Med. Imag.*, vol. 30, no. 11, pp. 1974–1986, 2011.
- [11] H. Tang, T. van Walsum, R. S. van Onkelen, R. Hameeteman, S. Klein, M. Schaap, F. L. Tori, Q. J. van den Bouwhuisen, J. C. Witteman, A. van der Lugt *et al.*, "Semiautomatic carotid lumen segmentation for quantification of lumen geometry in multispectral mri," *Medical image analysis*, vol. 16, no. 6, pp. 1202–1215, 2012.
- [12] Y. Cheng, X. Hu, J. Wang, Y. Wang, and S. Tamura, "Accurate vessel segmentation with constrained b-snake," *IEEE Transactions on Image Processing*, vol. 24, no. 8, pp. 2440–2455, 2015.
- [13] A. Taha, P. Lo, J. Li, and T. Zhao, "Kid-net: convolution networks for kidney vessels segmentation from ct-volumes," in *International Conference on Medical Image Computing and Computer-Assisted Intervention*. Springer, 2018, pp. 463–471.
- [14] C. Wang, H. R. Roth, T. Kitasaka, M. Oda, Y. Hayashi, Y. Yoshino, T. Yamamoto, N. Sassa, M. Goto, and K. Mori, "Precise estimation of renal vascular dominant regions using spatially aware fully convolutional networks, tensor-cut and voronoi diagrams," *Computerized Medical Imaging and Graphics*, vol. 77, p. 101642, 2019.
- [15] C. Wang, M. Oda, Y. Hayashi, Y. Yoshino, T. Yamamoto, A. F. Frangi, and K. Mori, "Tensor-cut: A tensor-based graph-cut blood vessel segmentation method and its application to renal artery segmentation," *Medical image analysis*, vol. 60, p. 101623, 2020.
- [16] A. Amir-Khalili, G. Hamarneh, and R. Abugharbieh, "Automatic vessel segmentation from pulsatile radial distension," in *International Conference on Medical Image Computing and Computer-Assisted Intervention*. Springer, 2015, pp. 403–410.
- [17] E. Smistad and L. Løvstakken, "Vessel detection in ultrasound images using deep convolutional neural networks," in *Deep Learning and Data Labeling for Medical Applications*. Springer, 2016.
- [18] W. N. McDicken, G. R. D. Sutherland, C. M. Moran, and L. N. Gordon, "Color Doppler velocity imaging of the myocardium," *Ultrasound Med.*

- Biol.*, vol. 18, no. 6-7, pp. 651–654, 1992.
- [19] J. Rubin, R. Bude, P. Carson, R. Bree, and R. Adler, "Power Doppler US: a potentially useful alternative to mean frequency-based color Doppler US," *Radiology*, vol. 190, pp. 853–856, 1994.
- [20] J. A. Jensen, S. I. Nikolov, A. Yu, and D. Garcia, "Ultrasound vector flow imaging I: Sequential systems," *IEEE Trans. Ultrason., Ferroelec., Freq. Contr.*, vol. 63, no. 11, pp. 1704–1721, 2016.
- [21] —, "Ultrasound vector flow imaging II: Parallel systems," *IEEE Trans. Ultrason., Ferroelec., Freq. Contr.*, vol. 63, no. 11, pp. 1722–1732, 2016.
- [22] S. B. Feinstein, B. Coll, D. Staub, D. Adam, A. F. Schinkel, J. Folkert, and K. Thomenius, "Contrast enhanced ultrasound imaging," *Journal of nuclear cardiology*, vol. 17, no. 1, pp. 106–115, 2010.
- [23] Y. Desailly, J. Pierre, O. Couture, and M. Tanter, "Resolution limits of ultrafast ultrasound localization microscopy," *Phys. Med. Biol.*, vol. 60, no. 22, pp. 8723–8740, 2015.
- [24] K. Christensen-Jeffries, R. J. Browning, M. Tang, C. Dunsby, and R. J. Eckersley, "In vivo acoustic super-resolution and super-resolved velocity mapping using microbubbles," *IEEE Trans. Med. Imag.*, vol. 34, no. 2, pp. 433–440, February 2015.
- [25] C. Errico, J. Pierre, S. Pezet, Y. Desailly, Z. Lenkei, O. Couture, and M. Tanter, "Ultrafast ultrasound localization microscopy for deep super-resolution vascular imaging," *Nature*, vol. 527, pp. 499–502, November 2015.
- [26] K. Christensen-Jeffries, O. Couture, P. A. Dayton, Y. C. Eldar, K. Hynynen, F. Kiessling, M. O'Reilly, G. F. Pinton, G. Schmitz, M. Tang *et al.*, "Super-resolution ultrasound imaging," *Ultrasound Med. Biol.*, vol. 46, no. 4, pp. 865–891, 2020.
- [27] V. Hingot, C. Errico, B. Heiles, L. Rahal, M. Tanter, and O. Couture, "Microvascular flow dictates the compromise between spatial resolution and acquisition time in ultrasound localization microscopy," *Scientific Reports*, vol. 9, no. 1, pp. 1–10, 2019.
- [28] K. Wei, E. Le, J. Bin, M. Coggins, J. Thorpe, and S. Kaul, "Quantification of renal blood flow with contrast-enhanced ultrasound," *Journal of the American College of Cardiology*, vol. 37, no. 4, pp. 1135–1140, 2001.
- [29] S. B. Andersen, C. A. V. Hoyos, I. Taghavi, F. Gran, K. L. Hansen, C. M. Sørensen, J. A. Jensen, and M. B. Nielsen, "Super-resolution ultrasound imaging of rat kidneys before and after ischemia-reperfusion," in *Proc. IEEE Ultrason. Symp.*, 2019, pp. 1–4.
- [30] S. B. Andersen, I. Taghavi, C. A. V. Hoyos, S. B. Søgaard, F. Gran, L. Lonn, K. L. Hansen, J. A. Jensen, M. B. Nielsen, and C. M. Sørensen, "Super-resolution imaging with ultrasound for visualization of the renal microvasculature in rats before and after renal ischemia: A pilot study," *Diagnostics*, vol. 10, no. 11, p. 862, 2020.
- [31] S. B. Søgaard, S. B. Andersen, I. Taghavi, C. A. V. Hoyos, K. L. Hansen, F. Gran, J. A. Jensen, M. B. Nielsen, and C. M. Sørensen, "Super-resolution ultrasound imaging of the renal microvasculature in rats with metabolic syndrome," in *Proc. IEEE Ultrason. Symp.*, 2020, pp. 1–4.
- [32] M. R. Lowerison, C. Huang, F. Lucien, S. Chen, and P. Song, "Ultrasound localization microscopy of renal tumor xenografts in chicken embryo is correlated to hypoxia," *Scientific reports*, vol. 10, no. 1, pp. 1–13, 2020.
- [33] I. Ozdemir, K. Johnson, S. Mohr-Allen, K. E. Peak, V. Varner, and K. Hoyt, "Three-dimensional visualization and improved quantification with super-resolution ultrasound imaging-validation framework for analysis of microvascular morphology using a chicken embryo model," *Phys. Med. Biol.*, vol. 66, no. 8, p. 085008, 2021.
- [34] S. Harput, M. Toulemonde, A. Ramalli, K. Christensen-Jeffries, E. Boni, P. Tortoli, C. Dunsby, and M. Tang, "Quantitative microvessel analysis with 3-D super-resolution ultrasound and velocity mapping," in *Proc. IEEE Ultrason. Symp.*, 2020, pp. 1–4.
- [35] J. A. Jensen, M. L. Ommen, S. H. Øygard, M. Schou, T. Sams, M. B. Stuart, C. Beers, E. V. Thomsen, N. B. Larsen, and B. G. Tomov, "Three-dimensional super resolution imaging using a row-column array," *IEEE Trans. Ultrason., Ferroelec., Freq. Contr.*, vol. 67, no. 3, pp. 538–546, 2020.
- [36] I. Taghavi, S. B. Andersen, S. B. Søgaard, M. B. Nielsen, C. M. Sørensen, M. B. Stuart, and J. A. Jensen, "Automatic classification of arterial and venous flow in super-resolution ultrasound images of rat kidneys," in *Proc. IEEE Ultrason. Symp.*, 2021, pp. 1–4.
- [37] S. Moccia, E. D. Momi, S. E. Hadji, and L. S. Mattos, "Blood vessel segmentation algorithms—review of methods, datasets and evaluation metrics," *Computer methods and programs in biomedicine*, vol. 158, pp. 71–91, 2018.
- [38] I. Taghavi, S. B. Andersen, C. A. V. Hoyos, M. B. Nielsen, C. M. Sørensen, and J. A. Jensen, "In vivo motion correction in super resolution imaging of rat kidneys," *IEEE Trans. Ultrason., Ferroelec., Freq. Contr.*, vol. 68, no. 10, pp. 3082–3093, 2021.
- [39] I. Taghavi, S. B. Andersen, C. A. V. Hoyos, M. Schou, S. H. Øygard, F. Gran, K. L. Hansen, C. M. Sørensen, M. B. Nielsen, M. B. Stuart, and J. A. Jensen, "Tracking performance in ultrasound super-resolution imaging," in *Proc. IEEE Ultrason. Symp.*, 2020, pp. 1–4.
- [40] D. A. Nordsletten, S. Blackett, M. D. Bentley, E. L. Ritman, and N. P. Smith, "Structural morphology of renal vasculature," *Am. J. Physiol. Heart Circ. Physiol.*, vol. 291, no. 1, pp. 296–309, 2006.
- [41] S. B. Andersen, I. Taghavi, H. M. Kjer, S. B. Søgaard, C. Gundlach, V. A. Dahl, M. B. Nielsen, A. B. Dahl, J. A. Jensen, and C. M. Sørensen, "Validation of 2D ultrasound super-resolution imaging of the rat renal vasculature using ex vivo micro-computed tomography," *Scientific Reports*, p. (Under review), 2021.
- [42] Z. Khan, J. P. Ngo, B. Le, R. G. Evans, J. T. Pearson, B. S. Gardiner, and D. W. Smith, "Three-dimensional morphometric analysis of the renal vasculature," *American Journal of Physiology-Renal Physiology*, vol. 314, no. 5, pp. F715–F725, 2018.
- [43] H. Ren, L. Gu, A. Andreasen, J. S. Thomsen, L. Cao, E. I. Christensen, and X. Zhai, "Spatial organization of the vascular bundle and the interbundle region: three-dimensional reconstruction at the inner stripe of the outer medulla in the mouse kidney," *American Journal of Physiology-Renal Physiology*, vol. 306, no. 3, pp. F321–F326, 2014.
- [44] C. Holliger, K. V. Lemley, S. L. Schmitt, F. C. Thomas, C. R. Robertson, and R. L. Jamison, "Direct determination of vasa recta blood flow in the rat renal papilla," *Circ. Research*, vol. 53, no. 3, pp. 401–413, 1983.
- [45] B. Zimmerhackl, C. R. Robertson, and R. L. Jamison, "Fluid uptake in the renal papilla by vasa recta estimated by two methods simultaneously," *Am. J. Physiol.*, vol. 248, no. 3, pp. F347–53, 1985.



Paper 6

Super-resolution ultrasound imaging can quantify alterations in intrarenal microbubble velocities in rats

Sofie Bech Andersen, **Iman Taghavi**, Stinne Byrholdt Søggaard, Carlos Armando Villagómez Hoyos, Michael Bachmann Nielsen, Jørgen Arendt Jensen, and Charlotte Mehlin Sørensen.

Name of journal in:

Diagnostics

Document Version:

Submitted

DOI:

—

General rights

Copyright and moral rights for the publications made accessible in the public portal are retained by the authors and/or other copyright owners and it is a condition of accessing publications that users recognise and abide by the legal requirements associated with these rights.

- Users may download and print one copy of any publication from the public portal for the purpose of private study or research.
- You may not further distribute the material or use it for any profit-making activity or commercial gain
- You may freely distribute the URL identifying the publication in the public portal

If you believe that this document breaches copyright please contact us providing details, and we will remove access to the work immediately and investigate your claim.

Super-resolution ultrasound imaging can quantify alterations in microbubble velocities in the renal vasculature of rats

Sofie Bech Andersen^{1,2,*}, Iman Taghavi³, Stinne Byrholdt Søgaard^{1,2}, Carlos Villagómez Hoyos⁴, Michael Bachmann Nielsen^{2,5}, Jørgen Arendt Jensen³, Charlotte Mehlin Sørensen¹

¹ Department of Biomedical Sciences, University of Copenhagen, 2200 Copenhagen, Denmark; anne.sofie.bech.andersen@regionh.dk (S.B.A.); stinnebyrholdt@gmail.com (S.B.S.); cmehlin@sund.ku.dk (C.M.S.)

² Department of Diagnostic Radiology, University Hospital Rigshospitalet, 2100 Copenhagen, Denmark; mbn@dadlnet.dk (M.B.N.)

³ Center for Fast Ultrasound Imaging, Department of Health Technology, Technical University of Denmark, 2800 Lyngby, Denmark; imat@dtu.dk (I.T.); jaje@dtu.dk (J.A.J.)

⁴ BK Medical ApS, 2880 Herlev, Denmark; carlos.villagomezhoyos@gmail.com (C.V.H.)

⁵ Department of Clinical Medicine, University of Copenhagen, 2200 Copenhagen, Denmark

* Correspondence: anne.sofie.bech.andersen@regionh.dk (S.B.A)

Abstract: Super-resolution ultrasound imaging, based on the localization and tracking of single intravascular microbubbles, makes it possible to map vessels below 100 μm . The microbubbles' velocities can be estimated as a surrogate for blood velocity, but their clinical potential is unclear. We investigated if a decrease in microbubble velocity in the arterial and venous beds of the renal cortex, outer medulla, and inner medulla was detectable after intravenous administration of the $\alpha 1$ -adrenoceptor antagonist prazosin. The left kidneys of seven rats were scanned with super-resolution ultrasound for 10 min before, during, and after prazosin administration using a bk5000 ultrasound scanner and hockey-stick probe. The super-resolution images were manually segmented, separating cortex, outer medulla, and inner medulla. Microbubble tracks from arteries/arterioles were separated from vein/venule tracks using the arterial blood flow direction. The mean microbubble velocity from each scan was compared. It showed a significant prazosin-induced velocity decrease only in the cortical arteries/arterioles (from 1.59 ± 0.38 to 1.14 ± 0.31 to 1.18 ± 0.33 mm/sec, $P = 0.013$) and outer medulla descending vasa recta (from 0.70 ± 0.05 to 0.66 ± 0.04 to 0.69 ± 0.06 mm/sec, $P = 0.026$). Conclusively, super-resolution ultrasound imaging makes it possible to detect and differentiate microbubble velocity responses to prazosin simultaneously in the cortical and medullary vascular beds.

Keywords: contrast-enhanced ultrasound; ultrasound localization microscopy; kidneys; microvascular flow; Sprague-Dawley rats; prazosin

1. Introduction

Super-resolution ultrasound (SRUS) imaging allows mapping of the vasculature below the diffraction limit of conventional ultrasound, making in vivo microvascular ultrasound imaging possible [1]. The unique arrangement of the renal vasculature is central in the filtration of plasma and the secretion/reabsorption processes that determine the final urine composition, all required for normal renal function. Additionally, renal blood flow alterations have been linked with, e.g., diabetic nephropathy and renal ischemia-reperfusion injury [2–6]. Measuring the intrarenal blood flow is difficult due to the lack of in-depth microvascular imaging methods. From 2D SRUS data, estimations of the in-plane velocities from every vessel in an entire image cross-section can be made. Accordingly, SRUS can evaluate renal cortical and medullary blood velocities simultaneously. The estimated velocities are based on tracking individual moving intravascular microbubbles (MBs) between image frames [7,8]. MBs have rheology similar to erythrocytes, so their velocity corresponds to blood velocity [9–11]. Many strategies have been undertaken to link individual MBs across frames to generate reliable velocity estimations. Initially, MBs were tracked by connecting an individual MB to the nearest MB in the next frame or cross-correlating each MB's intensity in small search windows between successive frames [7,8]. Since then, more advanced approaches have been proposed [12–17].

SRUS data have been used to study structural vascular alterations in different diseases, including chronic kidney disease, cancer, and vasa vasorum in atherosclerosis [18–22]. MB velocities have been extracted from healthy animal and human organs, including the kidneys [23,24]. Recently, the technique has shown turbulent flow inside a human cerebral aneurism [25]. In the cerebral vasculature of old mice, MB velocities were shown to decrease compared with younger animals [26].

The velocities are registered in MB velocity maps, showing the MB tracks from all types of vessels in the ultrasound field of view. In the mouse cerebral vasculature, the MB velocities were estimated across all vessel types in different functional brain areas [26]. Like the brain, the different anatomical areas of the kidneys have unique functions with a corresponding unique vascular anatomy and blood flow. This study aimed at investigating the quantitative possibilities of SRUS-derived MB velocities from rat kidneys using a setup with a clinical ultrasound scanner and a hierarchical Kalman tracker for MB velocity estimation [13]. Prazosin is an α 1-adrenoceptor antagonist that can substantially decrease mean arterial pressure and renal blood flow. We investigated if a decrease in MB velocity in the separated arterial and venous beds of the renal cortex, outer medulla, and inner medulla was detectable after intravenous prazosin administration.

2. Materials and Methods

2.1. Ethical considerations

All procedures presented in this paper were conducted following protocols approved by the National Animal Experiments Inspectorate under the Ministry of Environment and Food (license number 2020-15-0201-00547 issued on June 4th 2020). The experiments were ethically in accordance with the EU Directive 2010/63/EU for animal experiments. The rats were held in a 12/12-h light/dark cycle and could freely access standard chow and water. Trained animal caretakers were responsible for the rats' well-being until the experiments.

2.2. Animal preparations

Eight male Sprague Dawley rats were scanned; seven were included in the results (see exclusion criteria below). Physiological data on the rats are found in Supplementary Table S1. Initial anaesthetization was performed in a chamber supplied with 5% isoflurane in 65% nitrogen/35% oxygen, followed by tracheotomy, tube insertion, and ventilation with a mechanical ventilator (Ugo Basile, Gemonio, Italy; 69 breaths/min). 1–2% isoflurane maintained anesthesia. Two catheters were inserted in the left jugular vein: One for infusion of the muscle relaxant, Nimbex (0.85 mg/ml, GlaxoSmithKline, London, UK, 20 μ l/min) and injection of prazosin hydrochloride (0.1 mg/kg, Sigma-Aldrich, MO, USA), and one for infusion of SonoVue (Bracco, Milan, Italy). A catheter in the right carotid artery was connected to a Gould Statham P23-dB pressure transducer (Gould, CA, USA), continuously recording the mean arterial pressure (MAP). The rats lay on a heating table (\sim 37°C) and laparotomy exposed the left kidney. A metal retractor on the left side of the diaphragm reduced respiratory motion transferred to the kidney.

2.3. Ultrasound scanning and prazosin injection procedure

The rats were scanned directly on the left kidney using a commercial bk5000 ultrasound scanner (BK Medical, Herlev, Denmark) modified for long data acquisitions. An X18L5s hockey-stick probe (BK Medical, Herlev, Denmark) was secured with a holder on the lateral side of the kidney to obtain central coronal image slices that included both the renal cortex and medulla. The image plane was found using orientation with B-mode. The SRUS data were obtained with line-per-line imaging (center freq. 10 MHz, mechanical index 0.1, frame rate 54 Hz) using amplitude modulation, interleaved with B-mode imaging used for motion estimation. The rats were scanned for 10 min using a 1:20 dilution of the SonoVue infused at 40–55 μ l/min (SP210iw syringe pump, WPI, Friedberg, Germany). Infusion rate was adjusted according to visible MBs on the contrast-enhancing scanner display. For continuous MB inflow, the syringe turned 180°

every 10 sec. The rats were SRUS scanned three times (Figure 1). Prazosin was administered during the first minutes of SRUS scan 2. Triplex Doppler was acquired before SRUS scan 1 and after SRUS scan 3 on the renal artery or one of its branches. Rats were excluded if MAP < 70 mmHg at baseline or if there was no MAP response to prazosin. After the experiment, the rats were euthanized in anesthesia.

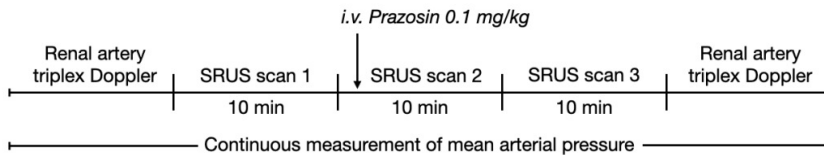


Figure 1. Timing of ultrasound scans and prazosin injection. Triplex Doppler includes B-mode imaging plus color and spectral Doppler. i.v. = intravenous, SRUS = super-resolution ultrasound.

2.4. Super-resolution ultrasound imaging post-processing and region labeling

The SRUS data were motion-compensated and MBs were tracked using a hierarchical Kalman tracker (maximum linking distance: 278 μm . Only MBs trajectories that spanned across min. three consecutive frames were considered a track) [13,27]. Afterward, the MB tracks were inserted in high-resolution images to generate the SRUS images. In MATLAB (R2020b, MathWorks, MA, USA), the resulting MB velocity maps were manually labeled by S.B.A. with the three separate areas: cortex, outer medulla, and inner medulla (see example in the Results section). The cortex was delineated with an inner boundary (toward the medulla) superficial to the larger arcuate vessels that run between cortex and medulla. The outer medullas superficial boundary was set $\sim 0.5\text{-}1$ mm from the arcuate or segmental vessels, meaning that the outer stripe of outer medulla was not fully included. The loss of vascular bundles defined the transition from outer to inner medulla. In each area, smaller regions of interest were drawn in which a mean flow angle for the arterial flow was defined. A span of vessels going 125° (cortex) or 90° (medulla) from the mean angle was included as artery/arteriole tracks. As the afferent arterioles radiate at different angles from the cortical radial arteries, the vessel span was wider in the cortex. Vein tracks were defined as tracks going in the opposite direction from the mean artery flow angle [28].

2.5. Microbubble velocity estimations

MB velocities were estimated in six different vascular beds: cortical arteries/arterioles, cortical veins/venules, outer medulla descending vasa recta, outer medulla ascending vasa recta, inner medulla descending vasa recta, and inner medulla ascending vasa recta. Generally, SRUS data must be acquired over a certain period depending on ultrasound equipment, acquisition technique, and vascular bed to obtain enough MB detections to generate a complete (or near-complete) image of the vasculature [29–32]. The MB velocities are typically calculated from the entire scan period to get the most reliable estimates; hence, the mean velocities from the three consecutive SRUS scans were compared. However, during a minute-long period, dynamic alterations in the blood flow can occur [33–35]. To better visualize dynamic alterations during scanning, the estimated MB velocities were displayed in graphs as moving averages (30-sec window). The MB velocities from the following shorter periods of SRUS scan 2 were also compared to investigate the possibilities of quantifying the immediate response to prazosin: Baseline velocity (first 30 sec), the velocity at the max effect of prazosin on MAP (30 sec with lowest MAP) and recovery velocity (30 last sec). Time for prazosin administration during SRUS scan 2 varied between animals from 51 to 184 sec after scan start. Therefore, MAP and MB velocities from SRUS scan 2 were aligned according to the prazosin injection time, with moving average MB velocities starting from 50 sec before injection and ending 410 sec after injection for all rats. The mean MB velocity for SRUS scan 2 was estimated after

prazosin injection resulting in 410 sec of data. For SRUS scans 1 and 3, the 410 first sec of the acquisition were used to match SRUS scan 2. An overview of the different periods is shown in Figure 2.

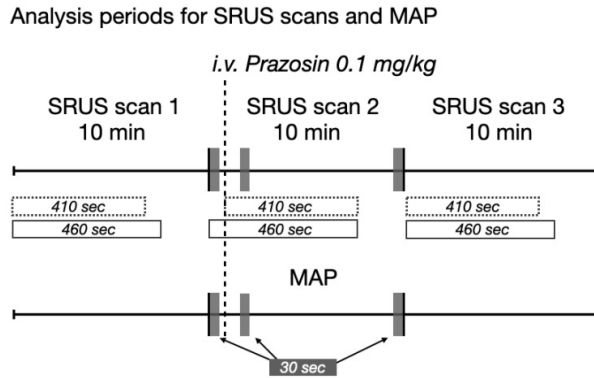


Figure 2. Overview of the analysis periods for the SRUS and MAP data. The 30-sec periods compared in SRUS scan 2 and during MAP measurement are marked with grey blocks. The 410 sec of SRUS data used to compare the mean microbubble velocity in the three scans are marked by the dotted-line blocks. The 460 sec periods shown in the graphs with moving average microbubble velocities are the solid-line blocks. MAP = mean arterial pressure, SRUS = super-resolution ultrasound.

2.6. Statistical analyses

Two variables (e.g. MB velocity in arteries vs. veins) were compared with paired t-test. Three consecutive measurements (e.g. MB velocities from the three SRUS scans) were compared with repeated measures one-way ANOVA with a Greenhouse-Geisser correction. Post-hoc between-group comparisons were made with Tukey's multiple comparisons test. The scatter plots and graphs all show the means from the raw data. Statistical tests were calculated on transformed data (log or square-rooted) if they had a non-normal distribution. Statistical tests, graphs, and plots were made in GraphPad Prism (version 9.2.0 for Mac, GraphPad Software, CA, USA).

3. Results

3.1. Segmentation and analysis of the normal renal vasculature

Figure 3 illustrates how the MB velocity map segmentation allowed separating the arterial and venous MB tracks in the three areas. By separating the descending from ascending vasa recta, the vascular organization of the medulla stood out, e.g., with a clear visualization of the descending vasa recta bundles of the outer medulla's inner stripe (Figure 3b). In the inner medulla, the bundle organization of the descending vasa recta is lost [36], which is also evident from Figure 3b. The MB velocities in the cortical arteries/arterioles and the descending vasa recta were higher than in the cortical veins/venules and ascending vasa recta, respectively (Figure 3c). The ascending vasa recta are more numerous and larger in diameter than the descending vasa recta, which matches the slower velocity [37]. However, the mean number of descending vasa recta tracks was higher than ascending ones (SRUS scan 1: 1581 ± 366 vs. 1338 ± 398 , $P = 0.024$), which could be because many MBs disrupt before reaching the ascending vasa recta, as hypothesized by Foiret et al. [23]. The baseline MB velocity in the cortical arteries/arterioles tended to decrease with decreasing MAP (Figure 3d). However,

some rats had a MAP below the lower limit of renal autoregulation, which usually ensures stable renal blood flow during acute changes in MAP.

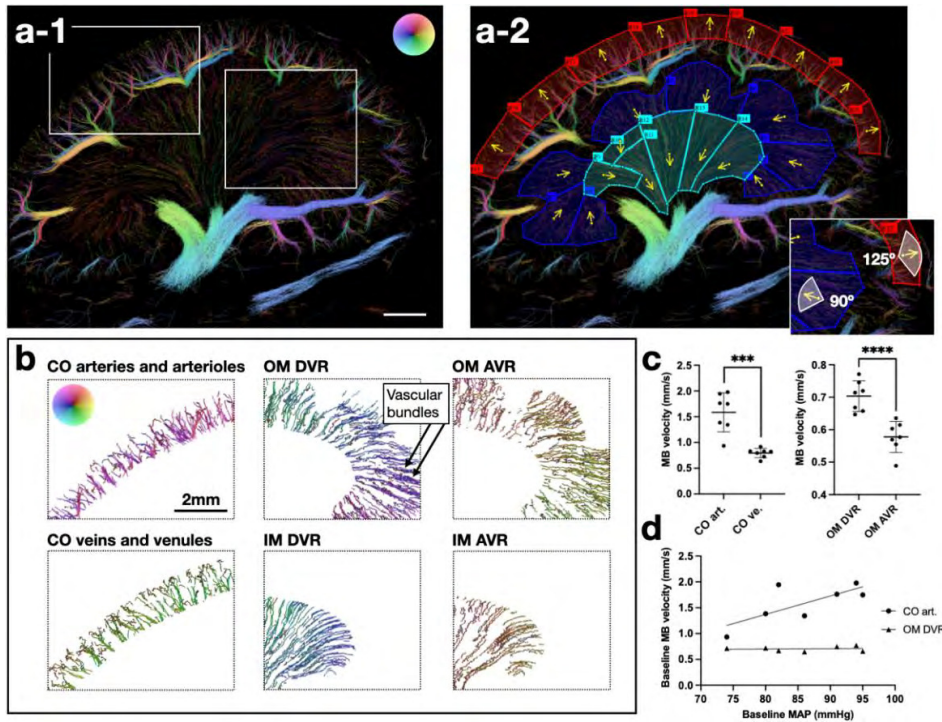


Figure 3. Segmentation of rat kidneys with separation of arteries/arterioles and veins/venules in the cortex, outer medulla, and inner medulla. (a-1) and (a-2) show an example of the regions used to separate arteries/arterioles and veins/venules in different areas. The colors of the wheel in a-1 show the direction of flow, the color intensity indicates velocity (range 0-20 mm/sec, brighter colors are faster). In a-2, red is the cortex, dark blue is the outer medulla, and turquoise is the inner medulla. The yellow arrows indicate the mean angle for arterial flow direction. Insert shows the 90° vs 125° span in the medulla and cortex, respectively, from which the arterial tracks were included. (b) Shows the separated tracks from the inserts in a-1. Notice how the descending vasa recta vascular bundles stand out. The brightest color corresponds to 5 mm/s in the outer and inner medulla regions and 20 mm/sec in the cortical regions. (c) Distribution of mean MB velocities from the raw data of arterial vs venous tracks. Asterisks indicate results of paired t-test on the log-transformed MB velocities in cortical arteries/arterioles vs cortical veins/venules (left graph, $P = 0.0006$) and square root-transformed MB velocities of the outer medulla descending vs. ascending vasa recta (right graph, $P < 0.0001$). (d) Shows the relationship between baseline MB velocity in the arteries/arterioles of cortex and outer medulla and the MAP. Pearson's correlation of log-transformed MB velocities from the cortical arteries/arterioles and MAP: $R^2 = 0.62$, $P = 0.035$. AVR = ascending vasa recta, CO = cortex, DVR = descending vasa recta, IM = inner medulla, MAP = mean arterial pressure, MB = microbubble, OM = outer medulla. Scale bar in a-1 = 2 mm.

3.2. Effects of prazosin on MAP and intrarenal microbubble velocities

The MAP was 84 ± 8 (mean \pm standard deviation) mmHg during the first 30 sec of SRUS scan 2 (Figure 4a-1), similar to MAP during SRUS scan 1 (86 ± 8 mmHg). The maximum drop in MAP occurred 52-82 sec after prazosin injection (54 ± 4 mmHg) (Figures 4a-1 and 4a-2). At the end of SRUS scan 2, MAP had increased to 65 ± 8 mmHg and remained low in

SRUS scan 3 (65 ± 6 mmHg). The renal artery's typical spectral Doppler pulsed-wave pattern with a high end-diastolic velocity (Figure 4b-1) changed to a pattern with low end-diastolic velocity after prazosin (Figure 4b-2), reflecting the decreased vascular tone. Triplex Doppler images from all rats are found in Supplementary Figure S1.

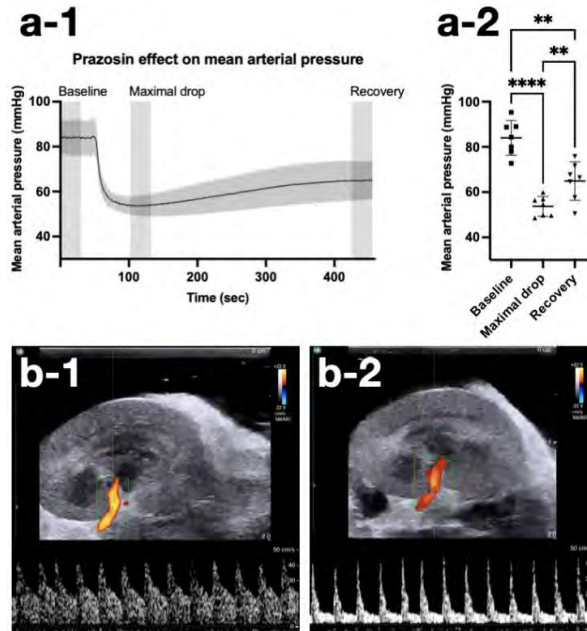


Figure 4. Effect of prazosin on mean arterial pressure and renal artery triplex Doppler. **(a-1)** Shows the effect of prazosin on mean arterial pressure during SRUS scan 2. The 30-sec periods (grey columns) were compared using a repeated measures one-way ANOVA with a Greenhouse-Geisser correction ($F(1.878, 11.27) = 65.00, P < 0.0001$). In **(a-2)**, the asterisks indicate the results of Tukey's multiple comparisons test (baseline vs. max drop $P < 0.0001$, max drop vs. recovery $P = 0.007$, baseline vs. recovery $P = 0.002$). **(b-1)** Shows an example of the color Doppler and spectral Doppler wave pattern from the renal artery or one of its branches at baseline before SRUS scan 1. **(b-2)** Shows color Doppler and the spectral Doppler wave pattern from the same artery after completion of SRUS scan 3. SRUS = super-resolution ultrasound.

To further support the estimated MB velocities, ultrasonic perivascular flow probe measurements of renal blood flow after prazosin injection from a separate unpublished trial are found in Supplementary Figure S2 (could not be included in this study due to ultrasonic signal distortion). They showed that prazosin at a lower dose (0.0125 mg/kg vs. 0.1 mg/kg) significantly decreased the renal blood flow.

The moving average MB velocities from the six vascular beds during SRUS scan 1-3 are displayed in Figure 5.

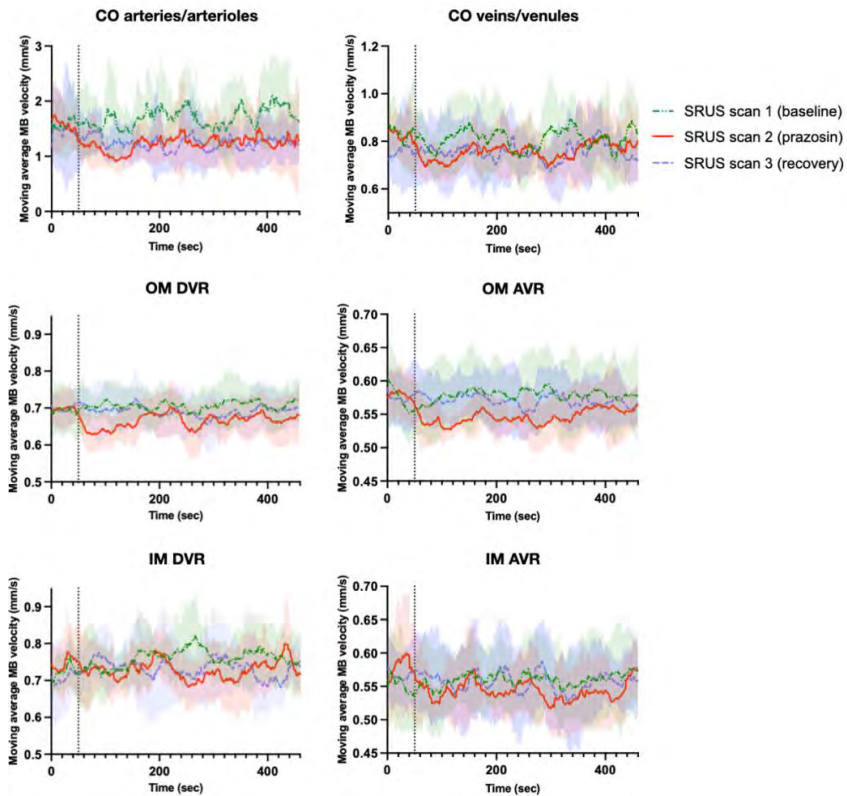


Figure 5. Moving average MB velocities (30-sec window) in the arterial and venous beds of the cortex, outer medulla, and inner medulla during the three consecutive SRUS scans. The vertical dotted line indicates the time for prazosin injection. The semisolid colored areas are the standard deviations. AVR = ascending vasa recta, CO = cortex, DVR = descending vasa recta, IM = inner medulla, MB = microbubble, OM = outer medulla, SRUS = super-resolution ultrasound.

In the cortical arteries/arterioles, outer medulla descending vasa recta, and outer medulla ascending vasa recta, a prazosin-induced MB velocity drop was visible in SRUS scan 2 when compared with SRUS scan 1. In the cortical arteries/arterioles, the decrease seemed to continue in SRUS scan 3, while in the outer medulla ascending vasa recta and outer medulla ascending vasa recta, the velocity increased to baseline levels in SRUS scan 3. A velocity decrease in the cortical veins/venules also seemed to occur after prazosin, but similar random fluctuations were seen during SRUS scan 1. In the inner medulla descending vasa recta and inner medulla ascending vasa recta, no apparent effect of prazosin was visible.

In Figure 6, the MB velocities from the cortical arteries/arterioles, outer medulla descending vasa recta, and outer medulla ascending vasa recta are displayed along with the MAP during each scan to illustrate the temporal relationship between the two parameters.

204
205
206
207
208
209
210
211
212
213
214
215
216
217
218
219
220
221

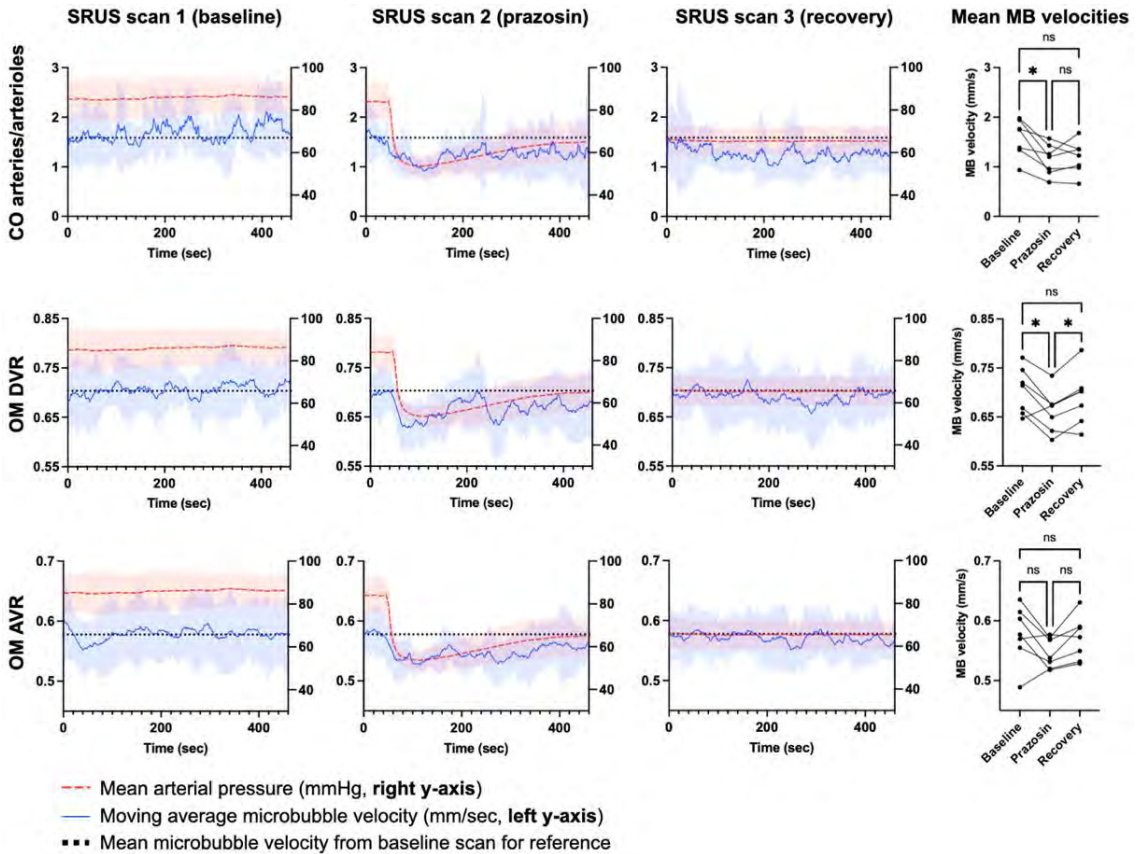


Figure 6. Moving average MB velocities (30-sec window) in the cortical arteries/arterioles, outer medulla descending vasa recta, and outer medulla ascending vasa recta for the three consecutive SRUS scans shown together with MAP. Moving average MB velocities are shown in the blue solid lines. The red dashed lines show the MAP. Semisolid areas represent the standard deviation of the measurements. The black dotted line indicates the mean MB velocity from SRUS scan 1 as a reference in the two succeeding scans for an easier immediate visual comparison. The scatter plots on the right show the mean velocities from the raw data of the three scans (410-sec periods). The asterisks indicate the result of the post-hoc Tukey's multiple comparisons test done on the normality-transformed data (log-transformed for cortical data, square root-transformed for outer medulla data). AVR = ascending vasa recta, CO = cortex, DVR = descending vasa recta, IM = inner medulla, MAP = mean arterial pressure, MB = microbubble, OM = outer medulla, SRUS = super-resolution ultrasound, * = $P \leq 0.05$, ns = non-significant.

In the cortical arteries/arterioles, prazosin lowered the MB velocities significantly ($P = 0.013$). Post-hoc comparison showed that the MB velocity decreased significantly from SRUS scan 1 to scan 2 ($P = 0.032$). Prazosin also significantly lowered the MB velocities in the outer medulla descending vasa recta ($P = 0.026$). The post-hoc comparison showed that the MB velocity decreased significantly from SRUS scan 1 to SRUS scan 2 ($P = 0.037$) and increased in SRUS scan 3 to a level significantly higher than SRUS scan 2 ($P = 0.013$). The decrease and increase in MB velocity in the outer medulla ascending vasa recta were not statistically significant ($P = 0.064$). The remaining vascular beds showed no statistically significant MB velocity alterations between scans and were not analyzed further.

The three 30-sec periods within SRUS scan 2 were also analyzed for cortical arteries/arterioles, outer medulla descending vasa recta, and outer medulla ascending vasa recta. The results were slightly different: In the cortical arteries/arterioles, the ANOVA was non-significant, but the post-hoc comparison still showed a decrease in MB velocity from the baseline period to the period with max MAP drop ($P = 0.031$). In the outer medulla descending vasa recta, all tests were non-significant. In the outer medulla ascending vasa recta, prazosin lowered the MB velocity significantly ($P = 0.012$), with the post-hoc test showing velocity decrease from baseline period to the period with max MAP drop ($P = 0.040$). Results from all ANOVA and post-hoc tests of the MB velocities are shown in Supplementary Table S2.

The cortical arteries/arterioles have a fast flow and complex geometry. In this area there were seconds with no generated tracks (271±46 of the 410 sec of SRUS scan 1 had velocity estimations). For the outer medulla descending vasa recta with a more homogenous slow flow and a simpler vascular geometry, 405±4 sec had velocity estimations. However, supplementary Figure S3a illustrates how the number of track positions/sec during SRUS scan 1 varied randomly and was area-dependent with a steady number of counted MBs/sec through scanning (Supplementary Figure S3b). There was no correlation between MB count/sec and number of seconds with velocity estimations in the cortical arteries/arterioles (Pearson's correlation, $R^2 = 0.088$, $P = 0.519$).

4. Discussion

In this study, manual segmentation of SRUS images was used to isolate unique renal vascular beds and extract MB velocities from arteries/arterioles or veins/venules separately. It was possible to detect and differentiate responses to prazosin in the separated vascular beds. An acute response to prazosin was detectable in the MB velocities from the renal outer medulla, which is usually difficult to examine in vivo due to its deep location, supporting that SRUS can be used to investigate the intrarenal distribution of blood velocities in different conditions. Simultaneous quantification of the outer and inner medulla blood velocity opens possibilities to investigate how regional blood flow alterations influence the corticomedullary gradients of NaCl and urea in the medulla [38,39]. Another clinically intriguing example is monitoring flow changes in the ischemia-vulnerable outer medulla [6,40].

The MB velocities decreased significantly in response to prazosin in the cortical arteries/arterioles, outer medulla descending vasa recta, and outer medulla ascending vasa recta (the latter only when analyzing the 30-sec periods of SRUS scan 2). Prazosin inhibits the $\alpha 1$ -adrenoceptor located on the vascular smooth muscle cells of the arteries and arterioles, causing vasodilation. When administered intravenously, prazosin lowers MAP, primarily due to a reduced total peripheral resistance, also causing the renal blood flow and the cortical artery/arteriole MB velocity to decrease [41,42]. The descending vasa recta do not have vascular smooth muscle cells but are surrounded by pericytes. One study has shown a higher pericyte density in the outer medulla compared with inner medulla [43]. Likewise, adrenergic nerve fibers have been shown to travel along the outer medulla descending vasa recta and diminish in the inner medulla [44]. These differences could account for the difference in our findings: Only in the outer medulla, a response to prazosin was measured. Norepinephrine has been shown to cause outer medulla vasoconstriction in vitro and reduce medullary blood flow in vivo, supporting the presence of $\alpha 1$ -adrenoceptors [34,43,45]. However, the mentioned studies do not directly demonstrate the existence of the $\alpha 1$ -adrenoceptor in the outer medulla descending vasa recta pericytes, and the MB velocity decrease could also be caused by dilation of the upstream efferent arterioles. The outer medulla ascending vasa recta have mostly been found not associated with pericytes [46,47], but a decrease in MB velocity was found when analyzing 30-sec periods of SRUS scan 2. It could be an effect of the velocity drop on the arterial side of the outer medulla circulation. Lastly, we did not find a response to prazosin in the cortical veins/venules. The $\alpha 1$ -adrenoceptors are present in veins, but the venous basal tone is low, and prazosin may not have dilated the veins enough.

Other studies have quantified MB velocity alterations, e.g., slower MB velocities in the brains of older compared with younger mice, or slower MB velocities in the retinal and retrobulbar vessels in the rabbit eye at high ocular pressures [26,48]. In the latter, arteries and veins were separated bi-directionally with flow towards (arteries) or away (veins) from

the probe. Due to the renal vascular complexity, that approach was not feasible in our study. Another recent SRUS study used the pulsatility of arteries to separate them from veins in cross-sectional images of the murine cerebral vasculature [49]. They used a high temporal resolution (1000-Hz frame rate) to capture the velocity fluctuations within a single cardiac cycle of mice with a 550 beats/min heart rate. For rats with ~350 beats/min, a framerate much higher than used in our study (54 Hz) would be required.

The MB velocity is typically estimated as a mean of all tracks generated during data acquisition [7,8,19,23,48], but this will not necessarily reveal dynamic vascular flow alterations. Therefore, we visualized the MB velocities as moving averages during scanning and compared MB velocities from shorter 30-sec intervals within the same scan. The data from the 30-sec periods should be interpreted cautiously, as they are based on a fewer velocity estimates. The estimated velocities at a given time point are highly dependent on the conditions for MB tracking, such as complexity of the vascular geometry and distribution of the MBs, variations in flow velocity and pulsatility, MB-to-noise ratio, out-of-plane motion, or errors in MB localization [29,50,51]. Such variations depending the on vascular complexity was illustrated with the difference in number of track positions between the intricate cortical arteries/arterioles versus the simpler outer medulla vessels (Supplementary Figure S3a). A way to optimize the regional velocity estimations would be to adjust MB infusion concentration according to the area of interest; the highly perfused cortex could be imaged with an even lower MB concentration for better tracking.

There are some limitations to this study. Firstly, we measured only the velocity of MBs in the flowing blood, not the blood volume flow, which would require precise estimations of vessel diameters. Vessel diameters are highly dynamic [52,53]. Therefore, the diameters estimated from the accumulated MB tracks do not necessarily represent a vessel diameter at a given time. As the velocity estimations from shorter periods are based on fewer tracks that most likely do not fill the vessel lumen, valid diameters cannot be extracted. The evaluation of tissue perfusion based on velocities alone should be done carefully, as higher velocities do not necessarily mean better blood flow, it depends also on the cross-sectional vessel area. Another limitation is the lack of a gold reference for verifying the MB velocities. The velocities derived from 2D SRUS are likely to be underestimated due to the out-of-plane vessels [17,30,54]. With a low framerate, one could also speculate that only the slowest moving MBs in the periphery of a vessel with a parabolic flow are tracked. A frame rate in the kHz range would improve tracking by increasing the number of detected MBs/sec and allow estimation of more realistic velocities, as exemplified in a rat brain with velocities ranging from mm/sec to cm/sec [7]. For dynamic evaluations of the vasculature, ultrafast Doppler or fast synthetic aperture vector flow imaging could be an alternative to SRUS [55,56]. However, these techniques still have lower spatial resolution than SRUS and Doppler will not allow, e.g., separation of the descending and ascending vasa recta in an entire cross-section of the kidney. The separation of the cortical MB tracks into arteries and veins also has limitations. The arterial tracks come from different vessel types with different velocities. Some tracks were from smaller branches of the arcuate arteries, many were from cortical radial arteries, some were probably from afferent or efferent arterioles, and some MBs might even have been tracked in the capillary network (not substantiated). Depending on the type of vessel in which the MBs were tracked, estimated velocities ranged from the minimum to the maximum of our tracking algorithm's velocity span (0-15 mm/s). Investigating them as a whole may blur the outcome of an intervention or a disease, as they may respond differently. Additionally, while most of the cortical arterioles project towards the renal surface, some have a direction toward the medulla, and the same goes for the veins [57]. Accordingly, separating vessels based on direction may mix arterioles with the venules and vice versa. Moreover, capillaries run in all directions and may occur in both regions. Therefore, the separation of vessels based on pulsatility is a compelling alternative for the renal cortex [49]. Finally, because we used a clinical ultrasound scanner with a low frame rate, a high prazosin dose was used to ensure a measurable response. For detection of subtler and more realistic velocity alterations, optimization of SRUS acquisition parameters,

such as frame rate or MB concentration, to better fit the renal vasculature is necessary [58], especially since transcutaneous scanning needed for longitudinal studies will introduce additional challenges for MB tracking.

5. Conclusions

In conclusion, super-resolution ultrasound imaging makes it possible to evaluate microbubble velocities in separated arterial and venous vascular beds of rat's renal cortex, outer medulla, and inner medulla. The technique has a promising potential as a tool to investigate the intrarenal distribution of the renal blood flow velocities under different physiological and pathological conditions.

6. Patents

Patent on the tissue motion correction algorithm by J.A.J. and I.T. used in this study has been purchased by BK Medical ApS, Herlev, Denmark.

Supplementary Materials: The following supporting information can be downloaded at: www.mdpi.com/xxx/s1, Table S1: Animal data.; Table S2: ANOVA of microbubble velocities; Figure S1: Triplex Doppler images; Figure S2: Prazosin effect on renal blood flow; Figure S3: Track positions and microbubble count.

Funding: This research was funded by Innovation Fund Denmark, grant number 7050-00004B.

Acknowledgments: The authors greatly appreciate the technical skills of animal technician Karin Larsen (Department of Biomedical Sciences, University of Copenhagen, Copenhagen, Denmark) who did the animal surgeries. We thank Shaun Theodor Sødergren for kindly borrowing the measurements of renal blood flow during prazosin administration, shown in Supplementary Figure S2.

Author Contributions: Conceptualization, S.B.A., S.B.S., C.M.S., I.T., C.V.H., J.A.J., M.B.N., C.M.S.; methodology, S.B.A., C.M.S., I.T., J.A.J.; software, I.T., J.A.J.; validation, I.T., J.A.J.; formal analysis, S.B.A., I.T.; investigation, S.B.A., S.B.S., C.M.S.; resources, C.M.S., J.A.J., M.B.N.; data curation, I.T., C.V.H., J.A.J.; writing—original draft preparation, S.B.A.; writing—review and editing, S.B.A.; S.B.S., I.T., C.V.H., J.A.J., M.B.N. C.M.S.; visualization, S.B.A., I.T.; supervision, J.A.J., M.B.N., C.M.S.; project administration, S.B.A., J.A.J., M.B.N., C.M.S.; funding acquisition, C.M.S., J.A.J., M.B.N. All authors have read and agreed to the published version of the manuscript.

Institutional Review Board Statement: The animal study protocol was approved by the Danish Animal Experiments Inspectorate under the Ministry of Environment and Food (license number 2020-15-0201-00547 issued on June 4th 2020).

Data Availability Statement: Raw data and image processing algorithms can be exchanged through a collaboration agreement. Processed data and analysis algorithms can be made available upon request.

Conflicts of Interest: The funders had no role in the design of the study; in the collection, analyses, or interpretation of data; in the writing of the manuscript, or in the decision to publish the results. The experiments were conducted as part of a jointly funded research collaboration between the Department of Biomedical Sciences at the University of Copenhagen, the Department of Radiology at University Hospital Rigshospitalet, Center for Fast Ultrasound Imaging at the Technical University of Denmark, and BK Medical ApS, Herlev, Denmark. BK Medical modified the bk5000 scanner bk5000 for super-resolution ultrasound imaging data acquisition. BK Medical put the scanner and probe (X18L5s) at our disposal. BK Medical ApS owns a patent for the motion compensation algorithm used for post-processing the super-resolution ultrasound images. The patent was sold to them by J.A.J. and I.T. C.V.H. is a former employee at BK Medical ApS. Aside from this, the authors declare no competing interests.

References

- Christensen-Jeffries, K.; Couture, O.; Dayton, P.A.; Eldar, Y.C.; Hynynen, K.; Kiessling, F.; O'Reilly, M.; Pinton, G.F.; Schmitz, G.; Tang, M.X.; et al. Super-resolution Ultrasound Imaging. *Ultrasound Med. Biol.* **2020**, *46*, 865–891, doi:10.1016/j.ultrasmedbio.2019.11.013.
- Li, B.; Yao, J.; Kawamura, K.; Oyanagi-Tanaka, Y.; Hoshiyama, M.; Morioka, T.; Gejyo, F.; Uchiyama, M.; Oite, T. Real-time observation of glomerular hemodynamic changes in diabetic rats: Effects of insulin and ARB. *Kidney Int.* **2004**, *66*, 1939–1948, doi:10.1111/j.1523-1755.2004.00979.x.
- Regner, K.R.; Zuk, A.; Van Why, S.K.; Shames, B.D.; Ryan, R.P.; Falck, J.R.; Manthathi, V.L.; McMullen, M.E.; Ledbetter, S.R.; Roman, R.J. Protective effect of 20-HETE analogues in experimental renal ischemia reperfusion injury. *Kidney Int.* **2009**, *75*, 511–517, doi:10.1038/ki.2008.600.

4. Fischer, K.; Meral, F.C.; Zhang, Y.; Vangel, M.G.; Jolesz, F.A.; Ichimura, T.; Bonventre, J. V High-resolution renal perfusion mapping using contrast-enhanced ultrasonography in ischemia-reperfusion injury monitors changes in renal microperfusion. *Kidney Int.* **2016**, *89*, 1388–98, doi:10.1016/j.kint.2016.02.004. 373–375
5. Post, E.H.; Kellum, J.A.; Bellomo, R.; Vincent, J.L. Renal perfusion in sepsis: from macro- to microcirculation. *Kidney Int.* **2017**, *91*, 45–60, doi:10.1016/j.kint.2016.07.032. 376–377
6. Andersen, S.B.; Taghavi, I.; Hoyos, C.A.V.; Sogaard, S.B.; Gran, F.; Lönn, L.; Hansen, K.L.; Jensen, J.A.; Nielsen, M.B.; Sørensen, C.M. Super-resolution imaging with ultrasound for visualization of the renal microvasculature in rats before and after renal ischemia: A pilot study. *Diagnostics* **2020**, *10*, 862, doi:10.3390/diagnostics10110862. 378–380
7. Errico, C.; Pierre, J.; Pezet, S.; Desailly, Y.; Lenkei, Z.; Couture, O.; Tanter, M. Ultrafast ultrasound localization microscopy for deep super-resolution vascular imaging. *Nature* **2015**, *527*, 499–502, doi:10.1038/nature16066. 381–382
8. Christensen-Jeffries, K.; Browning, R.J.; Tang, M.X.; Dunsby, C.; Eckersley, R.J. In Vivo Acoustic Super-Resolution and Super-Resolved Velocity Mapping Using Microbubbles. *IEEE Trans. Med. Imaging* **2015**, *34*, 433–440, doi:10.1109/TMI.2014.2359650. 383–384
9. Keller, M.W.; Segal, S.S.; Kaul, S.; Duling, B. The behavior of sonicated albumin microbubbles within the microcirculation: A basis for their use during myocardial contrast echocardiography. *Circ. Res.* **1989**, *65*, 458–467, doi:10.1161/01.RES.65.2.458. 385–386
10. Ismail, S.; Jayaweera, A.R.; Camarano, G.; Gimple, L.W.; Powers, E.R.; Kaul, S. Relation between air-filled albumin microbubble and red blood cell rheology in the human myocardium: Influence of echocardiographic systems and chest wall attenuation. *Circulation* **1996**, *94*, 445–451, doi:10.1161/01.CIR.94.3.445. 387–389
11. Lindner, J.R.; Song, J.; Jayaweera, A.R.; Sklenar, J.; Kaul, S. Microvascular rheology of definity microbubbles after intra-arterial and intravenous administration. *J. Am. Soc. Echocardiogr.* **2002**, *15*, 396–403, doi:10.1067/mje.2002.117290. 390–391
12. Tang, S.; Song, P.; Trzasko, J.D.; Lowerison, M.; Huang, C.; Gong, P.; Lok, U.W.; Manduca, A.; Chen, S. Kalman Filter-Based Microbubble Tracking for Robust Super-Resolution Ultrasound Microvessel Imaging. *IEEE Trans. Ultrason. Ferroelectr. Freq. Control* **2020**, *67*, 1738–1751, doi:10.1109/TUFFC.2020.2984384. 392–394
13. Taghavi, I.; Andersen, S.B.; Hoyos, C.V.A.V.; Schou, M.; Gran, F.; Hansen, K.L.; Nielsen, M.B.; Sørensen, C.M.; Jensen, J.A.; Stuart, M.B.; et al. Ultrasound Super-Resolution Imaging with a Hierarchical Kalman Tracker. *Ultrasonics* **2022**, *122*, doi:10.1016/j.ultras.2022.106695. 395–397
14. Song, P.; Trzasko, J.D.; Manduca, A.; Huang, R.; Kadirvel, R.; Kallmes, D.F.; Chen, S. Improved Super-Resolution Ultrasound Microvessel Imaging With Spatiotemporal Nonlocal Means Filtering and Bipartite Graph-Based Microbubble Tracking. *IEEE Trans. Ultrason. Ferroelectr. Freq. Control* **2018**, *65*, 149–167, doi:10.1109/TUFFC.2017.2778941. 398–400
15. Huang, C.; Lowerison, M.R.; Trzasko, J.D.; Manduca, A.; Bresler, Y.; Tang, S.; Gong, P.; Lok, U.W.; Song, P.; Chen, S. Short Acquisition Time Super-Resolution Ultrasound Microvessel Imaging via Microbubble Separation. *Sci. Rep.* **2020**, *10*, 1–13, doi:10.1038/s41598-020-62898-9. 401–403
16. Solomon, O.; Van Sloun, R.J.G.; Wijkstra, H.; Mischi, M.; Eldar, Y.C. Exploiting Flow Dynamics for Superresolution in Contrast-Enhanced Ultrasound. *IEEE Trans. Ultrason. Ferroelectr. Freq. Control* **2019**, *66*, 1573–1586, doi:10.1109/TUFFC.2019.2926062. 404–406
17. Espíndola, D.; Deruiter, R.M.; Santibanez, F.; Dayton, P.A.; Pinton, G. Quantitative sub-resolution blood velocity estimation using ultrasound localization microscopy ex-vivo and in-vivo. *Biomed. Phys. Eng. Express* **2020**, *6*, 035019, doi:10.1088/2057-1976/ab7f26. 407–408
18. Chen, Q.; Yu, J.; Rush, B.M.; Stocker, S.D.; Tan, R.J.; Kim, K. Ultrasound super-resolution imaging provides a noninvasive assessment of renal microvasculature changes during mouse acute kidney injury. *Kidney Int.* **2020**, *98*, 355–365, doi:10.1016/j.kint.2020.02.011. 410–412
19. Opacic, T.; Dencks, S.; Theek, B.; Piepenbrock, M.; Ackermann, D.; Rix, A.; Lammers, T.; Stickeler, E.; Delorme, S.; Schmitz, G.; et al. Motion model ultrasound localization microscopy for preclinical and clinical multiparametric tumor 413–414

- characterization. *Nat. Commun.* **2018**, *9*, 1527, doi:10.1038/s41467-018-03973-8. 415
20. Lowerison, M.R.; Huang, C.; Lucien, F.; Chen, S.; Song, P. Ultrasound localization microscopy of renal tumor xenografts in chicken embryo is correlated to hypoxia. *Sci. Rep.* **2020**, *10*, 1–13, doi:10.1038/s41598-020-59338-z. 416
417
21. Yu, J.; Lavery, L.; Kim, K. Super-resolution ultrasound imaging method for microvasculature in vivo with a high temporal accuracy. *Sci. Rep.* **2018**, *8*, 13918, doi:10.1038/s41598-018-32235-2. 418
419
22. Chen, Q.; Yu, J.; Lukashova, L.; Latoche, J.D.; Zhu, J.; Lavery, L.; Verdelis, K.; Anderson, C.J.; Kim, K. Validation of Ultrasound Super-Resolution Imaging of Vasa Vasorum in Rabbit Atherosclerotic Plaques. *IEEE Trans. Ultrason. Ferroelectr. Freq. Control* **2020**, *67*, 1725–1729, doi:10.1109/TUFFC.2020.2974747. 420
421
422
23. Foiret, J.; Zhang, H.; Ilovitsh, T.; Mahakian, L.; Tam, S.; Ferrara, K.W. Ultrasound localization microscopy to image and assess microvasculature in a rat kidney. *Sci. Rep.* **2017**, *7*, 13662, doi:10.1038/s41598-017-13676-7. 423
424
24. Huang, C.; Zhang, W.; Gong, P.; Lok, U.W.; Tang, S.; Yin, T.; Zhang, X.; Zhu, L.; Sang, M.; Song, P.; et al. Super-resolution ultrasound localization microscopy based on a high frame-rate clinical ultrasound scanner: An in-human feasibility study. *Phys. Med. Biol.* **2021**, *66*, doi:10.1088/1361-6560/abef45. 425
426
427
25. Demené, C.; Robin, J.; Dizeux, A.; Heiles, B.; Pernot, M.; Tanter, M.; Perren, F. Transcranial ultrafast ultrasound localization microscopy of brain vasculature in patients. *Nat. Biomed. Eng.* **2021**, *5*, 219–228, doi:10.1038/s41551-021-00697-x. 428
429
26. Lowerison, M.R.; Sekaran, N.V.C.; Zhang, W.; Dong, Z.; Chen, X.; Llano, D.A.; Song, P. Aging-related cerebral microvascular changes visualized using ultrasound localization microscopy in the living mouse. *Sci. Rep.* **2022**, *12*, 1–11, doi:10.1038/s41598-021-04712-8. 430
431
432
27. Taghavi, I.; Andersen, S.B.; Hoyos, C.A.V.; Nielsen, M.B.; Sørensen, C.M.; Jensen, J.A.J.A.; Sorensen, C.M.; Jensen, J.A.J.A. In vivo Motion Correction in Super Resolution Imaging of Rat Kidneys. *IEEE Trans. Ultrason. Ferroelectr. Freq. Control* **2021**, *68*, 3082–3093, doi:10.1109/TUFFC.2021.3086983. 433
434
435
28. Nordsletten, D.A.; Blackett, S.; Bentley, M.D.; Ritman, E.L.; Smith, N.P. Structural morphology of renal vasculature. *Am. J. Physiol. - Hear. Circ. Physiol.* **2006**, *291*, 296–309, doi:10.1152/ajpheart.00814.2005. 436
437
29. Christensen-Jeffries, K.; Brown, J.; Harput, S.; Zhang, G.; Zhu, J.; Tang, M.X.; Dunsby, C.; Eckersley, R.J. Poisson Statistical Model of Ultrasound Super-Resolution Imaging Acquisition Time. *IEEE Trans. Ultrason. Ferroelectr. Freq. Control* **2019**, *66*, 1246–1254, doi:10.1109/TUFFC.2019.2916603. 438
439
440
30. Hingot, V.; Errico, C.; Heiles, B.; Rahal, L.; Tanter, M.; Couture, O. Microvascular flow dictates the compromise between spatial resolution and acquisition time in Ultrasound Localization Microscopy. *Sci. Rep.* **2019**, *9*, 2456, doi:10.1038/s41598-018-38349-x. 441
442
443
31. Dencks, S.; Piepenbrock, M.; Schmitz, G. Assessing Vessel Reconstruction in Ultrasound Localization Microscopy by Maximum Likelihood Estimation of a Zero-Inflated Poisson Model. *IEEE Trans. Ultrason. Ferroelectr. Freq. Control* **2020**, *67*, 1603–1612, doi:10.1109/TUFFC.2020.2980063. 444
445
446
32. Lowerison, M.R.; Huang, C.; Kim, Y.; Lucien, F.; Chen, S.; Song, P. In Vivo Confocal Imaging of Fluorescently Labeled Microbubbles: Implications for Ultrasound Localization Microscopy. *IEEE Trans. Ultrason. Ferroelectr. Freq. Control* **2020**, *67*, 1811–1819, doi:10.1109/TUFFC.2020.2988159. 447
448
449
33. Postnov, D.D.; Holstein-Rathlou, N.-H.; Sosnovtseva, O. Laser speckle imaging of intra organ drug distribution. *Biomed. Opt. Express* **2015**, *6*, 5055, doi:10.1364/boe.6.005055. 450
451
34. Yang, S.; Silldorff, E.P.; Pallone, T.L. Effect of norepinephrine and acetylcholine on outer medullary descending vasa recta. *Am. J. Physiol. - Hear. Circ. Physiol.* **1995**, *269*, doi:10.1152/ajpheart.1995.269.2.h710. 452
453
35. Saito, H.; Togashi, H.; Yoshioka, M. A comparative study of the effects of $\alpha 1$ -adrenoceptor antagonists on sympathetic function in rats. *Am. J. Hypertens.* **1996**, *9*, 160S-169S, doi:10.1016/0895-7061(96)00292-0. 454
455
36. Ren, H.; Gu, L.; Andreasen, A.; Thomsen, J.S.; Cao, L.; Christensen, E.I.; Zhai, X.Y. Spatial organization of the vascular bundle 456

- and the interbundle region: Three-dimensional reconstruction at the inner stripe of the outer medulla in the mouse kidney. *Am. J. Physiol. - Ren. Physiol.* **2014**, *306*, doi:10.1152/ajprenal.00429.2013. 457
458
37. Holliger, C.; Lemley, K. V.; Schmitt, S.L.; Thomas, F.C.; Robertson, C.R.; Jamison, R.L. Direct Determination of Vasa Recta 459
Blood Flow in the Rat Renal Papilla. *Circ. Res.* **1983**, *53*, 401–413, doi:10.1161/01.RES.53.3.401. 460
38. Hansell, P. Evaluation of methods for estimating renal medullary blood flow. *Ren. Physiol. Biochem.* **1992**, *15*, 217–230, 461
doi:10.1159/000173457. 462
39. Kennedy-Lydon, T.M.; Crawford, C.; Wildman, S.S.P.; Peppiatt-Wildman, C.M. Renal pericytes: Regulators of medullary 463
blood flow. *Acta Physiol.* **2013**, *207*, 212–225, doi:10.1111/apha.12026. 464
40. Basile, D.P.; Anderson, M.D.; Sutton, T.A. Pathophysiology of acute kidney injury. *Compr. Physiol.* **2012**, *2*, 1303–1353, 465
doi:10.1002/cphy.c110041. 466
41. Tabrizchi, R.; Pang, C.C.Y. Comparative effects of rauwolscine, prazosin, and phentolamine on blood pressure and cardiac 467
output in anesthetized rats. *Can. J. Physiol. Pharmacol.* **1987**, *65*, 1421–1427, doi:10.1139/y87-223. 468
42. Luft, F.C.; Veelken, R.; Becker, H.; Ganten, D.; Lang, R.E.; Unger, T. Effect of urapidil, clonidine, and prazosin on sympathetic 469
tone in conscious rats. *Hypertension* **1986**, *8*, 303–311, doi:10.1161/01.HYP.8.4.303. 470
43. Crawford, C.; Kennedy-Lydon, T.; Sprott, C.; Desai, T.; Sawbridge, L.; Munday, J.; Unwin, R.J.; Wildman, S.S.P.; Peppiatt- 471
Wildman, C.M. An intact kidney slice model to investigate vasa recta properties and function in situ. *Nephron - Physiol.* **2012**, 472
120, p17, doi:10.1159/000339110. 473
44. McKenna, O.C.; Angelakos, E.T. Adrenergic innervation of the canine kidney. *Circ. Res.* **1968**, *22*, 345–354, 474
doi:10.1161/01.RES.22.3.345. 475
45. Correia, A.G.; Bergström, G.; Lawrence, A.J.; Evans, R.G. Renal medullary interstitial infusion of norepinephrine in 476
anesthetized rabbits: Methodological considerations. *Am. J. Physiol. - Regul. Integr. Comp. Physiol.* **1999**, *277*, 477
doi:10.1152/ajpregu.1999.277.1.r112. 478
46. Park, F.; Mattson, D.L.; Roberts, L.A.; Cowley, A.W. Evidence for the presence of smooth muscle α -actin within pericytes of 479
the renal medulla. *Am. J. Physiol. - Regul. Integr. Comp. Physiol.* **1997**, *273*, doi:10.1152/ajpregu.1997.273.5.r1742. 480
47. Moffat, D.B. The fine structure of the blood vessels of the renal medulla with particular reference to the control of the 481
medullary circulation. *J. Ultrastructure Res.* **1967**, *19*, 532–545, doi:10.1016/S0022-5320(67)80079-0. 482
48. Qian, X.; Huang, C.; Li, R.; Song, B.; Tchelepi, H.; Shung, K.K.; Chen, S.; Humayun, M.; Zhou, Q. Super-resolution Ultrasound 483
Localization Microscopy for Visualization of the Ocular Blood Flow. *IEEE Trans. Biomed. Eng.* **2021**, 484
doi:10.1109/TBME.2021.3120368. 485
49. Bourquin, C.; Poree, J.; Lesage, F.; Provost, J. In vivo pulsatility measurement of cerebral microcirculation in rodents using 486
Dynamic Ultrasound Localization Microscopy. *IEEE Trans. Med. Imaging* **2021**, doi:10.1109/tmi.2021.3123912. 487
50. Christensen-Jeffries, K.; Harput, S.; Brown, J.; Wells, P.N.T.; Aljabar, P.; Dunsby, C.; Tang, M.X.; Eckersley, R.J. Microbubble 488
Axial Localization Errors in Ultrasound Super-Resolution Imaging. *IEEE Trans. Ultrason. Ferroelectr. Freq. Control* **2017**, *64*, 489
1644–1654, doi:10.1109/TUFFC.2017.2741067. 490
51. Zhang, J.; Huang, L.; Liao, H.; Luo, J. Improved Background Noise Suppression in Ultrasound Localization Microscopy using 491
Spatial Coherence Beamforming. In Proceedings of the 2021 IEEE International Ultrasonics Symposium (IUS); IEEE, 2021; 492
pp. 1–4. 493
52. Nakamoto, H.; Ogasawara, Y.; Kajiya, F. Visualisation of the effects of dilazep on rat afferent and efferent arterioles in vivo. 494
Hypertens. Res. **2008**, *31*, 315–324, doi:10.1291/hyres.31.315. 495
53. Patzak, A.; Petzhold, D.; Wronski, T.; Martinka, P.; Babu, G.J.; Periasamy, M.; Haase, H.; Morano, I. Constriction velocities of 496
renal afferent and efferent arterioles of mice are not related to SMB expression. *Kidney Int.* **2005**, *68*, 2726–2734, 497
doi:10.1111/j.1523-1755.2005.00743.x. 498

-
54. Andersen, S.B.; Taghavi, I.; Kjer, H.M.; Søgaard, S.B.; Gundlach, C.; Dahl, V.A.; Nielsen, M.B.; Dahl, A.B.; Jensen, J.A.; Sørensen, C.M. Evaluation of 2D super-resolution ultrasound imaging of the rat renal vasculature using ex vivo micro-computed tomography. *Sci. Rep.* **2021**, *11*, 24335, doi:10.1038/s41598-021-03726-6. 499
500
55. Hingot, V.; Brodin, C.; Lebrun, F.; Heiles, B.; Chagnot, A.; Yetim, M.; Gauberti, M.; Orset, C.; Tanter, M.; Couture, O.; et al. Early ultrafast ultrasound imaging of cerebral perfusion correlates with ischemic stroke outcomes and responses to treatment in mice. *Theranostics* **2020**, *10*, 7480–7491, doi:10.7150/thno.44233. 501
502
503
504
56. Hoyos, C.A.V.; Stuart, M.B.; Hansen, K.L.; Nielsen, M.B.; Jensen, J.A. Accurate Angle Estimator for High-Frame-Rate 2-D Vector Flow Imaging. *IEEE Trans. Ultrason. Ferroelectr. Freq. Control* **2016**, *63*, 842–853, doi:10.1109/TUFFC.2016.2551689. 505
506
57. Bankir, L.; Bouby, N.; Trinh-Trang-Tan, M.-M. The role of the kidney in the maintenance of water balance. In *Baillière's Clinical Endocrinology and Metabolism, Volume 3, Issue 2*; 1989; pp. 249–311. 507
508
58. Couture, O.; Hingot, V.; Heiles, B.; Muleki-Seya, P.; Tanter, M. Ultrasound localization microscopy and super-resolution: a state-of-the-art. *IEEE Trans. Ultrason. Ferroelectr. Freq. Control* **2018**, 1–1, doi:10.1109/TUFFC.2018.2850811. 509
510
511



Paper 7

Super-Resolution Ultrasound Imaging of Rat Kidneys before and after Ischemia-Reperfusion

Sofie Bech Andersen, Carlos Armando Villagómez Hoyos, **Iman Taghavi**, Fredrik Gran, Kristoffer Lindskov Hansen, Charlotte Mehlin Sørensen, Jørgen Arendt Jensen, and Michael Bachman Nielsen

Published in:

Proceedings of the IEEE International Ultrasonic Symposium

Document Version:

Published

DOI:

10.1109/ULTSYM.2019.8926190

General rights

Copyright and moral rights for the publications made accessible in the public portal are retained by the authors and/or other copyright owners and it is a condition of accessing publications that users recognise and abide by the legal requirements associated with these rights.

- Users may download and print one copy of any publication from the public portal for the purpose of private study or research.
- You may not further distribute the material or use it for any profit-making activity or commercial gain
- You may freely distribute the URL identifying the publication in the public portal

If you believe that this document breaches copyright please contact us providing details, and we will remove access to the work immediately and investigate your claim.

Super-Resolution Ultrasound Imaging of Rat Kidneys before and after Ischemia-Reperfusion

Sofie Bech Andersen^{1,2,3}, Carlos Armando Villagómez Hoyos⁴, Iman Taghavi⁵, Fredrik Gran⁴,
Kristoffer Lindskov Hansen^{1,3}, Charlotte Mehlin Sørensen², Jørgen Arendt Jensen⁵, Michael Bachmann Nielsen^{1,3}

¹Department of Diagnostic Radiology, Rigshospitalet, Copenhagen, Denmark.

²Department of Biomedical Sciences, University of Copenhagen, Copenhagen, Denmark.

³Department of Clinical Medicine, University of Copenhagen, Copenhagen, Denmark.

⁴BK Medical ApS, Herlev, Denmark.

⁵Center for Fast Ultrasound, Department of Health Technology, Technical University of Denmark, Lyngby, Denmark.

Abstract—*In vivo* visualization of the microvasculature is feasible with super-resolution ultrasound imaging (SRI), but the method needs more affirmative data before clinical use. The kidneys have a rich vasculature, and microvascular dysfunction decreases the kidney function. Therefore, detection of subtle renal microvascular changes could benefit patients with renal disease. We hypothesized that our SRI setup can visualize the microvascular network of two healthy rat kidneys and subsequently demonstrate microvascular flow changes immediately after ischemia-reperfusion. The left kidney of two male Sprague-Dawley rats was scanned during laparotomy using a customized BK5000 scanner, an X18L5s transducer, and interleaved contrast and B-mode sequences with focused beam transmission. Images were acquired over 10 min using SonoVue (1:10) as the contrast agent. After a baseline scan, one rat had the renal vein clamped, while the other rat had the renal artery clamped, both for 45 min. The kidneys were rescanned immediately after clamp release and after 60 min of reperfusion. Motion correction was applied before microbubble (MB) detection. The characteristic renal microvascular structure was visualized with anatomical distinction between the dense cortical vascular network and the straight vessels of the medulla. Immediately after vein clamp release, almost no MBs perfused the medullary vessels. After 60 min of reperfusion, MBs refilled the renal vascular bed, but with a slower velocity compared with the baseline scan. The results after artery clamping were subtler, with more MBs perfusing the medulla immediately after clamp release compared with the vein clamping. The results imply that this SRI setup can evaluate different stages of ischemic kidney disease in rats as it can visualize the entire renal vascular bed and differentiate the pattern of reperfusion in two types of ischemic injury.

I. INTRODUCTION

The microvasculature of organs and tissues, including the kidneys of rats and rabbits, has been visualized *in vivo* with super-resolution ultrasound imaging (SRI) [1]–[4]. However, there are few studies concerning pathological changes in the microvasculature detected by SRI. SRI is based on the nonlinear

behavior of gas-filled microbubbles (MBs) injected into the bloodstream. By the use of a series of pulse transmissions, the echoes from individual MBs can be separated from the surrounding linearly-behaving tissue. The position of each MB centroid is accumulated over many frames. By processing a stack of frames, an image of the microvascular network is formed, and estimations of the MB velocity and direction can be made [1], [5]. The kidneys are highly vascular organs, and microvascular dysfunction decreases the kidney function considerably. Detection of modest changes in the structure or function of the renal microvasculature could improve diagnostics, treatment possibilities, and prognosis for patients with diseases such as ischemic kidney disease or diabetic nephropathy. Renal ischemia-reperfusion injuries are caused by a temporary loss of blood flow and can lead to acute kidney injury with a rapid loss of kidney function [6]. Ischemia-reperfusion injuries are often used as models for acute kidney injury in rodents. The injuries are induced by placing a micro-clamp on the renal artery, vein, or pedicle for 30-60 min with subsequent release and reperfusion. The renal vein clamp causes the severest tissue damage [7]. It has been shown that the blood flow in the kidneys is reduced after ischemia with subsequent reperfusion [8]–[10].

Using SRI, we aimed to visualize the renal microvasculature of two healthy male Sprague-Dawley rats and show subsequent pathological microvascular flow changes immediately after unilateral renal ischemia-reperfusion.

II. MATERIALS AND METHODS

A. Animal preparation

We conducted the experiment on two healthy male Sprague-Dawley rats (body weight 251 and 357g). The experiments were performed according to protocols approved by the Danish National Animal Experiments Inspectorate. The procedures were performed at the University of Copenhagen, and all local ethical standards were followed. The ethical policy of the university complies with that of the National Institutes of Health (NIH). All animals were housed in the animal facility at the University of Copenhagen (Department of Experimental Medicine), where trained animal caretakers were responsible for the animal welfare. Anesthesia was induced with 5% isoflurane. After tracheotomy, the animals were connected to a mechanical

ventilator with a respiration cycle of 72 respirations/min. A continuous infusion of Nimbex (cisatracurium, 0.85 mg/ml, GlaxoSmithKline) was given, and adequate anesthesia was maintained with 1-2% isoflurane. Polyethylene catheters (PE-10) were used for jugular vein catheterization and subsequent infusion of MBs (SonoVue, Bracco), isotonic saline, and Nimbex. The arterial pressure was monitored with a polyethylene catheter (PE-50) in the left carotid artery. The animals were placed in the supine position on a heating pad, and the left kidney was exposed through laparotomy. The left side of the diaphragm was pulled slightly in the cranial direction with a metal retractor to further expose the kidney and reduce respiratory motion. The kidney was kept warm with heated isotonic saline in-between ultrasound scans. After the last scan, the rats were euthanized.

B. Ultrasound scan procedure and SRI technique

A customized BK5000 scanner and a fixed X18L5s transducer (BK Medical ApS, Herlev, Denmark) were used to obtain data. The transducer was placed on the lateral surface of the left kidney, using ultrasound gel for coupling. The MBs were diluted in isotonic saline (1:10) and infused intravenously at 100 µl/min. The 10-min data recording started when the MBs appeared on the scanner display. To avoid floating of MBs in the syringe, a custom-built device turned the syringe 180° every 60 sec. After a baseline SRI scan, *Rat 1* had the renal vein clamped, and *Rat 2* had the renal artery clamped using a nontraumatic micro-clamp. After 45 min, the clamp was removed and immediately afterward, a second SRI scan was done. The last SRI scan was performed 60 min after clamp release. Before each scan, the imaging plane was readjusted with reference to the baseline B-mode scan. As a consequence, the three imaging planes were not identical. Power Doppler ultrasound (PRF: 400 Hz, wall filter cutoff: 80 Hz) was acquired immediately after the first and third SRI scans for comparison. The MBs were insonified by interleaved B-mode and contrast-enhancing sequences (amplitude modulation) with line-per-line focused beam transmissions (frame rate: 54 Hz, center frequency: 6 MHz, mechanical index: 0.2). Envelope B-mode data were used to estimate lateral and axial motion relative to a reference frame by tissue speckle tracking [11]. Motion was compensated using the motion estimation to adjust the position of each MB back to its location on the reference

frame. MB tracks were made by connecting the nearest MBs in consecutive images. The tracks were subsequently inserted in the high-resolution images to yield MB track density images, and the estimated MB velocities were used to create the super-resolution velocity images. To estimate both cortical and medullary blood flow, while also accounting for regional differences in ischemic damage, the MB velocity estimations were calculated for MBs flowing toward the renal surface (primarily interlobular arteries) in three separate cortical regions of interest (ROIs) and MBs flowing toward the papilla (descending straight vessels) in three separate ROIs of the outer medulla. The MB velocity was estimated for all the tracks in the ROIs. Additionally, a perfusion index, Q , was calculated:

$$\text{Perfusion index, } Q = \bar{v} \cdot A, \tag{1}$$

where \bar{v} is the mean velocity for all the tracks in the ROI and A is the area of the ROI.

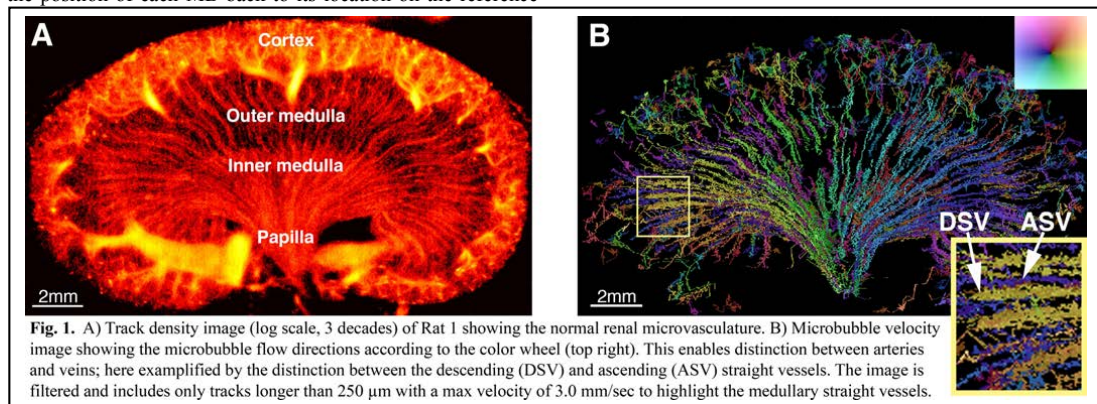
C. Histopathology

After euthanasia, the left kidney was removed and fixated in 4% paraformaldehyde for documentation of the tissue damage. A sham kidney that had undergone three SRI scans but no ischemic injury was also removed and fixated. The kidneys were embedded in paraffin, cut into 4 µm slices, and stained using a standard hematoxylin and eosin (H&E) staining protocol. The images were analyzed by a trained and blinded anatomist.

III. RESULTS

A. The microvasculature of the healthy rat kidneys

In the healthy kidneys, a mean of 106 MBs/frame (*Rat 1*) and 59 MBs/frame (*Rat 2*) were detected (32,300 frames/scan). The track density images revealed the anatomical structure of the renal vasculature with a clear distinction between the dense cortical vascular network and the straight vessels (*vasa recta*) of the outer and inner medulla (Fig. 1-A). As shown by the color wheel in Fig. 1-B, the velocity maps revealed opposing flow directions in adjacent arteries and veins, allowing further discrimination between vessels that were not separable on the track density images. The mean MB velocities in the descending straight vessels of the outer medulla in the two rats were 1.33±0.05 and 1.15±0.09 mm/sec, respectively. These velocities



were calculated only for vessels longer than 500 μm to increase the accuracy of the estimations.

B. Microvascular changes after renal ischemia-reperfusion

Changes in the renal microvasculature after ischemia-reperfusion were visible and measurable with SRI. During the first 10 min of reperfusion after clamping of the renal vein, the entire kidney was poorly perfused with MBs compared with the baseline scan (mean of 55 MBs/frame vs. 106 MBs/frame at baseline) (Fig. 2-A1). This was especially evident in the medulla where almost no MBs were detected. The mean of the estimated MB velocity and perfusion index in the ROIs was also lower compared with baseline (perfusion index shown in Fig. 2-A2). The results were similar, but subtler immediately after the artery clamping with some MB perfusion of the medullary vessels (Fig. 2-B1, mean of 29 MBs/frame vs. 59 MBs/frame at baseline). After 60 min of reperfusion, MBs refilled the entire renal vascular bed again (Fig. 2-A1 and -B1), with a mean of 89 MBs/frame after vein clamping and 50 MBs/frame after artery clamping. The vasculature appeared more irregular on the track density images after clamping. After vein clamping, the mean of the estimated MB velocity and perfusion index increased again, but to a lower level than baseline. After artery clamping, the mean of the estimated MB velocity and perfusion index remained low. However, there were differences among the individual ROIs in the response to the injuries, as seen in Fig. 2-A2 and -B2. The power Doppler ultrasound did not visualize the medullary blood flow. After 60 min of reperfusion, power Doppler showed a decreased cortical blood flow compared with baseline in both kidneys. The H&E stains showed signs of acute tubular necrosis in both specimens. Additionally, a large number of red blood cells were accumulated interstitially after vein clamping (Fig. 3). These changes were not present in the sham kidney.

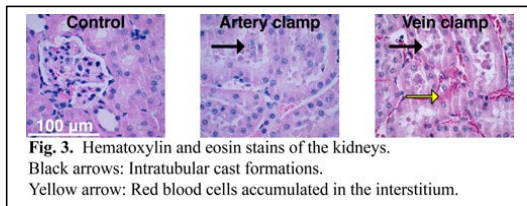
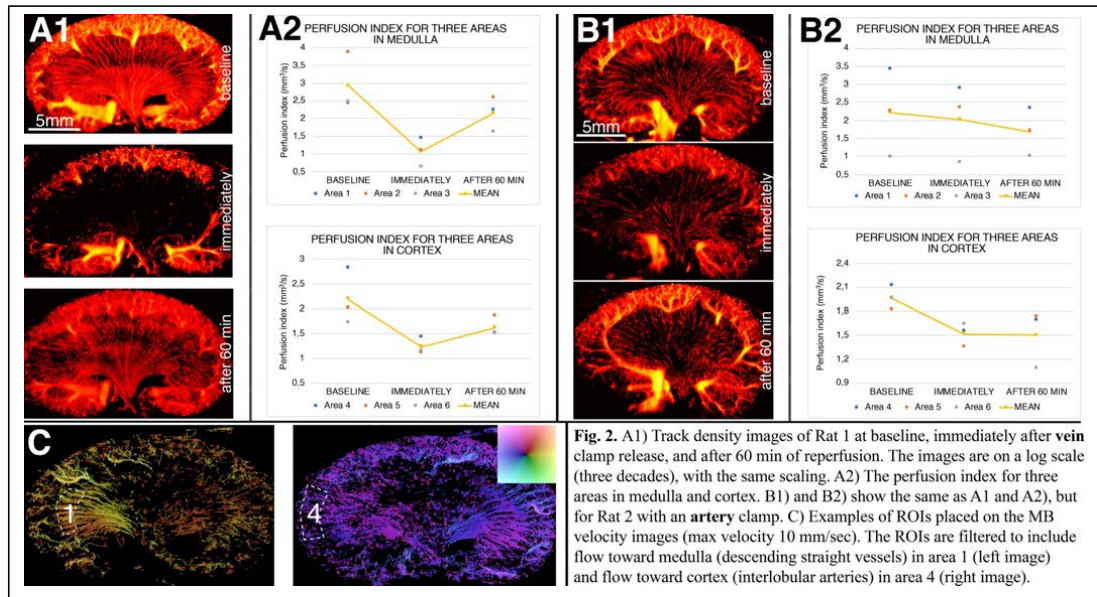


Fig. 3. Hematoxylin and eosin stains of the kidneys. Black arrows: Intratubular cast formations. Yellow arrow: Red blood cells accumulated in the interstitium.

IV. DISCUSSION AND CONCLUSION

In this small preclinical study, we investigated the ability of the presented SRI setup to visualize the microvasculature of two healthy rat kidneys. We found a detailed anatomical depiction of the renal vascular tree similar to descriptions from early anatomical studies [12] and nano-CT images of corrosion casts of mouse kidneys [13]. The mean MB velocities in the descending straight vessels are comparable to the 0.94 ± 0.24 mm/sec found by Foiret et al. [2]. The early effects of renal ischemia-reperfusion were also investigated: Immediately after vein clamp release, the SRI showed a more pronounced reduction in the refilling of the medullary vessels compared with the artery clamping. Visually and with B-mode ultrasound it was observed that the renal vein clamp caused subcapsular edema. Also, the H&E stains revealed a large amount of red blood cells clotted in the renal interstitial space. These findings are in accordance with a previous study that reported vein occlusion to inflict more tissue damage than artery occlusion [7]. The significant reduction in the refilling of the vessels is most likely due to compression, caused by the interstitial edema and accumulated red blood cells. Even though MBs returned to the renal vascular bed after 60 min of reperfusion, the MB velocity and perfusion index were lower compared with baseline; this is also in accordance with previous studies [8]–[10] and with our



power Doppler scans. Despite the differences in reperfusion immediately after clamp release and the differences between the H&E stains, a direct distinction between the 60 min SRI scans of the two rats could not be made. Also, the MB count differed between the two kidneys at baseline, making a direct comparison difficult. Nevertheless, this is—to our knowledge—the first time SRI has shown pathological changes in MB velocity in the small vessels of the outer renal medulla as well as the first time it has differentiated the reperfusion pattern after two types of ischemia-reperfusion.

Our estimations of the mean MB velocity and perfusion index in the cortex and medulla are not comparable: The renal cortex receives approximately 90% of the total renal blood flow and has a dense and complex microvascular network. This makes microbubble tracking and MB velocity estimation difficult, which is exemplified in Fig. 2-C: There are fewer cortical tracks that represent interlobular arteries than expected. Generally, the interlobular veins seem easier to track. It could be because the veins are larger than the arteries and sometimes partly encircle the arteries, thereby hindering the tracking of the MBs in the arteries. The 2D image sections were not identical in the three consecutive scans. This is particularly apparent for *Rat 2* (Fig. 2-B1). The difference in the image sections poses a potential issue with the comparison of the consecutive scans: The differences in MB velocity and perfusion index between the ROIs may represent physiologically determined differences, but may also result from a direct comparison of anatomically unidentical regions. That issue can be eliminated with 3D SRI. 3D SRI can also solve other limitations of 2D SRI: It will allow tracking of MBs that move in the elevation plane, eliminate the risk of missing essential information outside the image section, and allow scans from the skin surface. We scanned directly on the kidney surface to reduce respiratory motion and the motion that occurs when neighboring bowels push the kidney out of plane; both of which are problematic for 2D motion correction. The data from this study will be used to further optimize the motion correction algorithm, hopefully making transcutaneous 2D SRI scanning possible. Transcutaneous scanning would make SRI applicable for long-term studies, such as investigation of how or when the microvascular changes in diabetic nephropathy or the late stages of ischemia-reperfusion injuries occur [14], and how these correlate with the early changes in microvascular blood flow. If early changes could be used for prognostic evaluation of patients and allow timely treatment initiation, SRI could become a strong clinical tool.

Plane-wave techniques are often used in SRI to obtain images at a very high framerate [1]–[4], [9]. We used focused beam transmission, because it is a well-established technology already available in commercial platforms. This could enable a faster transfer to the clinic. A disadvantage of focused beam transmission is the lower frame rate and longer acquisition time. Generally, time consumption is an often-emphasized limitation of SRI, but in order to generate super-resolution images of a complete microvascular network using MBs, the acquisition time has to be lengthy. The MBs follow the blood flow, which is slow in the capillaries, and a sufficient amount of MB detections is needed to create the images [15]. Also, compared with other imaging modalities such as MRI that is expensive and less accessible or CT that poses a radiation hazard, the time spent

attaining ultrasound images of such high resolution should be acceptable when applied to the appropriate clinical settings.

In conclusion, this small study indicates that our SRI setup can be used to evaluate not only different stages of ischemic kidney disease, but also other renal diseases, since the method depicts all areas of the renal microvasculature and can detect differences in reperfusion after two different ischemia-reperfusion events. However, the experiments were performed using only two rats. A more extensive study will be conducted.

ACKNOWLEDGMENTS

Thanks to Henrik Koch Johansen (BK Medical ApS) for constructing the syringe-turning device. Financial study support: Innovation Fund Denmark (grant 7050-00004B).

REFERENCES

- [1] C. Errico *et al.*, 'Ultrafast ultrasound localization microscopy for deep super-resolution vascular imaging.', *Nature*, vol. 527, no. 7579, pp. 499–502, Nov. 2015.
- [2] J. Foiret, H. Zhang, T. Illovitch, L. Mahakian, S. Tam, and K. W. Ferrara, 'Ultrasound localization microscopy to image and assess microvasculature in a rat kidney.', *Sci. Rep.*, vol. 7, no. 1, p. 13662, Oct. 2017.
- [3] J. Yu, L. Lavery, and K. Kim, 'Super-resolution ultrasound imaging method for microvasculature in vivo with a high temporal accuracy', *Sci. Rep.*, vol. 8, no. 1, p. 13918, Dec. 2018.
- [4] T. Opacic *et al.*, 'Motion model ultrasound localization microscopy for preclinical and clinical multiparametric tumor characterization.', *Nat. Commun.*, vol. 9, no. 1, p. 1527, 2018.
- [5] K. Christensen-Jeffries, R. J. Browning, M. X. Tang, C. Dunsby, and R. J. Eckersley, 'In vivo acoustic super-resolution and super-resolved velocity mapping using microbubbles', *IEEE Trans. Med. Imaging*, vol. 34, no. 2, pp. 433–440, Feb. 2015.
- [6] A. S. Levey and M. T. James, 'Acute Kidney Injury', *Ann. Intern. Med.*, vol. 167, no. 9, p. ITC66, Nov. 2017.
- [7] S. M. Owji, E. Nikeghbal, and S. M. Moosavi, 'Comparison of ischaemia-reperfusion-induced acute kidney injury by clamping renal arteries, veins or pedicles in anaesthetized rats', *Exp. Physiol.*, vol. 103, no. 10, pp. 1390–1402, Oct. 2018.
- [8] W. Cao *et al.*, 'Contrast-Enhanced Ultrasound for Assessing Renal Perfusion Impairment and Predicting Acute Kidney Injury to Chronic Kidney Disease Progression', *Antioxid. Redox Signal.*, vol. 27, no. 17, pp. 1397–1411, Dec. 2017.
- [9] Y. Yang *et al.*, 'Assessment of Diabetic Kidney Disease Using Ultrasound Localization Microscopy: An in Vivo Feasibility Study in Rats', in *Proc. IEEE Ultrason. Symp.*, 2018, pp. 1–4.
- [10] K. Fischer *et al.*, 'High-resolution renal perfusion mapping using contrast-enhanced ultrasonography in ischemia-reperfusion injury monitors changes in renal microperfusion.', *Kidney Int.*, vol. 89, no. 6, pp. 1388–98, 2016.
- [11] J. A. Jensen, S. B. Andersen, C. A. V. Hoyos, K. L. Hansen, C. M. Sorensen, and M. B. Nielsen, 'Tissue Motion Estimation and Correction in Super Resolution Imaging', in *Proc. IEEE Ultrason. Symp.*, 2019.
- [12] D. B. Moffat and J. Fourman, 'A vascular pattern of the rat kidney. 1963.', *J. Am. Soc. Nephrol.*, vol. 12, no. 3, pp. 624–32, Mar. 2001.
- [13] R. Wagner, D. Van Loo, F. Hossler, K. Czymmek, E. Pauwels, and L. Van Hoorebeke, 'High-Resolution Imaging of Kidney Vascular Corrosion Casts with Nano-CT', *Microsc. Microanal.*, vol. 17, no. 2, pp. 215–219, Apr. 2011.
- [14] H.-J. Wang, A. Varner, T. AbouShwareb, A. Atala, and J. J. Yoo, 'Ischemia/Reperfusion-Induced Renal Failure in Rats as a Model for Evaluating Cell Therapies', *Ren. Fail.*, vol. 34, no. 10, pp. 1324–1332, Nov. 2012.
- [15] V. Hingot, C. Errico, B. Heiles, L. Rahal, M. Tanter, and O. Couture, 'Microvascular flow dictates the compromise between spatial resolution and acquisition time in Ultrasound Localization Microscopy.', *Sci. Rep.*, vol. 9, no. 1, p. 2456, Feb. 2019.



Paper 8

Tracking Performance in Ultrasound Super-Resolution Imaging

Iman Taghavi, Sofie Bech Andersen, Carlos Armando Villagómez Hoyos, Mikkel Schou, Sigrid Husebø Øygaard, Fredrik Gran, Kristoffer Lindkov Hansen, Charlotte Mehlin Sørensen, Michael Bachman Nielsen, Matthias Bo Stuart, and Jørgen Arendt Jensen

Published in:

Proceedings of the IEEE International Ultrasonic Symposium

Document Version:

Published

DOI:

10.1109/IUS46767.2020.9251605

General rights

Copyright and moral rights for the publications made accessible in the public portal are retained by the authors and/or other copyright owners and it is a condition of accessing publications that users recognise and abide by the legal requirements associated with these rights.

- Users may download and print one copy of any publication from the public portal for the purpose of private study or research.
- You may not further distribute the material or use it for any profit-making activity or commercial gain
- You may freely distribute the URL identifying the publication in the public portal

If you believe that this document breaches copyright please contact us providing details, and we will remove access to the work immediately and investigate your claim.

Tracking Performance in Ultrasound Super-Resolution Imaging

Iman Taghavi¹, Sofie B. Andersen^{2,3}, Carlos A. Villagomez Hoyos⁴, Mikkel Schou¹, Sigrid H. Øygard¹,
Fredrik Gran⁴, Kristoffer L. Hansen², Charlotte M. Sørensen³, Michael B. Nielsen²,
Matthias B. Stuart¹, Jørgen Arendt Jensen¹

¹Department of Health Technology, Technical University of Denmark

²Department of Diagnostic Radiology, Rigshospital, Denmark

³Department of Biomedical Sciences, University of Copenhagen,

⁴BK Medical, Herlev, Denmark

Abstract—Tracking plays an important role in super-resolution (SR) ultrasound imaging, as it improves the quality and sharpness of the final SR images. Moreover, tracking enables quantification of clinically important parameters, such as blood flow velocity. However, the tracking performance degrades in the presence of complex particle patterns and localization uncertainty due to noise and motion. This work presents and discusses multiple approaches for tracking evaluation and compares a nearest-neighbor (NN) with a Kalman tracker through simulations and an in vivo experiment. It is shown that in the presence of a localization uncertainty with a standard deviation (SD) of $\lambda/5$, the bias and SD of the velocity estimates reach -1.04 ± 0.9 mm/s and -0.12 ± 0.72 mm/s in the NN and Kalman tracker, respectively (relative to the peak velocity of 10 mm/s). The precision of individual track positions is estimated for an in vivo experiment as 37.95 ± 21.37 μm and 23.9 ± 11.82 μm for the NN and Kalman trackers, respectively. The results indicate that the Kalman tracker achieves a better velocity estimation and reduces localization uncertainty.

I. INTRODUCTION

Ultrasound super-resolution imaging (SRI) has been studied by various research groups over the last years [1]–[7]. The approach employs detection and tracking of microbubble (MB) contrast agents to visualize the micro-vasculature including the capillary network. A detector estimates the centroids of the MBs, and several factors including the non-linear imaging scheme, the signal to noise ratio (SNR), complex and nonuniform MB concentrations, and various MB dynamics affect the centroid estimation and tracking of the MB positions. The centroid localization is uncertain, since the above mentioned factors produce non-symmetrical, overlapped, dissimilar, and shifted target spread functions for the various MBs during the scan. These conditions are even worse for in vivo measurements, as several other ultrasound artifacts, organ motion, and uncontrolled MB concentrations depending on the 3D vessel structure, affect the images.

The tracking methods aim to link the detected MBs from frame to frame. The methods range from simple nearest-neighbor (NN) [8] to multi-frame data structure and using explicit motion models (e.g. Kalman filtering) [6], [9]–[11].

This work investigates several performance metrics for tracking evaluation. A NN and a Kalman tracker are compared through both simulations with known ground-truth and in an in vivo experiment with unknown ground-truth. Finally, a new tracking strategy that will likely address tracking difficulties in a wide range of scenarios is suggested.

II. METHODS

A. Simulation

The simulations were made by generating MB positions, each with uniformly random lifetime and known ground-truth, moving with different velocities across an X-shaped phantom. A random localization error was added to each MB position. The various parameters of the phantom are listed in Table I. The ground-truth tracks with different MB density and trajectories of MBs with localization uncertainty are shown in Fig. 1. These simulations provided a wide range of scenarios, including various MB concentrations, velocities, and localization uncertainties.

TABLE I: Parameters used in the in-silicon X-phantom

Parameters	Value
Tube length	10 mm
Tube radius	250 μm & 125 μm
Peak velocity	10 mm/s & 5 mm/s
Velocity profile	Parabolic
Angle between tubes	60°
Point Spread Function (PSF)	Unsymmetrical Gaussian
Axial / Lateral FWHM	0.7 λ / 1.5 λ
Number of MBs per frame (mean \pm standard deviation (SD))	Very low: 2 \pm 2 Low: 8 \pm 4 Medium: 28 \pm 13 High: 49 \pm 20
Uncertainty in localization (SD of localization error)	Very low: $\lambda/20$ Low: $\lambda/10$ Medium: $\lambda/5$ High: $\lambda/2$

B. In vivo measurement

The in vivo measurement was conducted using a modified BK5000 scanner, and an X18L5s transducer (BK Medical,

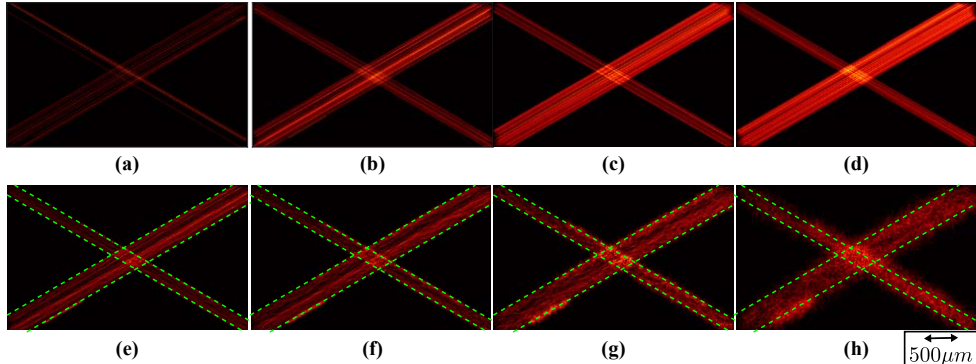


Fig. 1: Ground-truth tracks of various MB density scenarios for (a) a very low (b) low (c) medium or (d) high concentration. The tracks of uncertain MB positions with standard deviation of (e) $\lambda/20$ (f) $\lambda/10$ (g) $\lambda/5$ and (h) $\lambda/2$ for a low-density scenario are shown in the bottom row. The green dash lines show the wall of the tubes.

Herlev, Denmark) was used to record 10 minutes of contrast-enhanced and B-mode frames from a rat kidney with a frame rate of 53.85 Hz. A pulse amplitude modulation sequence was used for imaging with a transmit frequency of 6 MHz ($\lambda = 256 \mu\text{m}$). The transmit voltage was low with a corresponding mechanical index (MI) of 0.2 to prevent bursting of the MBs. The MBs (SonoVue, Bracco, Milan, Italy) were injected with a flow-rate of 100 $\mu\text{l}/\text{min}$ after a 1:10 dilution.

C. Tracking algorithms

In the NN tracker, the estimated MB positions in the next frame are linked to the MB positions in the current frame based on their minimum distance. Though NN is simple and fast, simple linking of MB positions generates false and flexuous tracks when the localization is uncertain. Considering the MB's smooth movement, more robust tracking is possible via Kalman filtering. This simple movement consideration can be modeled as $\vec{r}(t) = \vec{r}(t-1) + d\vec{r}(t) + \vec{\epsilon}(t)$, where $\vec{r}(t) = (r_z(t), r_x(t))$ is the position of MB at time t , $d\vec{r}(t) = (dr_z(t), dr_x(t))$ is the displacement of the MB and $\epsilon(t)$ is the uncertainty in the displacement. This model can be formulated within the Kalman framework as:

$$\begin{cases} \vec{x}(t) = \mathbf{F}x(t-1) + \epsilon(t) \\ \vec{z}(t) = \mathbf{H}\vec{x}(t) + v(t), \end{cases} \quad (1)$$

where $x(t) = [\vec{r}(t), d\vec{r}(t)]^T = [r_z(t), r_x(t), dr_z(t), dr_x(t)]^T$, $\vec{x}(t)$ is the prediction of MB position in the next frame, $\vec{z}(t)$ is the estimated uncertain position,

$$\mathbf{F} = \begin{bmatrix} 1 & 0 & 1 & 0 \\ 0 & 1 & 0 & 1 \\ 0 & 0 & 1 & 0 \\ 0 & 0 & 0 & 1 \end{bmatrix}, \quad \mathbf{H} = \begin{bmatrix} 1 & 0 & 0 & 0 \\ 0 & 1 & 0 & 0 \end{bmatrix},$$

$\epsilon(t) \sim \mathcal{N}(0, \sigma_\epsilon^2)$, and $v(t) \sim \mathcal{N}(0, \sigma_v^2)$.

In this study, the maximum linking distance was 500 μm , and the initial conditions of the Kalman filter were $\sigma_\epsilon = 1 \text{ mm}$ and $\sigma_v = 100 \mu\text{m}$. After tracking, the velocity of the MBs was estimated by calculating the time derivative of track positions.

D. Evaluation

The first group of performance metrics, proposed in [12], was based on an assignment problem. To evaluate tracking performance using this approach, estimated tracks were paired with ground-truth tracks based on their minimum distance using Hungarian algorithm [13]. Hungarian algorithm provides fast optimal assignment of the two sets. The gate size is equal to λ , meaning that any tracks outside this gate range were considered as false positive (FP), tracks within the gate range were assumed as true positive (TP) or false negative (FN), if they are paired or unpaired to the ground-truth. The Jaccard Similarity Coefficient (JSC) is defined as $\text{JSC} = \text{TP}/(\text{TP}+\text{FP}+\text{FN})$, which determines the similarity of the set of estimated tracks and set of ground-truth tracks. The root-mean-square error (RMSE) of velocity estimates was calculated for each paired track (TP), and the number of unpaired (spurious) tracks was also counted as an extra performance metric. For the paired tracks, JSC of track positions and RMSE of the estimated positions can also be calculated to provide metrics at the position level.

The second performance metric was calculated by considering the known velocity profile of flow in the tubes as a ground-truth. In this approach bias and standard deviation of velocity profiles over different cross sections of the tubes were calculated.

The localization uncertainty in the in vivo data, used as the last performance metric, was estimated by RMSE of a fitted piece-wise least-square line to the MB positions.

III. RESULTS

The super-resolution (SR) images shown in Fig. 2 indicate that the Kalman filter has more smooth tracks in this scenario. All of the assignment-based performance metrics for various density and uncertainty scenarios at the track and position levels are listed in Table II and Table III (the green labels show a better performance). At the position level, the Kalman filter outperformed the NN almost in all scenarios. Notice that the RMSE of the track positions are relevant to the localization

TABLE II: Performance Metrics at Track Level (Color scheme: green → higher performance, yellow → roughly the same).

MB Density	Tracker	Uncertainty in Localization											
		SD = $\lambda/20$ = 12.83 μm			SD = $\lambda/10$ = 25.67 μm			SD = $\lambda/5$ = 51.33 μm			SD = $\lambda/2$ = 128.34 μm		
		JSC	Spurious	RMSE	JSC	Spurious	RMSE	JSC	Spurious	RMSE	JSC	Spurious	RMSE
Very low	NN	0.731	14	0.01	0.731	14	0.01	0.731	14	0.05	0.132	250	0.33
	Kalman	1	0	0	1	0	0	1	0	0.03	0.528	34	0.01
Low	NN	0.961	13	3.19	0.953	16	0.01	0.835	64	3.22	0.148	1868	0.34
	Kalman	0.934	23	0.03	0.923	27	0	0.91	32	0.01	0.416	454	0.03
Medium	NN	0.892	104	0	0.839	165	0.02	0.642	478	0.9	0.104	7437	0.17
	Kalman	0.534	435	0.01	0.632	500	0.02	0.595	585	0.04	0.236	2194	0.19
High	NN	0.717	672	0.06	0.634	983	1.02	0.435	2209	0.3	0.095	16226	1.1
	Kalman	0.446	2079	0.04	0.418	2376	0.04	0.388	2681	0.01	0.215	6209	0.9

TABLE III: Performance Metrics at Position Level (Color scheme: green → higher performance, yellow → roughly the same).

MB Density	Tracker	Uncertainty in Localization							
		SD = $\lambda/20$		SD = $\lambda/10$		SD = $\lambda/5$		SD = $\lambda/2$	
		JSC	RMSE	JSC	RMSE	JSC	RMSE	JSC	RMSE
Very low	NN	0.639	15.02	0.639	29.49	0.576	52.27	0.127	135.23
	Kalman	1	11.99	1	20.34	0.937	37.63	0.584	88.92
Low	NN	0.754	14.3	0.672	25.12	0.557	38.86	0.154	115.25
	Kalman	0.92	13.96	0.836	22.18	0.788	36.61	0.463	76.55
Medium	NN	0.511	15.54	0.432	15.58	0.354	29.21	0.094	112.72
	Kalman	0.534	13.21	0.493	19.95	0.421	31.83	0.236	77.48
High	NN	0.446	16.52	0.36	22.62	0.266	40.09	0.078	111.92
	Kalman	0.432	15.98	0.38	22.92	0.319	38.99	0.189	79.75

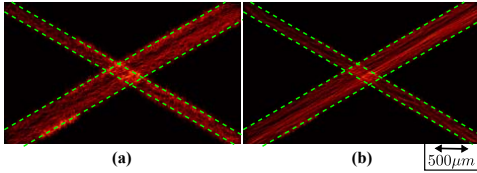


Fig. 2: A comparison between (a) NN tracker, and (b) Kalman tracker for low-density scenario and uncertainty of $\lambda/5$ in the localization.

uncertainty. This will be used later to estimate the uncertainty of localization from the in vivo measurements. At track level, NN achieved a better rank in JSC, and the number of spurious tracks was lower in several scenarios. However, the velocity estimates of paired tracks were more accurate when a Kalman filter was employed. This diverse behavior of trackers through different scenarios is discussed in Section IV. It can be seen that in some scenarios the Kalman filter can reduce the number of spurious tracks by more than 67%.

To avoid the ambiguities in an assignment problem, the estimated velocity profiles over 14 cross-sections of the larger vessel in the final SR image are illustrated in Fig. 3. The velocity estimates and the resolution were improved by the Kalman filter. This shows the superiority of the Kalman over NN in a scenario with high MB concentration and uncertainty in the localization.

While there is no ground-truth for the in vivo measurement, less flexuous tracks are expected for more accurate localization or robust trackers. To measure the precision of the tracks positions, a piece-wise least-square line was fitted to MB positions tracked for more than 5 frames. Table IV lists the mean and SD of the localization error relative to the fitted line after NN and Kalman tracking. It shows that the Kalman filter has reduced the localization uncertainty. Fig. 4 shows SR images produced by the two trackers for 90 seconds of the in

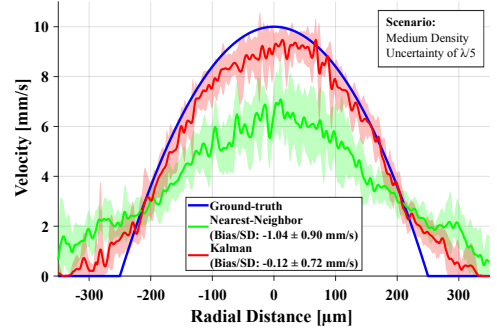


Fig. 3: Velocity estimation statistics over 14 cross-sections of the large vessel for medium density scenario with localization uncertainty of $\lambda/5$. The NN estimates had a bias and standard deviation of -1.04 ± 0.9 mm/s, while these values for the Kalman estimates were reduced to -0.12 ± 0.72 mm/s.

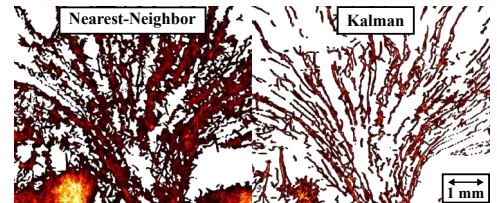


Fig. 4: Super-resolution images of renal inner medulla created using the NN (left) and Kalman (right) trackers. The NN generated a lot of spurious and flexuous tracks. However, the Kalman tracker reduced these uncertainties. The structure is clearly distinguishable in the right image, as it is resolved down to 25.6 μm for almost every position.

vivo data. It is clear that the Kalman tracker outperforms the NN tracker.

Finally, velocity SR images of the entire kidney, shown in Fig. 5, demonstrate the difference between two trackers in terms of less spurious and less uncertain tracks.

TABLE IV: Tracking performance on localization uncertainty

Tracker	Precision of individual track positions
NN	$37.95 \pm 21.37 \mu\text{m}$
Kalman	$23.9 \pm 11.82 \mu\text{m}$

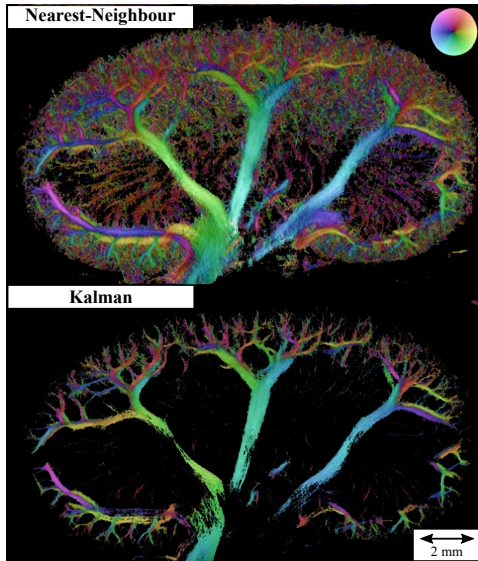


Fig. 5: Velocity SR images of the kidney show renal vascular tree with opposite flows (arteries and veins). The color wheel on top-right corner shows the flow direction of the color-coded tracks.

IV. DISCUSSION

Considering only the JSC and the number of spurious tracks, NN performed better than Kalman in some scenarios. Two key factors explain this behavior of the Kalman tracker. Firstly, based on the definition of optimal assignment, a unique estimated track must be assigned to a ground-truth track. A tracker might estimate a long track with multiple small tracks. In this case, while tracks are correct, the number of spurious tracks will increase, and JSC will decrease. Therefore, these two metrics cannot determine the overall performance of the tracker in all scenarios. Secondly, a single Kalman filter with specific initial conditions is employed for tracking in all scenarios. A Kalman filter might not reach a fair estimate within a short lifetime of these MBs. The question that may arise here is why we do not optimize the tracker for each specific scenario? The reason is that in an in vivo measurement, the tracker has to deal with a wide range of scenarios, as the MBs have uncontrolled concentrations as well as different velocities and flow dynamics when entering the blood stream. All of these scenarios are usually difficult to track with a simple tracking strategy. One solution would be tracking with a hierarchical structure. For example, a Kalman filter with a strict initial condition can apply to track slow flows. Then, the untracked MBs and the track positions with an overestimated velocity can be passed to another Kalman filter optimized to track faster MBs. This can be continued in a hierarchical structure to cover all range of scenarios [14].

V. CONCLUSION

Several performance metrics for the tracking algorithms in SRI were investigated. It was shown that in the presence of a high localization uncertainty, the Kalman tracker reached a better velocity estimate bias and SD of $-0.12 \pm 0.72 \text{ mm/s}$ compared to $-1.04 \pm 0.9 \text{ mm/s}$ in the NN relative to a peak velocity of 10 mm/s . The Kalman tracker reduced the precision of individual track positions in an in vivo experiment to $37.95 \pm 21.37 \mu\text{m}$ and $23.9 \pm 11.82 \mu\text{m}$ for the NN and Kalman trackers. Overall, the Kalman tracker was superior, as it estimated velocity with a higher precision and reduced localization uncertainty.

ACKNOWLEDGMENT

This work was financially supported by grant 82-2014-4 from the Danish National Advanced Technology Foundation, by grant 7050-00004B from Innovation Fund Denmark, and from BK Medical, Herlev, Denmark.

REFERENCES

- [1] O. M. Viessmann, R. J. Eckersley, K. Christensen-Jeffries, M. X. Tang, and C. Dunsby, "Acoustic super-resolution with ultrasound and microbubbles," *Phys. Med. Biol.*, vol. 58, pp. 6447–6458, 2013.
- [2] M. A. O'Reilly and K. Hynynen, "A super-resolution ultrasound method for brain vascular mapping," *Med. Phys.*, vol. 40, no. 11, pp. 110701–7, 2013.
- [3] Y. Desailly, J. Pierre, O. Couture, and M. Tanter, "Resolution limits of ultrafast ultrasound localization microscopy," *Phys. Med. Biol.*, vol. 60, no. 22, pp. 8723–8740, 2015.
- [4] K. Christensen-Jeffries, R. J. Browning, M. Tang, C. Dunsby, and R. J. Eckersley, "In vivo acoustic super-resolution and super-resolved velocity mapping using microbubbles," *IEEE Trans. Med. Imag.*, vol. 34, no. 2, pp. 433–440, February 2015.
- [5] C. Errico, J. Pierre, S. Pezet, Y. Desailly, Z. Lenkei, O. Couture, and M. Tanter, "Ultrafast ultrasound localization microscopy for deep super-resolution vascular imaging," *Nature*, vol. 527, pp. 499–502, November 2015.
- [6] D. Ackermann and G. Schmitz, "Detection and tracking of multiple microbubbles in ultrasound B-mode images," *IEEE Trans. Ultrason., Ferroelec., Freq. Contr.*, vol. 63, no. 1, pp. 72–82, January 2016.
- [7] K. Christensen-Jeffries, O. Couture, P. A. Dayton, Y. C. Eldar, K. Hynynen, F. Kiessling, M. O'Reilly, G. F. Pinton, G. Schmitz, M. Tang *et al.*, "Super-resolution ultrasound imaging," *Ultrasound Med. Biol.*, vol. 46, no. 4, pp. 865–891, 2020.
- [8] J. C. Crocker and D. G. Grier, "Methods of digital video microscopy for colloidal studies," *J. Colloid. vol.* 179, no. 1, pp. 298–310, 1996.
- [9] O. Solomon, R. J. G. van Sloun, H. Wijkstra, M. Mischi, and Y. C. Eldar, "Exploiting flow dynamics for super-resolution in contrast-enhanced ultrasound," *IEEE Trans. Ultrason., Ferroelec., Freq. Contr.*, vol. 60, no. 10, pp. 1573–1586, 2019.
- [10] S. Tang, P. Song, J. D. Trzasko, M. Lowerison, C. Huang, P. Gong, U. Lok, A. Manduca, and S. Chen, "Kalman filter-based microbubble tracking for robust super-resolution ultrasound microvessel imaging," *IEEE Trans. Ultrason., Ferroelec., Freq. Contr.*, vol. PP, no. 99, pp. 1–1, 2020.
- [11] W. J. Godinez, M. Lampe, S. Worz, B. Müller, R. Eils, and K. Rohr, "Deterministic and probabilistic approaches for tracking virus particles in time-lapse fluorescence microscopy image sequences," *Med. Image Anal.*, vol. 13, no. 2, pp. 325–342, 2009.
- [12] N. Chenouard, I. Smal, F. D. Chaumont, M. Maška, I. F. Sbalzarini, Y. Gong, J. Cardinale, C. Carthel, S. Coraluppi, M. Winter *et al.*, "Objective comparison of particle tracking methods," *Nature methods*, vol. 11, no. 3, pp. 281–290, 2014.
- [13] H. W. Kuhn, "The Hungarian method for the assignment problem," *Naval research logistics quarterly*, vol. 2, no. 1-2, pp. 83–97, 1955.
- [14] I. Taghavi *et al.*, "In vivo ultrasound super-resolution imaging with motion correction and robust tracking," *IEEE Trans. Med. Imag.*, p. submitted, 2020.



Paper 9

Super-resolution Ultrasound Imaging of the Renal Microvasculature in Rats with Metabolic syndrome

Stinne Byrholdt Søgaaard, Sofie Bech Andersen, **Iman Taghavi**, Carlos Armando Villagómez Hoyos, Kristoffer Lindskov Hansen, Fredrik Gran, Jørgen Arendt Jensen, Michael Bachmann Nielsen, and Charlotte Mehlin Sørensen

Published in:

Proceedings of the IEEE International Ultrasonic Symposium

Document Version:

Published

DOI:

10.1109/IUS46767.2020.9251652

General rights

Copyright and moral rights for the publications made accessible in the public portal are retained by the authors and/or other copyright owners and it is a condition of accessing publications that users recognise and abide by the legal requirements associated with these rights.

- Users may download and print one copy of any publication from the public portal for the purpose of private study or research.
- You may not further distribute the material or use it for any profit-making activity or commercial gain
- You may freely distribute the URL identifying the publication in the public portal

If you believe that this document breaches copyright please contact us providing details, and we will remove access to the work immediately and investigate your claim.

Super-resolution Ultrasound Imaging of the Renal Microvasculature in Rats with Metabolic syndrome

Stinne Byrholdt Sogaard^{1,2,3}, Sofie Bech Andersen^{1,2,3}, Iman Taghavi⁴, Carlos Armando Villagómez Hoyos⁵, Kristoffer Lindskov Hansen^{1,3}, Fredrik Gran⁵, Jørgen Arendt Jensen⁴, Michael Bachmann Nielsen^{1,3}, Charlotte Mehlin Sørensen³.

¹Department of Diagnostic Radiology, Rigshospitalet, Copenhagen, Denmark.

²Department of Biomedical Sciences, University of Copenhagen, Copenhagen, Denmark.

³Department of Clinical Medicine, University of Copenhagen, Copenhagen, Denmark.

⁴Center for Fast Ultrasound Imaging, Department of Health Technology, Technical University of Denmark, Lyngby, Denmark.

⁵BK Medical, Herlev, Denmark.

Abstract—Super-resolution Ultrasound imaging (SRI) can visualize and quantify changes in the microvasculature. Metabolic syndrome is associated with hypertension and hyperlipidemia that affects different organs, including the kidneys. *Ex vivo* studies have shown glomerular injury in Obese Zucker rats (OZR) over time. If *in vivo* SRI can diagnose renal disease earlier than currently possible, treatment can be initiated in time to postpone the onset of renal complications in persons with metabolic syndrome. The overall aim of this study was to investigate whether SRI can detect early microvascular changes in the kidneys of rats with metabolic syndrome. The rats presented in this work were scanned at an early age to get a baseline scan prior to further studies. An 11-week-old OZR and a healthy age-matched Zucker rat were investigated. During open surgery, the left kidney was scanned for 10 min using a modified BK5000 scanner (BK Medical, Denmark) and a fixated X18L5s transducer. SonoVue (Bracco, Italy) was injected intravenously (1:10 dilution). Contrast images were obtained using a pulse amplitude modulation sequence and interleaved B-mode images were obtained for tissue motion correction (focused beam transmission, 6 MHz, 50 Hz, MI: 0.2). An in-house tool was used to track microbubble (MB) movements between frames to estimate the MB velocities measured in a large region of the cortex and the outer medulla. Both the cortex and the medulla were well-perfused with MBs, and no morphological differences in the microvasculature were found between the two rats. The thickness of the cortex and the medulla was almost identical; *cortex* 1.8 mm, *medulla* 8 mm, *craniocaudal length* 2.0 vs. 1.9 cm (healthy vs. OZR). The same was true regarding the MB velocities (median (IQR); difference between upper and lower quartiles = Q3 – Q1) in mm/s) for healthy vs. OZR; *cortex* 0.75 (3.51) vs. 0.65 (2.64) and *medulla* 0.75 (0.32) vs. 0.62 (0.30). This is the first time SRI has been used on the kidneys of rats with metabolic syndrome. The results will be used as the foundation for further investigations of the renal microvascular changes, which occur in the course of metabolic syndrome.

Keywords—Obese Zucker rat, metabolic syndrome, chronic kidney disease

I. INTRODUCTION

Ultrasound super-resolution imaging (SRI) enables *in vivo* visualization of the microvasculature. Studies have proven the ability to perform *in vivo* SRI in different animals, but the literature on pathological microvascular changes is still sparse [1]–[6]. SRI uses gas-filled microbubbles (MBs) as intravascular tracers. Over a series of thousands of successive image frames, the location of each individual MB is detected,

and by accumulating all the MB positions, a single image of the microvascular network is created [1], [2]. Furthermore, by tracking the MBs in time across the image frames, estimations of MB velocity and direction are feasible.

Obese Zucker Rats (OZR) have a mutation in the leptin receptor gene which results in obesity, hyperinsulinemia and poorly regulated blood glucose causing hyperlipidemia and glomerulosclerosis at an early age. The rat-model can develop albuminuria as also seen in correlation with diabetes mellitus (DM). [7], [8]. DM is associated with microvascular disease in several organs including the kidneys. Microalbuminuria (excretion of 30-300 mg/24 hours of albumin in the urine) is the earliest measurable stage of microvascular kidney disease in DM. Macroalbuminuria is related to diabetic nephropathy (DN), and defined by urinary albumin excretion >300 mg/24 hours. DN is one of the main causes of end-stage renal failure and results in a poor prognosis for the patients and high medical costs [9]. Therefore, SRI of the kidneys of persons with metabolic syndrome and DM has a big potential. With current clinical measures and laboratory tests it is not possible to predict DN until the disease is manifest.

By the use of SRI, we aimed to confirm that there are no morphological and flow-wise differences in the renal microvasculature between a 11-week-old OZR and an age-matched lean rat. The results will serve as baseline prior to scanning of older rats with metabolic syndrome.

II. MATERIALS AND METHODS

A. Animals

The experiment was conducted on one 11-week-old OZR and one healthy age-matched Zucker rat (396 and 308g). The experiment was executed according to protocols approved by the Danish National Animal Experiments Inspectorate. The procedures were performed at the University of Copenhagen, and all local ethical standards were respected. The ethical policy of the university is consistent with that of the National Institutes of Health (NIH). The rats were obtained at 9 weeks, fed standard laboratory chow *ad libitum*, allowed free access to water and housed in an animal facility at the University of Copenhagen, Department of Experimental Medicine, under the responsibility

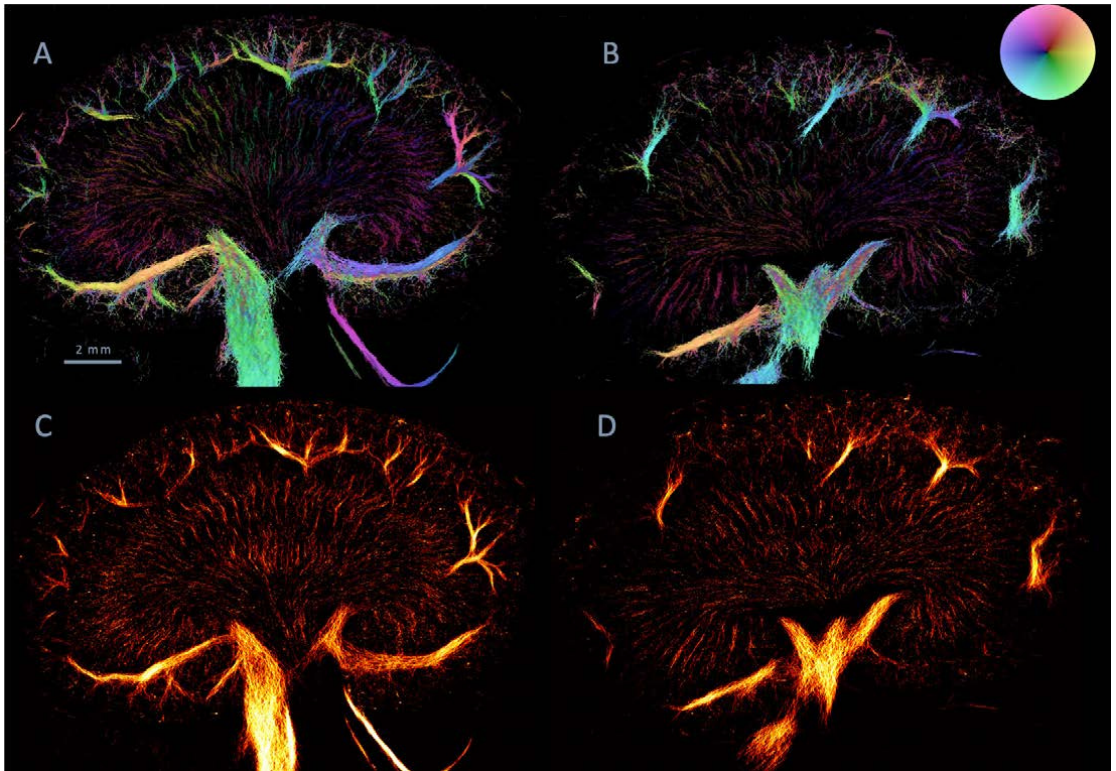


Fig.1 These images are filtered by inclusion of every track with a max velocity of 15 (mm/sec). Hierarchical-Kalman tracker and motion compensation is applied.

A: Microbubble velocity image of an 11-week-old lean Zucker rat, showing the microbubble flow directions according to the color wheel in the top right corner.

B: Microbubble velocity image of an 11-week-old obese Zucker rat.

C: Intensity image of an 11-week-old lean Zucker rat.

D: Intensity image of an 11-week-old obese Zucker rat.

of trained animal caretakers. Prior to the scans the rats were anesthetized with 5% isoflurane and placed on a heating table to maintain normal body temperature (37°C). The blood pressure was measured continuously by a catheter in the carotid artery. After initial anesthesia a final isoflurane concentration of 1-2% through a tracheostomy was maintained. The rat's ventilation was controlled by a mechanical ventilator with a respiration cycle of 72 respirations/min. After laparotomy and to further expose the left kidney and reduce the respiratory motion, a metal retractor under the left diaphragm pulling slightly cranially was established. Prior to every scan the rat was infused with Nimbex (cisatracurium, 0.85 mg/ml, GlaxoSmithKline). Before the scan, blood and urine samples were collected. After the scans the rats were euthanized in anesthesia.

B. Ultrasound scan procedure and SRI technique

The left kidney was scanned using a modified BK5000 scanner and a fixated X18L5s transducer (BK Medical Aps, Herlev, Denmark). Sonovue (Bracco, Milan, Italy) was used as

contrast. The contrast was diluted in isotonic saline (1:10) and injected through a jugular vein catheter. Each SRI scan lasted 10 minutes [10]. Contrast images were obtained using a pulse amplitude modulation sequence and interleaved B-mode images were obtained for tissue motion correction (line-per-line focused beam transmission; center frequency for transmission: 6 MHz, frame rate: 50 Hz, mechanical index: 0.2). The tissue motion correction was applied before the tracking of the MBs [11]. The MB tracks were made with the use of a Hierarchical-Kalman tracker [12]. In order to estimate MB velocity in a region of the cortex and a region of the outer medulla, respectively, the images were filtered using an in-house tool. The track images were filtered according to flow direction (cortex; flow toward the renal surface, medulla; flow toward the renal papilla) and a maximum velocity of 15 mm/second.

C. Blood samples

Blood glucose was measured to determine if the rat had developed DM. Blood glucose was measured prior to the

laparotomy to avoid surgical induced stress and thereby give a wrongly high result.

D. Histology

The left kidney was removed after euthanasia to document any possible tissue damage by staining. The kidneys were stored in 4% paraformaldehyde and stained by Sirius Red staining. The images were evaluated by an experienced anatomist, blinded to the samples.

III. RESULTS

A. The microvasculature of the rats

The thickness of the cortex and the medulla was identical in the two rat models, 1.8 mm and 8 mm, respectively. The craniocaudal length of the kidneys likewise; 2.0 cm and 1.9 cm (healthy versus OZR). No difference was found in the MB velocities (median (IQR; difference between upper and lower quartiles = $Q3 - Q1$) in mm/s) for healthy vs. OZR. Cortex 0.75 (3.51) vs. 0.65 (2.64) and medulla 0.75 (0.32) versus 0.62 (0.30). (Fig.1)

The Sirius Red stained tissue (Fig 2) showed normal glomeruli in both animals.

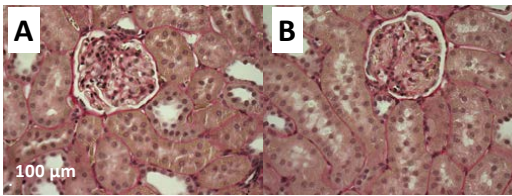


Fig 2
A: Histology image of kidney tissue stained with Sirius Red from an 11-week-old healthy Zucker rat showing a normal glomerulus with no glomerulosclerosis.

B: Normal glomerulus from an 11-week-old obese Zucker rat.

B. Clinical parameters

Mean arterial blood pressure during the scan for the healthy Zucker rat was 63 mmHg compared with 95 mmHg for the OZR. Blood glucose prior to the scan was 8.3 mmol/L for the healthy and 9 mmol/L for the OZR (<11 mmol/L is normal blood glucose when not fasting).

IV. DISCUSSION

The histology results supported our SRI exams. No morphological differences, including absence of glomerulosclerosis, between the two rats were found. This is the first time the renal microvasculature on a rat with metabolic syndrome has been visualized by the use of SRI. Others have studied ischemia on rats with SRI and visualized the renal microvasculature after acute kidney injury [3].

The intention with this study is to move further with SRI by scanning the kidneys of rats with metabolic syndrome at a later stage and to characterize the microvascular damage caused by this disease. Studies have found an increase in the microvascular density of OZR at week 32 of age [13]. It is challenging to

quantify the structural changes that occur in the renal microvasculature. The image quality is affected by e.g. uncertainty in tissue and out-of-plane motion, MB localization and scan plane. Also, the SR tracks represent many different vessel types at the same time. Specific areas of the microvasculature may be of particular interest, depending on the clinical question. We expect the earliest changes in the renal microvasculature of rats with metabolic syndrome to occur in the capillaries (glomeruli and peritubular capillary network) of the renal cortex. Therefore, filtration of the tracks is needed to achieve our goal. The tracks can be filtered by length of tracks, minimum and maximum velocity, life time of the individual MBs and track direction. The cortical capillaries have very slow velocities and are very tortuous which makes them look short on 2D. However, careful evaluation of the efforts of different filtrations is needed to avoid incorrect analyses and conclusions. Eventually, quantification will make it possible to look at differences in micro vessel density, branching, and tortuosity of the renal vessels as reported in the literature [6], [14]. Others have detected changes in the micro vessel density of rats with diabetes by looking at micro-CT ex vivo [15].

The overall aim is to scan patients from the skin to detect DN earlier than with current measures, to start treatment and to monitor the disease bedside. To investigate this a longitudinal study with rats scanned from the skin and given a reno-protective drug should be performed, to see if the changes in the renal microvasculature is reversible.

To translate this method into clinical use, several limitations needs to be addressed. Only two rats were included in the study and they were scanned intraabdominally. Prior to the scan of humans, the quality of the scans needs to be improved to make it possible to scan people with diabetes from the skin. Currently, with the scan-time of 10 minutes it would be a challenge to have the patient lying still for that long. Ideally, the scan-time should be reduced to a maximum of 2-3 minutes. Also, the data is reported off-line. Hypothetically, if one wants to inform the patient in the room when scanned, the data needs to be reported online to do the processing of the data promptly and get the result while still in the consultation room. Another limitation is that the rats are infused with contrast continuously to visualize the renal microvasculature. It would be favorable to avoid this, since it is invasive and a risk for the patients. The contrast is approved to be used as a bolus of a frequency of 2 and not as an infusion as used currently on the rats. For future studies, blood and urinary parameters need to be measured to evaluate the kidney function. Additionally, a Jones Silver staining of the tissue should be performed, since this staining provides a more detailed view on glomerulosclerosis.

Conclusively, we confirm, that the OZR is still too young to observe any vascular changes related to metabolic syndrome, and we can use rats at this young age as baseline for our future studies when scanning older rats.

Acknowledgment

Thanks to Karin Larsen (Department of Biomedical Sciences) for doing the surgery on the rats.

REFERENCES

- [1] C. Errico *et al.*, "Ultrafast ultrasound localization microscopy for deep super-resolution vascular imaging," *Nature*, vol. 527, no. 7579, pp. 499–502, Nov. 2015.
- [2] K. Christensen-Jeffries, R. J. Browning, M.-X. Tang, C. Dunsby, and R. J. Eekersley, "In Vivo Acoustic Super-Resolution and Super-Resolved Velocity Mapping Using Microbubbles," *IEEE Trans. Med. Imaging*, vol. 34, no. 2, pp. 433–440, Feb. 2015.
- [3] S. B. Andersen *et al.*, "Super-Resolution Ultrasound Imaging of Rat Kidneys before and after Ischemia-Reperfusion," in *IEEE International Ultrasonics Symposium, IUS*, 2019, vol. 2019-October, pp. 1169–1172.
- [4] J. Foiret, H. Zhang, T. Ilovitsh, L. Mahakian, S. Tam, and K. W. Ferrara, "Ultrasound localization microscopy to image and assess microvasculature in a rat kidney," *Sci. Rep.*, vol. 7, no. 1, p. 13662, Dec. 2017.
- [5] J. Yu, L. Lavery, and K. Kim, "Super-resolution ultrasound imaging method for microvasculature in vivo with a high temporal accuracy," *Sci. Rep.*, vol. 8, no. 1, p. 13918, Dec. 2018.
- [6] Q. Chen, J. Yu, B. M. Rush, S. D. Stocker, R. J. Tan, and K. Kim, "Ultrasound super-resolution imaging provides a noninvasive assessment of renal microvasculature changes during mouse acute kidney injury," *Kidney Int.*, Mar. 2020.
- [7] P. G. Schmitz, M. P. O'Donnell, B. L. Kasiske, S. A. Katz, and W. F. Keane, "Renal injury in obese Zucker rats: Glomerular hemodynamic alterations and effects of enalapril," *Am. J. Physiol. - Ren. Fluid Electrolyte Physiol.*, vol. 263, no. 3 32-3, 1992.
- [8] B. L. Kasiske, M. P. O'Donnell, M. P. Cleary, and W. F. Keane, "Treatment of hyperlipidemia reduces glomerular injury in obese Zucker rats," *Kidney Int.*, vol. 33, no. 3, pp. 667–672, Mar. 1988.
- [9] M. Narres *et al.*, "The Incidence of End-Stage Renal Disease in the Diabetic (Compared to the Non-Diabetic) Population: A Systematic Review," *PLoS One*, vol. 11, no. 1, p. e0147329, Jan. 2016.
- [10] V. Hingot, C. Errico, B. Heiles, L. Rahal, M. Tanter, and O. Couture, "Microvascular flow dictates the compromise between spatial resolution and acquisition time in Ultrasound Localization Microscopy," *Sci. Rep.*, vol. 9, no. 1, p. 2456, Dec. 2019.
- [11] J. A. Jensen, S. B. Andersen, C. A. V. Hoyos, K. L. Hansen, C. M. Sørensen, and M. B. Nielsen, "Tissue Motion Estimation and Correction in Super Resolution Imaging," in *Proc. IEEE Ultrason. Symp.*, 2019, pp. 1–4.
- [12] I. Taghavi *et al.*, "In vivo Super-resolution Ultrasound Imaging with Motion Correction and Robust Tracking," *Submitt. to IEEE TMI*, 2020.
- [13] R. Iliescu and A. R. Chade, "Progressive renal vascular proliferation and injury in obese zucker rats," *Microcirculation*, vol. 17, no. 4, pp. 250–258, May 2010.
- [14] J. Ehling *et al.*, "Quantitative micro-computed tomography imaging of vascular dysfunction in progressive kidney diseases," *J. Am. Soc. Nephrol.*, vol. 27, no. 2, pp. 520–532, Feb. 2016.
- [15] C. Maric-Bilkan, E. R. Flynn, and A. R. Chade, "Microvascular disease precedes the decline in renal function in the streptozotocin-induced diabetic rat," *Am. J. Physiol. Physiol.*, vol. 302, no. 3, pp. F308–F315, Feb. 2012.



Paper 10

Automatic Classification of Arterial and Venous Flow in Super-resolution Ultrasound Images of Rat Kidneys

Iman Taghavi, Sofie Bech Andersen, Stinne Byrholdt Søggaard, Michael Bachmann Nielsen, Charlotte Mehlin Sørensen, Matthias Bo Stuart, and Jørgen Arendt Jensen

Published in:

Proceedings of the IEEE International Ultrasonic Symposium

Document Version:

Published

DOI:

10.1109/IUS52206.2021.9593655

General rights

Copyright and moral rights for the publications made accessible in the public portal are retained by the authors and/or other copyright owners and it is a condition of accessing publications that users recognise and abide by the legal requirements associated with these rights.

- Users may download and print one copy of any publication from the public portal for the purpose of private study or research.
- You may not further distribute the material or use it for any profit-making activity or commercial gain
- You may freely distribute the URL identifying the publication in the public portal

If you believe that this document breaches copyright please contact us providing details, and we will remove access to the work immediately and investigate your claim.

Automatic Classification of Arterial and Venous Flow in Super-resolution Ultrasound Images of Rat Kidneys

Iman Taghavi¹, Sofie Bech Andersen^{2,3}, Stinne Byrholdt Sogaard³, Michael Bachmann Nielsen², Charlotte Mehlin Sørensen³, Matthias Bo Stuart¹, and Jørgen Arendt Jensen¹

¹Center for Fast Ultrasound Imaging, DTU Health Tech., Technical University of Denmark

²Department of Diagnostic Radiology, Rigshospitalet, Denmark

³Department of Biomedical Sciences, University of Copenhagen, Denmark

Abstract—Velocity is one of the clinically interesting parameters. A number of studies have shown the ability of super-resolution (SR) ultrasound imaging to visualize this parameter using velocity maps. However, manual separation of the velocity estimates for arteries from veins can be quite demanding. This study used the anatomical knowledge of rat kidneys for automatic classification of arterial and venous blood velocities in SR images and measured their variations in the medullary regions of four healthy Sprague-Dawley rat kidneys. The measurements were conducted using a modified bk5000 scanner (BK Medical, Herlev, Denmark) and a BK 9009 linear array probe with a pulse amplitude modulation scheme. Ten minutes of acquired B-mode and contrast images with frame-rate of 54 Hz were processed using a SR processing pipeline. The micro-bubble trajectories were filtered using coarse anatomy labels for classification of arterial and venous flow. The velocity estimates of separated arterioles and venules of the outer medulla showed separation of data in all rats. A Wilcoxon test showed that this difference was statistically significant ($p=0.002$). Considering the sample size for this study, the t -distributions predicted that the median velocity in the OM arterioles and venules were in the range of 0.84 ± 0.09 mm/s and 0.70 ± 0.07 mm/s with 95% confidence. The result showed how the blood flow in outer medulla arterioles and venules of rat kidneys can be automatically distinguished using the known anatomical information about the renal vasculature.

I. INTRODUCTION

Ultrasound is well known for its ability for non-invasive flow imaging. Several ultrasound imaging techniques have been used for this purpose. These methods range from color Doppler [1], power Doppler [2], vector flow imaging [3], [4] to contrast-enhanced ultrasound (CEUS) [5], and super-resolution ultrasound imaging (SRI) [6]–[9]. The latter technique enables the visualization of flow in the microvasculature. One of the biggest challenges in super-resolution (SR) ultrasound imaging is valid quantification of the huge amount of data within the *in vivo* SR images. In conventional ultrasound imaging, vessels or regions-of-interest are usually selected manually by an operator for morphological or dynamic quantification. However, the abundance of vessels in SRI makes the manual labeling or identification of arteries and veins quite demanding. In this study, we hypothesized that the prior knowledge about the anatomy of the kidney can be

used for automatic classification of arteries and veins. The hypothesis was evaluated by statistics of velocity estimations for separating arteries and veins in the medullary regions of four healthy rat kidneys.

II. METHODS

Four rat kidneys were scanned during laparotomy using a modified BK5000 scanner and X18L5s transducer (center-frequency = 6 MHz, mechanical index: 0.2, frame-rate: 54 fps). The *in vivo* kidney data were collected previously for a pilot clinical study [10] and contained 10-minute of B-mode and contrast images for each kidney. The motion-field was estimated locally using the B-mode images [11], [12], for patches of 3×3 mm with an 80% overlap. The estimated motion-field was applied to the MB positions detected in the contrast images to compensate for the tissue motion of the rat. The corrected MB positions were then tracked using a series of Kalman filters with different initial conditions to estimate tracks and velocity information [13]. The outer medulla region of the rat kidneys, as well as the arterial flow directions in these regions, were manually labeled. Fig. 1 shows an example of this labeling on the SR velocity map of a kidney, in which the red region is the outer medulla of the kidney, and the yellow arrows indicate the arterial flow directions in this region. A filtration of the track locations and flow directions automatically classified tracks to form separated arterial and venous velocity maps with opposite flow directions. The track filter excluded MBs that were out of the labeled regions or had more than a 45-degree deviation from the artery or vein flow direction. The median of the velocity estimates for the separated arterioles and venules of the outer medulla for 4 rats were compared using a Wilcoxon signed rank test. Assuming that the estimated parameter for 4 regions has a t -distribution, the confidence intervals of the median velocity in the separated arterioles and venules were also calculated and compared with each other.



Fig. 1: Anatomical labeling of the kidney: Red region is the outer medulla, and the yellow arrows indicate the arterial flow direction. The color wheel on top right corner shows the flow direction for the different colors in the velocity map (background image). The scale bar is a wavelength (λ).

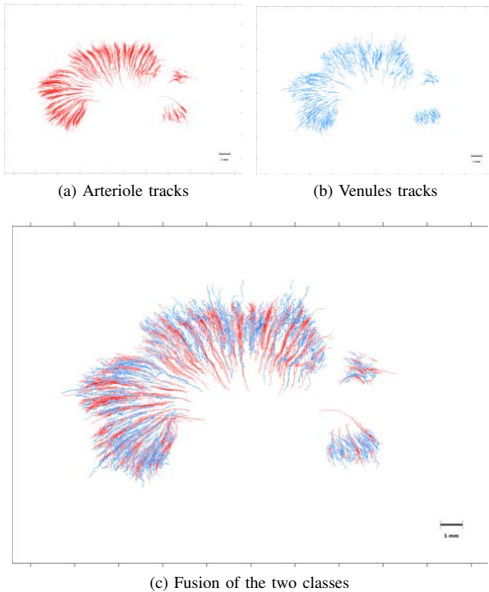


Fig. 2: Classified tracks of the outer medulla into groups of arterioles and venules

III. RESULTS AND DISCUSSION

The tracks after classification are shown in Fig. 2. The red tracks are for descending flow direction, showing the descending vasa recta. The blue tracks are showing the trajectories of MBs with opposite flow directions and depict the ascending vasa recta. Many of the MBs will be disrupted, when they are exposed to the ultrasound for a longer time. This could be explain the abundance of MBs and their trajectories in the descending vasa recta (Fig 2.a) compared with ascending ones (Fig. 2.b).

A moving average over the instantaneous blood velocity of the two groups of tracks is shown in Fig. 3, demonstrating

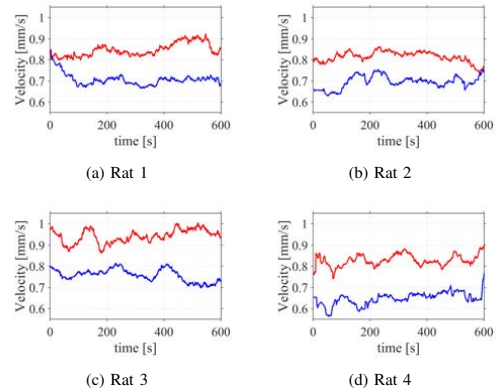


Fig. 3: The moving average blood velocity in the arterioles (red) and venules (blue) of the outer medulla in 4 healthy kidneys. The moving average window size is 1 minute. In all the cases, a lower velocity in the venules were observed.

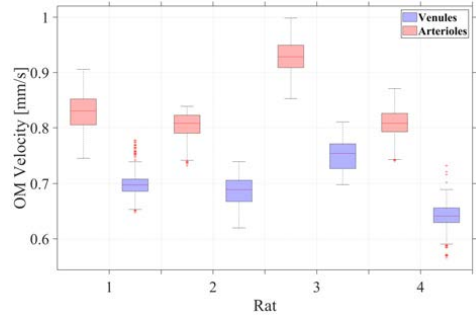


Fig. 4: Velocity distribution in the outer medulla (OM)

that the velocity of blood in the arterioles of the outer medulla was higher compared with the blood velocity in the venules. This result was consistent among all 4 rats and the Wilcoxon signed ranked test on the median velocity in the two groups of arterioles and venules of the 4 rats showed that the difference of the velocity estimates for the classified tracks were statistically significant ($p = 0.002$). This is also immediately perceivable from box plots shown in Fig. 4. The 95% confidence interval of median velocity in arterioles and venules of the outer medulla for the 4 rats were in the range of 0.84 ± 0.09 mm/s and 0.70 ± 0.07 mm/s, respectively.

IV. CONCLUSION

This paper presented a method for classification of arteries and veins based on track filtration and a priori anatomical information. The method showed that the median of estimated velocities in the classified group of tracks was statistically significantly different. In all 4 cases, the median velocity in the arterioles of the outer medulla were consistently higher than the median velocity its venules.

ACKNOWLEDGMENT

This work was financially supported by grant 82-2014-4 from the Danish National Advanced Technology Foundation, by grant 7050-00004B from Innovation Fund Denmark, and from BK Medical, Herlev, Denmark.

REFERENCES

- [1] W. N. McDicken, G. R. D. Sutherland, C. M. Moran, and L. N. Gordon, "Color Doppler velocity imaging of the myocardium," *Ultrasound Med. Biol.*, vol. 18, no. 6-7, pp. 651-654, 1992.
- [2] J. Rubin, R. Bude, P. Carson, R. Bree, and R. Adler, "Power Doppler US: a potentially useful alternative to mean frequency-based color Doppler US," *Radiology*, no. 190, pp. 853-856, 1994.
- [3] J. A. Jensen, S. I. Nikolov, A. Yu, and D. Garcia, "Ultrasound vector flow imaging I: Sequential systems," *IEEE Trans. Ultrason., Ferroelec., Freq. Contr.*, vol. 63, no. 11, pp. 1704-1721, 2016.
- [4] —, "Ultrasound vector flow imaging II: Parallel systems," *IEEE Trans. Ultrason., Ferroelec., Freq. Contr.*, vol. 63, no. 11, pp. 1722-1732, 2016.
- [5] S. B. Feinstein, B. Coll. D. Staub, D. Adam, A. F. Schinkel, J. Folkert, and K. Thomenius, "Contrast enhanced ultrasound imaging," *Journal of nuclear cardiology*, vol. 17, no. 1, pp. 106-115, 2010.
- [6] Y. Desailly, J. Pierre, O. Couture, and M. Tanter, "Resolution limits of ultrafast ultrasound localization microscopy," *Phys. Med. Biol.*, vol. 60, no. 22, pp. 8723-8740, 2015.
- [7] K. Christensen-Jeffries, R. J. Browning, M. Tang, C. Dunsby, and R. J. Eckersley, "In vivo acoustic super-resolution and super-resolved velocity mapping using microbubbles," *IEEE Trans. Med. Imag.*, vol. 34, no. 2, pp. 433-440, February 2015.
- [8] C. Errico, J. Pierre, S. Pezet, Y. Desailly, Z. Lenkei, O. Couture, and M. Tanter, "Ultrafast ultrasound localization microscopy for deep super-resolution vascular imaging," *Nature*, vol. 527, pp. 499-502, November 2015.
- [9] K. Christensen-Jeffries, O. Couture, P. A. Dayton, Y. C. Eldar, K. Hynynen, F. Kiessling, M. O'Reilly, G. F. Pinton, G. Schmitz, M. Tang *et al.*, "Super-resolution ultrasound imaging," *Ultrasound Med. Biol.*, vol. 46, no. 4, pp. 865-891, 2020.
- [10] S. B. Andersen, I. Taghavi, C. A. V. Hoyos, S. B. Sogaard, F. Gran, L. Lonn, K. L. Hansen, J. A. Jensen, M. B. Nielsen, and C. M. Sorensen, "Super-resolution imaging with ultrasound for visualization of the renal microvasculature in rats before and after renal ischemia: A pilot study," *Diagnostics*, vol. 10, no. 11, p. 862, 2020.
- [11] J. A. Jensen, S. B. Andersen, C. A. V. Hoyos, K. L. Hansen, C. M. Sorensen, and M. B. Nielsen, "Tissue motion estimation and correction in super resolution imaging," in *Proc. IEEE Ultrason. Symp.*, 2019, pp. 1-4.
- [12] I. Taghavi, S. B. Andersen, C. A. V. Hoyos, M. B. Nielsen, C. M. Sorensen, and J. A. Jensen, "In vivo motion correction in super resolution imaging of rat kidneys," *IEEE Trans. Ultrason., Ferroelec., Freq. Contr.*, p. Early Access, 2021.
- [13] I. Taghavi, S. B. Andersen, C. A. V. Hoyos, M. Schou, S. H. Oygard, F. Gran, K. L. Hansen, C. M. Sorensen, M. B. Nielsen, M. B. Stuart, and J. A. Jensen, "Tracking performance in ultrasound super-resolution imaging," in *Proc. IEEE Ultrason. Symp.*, 2020, pp. 1-4.



Paper 11

Microbubble tracking with a forward-backward strategy

Iman Taghavi, Sofie Bech Andersen, Mikkel Schou, Michael Bachmann Nielsen, Charlotte Mehlin Sørensen, Matthias Bo Stuart, and Jørgen Arendt Jensen

Published in:

Proceedings of SPIE Medical Imaging

Document Version:

Accepted

DOI:

—

General rights

Copyright and moral rights for the publications made accessible in the public portal are retained by the authors and/or other copyright owners and it is a condition of accessing publications that users recognise and abide by the legal requirements associated with these rights.

- Users may download and print one copy of any publication from the public portal for the purpose of private study or research.
- You may not further distribute the material or use it for any profit-making activity or commercial gain
- You may freely distribute the URL identifying the publication in the public portal

If you believe that this document breaches copyright please contact us providing details, and we will remove access to the work immediately and investigate your claim.

Microbubble tracking with a forward-backward strategy

Iman Taghavi¹, Sofie Bech Andersen^{2,3}, Mikkel Schou¹, Michael Bachmann Nielsen³, Charlotte Mehlin Sørensen², Matthias Bo Stuart¹, and Jørgen Arendt Jensen¹

¹Technical University of Denmark, Kgs. Lyngby, Denmark

²Department of Biomedical Sciences, University of Copenhagen, Copenhagen, Denmark

³Department of Diagnostic Radiology, Rigshospitalet, Copenhagen, Denmark

ABSTRACT

Microbubble (MB) tracking is an integral part of super-resolution ultrasound imaging by providing sharper images and enabling velocity estimation. Tracking the MBs from the last to the first frame can generate different trajectories than tracking from the first to the last frame, when the next positions of a track depends on its previous positions, *e.g.*, in Kalman-based methods. Our hypothesis is that tracking in a forward-backward manner can increase the overall tracking performance. In simulations, MB positions with a parabolic flow profile were generated inside two tubes. Three different tracking methods, including nearest-neighbor, Kalman, and hierarchical Kalman, were investigated. Using the proposed forward-backward strategy, all estimated velocity profiles for all trackers were improved and were closer to the actual velocity profiles with an improvement between 28% to 40% in the relative standard deviation (RSD) of the velocity values over 10 cross-sections of the tubes. A Sprague Dawley rat kidney was scanned for 10 minutes using a BK5000 scanner and X18L5s transducer, which is a linear array probe with 150 elements. The tracking results from the *in vivo* experiments showed that the combined image of the forward and backward tracks had 35% additional unique track positions. It showed a clear visual enhancement in the super-resolved velocity map. Overall, the improvement in visual aspects and velocity estimates suggest forward-backward strategy as an upgrade for Kalman-based trackers.

Keywords: Particle tracking, Super-resolution imaging, velocity estimation, ultrasound microscopy

1. INTRODUCTION

Super-resolution ultrasound imaging (SRI) has been introduced in recent years by a number of research groups.¹⁻⁵ The approach draws trajectories of microbubble (MB) contrast agents to visualize the microvasculature. Since conventional ultrasound is limited to the macrovasculature, SRI opens a new window of possibilities for identification of early changes in small vessel morphology and its flow dynamics. Tracking of MBs is an integral part of ultrasound SRI, as it improves the quality of the super-resolution (SR) images. Tracking also enables the estimation of blood flow speed and direction. However, tracking performance degrades in the presence of high MB concentrations and high localization uncertainty. Various particle tracking methods for optical microscopy, ranging from simple nearest-neighbor (NN) to more advanced techniques, have been objectively compared using different scenarios for tracking, and it was shown that tracking based on the Kalman (K) filtering was among the best methods in most of these scenarios.⁶ However, none of the methods performed best across all scenarios.⁶ Many of the particle tracking methods have potential for use in SRI, which is inspired by optical microscopy. The first tracking methods used for *in vivo* SRI were very simple, and included a basic maximum intensity cross-correlation within a small search window and an NN tracker.^{2,3} These studies revealed great potential for estimating MB velocities in closely packed vessels. In 2016, a modified Markov chain Monte Carlo data association was used for detection and tracking of MBs.⁴ In 2017, a partial assignment tracking based on a bipartite graph was proposed,⁷ which improved image quality in comparison with the optimal total distance assignment.⁸ The Kalman-based trackers were employed in ultrasound SRI in 2019 and 2020.^{9,10} Finally, an improvement for the K tracker by hierarchical Kalman (HK) tracking of MBs with different velocities was proposed, and its performance was compared with the NN and K trackers.^{11,12}

Further author information: (Send correspondence to Iman Taghavi)
I.T.: E-mail: imat@dtu.dk

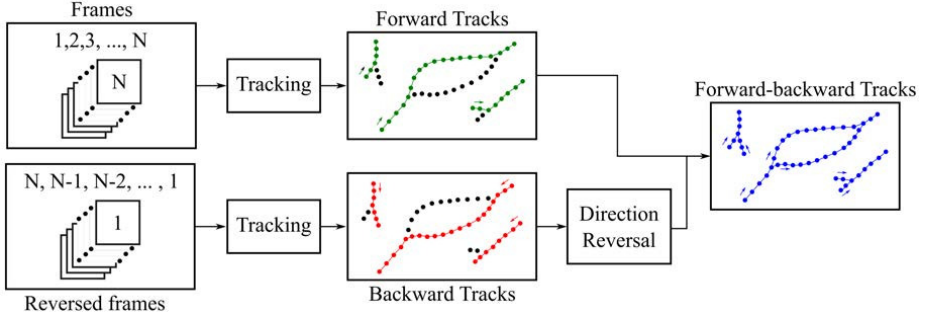


Figure 1: Block diagram for tracking MBs in a forward-backward manner

This paper investigates further improvements of the tracking performance when using backward tracks in the conventional tracking strategies. The three trackers (NN, K, and HK) were compared in both forward and forward-backward fashion through *in vivo* experiments and simulations.

2. METHOD

2.1 Tracking algorithm

The block diagram for tracking MBs in a forward-backward manner is shown in Fig. 1. The MB positions were tracked conventionally from the first to the last frame, forming the forward tracks. Next, the frames were reversed and MB positions were tracked from the last to the first frame, forming the backward tracks. The direction of tracked MBs in the backward tracks was reversed, and then inserted into an image together with the forward tracks, forming forward-backward tracks. Tracking was performed using the NN, K, and HK trackers. The following is an explanation of the general and simple Kalman model used for MB tracking. Kalman filters require certain models of the physics of the system. Simple models of blood flow suggest MBs follow the bloodstream and cannot jump into random directions. This can be modeled linearly as $\vec{r}(n) = \vec{r}(n-1) + d\vec{r}(n) + \epsilon(n)$ where $\vec{r}(n) = (r_z(n), r_x(n))^T$ is the correct MB location at frame index n , $d\vec{r}(n) = (dr_z(n), dr_x(n))^T$ is the displacement vector of the MB from frame index $n-1$ to n , and $\epsilon(n)$ is the error term for this model. According to this formulation, the new position of a MB is determined by its previous position, in addition to its displacement and an error. MB positions are assumed to be accurate and precise in order to form the Kalman filter prediction state in the above equation. Observations and measurements, however, are always subject to some noise and uncertainty. This measurements can be formulated as $\vec{r}(n) + \nu(n)$, where $\nu(n)$ is a random noise signal. In the Kalman framework, the above predictions and observations can be written as follows:

$$\begin{cases} \text{Prediction State: } \vec{a}(n) = \mathbf{F}\vec{a}(n-1) + \epsilon(n) \\ \text{Observation State: } \vec{b}(n) = \mathbf{H}\vec{a}(n) + \nu(n), \end{cases} \quad (1)$$

where $\vec{a}(n) = [\vec{r}(n), d\vec{r}(n)]^T = [r_z(n), r_x(n), dr_z(n), dr_x(n)]^T$, $\vec{b}(n)$ is the uncertain position, $\epsilon(n) \sim \mathcal{N}(0, \sigma_\epsilon^2)$ is the error for the flow model, where $\mathcal{N}(0, \sigma_\epsilon^2)$ is zero mean Gaussian distribution with standard deviation of σ_ϵ , and $\nu(n) \sim \mathcal{N}(0, \sigma_\nu^2)$ is the measurement noise, which has a standard deviation of σ_ν . According to the linear model of $\vec{r}(n) = \vec{r}(n-1) + d\vec{r}(n) + \epsilon(n)$ and measurement model $\vec{r}(n) + \nu(n)$, \mathbf{F} and \mathbf{H} are

$$\mathbf{F} = \begin{bmatrix} 1 & 0 & 1 & 0 \\ 0 & 1 & 0 & 1 \\ 0 & 0 & 1 & 0 \\ 0 & 0 & 0 & 1 \end{bmatrix}, \quad \mathbf{H} = \begin{bmatrix} 1 & 0 & 0 & 0 \\ 0 & 1 & 0 & 0 \end{bmatrix}.$$

In a Kalman filter, both prediction and observation states are used to estimate MBs' true position. When the MB positions were estimated, they were linked to the estimated positions for the next frame in a similar

Table 1: Parameters used in the hierarchical Kalman tracker

Level	1	2	3	4	5
Velocity [mm/s]	0 ~ 3	3 ~ 6	6 ~ 9	9 ~ 12	12 ~ 15
σ_ϵ	0.006	0.012	0.018	0.024	0.03
σ_ν	0.025	0.0125	0.00625	0.003125	0.0015

fashion to the NN tracker. So a Kalman tracker can be considered a location estimator that uses a Kalman filter followed by a linking stage. In both the NN and K trackers, the linking distance of $250 \mu\text{m}$ was used. The initial values of the σ_ϵ and σ_ν in the K tracker were set to $\sigma_\nu = 0.0025$ and $\sigma_\epsilon = 0.025$. The parameters were chosen experimentally by generating SR images of the kidney with different combinations of parameters and looking for visually more smooth and longer tracks. In the HK tracker, 5 levels of the Kalman filters were employed to track 5 different velocity ranges. At each level, the maximum linking distance was v_{max}/f_r , where v_{max} is the maximum of velocity range and f_r is the system frame rate. Additionally, the values of σ_ϵ and σ_ν were updated at each level as listed in Table 1. The experimental procedure of parameter tuning for the HK tracker was described in our previous study.¹²

2.2 Simulation

The MB positions inside two tubes with radii of $125 \mu\text{m}$ and $250 \mu\text{m}$ were simulated in MATLAB (Mathworks, U.S.). An average of 31 MBs per frame with a frame-rate of 55 Hz were generated for 2 minutes. The MBs inside the tubes followed a parabolic flow with peak velocities of 5 mm/s and 10 mm/s, with a uniformly random lifetime. An uncertainty in the localization was included by adding a random Gaussian error with standard deviation of $50 \mu\text{m}$ to the MB positions. The MB positions were tracked using the three different tracking algorithms. The velocity maps were obtained by inserting the tracks and the estimated velocities into a high-resolution image. The velocity profiles over 14 cross-sections of the tubes were calculated and their relative bias (RB) and relative standard deviation (RSD) were used for assessment of accuracy and precision of velocity estimation.

2.3 In vivo experiment

The *in vivo* motion-corrected data from a rat kidney were processed using the HK tracker in both the forward and forward-backward manner. The data were collected with the similar procedure as our previous clinical pilot study,¹³ and the MB positions were corrected for the tissue motion.¹⁴ The wavelength (λ) of the imaging system was $154 \mu\text{m}$. To assess the new unique track positions, forward and backward tracks were inserted into two high resolution images with a pixel size of $5 \mu\text{m}$. Then, the percentage of the new backward track positions compared with the forward tracks was calculated as

$$P_{new} = \frac{\sum_{i=1}^n \sum_{j=1}^m I_b(i, j) \bar{I}_f(i, j)}{\sum_{i=1}^n \sum_{j=1}^m I_f(i, j)} \times 100, \quad (2)$$

where I_f and I_b are the binary images of forward and backward tracks with the image dimensions of $n \times m$, and $\bar{I}_f(i, j) = 1 - I_f(i, j)$.

3. RESULTS

The velocity profiles of tracked MBs in simulations with known ground truth profiles are shown in Fig. 2. The RSD of the profiles with forward tracks was the same as the RSD in forward-backward ones, when the NN tracker was employed. On the other hand, the improvement of RSD was between 28% to 40%, when the forward-backward strategy was employed with the K and HK trackers. The RB was not affected by the forward-backward strategy.

The SR images of the cortical region of a rat kidney, shown in Fig. 3, demonstrates a clear difference between the two strategies. Fig. 3.c includes roughly double the amount of tracks in comparison with Fig. 3.a (28,681 tracks vs. 14,510 tracks). It seems that the cortical radial veins (green) and arteries (red) in the cortex were

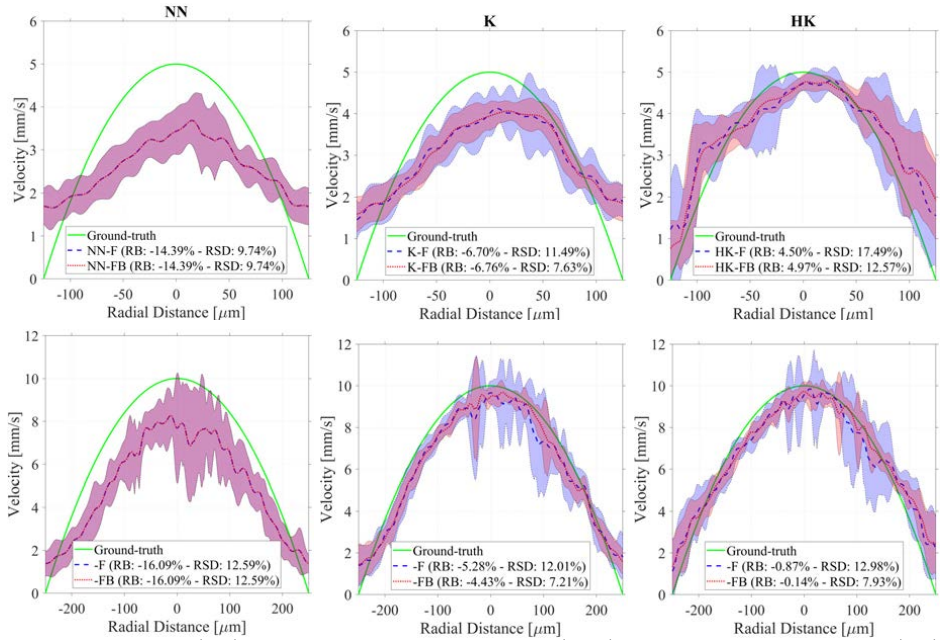


Figure 2: Relative bias (RB) and relative standard deviation (RSD) of velocity profiles of small (top) and large (bottom) tubes. The velocity is estimated using the nearest-neighbor (NN), Kalman (K), and hierarchical Kalman (HK) trackers with forward (F) and forward-backward (FB) configurations. The forward and forward-backward estimates are shown by blue and red colors, respectively. The dashed lines shows the mean profile and shaded area is the standard deviation around the mean value. The ground-truth profile is shown by the green line.

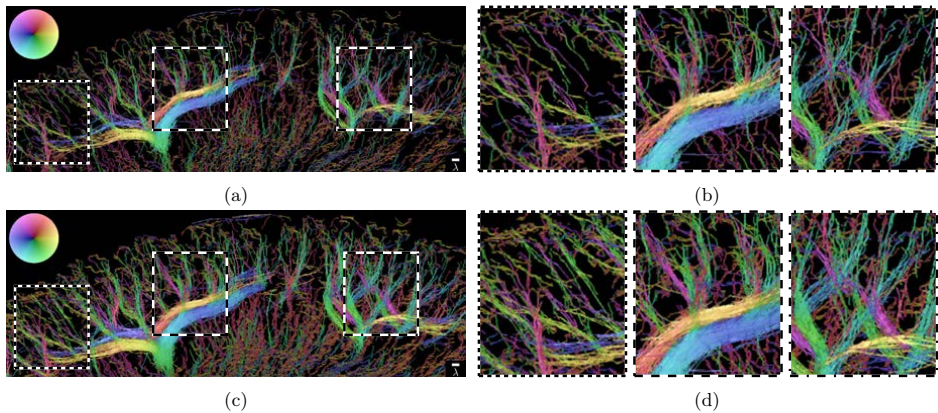


Figure 3: Super-resolved velocity map of the cortical region of a rat kidney with hierarchical Kalman tracking in (a) forward and (c) forward-backward manner. The color-wheel in the top left corner indicates the flow direction in the image. The scale bar in the bottom right is one wavelength. Three regions of (a) and (c), marked by rectangles, are zoomed in (b) and (d).

filled more with the MB trajectories in Fig. 3.c. This is shown better in the zoomed images Fig. 3.b and Fig. 3.d. Calculating new track positions for the backward tracks using (2), showed 35% additional positions that were not found in the forward tracks.

4. CONCLUSION

Tracking MBs in a forward-backward manner can improve the quality of ultrasound SR images. It also enables velocity estimation with lower RB and RSD. Simulations showed that the relative standard deviation of the velocity estimates can decrease up to 40% by adopting forward-backward strategy. In all forward-backward trackers, the velocity profiles were closer to the actual velocity profiles. Finally, the forward-backward tracking of the MBs in a rat kidney resulted in 35% additional unique track positions.

5. ACKNOWLEDGMENT

This work was financially supported by grant 82-2014-4 from the Danish National Advanced Technology Foundation, by grant 7050-00004B from Innovation Fund Denmark, and BK Medical.

REFERENCES

- [1] Desailly, Y., Pierre, J., Couture, O., and Tanter, M., “Resolution limits of ultrafast ultrasound localization microscopy,” *Phys. Med. Biol.* **60**(22), 8723–8740 (2015).
- [2] Christensen-Jeffries, K., Browning, R. J., Tang, M., Dunsby, C., and Eckersley, R. J., “In vivo acoustic super-resolution and super-resolved velocity mapping using microbubbles,” *IEEE Trans. Med. Imag.* **34**, 433–440 (February 2015).
- [3] Errico, C., Pierre, J., Pezet, S., Desailly, Y., Lenkei, Z., Couture, O., and Tanter, M., “Ultrafast ultrasound localization microscopy for deep super-resolution vascular imaging,” *Nature* **527**, 499–502 (November 2015).
- [4] Ackermann, D. and Schmitz, G., “Detection and tracking of multiple microbubbles in ultrasound B-mode images,” *IEEE Trans. Ultrason., Ferroelec., Freq. Contr.* **63**, 72–82 (January 2016).
- [5] Christensen-Jeffries, K., Couture, O., Dayton, P. A., Eldar, Y. C., Hynynen, K., Kiessling, F., O’Reilly, M., Pinton, G. F., Schmitz, G., Tang, M., et al., “Super-resolution ultrasound imaging,” *Ultrasound Med. Biol.* **46**(4), 865–891 (2020).
- [6] Chenouard, N., Smal, I., Chaumont, F. D., Maška, M., Sbalzarini, I. F., Gong, Y., Cardinale, J., Carthel, C., Coraluppi, S., Winter, M., et al., “Objective comparison of particle tracking methods,” *Nat. Methods* **11**(3), 281–290 (2014).
- [7] Song, P., Trzasko, J. D., Manduca, A., Huang, R., Kadirvel, R., Kallmes, D. F., and Chen, S., “Improved super-resolution ultrasound microvessel imaging with spatiotemporal nonlocal means filtering and bipartite graph-based microbubble tracking,” *IEEE Trans. Ultrason., Ferroelec., Freq. Contr.* **65**(2), 149–167 (2017).
- [8] Kuhn, H. W., “The Hungarian method for the assignment problem,” *Naval research logistics quarterly* **2**(1-2), 83–97 (1955).
- [9] Solomon, O., van Sloun, R. J. G., Wijkstra, H., Mischi, M., and Eldar, Y. C., “Exploiting flow dynamics for super-resolution in contrast-enhanced ultrasound,” *IEEE Trans. Ultrason., Ferroelec., Freq. Contr.* **60**(10), 1573–1586 (2019).
- [10] Tang, S., Song, P., Trzasko, J. D., Lowerison, M., Huang, C., Gong, P., Lok, U., Manduca, A., and Chen, S., “Kalman filter-based microbubble tracking for robust super-resolution ultrasound microvessel imaging,” *IEEE Trans. Ultrason., Ferroelec., Freq. Contr.* **67**(9), 1738–1751 (2020).
- [11] Taghavi, I., Andersen, S. B., Hoyos, C. A. V., Schou, M., Øygaard, S. H., Gran, F., Hansen, K. L., Sørensen, C. M., Nielsen, M. B., Stuart, M. B., and Jensen, J. A., “Tracking performance in ultrasound super-resolution imaging,” in [*Proc. IEEE Ultrason. Symp.*], 1–4 (2020).
- [12] Taghavi, I., Andersen, S. B., Schou, M., Hoyos, C. A. V., Gran, F., Nielsen, M. B., Sørensen, C. M., and Jensen, J. A., “Ultrasound super-resolution imaging with a hierarchical Kalman tracker,” *Ultrasonics* (2022).

- [13] Andersen, S. B., Taghavi, I., Hoyos, C. A. V., Søggaard, S. B., Gran, F., Lonn, L., Hansen, K. L., Jensen, J. A., Nielsen, M. B., and Sørensen, C. M., “Super-resolution imaging with ultrasound for visualization of the renal microvasculature in rats before and after renal ischemia: A pilot study,” *Diagnostics* **10**(11), 862 (2020).
- [14] Taghavi, I., Andersen, S. B., Hoyos, C. A. V., Nielsen, M. B., Sørensen, C. M., and Jensen, J. A., “In vivo motion correction in super resolution imaging of rat kidneys,” *IEEE Trans. Ultrason., Ferroelec., Freq. Contr.* **68**(10), 3082–3093 (2021).



Patent

Ultrasound Super-resolution Imaging

Jørgen Arendt Jensen, **Iman Taghavi**

Type:

US Patent Application

Document Version:

Published

Pub. No.:

US20210407043A1

General rights

Copyright and moral rights for the publications made accessible in the public portal are retained by the authors and/or other copyright owners and it is a condition of accessing publications that users recognise and abide by the legal requirements associated with these rights.

- Users may download and print one copy of any publication from the public portal for the purpose of private study or research.
- You may not further distribute the material or use it for any profit-making activity or commercial gain
- You may freely distribute the URL identifying the publication in the public portal

If you believe that this document breaches copyright please contact us providing details, and we will remove access to the work immediately and investigate your claim.



US 20210407043A1

(19) **United States**

(12) **Patent Application Publication**
Jensen et al.

(10) **Pub. No.: US 2021/0407043 A1**

(43) **Pub. Date: Dec. 30, 2021**

(54) **ULTRASOUND SUPER RESOLUTION IMAGING**

(71) Applicant: **B-K Medical ApS**, Herlev (DK)

(72) Inventors: **Jorgen Arendt Jensen**, Horsholm (DK); **Iman Taghavi**, Kongens Lyngby (DK)

(73) Assignee: **B-K Medical ApS**, Herlev (DK)

(21) Appl. No.: **16/929,398**

(22) Filed: **Jul. 15, 2020**

Related U.S. Application Data

(60) Provisional application No. 63/043,839, filed on Jun. 25, 2020.

Publication Classification

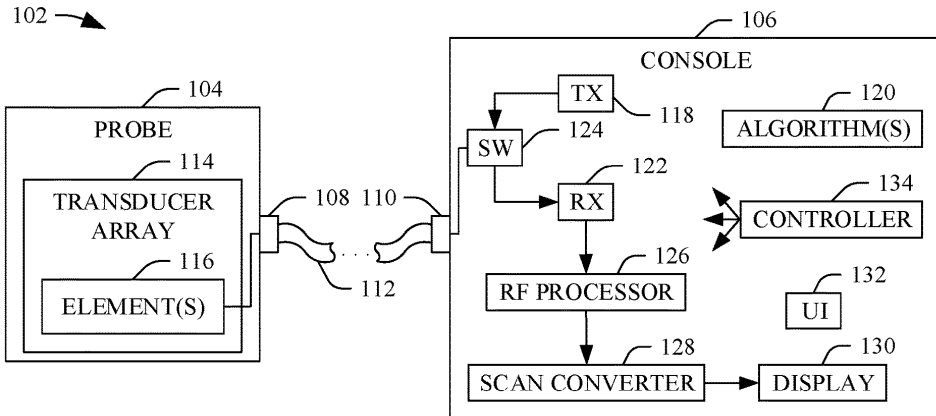
(51) **Int. Cl.**
G06T 3/40 (2006.01)
G06T 7/20 (2006.01)
G06T 7/00 (2006.01)
G06T 7/70 (2006.01)
G06T 5/00 (2006.01)
A61B 8/08 (2006.01)
A61B 8/14 (2006.01)

(52) **U.S. Cl.**

CPC *G06T 3/4053* (2013.01); *G06T 7/20* (2013.01); *G06T 7/0012* (2013.01); *G06T 7/70* (2017.01); *G06T 5/002* (2013.01); *G06T 2207/30004* (2013.01); *A61B 8/5246* (2013.01); *A61B 8/5276* (2013.01); *A61B 8/14* (2013.01); *G06T 2207/10132* (2013.01); *A61B 8/481* (2013.01)

(57) **ABSTRACT**

An apparatus includes a processor and a display. The processor includes a combiner configured to combine contrast data acquired with a same sub-aperture, for each of a plurality of sub-apertures, to create a contrast frame for each of the sub-apertures. The processor includes a microbubble detector configured to determine positions of microbubbles in the contrast frames. The processor includes a motion estimator configured to estimate a motion field based on frames of B-mode data for each of the plurality of sub-apertures. The processor includes a motion corrector configured to motion correct the positions of the microbubbles in the contrast frames based on the motion field and time delays between emissions for the sets of contrast data and the emission for B-mode data, for each of the plurality of sub-apertures, to produce motion corrected contrast frames. The display is configured to display the motion corrected contrast frames as super resolution images.



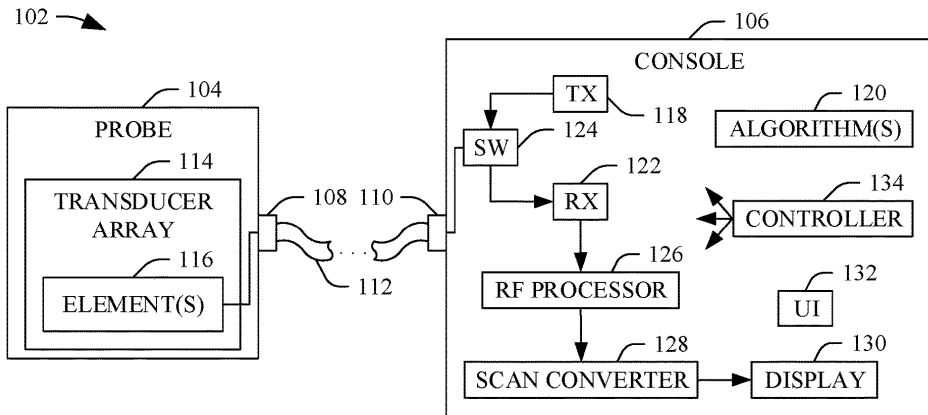


FIGURE 1

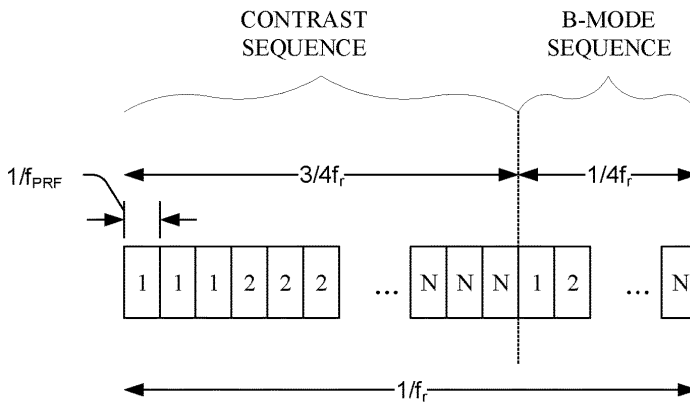


FIGURE 2

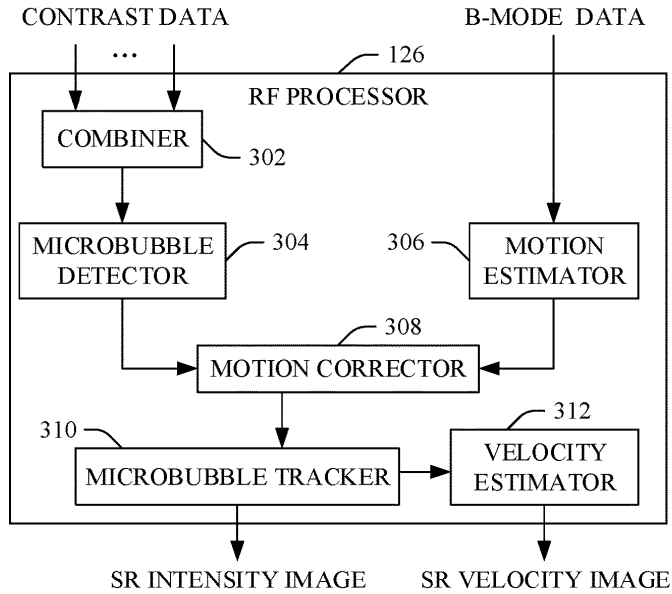


FIGURE 3

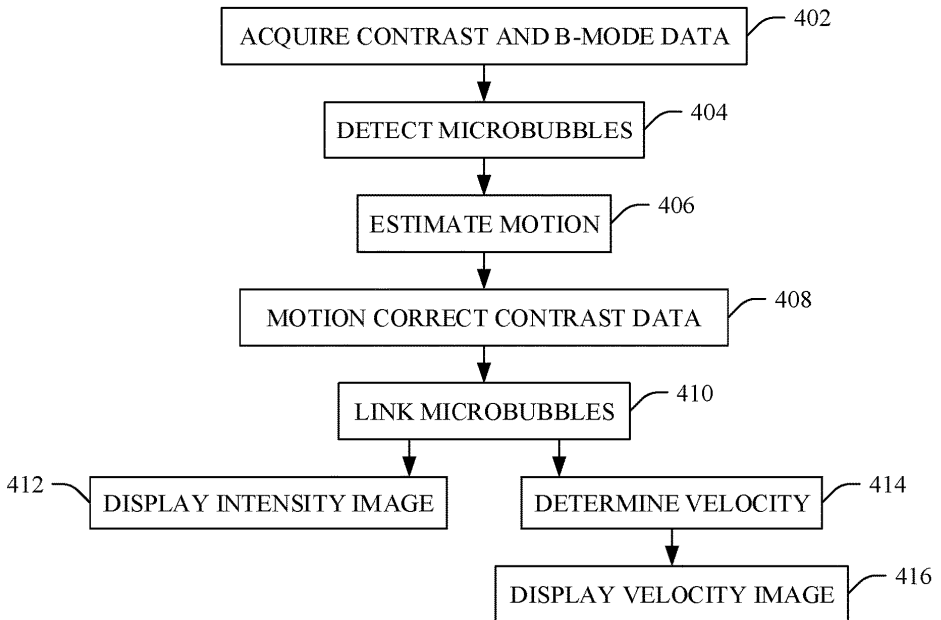


FIGURE 4

ULTRASOUND SUPER RESOLUTION IMAGING

TECHNICAL FIELD

[0001] The following generally relates to ultrasound and more particularly to ultrasound super resolution imaging.

BACKGROUND

[0002] Super resolution imaging is a technique to enhance a resolution of an image. Ultrasound super resolution imaging relies on tracking microbubbles of a microbubble based contrast agent to visualize microvasculature. However, tissue motion, e.g., from breathing, the heart beating, muscle contracting, etc., that is larger than a size of microvasculature limits the resolution of the super resolution image. For example, motion in the range of 100-200 μm in both the axial and lateral directions would limit the resolution of the ultrasound super resolution image to 100-200 μm , and vessels smaller than 100-200 μm such as microvasculature (e.g., 10 μm), would not be visible.

[0003] One motion correction scheme excludes frames with higher motion. (See J. Foiret et al., "Ultrasound localization microscopy to image and assess microvasculature in a rat kidney," Scientific Reports, vol. 7, no. 1, pp. 13 662:1-12, 2017). Another scheme combines ultrasound microscopy and dual-frequency imaging, but the B-mode frame rate is only sufficient to capture motion from breathing and more rapid movements (e.g., a beating heart) are discarded. (See T. M. Kierski et al., "Superharmonic ultrasound for motion-independent localization microscopy: Applications to microvascular imaging from low to high flow rates," IEEE Trans. Ultrason., Ferroelec., Freq. Contr., vol. 67, no. 5, pp. 957-967, 2020).

[0004] Unfortunately, the above and other approaches do not address spatial and temporal differences between the motion estimates from the B-mode frames and the contrast frames. As such, there is an unresolved need for an improved approach to super resolution imaging.

SUMMARY

[0005] Aspects of the application address the above matters, and others.

[0006] In one aspect, an apparatus included a processor and a display. The processor includes a combiner configured to combine sets of contrast data acquired with a same sub-aperture, for each of a plurality of sub-apertures, to create a contrast frame for each of the sub-apertures. The processor further includes a microbubble detector configured to determine positions of microbubbles in the contrast frames. The processor further includes a motion estimator configured to estimate a motion field based on frames of B-mode data for each of the plurality of sub-apertures. The processor further includes a motion corrector configured to motion correct the positions of the microbubbles in the contrast frames based on the motion field and time delays between emissions for the sets of contrast data and the corresponding emission for B-mode data, for each of the plurality of sub-apertures, to produce motion corrected contrast frames. The display is configured to visually display the motion corrected contrast frames, wherein the motion corrected contrast frames include super resolution images.

[0007] In another aspect, a method includes combining sets of contrast data acquired with a same sub-aperture, for

each of a plurality of sub-apertures, to create a contrast frame for each of the sub-apertures. The method further includes determining positions of microbubbles in the contrast frames. The method further includes estimating a motion field based on frames of B-mode data for each of the plurality of sub-apertures. The method further includes motion correcting the positions of the microbubbles in the contrast frames based on the motion field and time delays between emissions for the sets of contrast data and the corresponding emission for B-mode data, for each of the plurality of sub-apertures, to produce motion corrected contrast frames. The method further includes displaying the motion corrected contrast frames, wherein the motion corrected contrast frames include super resolution images.

[0008] In yet another aspect, a computer-readable storage medium storing instructions that when executed by a computer cause the computer to: combine sets of contrast data acquired with a same sub-aperture, for each of a plurality of sub-apertures, to create a contrast frame for each of the sub-apertures, determine positions of microbubbles in the contrast frames, estimate a motion field based on frames of B-mode data for each of the plurality of sub-apertures, motion correcting the positions of the microbubbles in the contrast frames based on the motion field and time delays between emissions for the sets of contrast data and the corresponding emission for B-mode data, for each of the plurality of sub-apertures, to produce motion corrected contrast frames, and display the motion corrected contrast frames, wherein the motion corrected contrast frames include super resolution images.

[0009] Those skilled in the art will recognize still other aspects of the present application upon reading and understanding the attached description.

BRIEF DESCRIPTION OF THE DRAWINGS

[0010] The application is illustrated by way of example and not limited by the figures of the accompanying drawings, in which like references indicate similar elements and in which:

[0011] FIG. 1 diagrammatically illustrates an example ultrasound system configured to generate super resolution images, in accordance with an embodiment(s) herein;

[0012] FIG. 2 illustrates an example contrast-enhanced imaging acquisition sequence for the system of FIG. 1, in accordance with an embodiment(s) described herein;

[0013] FIG. 3 diagrammatically illustrates an example configuration of the processor of the ultrasound system of FIG. 1, in accordance with an embodiment(s) described herein, and

[0014] FIG. 4 illustrates an example method, in accordance with an embodiment(s) herein.

DETAILED DESCRIPTION

[0015] FIG. 1 illustrates an example imaging system 102 such as an ultrasound imaging system/scanner. The imaging system 102 includes a probe 104 and a console 106, which interface with each other through suitable complementary hardware (e.g., cable connectors 108 and 110 and a cable 112 as shown, etc.) and/or wireless interfaces (not visible).

[0016] The probe 104 includes a transducer array 114 with one or more transducer elements 116. The transducer array 114 includes a one or two dimensional (1 or 2-D), linear, curved and/or otherwise shaped, fully populated or sparse,

etc. array. The elements **116** are configured to convert excitation electrical pulses into an ultrasound pressure field and a received ultrasound pressure field (echo) into an electrical (e.g., a radio frequency (RF)) signal. Generally, the received pressure field is in response to the transmitted pressure field interacting with matter, e.g., contrast agent microbubbles, tissue, etc.

[0017] The console **106** includes transmit circuitry (TX) **118** configured to generate the excitation electrical pulses based on an algorithm(s) **120**. For B-mode imaging, a suitable acquisition results in data that can be used to detect the linear signals from tissue (i.e. tissue data). For contrast-enhanced imaging using a contrast agent with microbubbles (which is administered to a subject prior to and/or during the scan), a suitable acquisition results in data that can be used to detect non-linear signals from the microbubbles (i.e. contrast data) and suppress the linear signals.

[0018] Briefly turning to FIG. 2, an example algorithm is illustrated. In this example, the algorithm is a contrast-enhanced imaging acquisition amplitude modulation algorithm. In FIG. 2, f_{prf} represents a pulse repetition frequency, and f_r represents an imaging framerate frequency of a complete sequence, i.e. contrast+B-mode ($4Nf_r$ in FIG. 2). The illustrated contrast-enhanced imaging acquisition amplitude modulation algorithm includes a sliding aperture of k elements, where k is an integer greater than zero. N represents a number of the sub-apertures of the sliding aperture.

[0019] For contrast data, a first sub-aperture emits three times, one with full amplitude and two with half amplitude. This is shown in FIG. 2 as three sub-aperture emission **1, 1** and **1**. The sub-aperture then slides to a next position and again emits three times. This is shown in FIG. 2 as three sub-aperture emission **2, 2** and **2**. This is repeated for the remaining N sub-apertures. For B-mode data, each of the N sub-apertures emits only once (**1, 2, . . . , N**). A time delay between contrast emissions (e.g., **1, 1** and **1**) and the corresponding B-mode emission (e.g., **1**) for a sub-aperture varies from $f_r/4$ to $3f_r/4$.

[0020] Returning to FIG. 1, the console **106** further includes receive circuitry (RX) **122** configured to process the RF signals, e.g., amplify, digitize, and/or otherwise process the RF signals. For the contrast data, the received echoes for each of the three emission provide data for enhancing the non-linear signal/microbubbles. For the B-mode data, the received echoes for each of the single emissions provide data for enhancing the linear signal/tissue.

[0021] The console **106** further includes a switch (SW) **124** configured to switch between the TX **118** and RX **122** for transmit and receive operations, e.g., by electrically connecting and electrically disconnecting the TX **118** and RX **122**. In a variation, separate switches are utilized to switch between the TX **118** and RX **122**.

[0022] The console **106** includes further an RF processor **126**. The RF processor **126** is configured to process the contrast and B-mode data to create ultrasound super resolution images. As described in greater detail below, creating contrast frames, detecting microbubbles in the contrast frames, estimating a local motion field from the B-mode frames, motion correcting the position of the microbubbles based on the local motion estimation, and registering the microbubbles across the contrast frames.

[0023] Generally, this approach utilizes a full motion field that is estimated as a function of space and time from all B-mode frames to co-register estimated tracks of microbubbles to a reference frame. In one instance, this ensures that no frame is skipped. In addition, this approach can reduce microbubble localization uncertainty relative to a configuration that does not utilize this approach.

[0024] The console **106** further includes a scan converter **128** and a display **130**. The scan converter **128** is configured to scan convert the motion corrected contrast frames and/or B-mode frames for display, e.g., by converting the motion corrected contrast frames and/or the B-mode frames to the coordinate system of the display **130**. The display **130** can display a motion corrected contrast frame and/or a B-mode frame alternately or concurrently, e.g., next to each other and/or on combined.

[0025] The console **106** further includes a user interface **132**, which includes one or more input devices (e.g., a button, a touch pad, a touch screen, etc.) and one or more output devices (e.g., a display screen, a speaker, etc.). The console **106** further includes a controller **134** configured to control one or more of the transmit circuitry **118**, the receive circuitry **122**, the switch **124**, the RF processor **126**, the scan converter **128**, the display **130**, and/or the user interface **132**.

[0026] It is to be appreciated that at least the RF processor **126** can be implemented by a hardware processor (e.g., a central processing unit (CPU), graphics processing unit (GPU), a microprocessor, etc.) executing computer readable instructions encoded or embedded on computer readable storage medium, which excludes transitory medium.

[0027] FIG. 3 diagrammatically illustrates an example configuration of the RF processor **126**.

[0028] The RF illustrated processor includes a combiner **302**. The combiner **302** is configured to combine the contrast data from the three emissions for each a sub-aperture to generate a contrast frame for the sub-aperture, for each of the sub-apertures. In one instance, this includes subtracting the data for the half amplitude acquisitions from the data for the full amplitude acquisition. Other approaches are also contemplated herein.

[0029] The RF processor further includes a microbubble detector **304**. The microbubble detector **304** is configured to determine a centroid (or other region) of each of the microbubbles in each of the contrast frames. In one instance, this includes signal-to-noise (SNR) enhancement followed by microbubble localization. For SNR Enhancement, suitable approaches include thresholding, spatial filtering (e.g. Gaussian, Laplacian of Gaussian, etc.), spatio-temporal filtering, model fitting, and/or other approaches. For localization, suitable approaches include peak detection, centroid estimation (e.g. weighted centroid, etc.), learning-based, and/or other approaches.

[0030] The RF processor further includes a motion estimator **306**. The motion estimator **306** is configured to process the B-mode frames to estimate tissue motion. In one instance, this includes using speckle tracking on the envelope data. An example of speckle tracking can be found in G. E. Trahey et al., "IEEE Trans. Biomed. Eng., vol. BME-34, no. 12, pp. 965-967, 1987. For local motion estimation, each B-mode frame is divided into a plurality of partially overlapping sub-regions, with one of the frames being identified as a reference frame. Examples of suitable sub-region sizes include, but are not limited to, 1×1 to 10×10 millimeters square (mm^2), larger, smaller, non-square, etc.

Examples of a suitable B-mode reference frame includes a B-mode frame near the middle B-mode frame and/or other B-mode frame. In another instance, more than one B-mode reference frame is utilized.

[0031] The motion estimator **306** cross-correlates each sub-region in the B-mode reference frame with the corresponding sub-region in the other B-mode frames, and motion in the axial and lateral directions is estimated. The estimated motion for each sub-region is assigned to a center (and/or other location) of the corresponding sub-region, and the collection of motion estimates for a frame provides a discrete motion field through that frame. The estimated displacements vary spatially and temporally. Motion can be estimated at any point in any frame (i.e. space and/or time) using interpolation such a 3-D spline, etc. on the 3-D motion field.

[0032] The RF processor further includes a motion corrector **308**. The motion corrector **308** is configured to apply the local motion estimates on the detected microbubble locations. By way of non-limiting example, for a detected microbubble in the kth frame at position $\hat{\vec{r}} = (z_0, x_0)$, the correct position \vec{r} of the microbubble can be approximated as shown in Equation 1:

Equation 1:

$$\vec{r} \approx \hat{\vec{r}} - \vec{M}(t, \hat{\vec{r}}),$$

where $\vec{M}(t, \vec{r})$ represents the motion field,

$$t = \frac{k-1}{f_r} - t_d(n, m),$$

where k represents the frame position, f_r represents the imaging framerate frequency, and $t_d(n, m)$ represents a time difference between an nth line of a contrast frame and an mth line of the corresponding B-mode frame. In one instance, e.g., in FIG. 2, $t_d(n, m)$ is determined as shown in Equation 2:

$$t_d(n, m) = \frac{3N_{lines} - 3n + m + 1}{f_{prf}}, \quad \text{Equation 2}$$

where n, m $\in \{1, 2, \dots, N_{lines}\}$, N_{lines} represents a number of lines in the frame, and f_{prf} represents the pulse repetition frequency.

[0033] The position of the detected microbubble at $\hat{\vec{r}} = (z_0, x_0)$ in the kth frame can be expressed as a function of the corrected microbubble position and value of the motion field at that position and time as shown in Equation 3:

$$\hat{\vec{r}} = \vec{r} + \vec{M}\left(\frac{k-1}{f_r} - t_d(\hat{n}, m), \hat{\vec{r}}\right), \quad \text{Equation 3}$$

where $\hat{\vec{r}} = (\hat{z}_0, \hat{x}_0)$ and \hat{n} are the unknown correct position and its relative image line in the contrast image, respectively. In one instance, \vec{r} is computed using an optimization techniques such as a least-squares optimization as shown in Equation 4:

$$\left[\hat{\vec{r}}, \hat{n}\right] = \underset{\vec{p}, \hat{n}}{\text{argmin}} \left\| \vec{p} - \vec{r} + \vec{M}\left(\frac{k-1}{f_r} - t_d(q, m), \vec{p}\right) \right\|_2^2, \quad \text{Equation 4}$$

where \vec{p} and q are arguments.

[0034] An example algorithm for solving Equation 4 is provided next.

Initialization:

$$N_{itr} = 0,$$

$$\hat{\vec{r}} = \vec{r}$$

$\hat{n} = m = (x_0 - x_{min}) / dx$, where x_{min} and dx are a minimum lateral position and a lateral pixel size of the frame.

- 1: while (error $\geq \epsilon_{max}$) or ($N_{itr} \leq N_{max}$) do
- 2: Calculate a time delay between the mth line of the B-mode frame and the nth line of the contrast frame

$$t_d(\hat{n}, m) = \frac{3N_{lines} - 3\hat{n} + m + 1}{f_{prf}}.$$

- 3: Update the position of the estimated microbubble

$$\hat{\vec{r}} \approx \vec{r} - \vec{M}\left(\frac{k-1}{f_r} - t_d(\hat{n}, m), \hat{\vec{r}}\right),$$

- 4: Update \hat{n}

$$\hat{n} = \frac{x_{lines(1)} - \hat{x}_0}{dx}.$$

- 5: Calculate assignment error

$$\text{error} = \left\| \hat{\vec{r}} - \vec{r} + \vec{M}\left(\frac{k-1}{f_r} - t_d(\hat{n}, m), \hat{\vec{r}}\right) \right\|_2.$$

- 6: Update iteration

$$N_{itr} = N_{itr} + 1.$$

- 7: end while

[0035] In general, the motion corrector **308** iteratively assigns motion estimates by calculating a time delay between each an image line of a contrast frame and an image line of the B-mode frame for a sub-aperture (the three emissions of the contrast sequence corresponded to the same image line as one emission in the B-mode sequence), updating a position of an estimated bubble in the contrast frame based on the motion field and the time delay, updating the image line in the contrast frame, and repeating the above until stopping criteria is satisfied or the maximum number of iterations is reached.

[0036] The RF processor further includes a microbubble tracker **310**. The microbubble tracker **310** is configured to generate tracks that link microbubbles from frame to frame. Suitable approaches include, but are not limited to, nearest-neighbor, multi-frame data structure, dynamic programming, combinatorial, multi hypothesis, explicit motion models (e.g. Kalman filtering), learning-based, and/or other techniques. Provided herein is an example approach based on Kalman filtering.

[0037] This approach can be modeled as $\vec{r}(t) = \vec{r}(t-1) + d\vec{r}(t) + \epsilon(t)$, where $\vec{r}(t) = (r_x(t), r_y(t))$ represents the position of a microbubble at time t, $d\vec{r}(t) = (dr_x(t), dr_y(t))$ represents the displacement of the microbubble, and $\epsilon(t)$ represents an

uncertainty in the displacement. This model can be formulated, e.g., within the Kalman framework as shown below:

$$\begin{cases} \text{Prediction State: } \bar{x}(t) = Fx(t-1) + \varepsilon(t) \\ \text{Observation State: } \bar{z}(t) = H\bar{x}(t) + v(t) \end{cases}, \text{ where}$$

$$x(t) = [\bar{r}(t), d\bar{r}(t)]^T = [r_z(t), r_x(t), dr_z(t), dr_x(t)]^T,$$

$$F = \begin{bmatrix} 1 & 0 & 1 & 0 \\ 0 & 1 & 0 & 1 \\ 0 & 0 & 1 & 0 \\ 0 & 0 & 0 & 1 \end{bmatrix},$$

$$H = \begin{bmatrix} 1 & 0 & 0 & 0 \\ 0 & 1 & 0 & 0 \end{bmatrix},$$

$$\varepsilon(t) \sim \mathcal{N}(0, \sigma_\varepsilon^2), \text{ and}$$

$$v(t) \sim \mathcal{N}(0, \sigma_v^2).$$

[0038] When entering the blood stream, the microbubbles have uncontrolled concentrations as well as different velocities and flow dynamics in different parts of the kidney. To track these different scenarios, a hierarchical structure of Kalman filters is utilized. Table 1 shows examples parameters for a hierarchical structure of Kalman filter.

TABLE 1

Examples parameters for a hierarchical structure of Kalman filter.					
Level	1	2	3	4	5
Velocity (mm/s)	0-3	3-6	6-9	9-12	12-15
σ_v	0,006	0,012	0,018	0,024	0,03
σ_x	0,025	0,0125	0,00625	0,003125	0,0015
Max Linking	6/ f_r	12/ f_r	18/ f_r	24/ f_r	15/ f_r
Gap-closing	3	2	2	1	1

[0039] At each level in Table 1, a Kalman filter is applied to the remaining untracked microbubbles from the previous levels. The tracked microbubbles at deeper levels have higher velocities. A maximum linking distance is a maximum acceptable distance between the estimated microbubble position by the Kalman filter and the nearest motion-corrected microbubble position in the next frame. Linking of multiple microbubbles can be performed using Hungarian assignment. If a microbubble is miss-detected over a couple of frames, the Kalman filter can predict its trajectory based on its previous detected positions. The gap closing parameter is a number of frames a microbubble can be miss-detected.

[0040] The motion-corrected and linked microbubbles provide ultrasound super resolution intensity image. In the illustrated embodiment, the RF processor 126 includes a velocity estimator 312 configured to process track locations to generate a super resolution velocity image. By way of non-limiting example, the velocity estimator 312 can be configured to determine a time derivative of track locations, which yields both the axial and lateral velocities. An axial and a lateral velocity image can then be constructed by drawing anti-aliased velocity weighted lines at the track positions. A mean velocity at each pixel in the velocity images can be found by dividing with a weighting image if it was different from zero. A Vector Flow Image (VFI) of the

microbubble can be generated by combining the axial and lateral velocity images. In another instance, the velocity estimator 312 is omitted.

[0041] It is to be appreciated that the hierarchical tracking approach described herein provides a better visualization of opposite flows and improved flow quantification, relative to a configuration that does not employ the hierarchical tracking approach. The ultrasound super resolution intensity and/or velocity images can be displayed via the display 130.

[0042] FIG. 4 illustrates an example method in accordance with an embodiment herein.

[0043] The ordering of the following acts is for explanatory purposes and is not limiting. As such, one or more of the acts can be performed in a different order, including, but not limited to, concurrently. Furthermore, one or more of the acts may be omitted and/or one or more other acts may be added.

[0044] At 402, contrast and B-mode data are acquired, as described herein and/or otherwise.

[0045] At 404, microbubbles are detected in the contrast data, as described herein and/or otherwise.

[0046] At 406, motion is estimated from the B-mode data, as described herein and/or otherwise.

[0047] Although act 404 is described before act 406, it is to be understood that act 404 can be performed before act 406 or in parallel with act 406.

[0048] At 408, the microbubbles in the contrast data are motion corrected based on the estimated motion, as described herein and/or otherwise.

[0049] At 410, the microbubble are linked between frames of the contrast data, creating a super resolution intensity image, as described herein and/or otherwise.

[0050] At 412, the super resolution intensity image is displayed, as described herein and/or otherwise.

[0051] At 414, a vector velocity is determined, as described herein and/or otherwise.

[0052] At 416, a super resolution vector velocity image is displayed, as described herein and/or otherwise.

[0053] The above may be implemented by way of computer readable instructions, encoded or embedded on computer readable storage medium (which excludes transitory medium), which, when executed by a computer processor(s) (e.g., central processing unit (CPU), microprocessor, etc.), cause the processor(s) to carry out acts described herein. Additionally, or alternatively, at least one of the computer readable instructions is carried by a signal, carrier wave or other transitory medium (which is not computer readable storage medium).

[0054] The application has been described with reference to various embodiments. Modifications and alterations will occur to others upon reading the application. It is intended that the invention be construed as including all such modifications and alterations, including insofar as they come within the scope of the appended claims and the equivalents thereof.

What is claimed is:

1. An apparatus, comprising:

a processor, including:

a combiner configured to combine sets of contrast data acquired with a same sub-aperture, for each of a plurality of sub-apertures, to create a contrast frame for each of the sub-apertures;

- a microbubble detector configured to determine positions of microbubbles in the contrast frames;
 - a motion estimator configured to estimate a motion field based on frames of B-mode data for each of the plurality of sub-apertures; and
 - a motion corrector configured to motion correct the positions of the microbubbles in the contrast frames based on the motion field and time delays between emissions for the sets of contrast data and the corresponding emission for B-mode data, for each of the plurality of sub-apertures, to produce motion corrected contrast frames; and
 - a display configured to visually display the motion corrected contrast frames, wherein the motion corrected contrast frames include super resolution images.
2. The apparatus of claim 1, wherein the motion corrector iteratively assigns motion estimates by:
- 1) calculating a time delay between each an image line of a contrast frame and an image line of the B-mode frame for a same sub-aperture;
 - 2) updating a position of an estimated bubble in the contrast frame based on the motion field and the time delay;
 - 3) updating the image line in the contrast frame; and repeating 1), 2) and 3) until stopping criteria is satisfied.
3. The apparatus of claim 1, wherein the processor further comprises:
- a microbubble tracker configured to link the microbubbles from frame to frame across the motion corrected contrast frames to produce the super resolution images.
4. The apparatus of claim 3, wherein the processor links the microbubbles across the motion corrected contrast frames based on hierarchical tracking.
5. The apparatus of claim 1, wherein the microbubble detector extracts a centroid of a microbubble to determine a position of the microbubble in a contrast frame.
6. The apparatus of claim 5, wherein the microbubble detector extracts the centroid of the microbubble by enhancing a signal-to-noise ratio of the frame and then localizing the centroid in the signal-to-noise ratio enhanced frame.
7. The apparatus of claim 1, wherein the motion estimator determines the motion field using speckle tracking on envelope data.
8. The apparatus of claim 1, wherein the motion estimator cross-correlates each of a plurality of sub-regions of a reference B-mode frame with corresponding sub-regions in the other B-mode frames, and motion in axial and lateral directions is determined.
9. The apparatus of claim 8, wherein the sub-regions are partially overlapping sub-regions.
10. The apparatus of claim 8, wherein the motion estimator assigns a motion estimate for a sub-region to a center region of the sub-region, and a collection of all of the motion estimates for all of the sub-regions of a frame is a discrete motion field through the frame.
11. The apparatus of claim 1, wherein the super resolution images includes an intensity super resolution image.
12. The apparatus of claim 1, wherein the super resolution images includes a velocity super resolution image.
13. The apparatus of claim 1, further comprising: a transducer array configured to transmit an ultrasound pressure field and receive an echo pressure field for a contrast-enhanced scan to acquire the contrast data and the B-mode data.
14. The apparatus of claim 13, wherein the processor is configured employ a pulse amplitude modulation sequence to acquire the contrast data and the B-mode data.
15. A method, comprising:
- combining sets of contrast data acquired with a same sub-aperture, for each of a plurality of sub-apertures, to create a contrast frame for each of the sub-apertures;
 - determining positions of microbubbles in the contrast frames;
 - estimating a motion field based on frames of B-mode data for each of the plurality of sub-apertures;
 - motion correcting the positions of the microbubbles in the contrast frames based on the motion field and time delays between emissions for the sets of contrast data and the corresponding emission for B-mode data, for each of the plurality of sub-apertures, to produce motion corrected contrast frames; and
 - displaying the motion corrected contrast frames, wherein the motion corrected contrast frames include super resolution images.
16. The method of claim 15, further comprising:
- 1) calculating a time delay between an image line of a contrast frame and an image line of the B-mode frame for a same sub-aperture;
 - 2) updating a position of an estimated bubble in the contrast frame based on the motion field and the time delay;
 - 3) updating the image line in the contrast frame; and repeating 1), 2) and 3) until stopping criteria is satisfied.
17. The method of claim 15, further comprising: linking the microbubbles across the motion corrected contrast frames to produce the super resolution images via a hierarchical tracking.
18. A computer-readable storage medium storing instructions that when executed by a computer cause the computer to:
- combine sets of contrast data acquired with a same sub-aperture, for each of a plurality of sub-apertures, to create a contrast frame for each of the sub-apertures;
 - determine positions of microbubbles in the contrast frames;
 - estimate a motion field based on frames of B-mode data for each of the plurality of sub-apertures; and
 - motion correcting the positions of the microbubbles in the contrast frames based on the motion field and time delays between emissions for the sets of contrast data and the corresponding emission for B-mode data, for each of the plurality of sub-apertures, to produce motion corrected contrast frames.
19. The computer-readable storage medium of claim 18, wherein, for microbubble position determination and motion correcting the positions, the instructions cause the computer to:
- 1) calculate a time delay between an image line of a contrast frame and an image line of the B-mode frame for a same sub-aperture;
 - 2) update a position of an estimated bubble in the contrast frame based on the motion field and the time delay;

3) update the image line in the contrast frame; and repeating 1), 2) and 3) until stopping criteria is satisfied.

20. The computer-readable storage medium of claim **18**, wherein the instructions further cause the computer to: link the microbubbles across the motion corrected contrast frames to produce a super resolution images via a hierarchical tracking; and display the super resolution image.

* * * * *